Multimodal imaging of holmium-loaded microspheres for internal radiation therapy

Peter R. Seevinck

Multimodal imaging of holmium-loaded microspheres for internal radiation therapy

Dissertation, Utrecht University, the Netherlands

The research described in this dissertation was carried out at the Department of Radiology and Nucleair Medicine and the Image Sciences Institute, University Medical Center Utrecht (Utrecht, the Netherlands), under the auspices of ImagO, the Graduate Programme Medical Imaging. The project was financially supported by the Dutch Technology Foundation STW under grant 06648.

ISBN:	978-90-393-5223-6
Layout:	Roy Sanders
Printing:	Gildeprint Drukkerijen B.V., Enschede
Cover:	Micro CT image of holmium-loaded microspheres lodged in the highly vascularised periphery of a Vx2 tumor in a rabbit liver
Cover design:	Roy Sanders

Multimodal imaging of holmium-loaded microspheres for internal radiation therapy

Multimodale beeldvorming van holmium-geladen microsferen voor interne radiotherapie

(met een samenvatting in het Nederlands)

Proefschrift

ter verkrijging van de graad van doctor
aan de Universiteit Utrecht
op gezag van de rector magnificus, prof.dr. J.C. Stoof,
ingevolge het besluit van het college voor promoties
in het openbaar te verdedigen
op donderdag 26 november 2009 des middags te 4.15 uur

door

Peter Roland Seevinck

geboren op 20 januari 1979
te Pretoria, Zuid-Afrika

Promotor: Prof.dr. M.A. Viergever

Co-promotor: Dr. C.J.G. Bakker

Financial support for the reproduction of this thesis was generously provided by:
Philips Healthcare, Röntgenstichting, Novartis Oncology and Veenstra instruments

Contents

Chapter 1

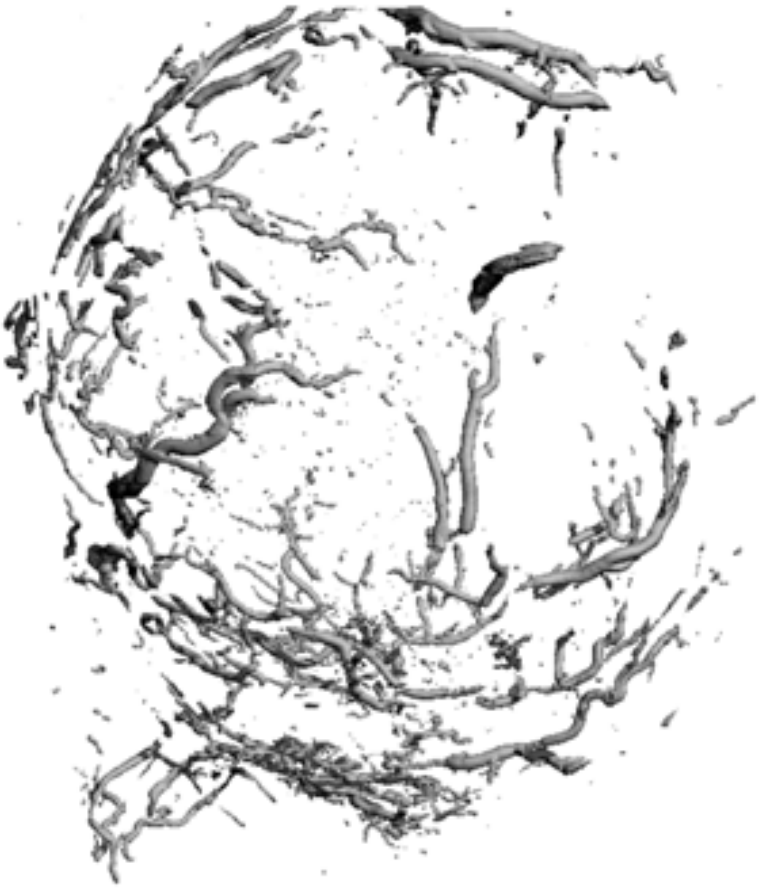

Introduction

Liver cancer, whether primary or metastatic, is a major cause of morbidity and mortality worldwide (1). A limited number of patients is eligible for surgical resection (partial hepatectomy or liver transplantation), which is the treatment option of choice (2, 3). Despite recent improvements in response rates and in median survival, the effect of systemic chemotherapy on overall survival in patients with malignant liver disease remains insignificant for most tumor types (4, 5). Promising developments in external beam radiation therapy using intensity-modulated radiotherapy were reported (6), however, due to the low tolerance of healthy liver parenchyma to radiation the role of external radiotherapy remains limited. A relatively novel radiotherapy treatment option, aiming to increase radiation dose to malignant tissue while reducing radiation exposure to healthy liver tissue, is selective internal radiation therapy using microspheres loaded with the high-energy beta-emitting radioisotope yttrium-90 (^{90}Y). In this treatment modality, often referred to as radioembolization, ^{90}Y-microspheres (^{90}Y-MS) are administered directly into the hepatic artery using a catheter. Targeting of tumors is accomplished by exploiting the predominance of the arterial blood supply to liver tumors, while normal parenchyma largely depends on portal blood supply (7, 8). This results in a high tumor-to-liver ratio, leading to an increased radiation dose to the tumor tissue while minimizing exposure to healthy liver parenchyma (9, 10). To date, over 10,000 patients have undergone ^{90}Y radioembolization and high response rates have been reported, but the effect on overall survival has not been established yet (11-14).

An essential element of successful radioembolization of hepatic malignancies is preprocedural biodistribution assessment. The large variation in vascularity of tumor and liver tissue observed between patients, including possible arteriovenous shunting, necessitates extensive treatment planning, to assure a favorable dose distribution in each individual patient (15, 16). A disadvantage of ^{90}Y-MS is the lack of high quality imaging opportunities, preventing direct biodistribution assessment, dosimetry and real-time feedback during microsphere instillation. Instead, image-based preprocedural treatment planning and dosimetry is performed using planar scintigraphy and single photon computed tomography (SPECT) scans of technetium 99m (^{99m}Tc) macroaggregated albumin (MAA) particles as a surrogate. However, ^{99m}Tc-MAA offer a rather poor approximation of the ^{90}Y-MS biodistribution in the liver (15, 17), which may be attributed to the differences in size, density, integrity and hemodynamic properties of ^{99m}Tc-MAA as compared to ^{90}Y-MS.

In the mid-nineties, researchers at the Department of Nuclear Medicine of the University Medical Center Utrecht started the development of holmium-166 loaded poly (L-lactic acid) microspheres (^{166}Ho-PLLA-MS) (18, 19), an alternative radioembolization microdevice possessing favorable radiation characteristics as well as imaging possibilities (20). The radioisotope ^{166}Ho emits high-energy beta particles, allowing for local radiation therapy (21, 22), and low-energy gamma rays suitable for quantitative nuclear imaging using SPECT (23). Currently, quantitative SPECT is the method of choice for hepatic arterial radioembolization treatment planning with ^{166}Ho-PLLA-MS (23-25), fully exploiting the high sensitivity of the imaging modality. Clinical SPECT imaging, however, has a low resolution, long acquisition times and does not provide anatomical reference. Interestingly, being a lanthanide, the element holmium is highly paramagnetic and has a high linear attenuation coefficient, allowing for visualization by magnetic resonance imaging (MRI) (26, 27) and X-ray computed tomography (CT) (28), respectively. In particular MRI, with its superior soft tissue contrast and high image resolution, is an attractive imaging modality for planning, image-guidance and evaluation of hepatic arterial radioembolization with ^{166}Ho-PLLA-MS. Pioneering work performed in the last decade by the Departments of Nuclear Medicine and Radiology (18, 27, 29-31) demonstrated the multimodal imaging opportunities of ^{166}Ho-PLLA-MS, which opened up a promising and challenging but largely unexplored field of research.

In this dissertation, the qualitative and quantitative multimodal imaging possibilities of ^{166}Ho-PLLA-MS are explored and exploited to improve biodistribution assessment and dose calculations for planning, image-guidance and evaluation of hepatic arterial radioembolization of liver malignancies, both on microscopic and on macroscopic scale.

Outline

The dissertation is organized as follows: **Chapter 2** gives an overview of the factors that influence sensitivity and detection limits of multimodal diagnostic and therapeutic agents in general, focusing on MRI, CT and SPECT. In vitro experiments were performed to investigate the multimodal imaging opportunities of ^{166}Ho-PLLA-MS in particular. **Chapter 3** reports on the development and characterization of microspheres with ultra high holmium content, aiming to increase specific activity for therapeutic purposes and enhance multimodal diagnostic properties for SPECT, MRI and CT. In **Chapter 4** microCT was explored on its capabilities to qualitatively and quantitatively assess the 3D biodistribution of ^{166}Ho-PLLA-MS after radioembolization of Vx2 tumor in a rabbit liver on a microscopic level. Chapters 5 and 6 present qualitative results obtained with two MR-based positive contrast techniques. In **Chapter 5** susceptibility gradient mapping was investigated on its ability to selectively depict Ho-PLLA-MS in liver tissue both ex vivo and in vivo in the presence of macroscopic magnetic field distortions. **Chapter 6** presents a novel positive contrast technique, radial sampling with off-resonance reception (RASOR), which will be shown to accurately depict and localize small paramagnetic objects, such as brachytherapy seeds and biopsy needles, with high positive contrast while suppressing long T_2^* components. In **Chapters 7, 8 and 9**, MR methodologies are presented aiming to improve quantitative assessment of the distribution of Ho-PLLA-MS in liver tissue. **Chapter 7** demonstrates that sampling of the free induction decay is superior to sampling of the SE for T_2^*-based quantification of Ho-PLLA-MS, due to its insensitivity to diffusion effects. **Chapter 8** presents a method which increases the upper detection limit of the Ho-PLLA-MS concentration by estimating the S_0 value of the signal decay curve to be used in the quantitative fitting procedure. In **Chapter 9**, the influence of strongly magnetized micro-sized particles subjected to diffusion on MR signal behavior was investigated theoretically, experimentally and using Monte Carlo simulations, to accurately predict transverse relaxivity for MR-based quantification **Chapter 10** demonstrates the feasibility of MR-based dosimetry of ^{166}Ho-PLLA-MS, in an anthropomorphic gel phantom and indicates the potential of MR-based dosimetry for the planning, guidance and evaluation of transcatheter radioembolization of hepatic malignancies.

References

1. Parkin DM, Bray F, Ferlay J, Pisani P. Global cancer statistics, 2002. CA Cancer J Clin **2005**;55(2):74-108.
2. Yamane B, Weber S. Liver-directed treatment modalities for primary and secondary hepatic tumors. Surg Clin North Am **2009**;89(1):97-113, ix.
3. Vibert E, Canedo L, Adam R. Strategies to treat primary unresectable colorectal liver metastases. Semin Oncol **2005**;32(6 Suppl 8):33-39.
4. Adam R, Wicherts DA, de Haas RJ, Ciacio O, Levi F, Paule B, Ducreux M, Azoulay D, Bismuth H, Castaing D. Patients with initially unresectable colorectal liver metastases: is there a possibility of cure? J Clin Oncol **2009**;27(11):1829-1835.
5. Edeline J, Raoul JL, Vauleon E, Guillygomac'h A, Boudjema K, Boucher E. Systemic chemotherapy for hepatocellular carcinoma in non-cirrhotic liver: a retrospective study. World J Gastroenterol **2009**;15(6):713-716.
6. Eccles CL, Bissonnette JP, Craig T, Taremi M, Wu X, Dawson LA. Treatment planning study to determine potential benefit of intensity-modulated radiotherapy versus conformal radiotherapy for unresectable hepatic malignancies. Int J Radiat Oncol Biol Phys **2008**;72(2):582-588.
7. Bierman HR, Byron RL, Jr., Kelley KH, Grady A. Studies on the blood supply of tumors in man. III. Vascular patterns of the liver by hepatic arteriography in vivo. J Natl Cancer Inst **1951**;12(1):107-131.
8. Breedis C, Young G. The blood supply of neoplasms in the liver. Am J Pathol **1954**;30(5):969-977.
9. Campbell AM, Bailey IH, Burton MA. Tumour dosimetry in human liver following hepatic yttrium-90 microsphere therapy. Phys Med Biol **2001**;46(2):487-498.
10. Kennedy AS, Nutting C, Coldwell D, Gaiser J, Drachenberg C. Pathologic response and microdosimetry of (90)Y microspheres in man: review of four explanted whole livers. Int J Radiat Oncol Biol Phys **2004**;60(5):1552-1563.
11. Kennedy AS, Coldwell D, Nutting C, Murthy R, Wertman DE, Jr., Loehr SP, Overton C, Meranze S, Niedzwiecki J, Sailer S. Resin 90Y-microsphere brachytherapy for unresectable colorectal liver metastases: modern USA experience. Int J Radiat Oncol Biol Phys **2006**;65(2):412-425.
12. Salem R, Thurston KG. Radioembolization with yttrium-90 microspheres: a state-of-the-art brachytherapy treatment for primary and secondary liver malignancies: part 3: comprehensive literature review and future direction. J Vasc Interv Radiol **2006**;17(10):1571-1593.
13. van Hazel G, Blackwell A, Anderson J, Price D, Moroz P, Bower G, Cardaci G, Gray B. Randomised phase 2 trial of SIR-Spheres plus fluorouracil/leucovorin chemotherapy versus fluorouracil/leucovorin chemotherapy alone in advanced colorectal cancer. J Surg Oncol **2004**;88(2):78-85.
14. Vente MAD, Wondergem M, van der Tweel I, van den Bosch MAAJ, Zonnenberg BA, Lam MGEH, van het Schip AD, Nijsen JFW. Yttrium-90 microsphere radioembolization for the treatment of liver malignancies: a structured meta-analysis. Eur Radiol **2008**.

15. Gupta T, Virmani S, Neidt TM, Szolc-Kowalska B, Sato KT, Ryu RK, Lewandowski RJ, Gates VL, Woloschak GE, Salem R, Omary RA, Larson AC. MR Tracking of Iron-labeled Glass Radioembolization Microspheres during Transcatheter Delivery to Rabbit VX2 Liver Tumors: Feasibility Study. Radiology **2008**;249(3):845-854.
16. Vente MAD, Hobbelink MGG, van het Schip AD, Zonnenberg BA, Nijsen JFW. Radionuclide liver cancer therapies: from concept to current clinical status. Anticancer Agents Med Chem **2007**;7(4):441-459.
17. Dhabuwala A, Lamerton P, Stubbs RS. Relationship of 99mtechnetium labelled macroaggregated albumin (99mTc-MAA) uptake by colorectal liver metastases to response following Selective Internal Radiation Therapy (SIRT). BMC Nucl Med **2005**;5:7.
18. Nijsen JFW. Radioactive holmium poly(L-lactic acid) microspheres for trearment of liver malignancies [dissertation]. Utrecht University, The Netherlands; **2004**.
19. Nijsen JFW, Zonnenberg BA, Woittiez JR, Rook DW, Swildens-van Woudenberg IA, van Rijk PP, van het Schip AD. Holmium-166 poly lactic acid microspheres applicable for intra-arterial radionuclide therapy of hepatic malignancies: effects of preparation and neutron activation techniques. Eur J Nucl Med **1999**;26(7):699-704.
20. Zielhuis SW. Lanthanide bearing radioactive particles for cancer therapy and multimodality imaging [dissertation]. Utrecht University, The Netherlands; **2009**.
21. Mumper RJ, Ryo UY, Jay M. Neutron-activated holmium-166-poly (L-lactic acid) microspheres: a potential agent for the internal radiation therapy of hepatic tumors. J Nucl Med **1991**;32(11):2139-2143.
22. Nijsen JF, Zonnenberg BA, Woittiez JR, Rook DW, Swildens-van W, I, van Rijk PP, van het Schip AD. Holmium-166 poly lactic acid microspheres applicable for intra-arterial radionuclide therapy of hepatic malignancies: effects of preparation and neutron activation techniques. Eur J Nucl Med **1999**;26(7):699-704.
23. de Wit TC, Xiao J, Nijsen JF, van het Schip FD, Staelens SG, van Rijk PP, Beekman FJ. Hybrid scatter correction applied to quantitative holmium-166 SPECT. Phys Med Biol **2006**;51(19):4773-4787.
24. Vente MAD, Nijsen JFW, de Wit TC, Seppenwoolde JH, Krijger GC, Seevinck PR, Huisman A, Zonnenberg BA, Van den Ingh TSGAM, van het Schip AD. Clinical effects of transcatheter hepatic arterial embolization with holmium-166 poly(L: -lactic acid) microspheres in healthy pigs. Eur J Nucl Med Mol Imaging **2008**;35(7):1259-1271.
25. Vente MAD. Preclinical studies on holmium-166 poly(L-lactic acid) microspheres for hepatic arterial radioembolization [dissertation]. Utrecht University, The Netherlands; 2009.
26. Nijsen JF, Seppenwoolde JH, Havenith T, Bos C, Bakker CJ, van het Schip AD. Liver tumors: MR imaging of radioactive holmium microspheres--phantom and rabbit study. Radiology 2004;231(2):491-499.

27. Seppenwoolde JH, Nijsen JF, Bartels LW, Zielhuis SW, van het Schip AD, Bakker CJ. Internal radiation therapy of liver tumors: qualitative and quantitative magnetic resonance imaging of the biodistribution of holmium-loaded microspheres in animal models. Magn Reson Med **2005**;53(1):76-84.
28. Schmitz SA, Wagner S, Schuhmann-Giampieri G, Krause W, Bollow M, Wolf KJ. Gd-EOB-DTPA and Yb-EOB-DTPA: two prototypic contrast media for CT detection of liver lesions in dogs. Radiology **1997**;205(2):361-366.
29. Nijsen JFW, Seppenwoolde JH, Havenith T, Bos C, Bakker CJG, van het Schip AD. Liver tumors: MR imaging of radioactive holmium microspheres--phantom and rabbit study. Radiology **2004**;231(2):491-499.
30. Seppenwoolde JH, Bartels LW, van der WR, Nijsen JF, van het Schip AD, Bakker CJ. Fully MR-guided hepatic artery catheterization for selective drug delivery: a feasibility study in pigs. J Magn Reson Imaging **2006**;23(2):123-129.
31. Seppenwoolde JH. Magnetic Susceptibility Effects in Diagnostic and Interventional MRI [dissertation]. Utrecht University, The Netherlands; **2009**.

Chapter 2

P.R. Seevinck, J-H Seppenwoolde, T.C. de Wit, J.F.W. Nijsen, F.J. Beekman, A.D. van het Schip, and C.J.G. Bakker

Anti-Cancer Agents in Medicinal Chemistry 2007;7:317-334

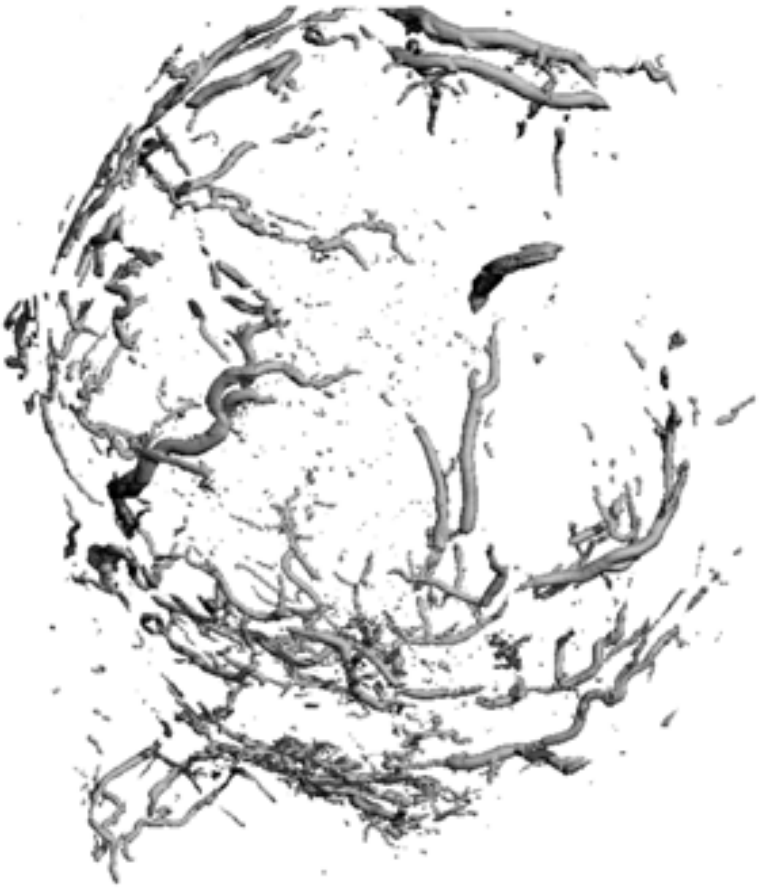

Factors affecting the sensitivity and detection limits of MRI, CT, and SPECT for multimodal diagnostic and therapeutic agents

Abstract

Noninvasive imaging techniques like magnetic resonance imaging (MRI), computed tomography (CT) and single photon emission computed tomography (SPECT) play an increasingly important role in the diagnostic workup and treatment of cancerous disease. In this context, a distinct trend can be observed towards the development of contrast agents and radiopharmaceuticals that open up perspectives on a multimodality imaging approach, involving all three aforementioned techniques. To promote insight into the potentialities of such an approach, we prepared an overview of the strengths and limitations of the mentioned imaging techniques, in particular with regard to their capability to quantify the spatial distribution of a multimodal diagnostic agent. To accomplish this task, we used a two-step approach.

In the first step, we examined the situation for a particular therapeutic anti-cancer agent with multimodal imaging opportunities, viz. holmium-loaded microspheres (HoMS). Phantom experiments were performed to enable a comparative evaluation of the three modalities assuming the use of standard equipment, standard clinical scan protocols, and signal-known-exactly conditions. These phantom data were then analyzed so as to obtain first order estimates of the sensitivity and detection limits of MRI, CT and SPECT for HoMS.

In the second step, the results for HoMS were taken as a starting point for a discussion of the factors affecting the sensitivity and detection limits of MRI, CT and SPECT for multimodal agents in general. In this, emphasis was put on the factors that must be taken into account when extrapolating the findings for HoMS to other diagnostic tasks, other contrast agents, other experimental conditions, and other scan protocols.

1. Introduction

Noninvasive imaging techniques like magnetic resonance imaging (MRI), computed tomography (CT) and nuclear imaging techniques (single photon emission computed tomography (SPECT), positron emission tomography (PET)) play an increasingly important role in the diagnostic workup and treatment of cancerous disease (1-6). In this context, a distinct trend can be observed towards the development of multimodal scanning hardware (i.e. CT/ PET, CT/ SPECT, X-ray/ MRI (XMR)) (7-13) as well as contrast agents and radiopharmaceuticals (14-16) that open up perspectives on a multimodality imaging approach. A multimodal approach may yield a better understanding of clinical situations by allowing a natural integration of functional (MRI, SPECT, PET) and anatomical (CT, MRI) information (6, 17-19). A more detailed characterization of pathology, morphology and physiology of the diseased structure will be possible. Furthermore, multimodal agents allow validation and integration of new diagnostic and therapeutic procedures by enabling quantification of the biodistribution of the agent, using different imaging modalities (20, 21). Since each imaging modality possesses different ranges of sensitivity and detectability, they can be used in a complementary way (18). In addition, a multimodality approach is expected to pay off for real-time monitoring drug delivery and image-guided drug therapy (22, 23). Ultimately, multimodal agents in combination with multimodal imaging could replace several conventional agents and imaging techniques and fulfill a crucial role in the treatment of a wide spectrum of cancerous disease (16, 23, 24).

To date, essentially two types of multimodal agents have been proposed: combined agents and single agents. In the former, the multimodal character is established by a system linking separate contrast agents together. Most agents of this type are constructed using a carrier system. Possible carrier systems include microspheres, liposomes, and living cells (14, 22, 25-30). These systems are frequently used to monitor physiological processes in vivo, revealing cellular and molecular pathways in living organisms, using medical imaging modalities such as MRI, nuclear imaging techniques (SPECT, PET), X-ray CT, optical imaging and ultrasound imaging. In the field of molecular and cellular imaging, molecular imaging probes are coupled to specific antibodies or cells so as to create image contrast at locations specific for the used antibody or cells (31-33). This allows the investigator to monitor all sorts of biological processes including gene expression, cell migration, and drug effects (31, 34-36). In the second type of multimodal agents, the multimodal character of the agent finds its origin in the combination of physical properties of a single element. Elements of the group of lanthanides, for instance, possess a high magnetic susceptibility and a high atomic number

(16, 37, 38), which potentially makes them bimodal contrast agents for MRI and CT. This has been demonstrated for several lanthanides, including gadolinium, dysprosium, ytterbium, europium and holmium (37, 39-43). Lanthanides, however, are also used for therapeutic purposes, especially for internal radiation therapy with beta particles. Interestingly, some of these radioactive lanthanides, including dysprosium, lutetium and holmium, also emit γ-rays which makes them amenable to nuclear imaging (44-47). In principle, holmium, dysprosium and terbium can be used as multimodal diagnostic agents in MRI, CT and SPECT. So far, only few attempts to exploit the multimodal character of these elements have been reported in the literature (16, 23, 24, 48, 49).

A typical example of a multimodal imaging approach is given in Figure 1, showing an excised rabbit liver embolized with holmium-loaded microspheres (HoMS) (23). The images in Figure 1 illustrate the possibilities of HoMS as a multimodal diagnostic agent as well as the different modality-specific imaging properties, regarding image resolution, soft tissue contrast, sensitivity, detectability and anatomical background. The implications of the differences in imaging properties of MRI, CT and SPECT on the diagnostic value of a multimodal agent will be examined in this paper.

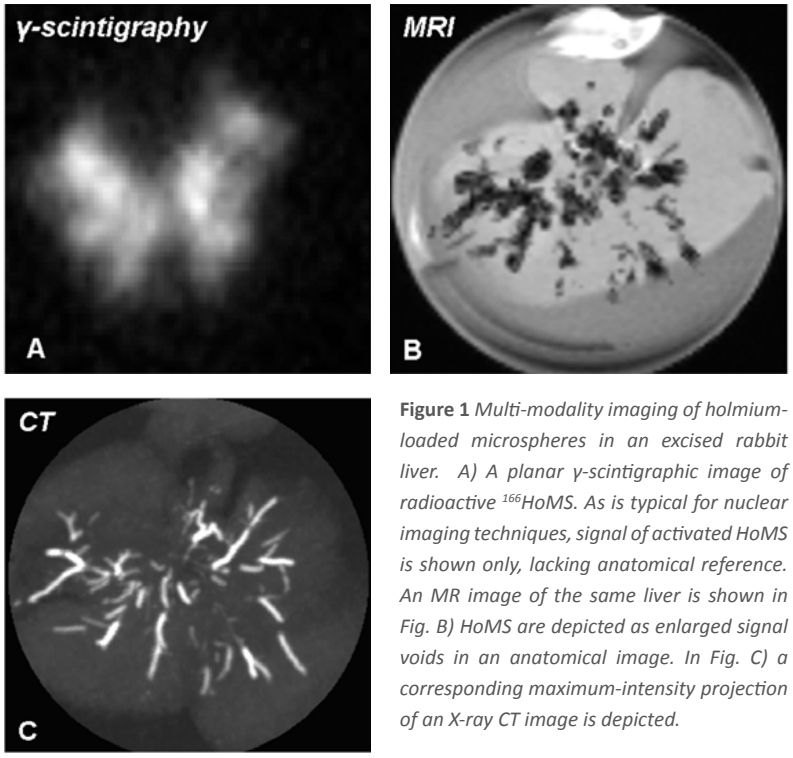

Figure 1 *Multi-modality imaging of holmium-loaded microspheres in an excised rabbit liver. A) A planar γ-scintigraphic image of radioactive ^{166}HoMS. As is typical for nuclear imaging techniques, signal of activated HoMS is shown only, lacking anatomical reference. An MR image of the same liver is shown in Fig. B) HoMS are depicted as enlarged signal voids in an anatomical image. In Fig. C) a corresponding maximum-intensity projection of an X-ray CT image is depicted.*

Observing the rapidly growing interest in multimodality imaging and our own involvement in this field (16, 23, 24), we thought it would be an interesting and possibly rewarding exercise to prepare an overview of the strengths and limitations of the various imaging techniques, in particular with regard to their capability to quantify the spatial distribution of a multimodal agent. To accomplish this task, we decided to restrict ourselves to MRI, CT and SPECT and to adopt a two-step approach.

In the first step, we examine the situation for a particular therapeutic anti-cancer agent with multimodal imaging opportunities, viz. holmium-loaded microspheres (46). In this, we start with a short introduction to internal radiation therapy of liver malignancies, focused on the potential of HoMS as a therapeutic and diagnostic agent (Section 2). Then we take a closer look at the basics of MRI, CT and SPECT, describe the mechanisms by which HoMS acts as a contrast agent or tracer in these imaging modalities, and summarize the phantom experiments that were performed to enable a comparative evaluation of the three modalities assuming the use of standard equipment, standard clinical scan protocols, and signal-known-exactly conditions (Section 3). In Section 4, we analyze the phantom data so as to obtain first order estimates of the sensitivity and detection limits of MRI, CT and SPECT for HoMS for this simple diagnostic task.

In the second step (Section 5), we take the results obtained for HoMS as a starting point for a discussion of the factors affecting the sensitivity and detection limits of MRI, CT and SPECT for multimodal agents in general. In this part, emphasis will be put on the factors that must be taken into account when extrapolating the findings to other diagnostic tasks, other agents, other experimental conditions, and other scan protocols.

2. Holmium-loaded microspheres

In the first part of our study (Sections 2-4), the performance of MRI, CT and SPECT for HoMS will be examined. This choice was motivated by the fact that HoMS represents an agent of the single element type and can be considered a multimodal agent par excellence. On the one hand, HoMS has great potential as a therapeutic agent for internal radionuclide therapy of tumors since activated HoMS (Ho-166) emits high-energy β-particles. On the other hand, HoMS displays all the properties of a true multimodal diagnostic agent since it is strongly paramagnetic (MRI) has a high linear attenuation coefficient (CT) and, when activated, emits γ-rays (SPECT). However, when comparing the sensitivity and detectability of HoMS on MRI, CT or SPECT with the sensitivity and detectability of “monomodal” diagnostic agents, one should bear in mind that these agents

are optimized for the particular imaging modality and task. In contrast, HoMS is primarily a therapeutic agent for intra-arterial radiation therapy and has not been optimized to operate as a multimodal diagnostic agent.

In the following, we will provide some background information with regard to the potential application of activated HoMS for internal radiation therapy of liver tumors and describe how HoMS are currently being prepared and activated.

Internal radiation therapy of liver tumors with HoMS

Primary and metastatic liver tumors represent a difficult clinical challenge with regard to treatment and management. The prognosis for patients suffering from malignant hepatic tumors is limited and depends on the stage of the disease and the number of lesions, which determines the possible treatment. The currently available treatment options for these tumors include surgical resection, conventional chemotherapy and external beam radiation therapy. Surgical resection of malignant hepatic tumors clearly improves the patients prognosis, but is suitable in only 20 % of all cases (50, 51). External beam radiation therapy plays no role of significance in the treatment of non-resectable hepatic tumors because of radiation dose limitations on healthy liver tissue (52, 53). Conventional chemotherapy has shown limited improvement in patient survival (54, 55). An alternative treatment option for malignant hepatic tumors is selective internal radiation therapy by intra-arterial administration of radionuclides (45, 56). In the Department of Nuclear Medicine of the University Medical Center of Utrecht, The Netherlands, the use of radioactive HoMS for internal radiation therapy was investigated since the mid-nineties. This involvement in HoMS research has led to improvements in the preparation and characterization of HoMS for intra-arterial radionuclide therapy of hepatic malignancies (46, 57, 58). In addition, we were able to successfully demonstrate tumor targeting by selective delivery of activated HoMS in various animal models using nuclear imaging techniques and MRI (23, 24, 59). These studies have shown the potential of HoMS as a multimodal diagnostic agent as well as a therapeutic anti-cancer agent with many tentative applications, including pre-imaging of the biodistribution, image guided therapy, image fusion and verification and evaluation quantitative imaging techniques (23-25).

Activation of HoMS by neutron irradiation causes only a small fraction of Ho-165 to be activated into Ho-166. Ho-166 (t1/2 = 26.8h) emits high energy b-particles (E_{max} = 1.77 MeV (49 %)/ E_{max} = 1.85 MeV (50 %)), which is attractive for internal radionuclide therapy of tumors. The maximum range of b-particles in soft tissue is 8.6 mm (effective range is 2.2 mm), which is adequate for

therapeutic use. As said before, activated HoMS emit γ-rays (80.6 keV, 6.7 %) as well, suitable for imaging with a SPECT system. Activated HoMS are delivered to the hepatic tumor through a catheter placed in the hepatic artery (24, 60). Since liver tumors are fed primarily by the arterial blood supply and the healthy liver tissue predominantly by the portal venous system, intra-arterially administered HoMS mainly reach tumors. The microspheres are unable to traverse the tumor vasculature because of their size and therefore mainly lodge in the periphery of the tumor, leading to a specific distribution of HoMS within the liver. An average tumor-to-liver ratio of about 6:1 is obtained following selective intra-arterial administration of microspheres (59-62). Such a distribution of activated HoMS locally induces radiation damage to the tumor while minimizing the damage to most of the healthy liver tissue.

Preparation and activation of HoMS

The holmium microspheres that are currently being tested in preclinical investigations (23, 24) – and that we used in our phantom experiments (Section 3) – are prepared by means of a solvent evaporation technique, incorporating holmium-acetylacetonate into poly(L-lactic acid), resulting in holmium-loaded microspheres with a size distribution of 20-50 mm after sieving (Figure 2a), a density of 1.4 g/ml and a reproducible Ho-165 content of 17% ± 0.6 % by weight (46). Figure 2b shows a scanning electron micrograph of the resulting HoMS. Activation of Ho-165 into Ho-166 is accomplished by neutron irradiation (58) and results in an activated fraction of Ho-166 between 0 and 8 ppm, depending on the duration of irradiation and the neutron flux. A typical activated fraction of 1.5 ppm is used at the beginning of treatment. Relative to most radionuclides used in nuclear imaging techniques an activated fraction of only a few ppm is very low. Activation of HoMS towards higher activated fractions is hampered since it causes loss of integrity of the poly(L lactic acid) microspheres (58).

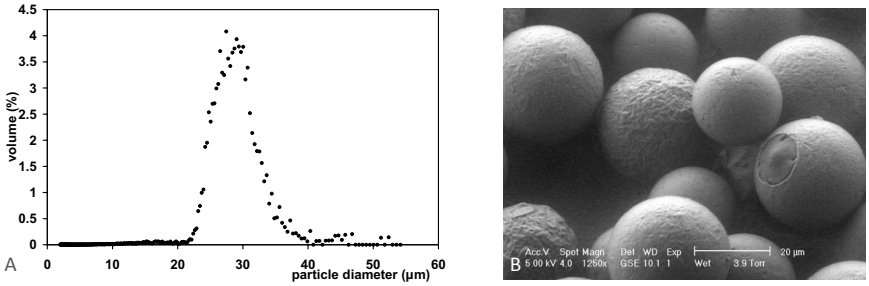

Figure 2 *Size distribution (A) and a scanning electron micrograph (B) (original magnification, x 1250) of HoMS that were used in this study (Section 3) and are currently being tested for clinical application. The mean diameter of the microspheres is 30 µm, the Ho-165 content 17% by weight, and the activated fraction of Ho-166 ranges between 0-8 ppm.*

3. Multimodal imaging of HoMS

In this section, we describe the mechanisms by which HoMS acts as a contrast agent in MRI, CT and SPECT and summarize the experiments that were performed to enable a global comparison of the quantitative capabilities of these modalities. Phantom experiments were conducted with homogeneous suspensions of HoMS in an agar gel matrix using standard equipment and typical clinical liver scan protocols. Quantities of activated HoMS representative for intra-arterial radionuclide therapy of hepatic tumors were investigated. In the next section, the resultant calibration curves will be used to characterize the performance of MRI, CT and SPECT for HoMS.

MRI

Signal model

In the case of MRI, signal formation is influenced by magnetic field inhomogeneities (63) arising from the paramagnetic nature of HoMS (64). The paramagnetic behavior of HoMS is characterized by the magnetic susceptibility, which is high in holmium. The susceptibility difference between HoMS and the surrounding tissue induces local magnetic field variations that cause phase dispersion of the complex MR signal. This results in local signal voids. The resultant signal loss is characterized by the size of the magnetic field inhomogeneity and the used imaging parameters. The theoretical volume susceptibility of HoMS is 823 ppm (24). Due to this large magnetic moment, HoMS is considered predominantly a T_2* contrast agent (65). T_2*-weighted gradient echo acquisitions are generally employed to study such effects. Assuming a homogeneous distribution of microspheres at the voxel level, and assuming T_1 relaxation effects to be suppressed or negligible (as is the case for HoMS (23)), the signal change in such a sequence can be modeled by Eq. [1] and [2]:

$$S(TE) = S_0 \cdot \exp(-TE / T^*_{2,HoMS}) \quad [1]$$

$$R^*_{2,HoMS} = 1/T^*_{2,HoMS} = 1/T^*_{2,0} + r^*_2[HoMS] \quad [2]$$

where [HoMS] represents the concentration of HoMS in mg/ml, S the signal amplitude, S0 the initial signal amplitude at TE = 0, TE the echo time in ms, T2* the transverse relaxation time in ms, T2,0* the transverse relaxation time without HoMS present in ms, R2*,HoMS the transverse relaxation rate with HoMS present in s-1 and r2* the relaxivity of HoMS in [s-1.mg-1.ml]. More detailed information on MRI can be found in several textbooks (63, 66).

MRI experiments

Phantom setup

Duplicate samples with HoMS concentrations ranging from 0 to 10 mg/ml were obtained by suspending HoMS in a 2 % agar gel matrix. To adapt the MR-relaxation properties of the native gel to those of liver tissue, manganese-chloride ($MnCl_2.4H_2O$) was added (24). Samples were sealed in tubes with an inner diameter of 2.2 cm (area = 3.8 cm^2) and a length of 7.0 cm. The samples were positioned co-axially in the center of a cylindrical phantom made of perspex and measured individually parallel to the B_0 field. The phantom was made of a solid perspex cylinder with a diameter of 20.0 cm. To accommodate the sample tubes, a cylindrical hole with an inner diameter of 2.6 cm was drilled in the center of the cylinder. The phantom material did not interact with the process of signal formation. Coil loading was adapted to simulate a realistic signal-to-noise ratio.

Imaging parameters MRI experiments were done on a 1.5 T whole-body scanner (Achieva, Philips Medical Systems, Best, The Netherlands) with a quadrature birdcage coil. T_2^*-weighted images were obtained for each concentration with a multi-echo gradient-echo sequence with 15 echoes at equal intervals of 1.23 ms. Other imaging parameters included: repetition time (TR) = 31 ms; minimal echo time (TE) = 2.4 ms; flip angle = 25°; Field-of-view (FOV) = 256x256 mm^2; matrix = 192x192; number of sample averages (NSA) = 8; slice thickness = 10 mm; total scan time = 48 s. This scan protocol represents a typical T_2^*-weighted sequence for detecting T_2^* modifying agents (67).

Data analysis Data analysis was performed on a cylindrical volume of interest (VOI, area = 3.56 cm^2, slice thickness = 1cm) within a transverse slice of the sample, which was set in the center of the sample by visual inspection. No image registration was necessary because of accurate repositioning of the samples in between scans. A calibration curve was obtained by linear regression analysis of the mean values of the VOI data. The calculated R_2^* maps were used for data analysis (Figure 3A). The signal (S) is represented here by the change in effective relaxation rate ΔR_2^* ([s^{-1}]). The sample mean, <S>, and variance, u_S^2, of the signal were determined by calculating the mean and variance in the VOI (n = 200).

Results

Figure 3A shows an R_2^* map of a slice perpendicular to the sample tube, illustrating a cross section of the homogeneous HoMS suspension. Outside the sample (inside the massive perspex phantom) the signal was solely determined by noise, which makes the calculation of an R_2^* value impossible. In this area the R_2^* was set to zero. The R_2^* level inside the sample is practically homogeneous,

with a certain amount of noise present. The signal uncertainty is visualized in the intensity profile given in Figure 3B.

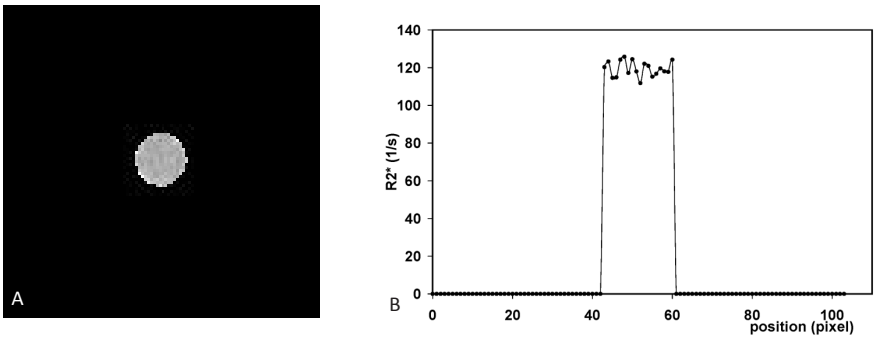

Figure 3 *A calculated R_2* map (A) and corresponding intensity profile (B) of a transversal slice of a homogeneous HoMS suspension (1 mg/ml) in the perspex phantom. The phantom did not generate a detectable MR signal, therefore no R_2* value was calculated for the phantom, which was set to zero. The intensity profile shows the signal uncertainty across the HoMS suspension in the x-direction.*

The calibration curve, as presented in Figure 4, shows a linear relationship between the change in the effective relaxation rate (ΔR_2^*) and the HoMS concentration, according to $\Delta R_2^* = r_2^*$[HoMS], [HoMS] in mg/ml. The slope of the calibration curve, which corresponds to the transverse relaxivity r_2^*, is given by $r_2^* = (92.6 \pm 3.2)\ s^{-1}\ mg^{-1}ml$. The uncertainty of the data points is given by the standard deviation u_S, which is about constant: $u_{S,MRI} = 3.06\ s^{-1}$.

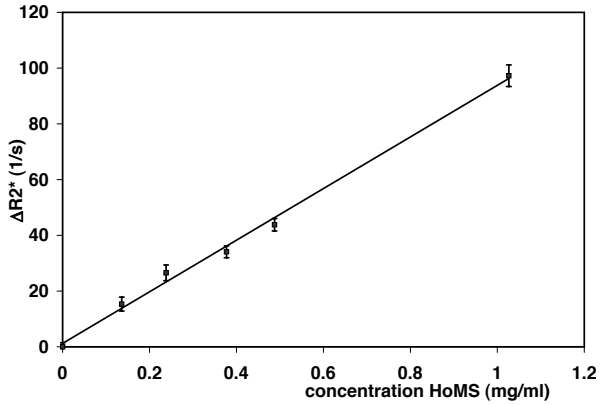

Figure 4 *ΔR_2* versus HoMS concentration. The solid line is a least squares fit to the data points given as mean ± SD (r_2= 0.995).*

X-ray CT

Signal model

In general terms, the principle of computed tomography (CT) consists of measuring the spatial distribution of a certain physical quantity by taking projections from many different angles around the object in order to compute a 3D distribution of the quantity. For an X-ray CT experiment the quantity to be measured is the spatial distribution of the attenuation coefficient, $\mu(x,y,z)$, of the object. For quantitative considerations the intensity in the reconstructed image is displayed in CT-values, expressed in Hounsfield units (HU) (68). CT-values are defined relative to the attenuation coefficient of water, μ_{water}. For a tissue with attenuation coefficient μ_t, the CT-value is defined as

$$CT = 1000(\mu_t - \mu_{water}) / \mu_{water} \; HU \qquad [3]$$

Eq. [3] shows that an increase in CT-value corresponds to an increase in attenuation coefficient. The attenuation coefficient is defined as $\mu = \mu_m(E,Z)\rho$ (in m^{-1}), where ρ is the density (in mg/ml) and $\mu_m = (\mu/\rho)$ is the mass attenuation coefficient (in $m^{-1}.mg^{-1}.ml$). The attenuation coefficient of a tissue can be increased by introducing an X-ray contrast agent with a high mass attenuation coefficient. The mass attenuation coefficient or opacity of the agent is dependent on the energy (E) of the X-rays, and on Z, the average atomic number of the agent. The high mass attenuation coefficient and atomic number of holmium give HoMS the capabilities to act as an X-ray contrast agent. The attenuation coefficient of a tissue containing HoMS is linearly dependent on the HoMS concentration.

During a basic CT experiment, a radiation source emits an X-ray beam in the direction of the object and the detector. Suppose that the intensity (I_0) of the X-ray beam without additional attenuation caused by HoMS is attenuated by a homogeneous object containing HoMS with an attenuation coefficient μ_{HoMS}, resulting in a lower intensity (I_{HoMS}) at the position of the detector. The intensity change caused by the attenuation in a HoMS suspension is given by

$$I_{HoMS} = I_0 \cdot \exp(-\mu_{HoMS}\, d) \qquad [4]$$

where d represents the absorber thickness i.e. the object and μ_{HoMS} the attenuation coefficient of HoMS. A detector on the opposite side of the object registers the penetrated X-rays, resulting in a 2D projection image. Repeating this procedure while rotating the X-ray source and detector continuously relative to the object, results in projection images originating from many angles in a circular

orbit. The complete set of projections is used to reconstruct cross-sectional 2D images of the spatial distribution of the attenuation coefficient in the object, which is related to the HoMS concentration. A variety of filters as well as reconstruction algorithms can be used, including filtered back projection (FBP) and reconstruction algorithms based on an iterative process. In a reconstructed X-ray CT image the CT-value in a HoMS suspension (CT_{HoMS}) can be modeled by

$$CT_{HoMS} = CT_0 + ct_{m,HoMS}[HoMS] \quad [5]$$

where CT_0 represents the CT-value without HoMS present and $ct_{m,HoMS}$ represents the mass attenuation coefficient of HoMS in HU $mg^{-1}ml$. More detailed information on X-ray CT can be found in several textbooks (69, 70).

CT experiments

Phantom setup

For the X-ray CT experiments the same set of samples and phantom setup were used as were used for the MRI experiments. Signal attenuation in the perspex phantom simulated attenuation caused by the tissue of a human patient.

Imaging parameters

Experiments were done on a clinical CT scanner (Brilliance, Philips Medical Systems, Best, The Netherlands). Imaging parameters included a FOV of 350x350 mm^2, matrix = 512x512, collimation of 32x1.25 mm, slice thickness of 3 mm, pitch = 0.671, rotation time = 0.75 s and total scan time = 2.82 s. X-ray tube voltage and current were 120 kV and 200 mA, respectively, leading to a tube current time product of 267 mAs. A soft tissue reconstruction filter was used.

Data analysis

Data analysis was performed on a cylindrical VOI (area = 3.56 cm^2, slice thickness = 1cm) within a transverse slice of the sample. No image registration was necessary because of precise repositioning of the samples in between scans. A calibration curve was obtained by linear regression analysis of the mean values of the VOI data. The reconstructed images were used for data analysis. The signal (S) is represented by the change in CT-value in the object, ΔCT, in HU. The sample mean, <S>, and variance of the signal, u_S^2, were determined by calculating the mean and variance in the VOI (n = 2280).

Results

Figure 5A shows a CT image of a slice perpendicular to the sample tube, illustrating a cross section of the homogeneous HoMS distribution. The CT value across the

sample can be considered constant, with a certain amount of noise added. This signal uncertainty is visualized in the intensity profile given in Figure 5B. The hypointensities at the edges of the sample tubes are caused by the material the sample tube is made of.

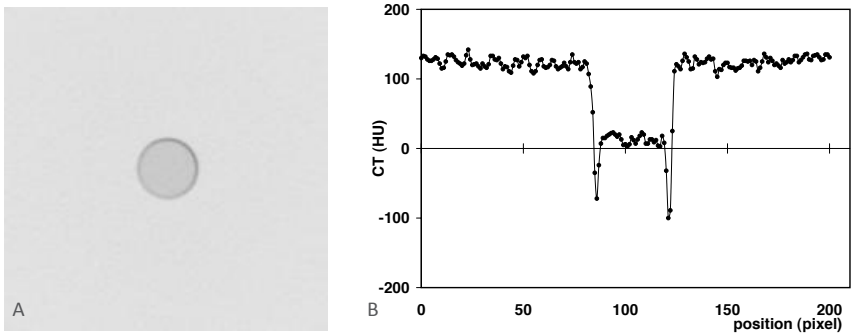

Figure 5 *CT image (A) and an intensity profile (B) of a transversal slice of a homogeneous HoMS suspension (1 mg/ml) in the perspex phantom. The perspex phantom setup was used to simulate attenuation in the patient. The intensity profile shows the signal uncertainty across the HoMS sample in the x-direction.*

The calibration curve (Figure 6) shows a linear relationship between the change in CT value and the HoMS concentration, according to $\Delta CT_{HoMS} = ct_{m,HoMS}$ [HoMS], [HoMS] in mg/ml. The slope of the calibration curve, which corresponds to the mass attenuation coefficient in HU mg^{-1} ml, is given by $ct_{m,HoMS} = (6.7 \pm 0.1)$ HU mg^{-1} ml. The uncertainty of the data points is found to slightly increase with the HoMS concentration in the following way: $u_{S,CT}(C) = 0.26$[HoMS] + 4.49 HU. An increase in signal uncertainty with increasing CT value can be expected, since a lower number of X-ray quanta are detected, which increases quantum noise (69). This is explained in more detail in Section 5.

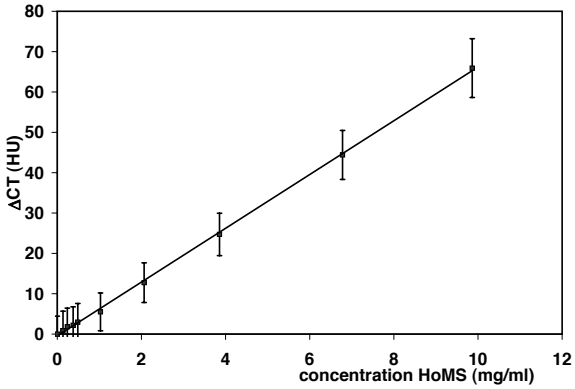

Figure 6 *ΔCT_{HoMS} versus HoMS concentration. The solid line is a least squares fit to the data points, given as mean ± SD (r2 = 0.999).*

SPECT

Nuclear imaging techniques are well-known for their high sensitivity, especially in comparison with MRI and CT (18, 35). Another important difference between SPECT and both MRI and X-ray CT imaging is the lack of an anatomical reference image in SPECT imaging. In MRI and X-ray CT a diagnostic agent becomes visible by locally changing the present signal, introducing contrast in an image. In SPECT imaging, it is only the diagnostic agent (the radionuclide) that is visualized in an image, which can simplify detection tasks. The specific implications for low contrast detection tasks will be discussed in Section 5.

Signal model

In SPECT imaging, a γ-camera is used to acquire 2D projection images of a γ-emitting radionuclide distribution. The detectors of the γ-camera acquire projections at equally spaced angular intervals typically in a 180° or 360° orbit around the object under investigation. Since the detectors are collimated, (ideally) only photons traveling perpendicular to the detector are detected, allowing them to be traced back to the origin of emission. A three-dimensional distribution of the radiopharmaceutical can be reconstructed by back-projection of the 2D projection images. Possible reconstruction algorithms include filtered back-projection (FBP) and iterative (statistical) reconstruction. Compared to transmission CT imaging, the projection counts are relatively low; therefore projection or post-reconstruction filtering is often required to reduce the noise. Apart from noise-issues, images are also degraded by attenuation of the photon flux, by detector and collimator blurring, by the detection of photons scattered in the object, and by septal penetration of photons through the lead septa between the collimator holes. Accurate correction for all of these effects is required in order to provide absolute quantification of SPECT images. More detailed information on SPECT imaging can be found in several textbooks (71, 72).

SPECT experiments

Phantom setup

SPECT experiments were conducted using a water filled phantom. A single sample was used containing a suspension of 51.1 mg activated HoMS in 25 ml of a 2 % agar gel matrix ([HoMS] = 2.05 mg/ml). The activated fraction (Ho-166) at the moment of the first SPECT scan was 1.38 ppm with a total activity of 314 MBq. The sample tube was fixed coaxially in a hollow perspex cylinder (inner diameter = 21.6 cm, inner height = 18.6cm) filled with distilled water. Signal attenuation in the surrounding water simulated attenuation in the surrounding tissue. The same phantom setup was used for the following 10 days and measured at least every 12

hours. Phantom positioning was done with great care to prevent mismatching of the sample position. The decaying activity level was used to simulate a decreasing HoMS concentration with constant activated fraction.

Imaging parameters

Experiments were done on a clinical dual-head SPECT scanner (ADAC Vertex, Philips Medical Systems, Best, The Netherlands). A medium energy general purpose (MEGP) collimator was used. A 15% wide energy window was set around the Ho-166 photopeak at 81 keV. Other imaging parameters included: matrix = 128x128, isotropic projection pixel and reconstructed voxel size of 4.72 mm, 2 detector heads at 180˚, 30 angular positions over 360˚, 40 s per angle, resulting in a total scan time of 24 min. No attenuation correction or scatter correction was applied. Reconstruction was done iteratively (12 iterations), using the manufacturers software (ADAC). A Butterworth pre-filter of order 5 with cut-off frequency = 0.5 was used in concert with a filtered back-projection image for initialization.

Data analysis

Data analysis was performed on a cylindrical VOI (area = 3.56 cm^2, slice thickness = 1 cm) within a transverse slice of the sample in the reconstructed images, which was set in the most intense area by visual inspection. Variance of the sample signal was determined by using pixel values of four neighboring VOI's in transversal slices, since individual intensity profiles of transversal slices showed a strong position dependent signal variation, caused by a relatively wide point spread function (Figure 7B). This can be improved if resolution recovery is used in the iterative reconstruction. A calibration curve was obtained by linear regression analysis of the mean values of the VOI data. The signal (S) is represented by intensity (I) in arbitrary units, (a.u.) for SPECT. For all measurements with the radially symmetric phantom setup described above, the object dependent image degrading factors only contribute a global multiplication factor to the reconstructed image. Therefore, even without correcting for these factors, the arbitrary units used for the analysis of the SPECT data can be related linearly to source activity concentration (Bq/ml) and have constant gain for all data points.

Results

Figure 7A illustrates a typical reconstructed SPECT image, showing a cross section of the sample that was located inside the phantom and contained a homogeneous distribution of activated HoMS. The signal intensity is spread out over a region larger than the sample, caused by blurring artifacts. This is highlighted in Figure 7B, which shows an intensity profile of the image in Figure 7A. The origin of the blurring artifacts as well as some possible methods to reduce such artifacts are discussed in Section 5.

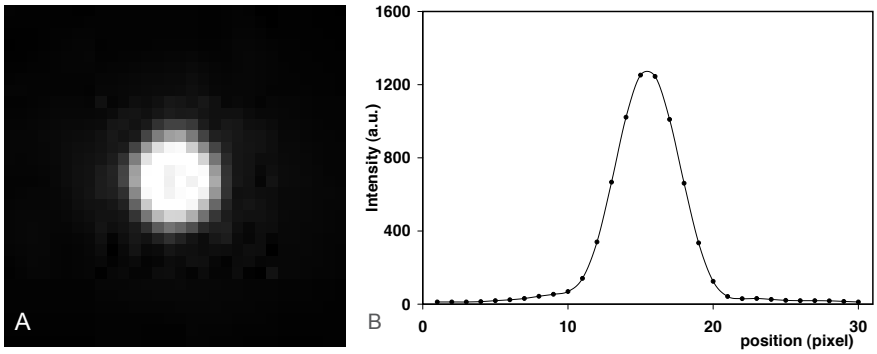

Figure 7 *A SPECT reconstructed image (A) and a corresponding intensity profile (B) of a transversal slice of a homogeneous HoMS suspension (1 mg/ml) in the SPECT phantom. The SPECT phantom setup was used to simulate attenuation caused by the patient. The intensity profile shows the signal uncertainty in the HoMS sample in the x-direction, which is bell-shaped, caused by blurring.*

The calibration curve, as presented in Figure 8A, shows a linear relationship between the change in intensity and the activated HoMS concentration, according to $\Delta I = A_m$[HoMS] a.u., [HoMS] in mg/ml. The slope of the calibration curve, which corresponds to A_m, is given by $A_m = (1435.3 \pm 11.6)$ a.u. mg^{-1} ml., for an activated fraction of 1.38 ppm. For lower concentrations (Figure 8B), the uncertainty is best estimated by an exponential model, in this specific case: $u_{S,SPECT}(C) = 28\sqrt{}$ [HoMS] a.u.

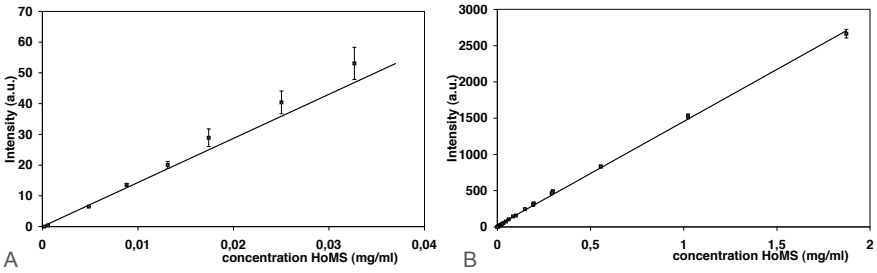

Figure 8 *A. Intensity versus HoMS concentration. The solid line is a least squares fit to the data points, given as mean ± SD (r2 = 0.998). B. Intensity versus HoMS concentration zoomed in on the low concentration region.*

4. Sensitivity and detection limits of HoMS

The calibration curves (Figure 4, 6, 8) and levels of uncertainty that were determined in the previous section are taken as a starting point in this section. These results are summarized in Table 1, and were used to derive some figures of merit for the performance of MRI, CT and SPECT with regard to the detection of HoMS under signal-known-exactly (SKE) conditions. SKE conditions refer to the situation where an ideal observer evaluates signal changes at a pre-specified region in the image. Such conditions greatly limit the number of parameters that have to be taken into account when characterizing the performance of observers, devices, etc. and constitute a popular provision in many areas of research (73-78). SKE conditions evidently apply to our phantom experiments.

Table 1 *Experimentally determined models for the signal behavior (S(C)) and signal uncertainty ($u_S(C)$) for MRI, CT and SPECT as a function of the HoMS concentration (C, [mg/ml]).*

Modality	S(C)	$u_S(C)$
MRI	$R_2^* = R_{2,0}^* + (92.6 \pm 3.2)\ C\ [s^{-1}\ mg^{-1}\ ml]$	$u_{R2^*} = 3.06\ [s^{-1}\ mg^{-1}\ ml]$
CT	$CT = CT_0 + (6.7 \pm 0.1)\ C\ [HU]$	$u_{CT} = 0.26\ C + 4.49\ [HU]$
SPECT	$I = I_0 + (1435.3 \pm 11.6)\ C\ [a.u.]$	$u_I = 28\sqrt{C}\ [a.u.]$

The figures of merit that we will employ are the sensitivity and the minimal change in HoMS concentration necessary to establish a significant signal change. To derive these figures from the calibration curves, S = f(C), as summarized in Table 1, we will adopt a procedure originally used for the determination of the dose resolution in radiotherapy dosimetry (79). In this procedure it is assumed that the measured signal S and the contrast agent's concentration C in a VOI are normally distributed with means μ_S and μ_C and uncertainties σ_S and σ_C. The mean value μ_C and uncertainty σ_C of the agent present in a VOI are estimated by <C> and $u_C(C)$, respectively, using the mean of the sampling distribution in the VOI, <S>, and the uncertainty of this distribution, $u_S(C)$. For each observed signal, S, the corresponding concentration, C, can be calculated using the inverse relationship of the calibration curve:

$$C = f^{-1}(S) \qquad [6]$$

From the estimated uncertainty of the observed signal, an estimate of the uncertainty of the agent's concentration probability distribution, $u_C(C)$, is determined using standard methods of error propagation,

$$u_S(C) = (\partial S / \partial C) u_C(C) \quad [7]$$

$$u_C(C) = 1/(\partial S / \partial C) u_S(C) \quad [8]$$

where ∂S/∂C represents the local slope of the calibration curve.

Sensitivity

The sensitivity, η, is defined as the slope (∂S/∂C) of the calibration curve. It indicates the signal change as a result of a change in concentration. A high sensitivity implies that a small change in concentration induces a relatively large change in signal. According to the results summarized Table 2, SPECT shows the highest sensitivity, followed by MRI and CT.

Table 2 *Sensitivity (η), signal uncertainty ($u_s(0^+)$) and relative sensitivity ($\eta'(0^+)$). Signal uncertainty and relative sensitivity are determined at a concentration close to zero (0^+).*

Modality	η	$u_s(0^+)$	$\eta'(0^+)$, [ml.mg^{-1}]
MRI	*92.6 ± 3.2 s^{-1}.ml.mg^{-1}*	*3.1 s^{-1}*	*31.6*
CT	*6.7 ± 0.1 HU ml.mg^{-1}*	*4.5 HU*	*1.5*
SPECT	*1435.3 ± 11.6 ml.mg^{-1}*	*1.3 a.u.*	*1071*

The relevance of the sensitivity as defined above is related to the level of uncertainty in the image. To be able to compare the signal change induced by a change in HoMS concentration for the different imaging modalities, the sensitivity is related to the uncertainty. Therefore, the relative sensitivity, η', is introduced, being the signal change relative to the noise level per change in concentration, which has equal dimensions for all three imaging modalities.

$$\eta'(C) = \eta(C) / u_S(C) \quad [9]$$

Table 2 shows the relative sensitivities in the low HoMS concentration region, $\eta'(0^+)$, for MRI, CT and SPECT. SPECT clearly shows the highest relative sensitivity, followed by MRI and CT. Since the relative sensitivity depends on the uncertainty level, which changes with HoMS concentration, SPECT shows a strong exponential reduction in relative sensitivity with increasing HoMS concentration, where MRI and CT show a more or less constant relative sensitivity. Figure 9 shows the relative sensitivity as a function of the HoMS concentration. Note that different scales are used in Figure 9.

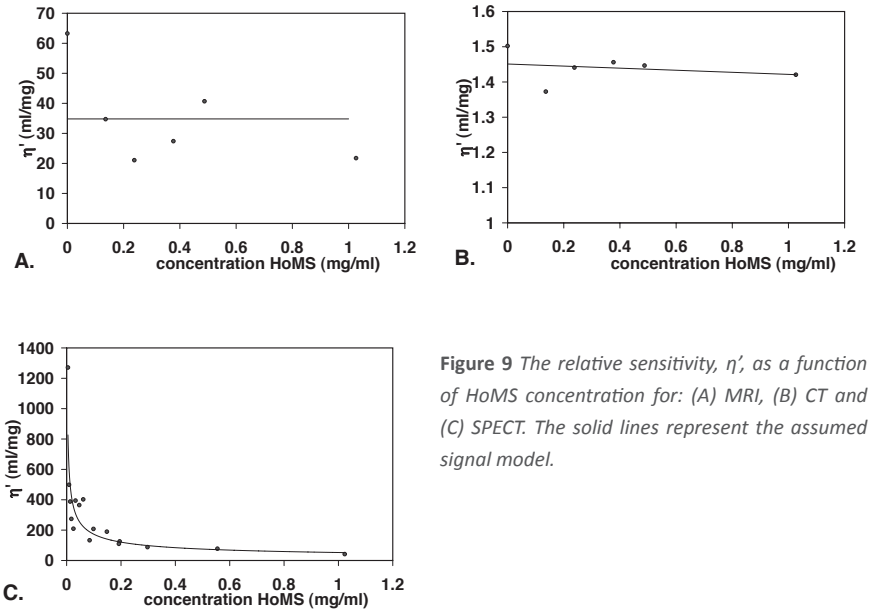

Figure 9 *The relative sensitivity, η', as a function of HoMS concentration for: (A) MRI, (B) CT and (C) SPECT. The solid lines represent the assumed signal model.*

Minimal detectable concentration

We now define the minimal detectable concentration difference as the minimal separation between two concentration probability distributions $\langle C_1 \rangle \pm u_{C_1}$ and $\langle C_2 \rangle \pm u_{C_2}$ that can be considered to be significantly different with a certain level of confidence, p. Applying t-statistics for two-sample comparison using a two-sided alternative hypothesis, we can define the minimal detectable concentration difference with a level of significance of 95 %, represented by $C_\Delta^{95\%}(C)$, as follows

$$C_\Delta^{95\%}(C) = 1.96\sqrt{2} \cdot u_C(C) / \sqrt{n} \qquad [10]$$

where n represents the number of voxels in the VOI. To calculate $C_\Delta^{p}(0^+)$, the level of uncertainty is needed. The minimal detectable concentration difference depends on the HoMS concentration, since the level of uncertainty is dependent on the HoMS concentration. Figure 10 shows the $C_\Delta^{95\%}(C)$ as a function of the HoMS concentration.

The dependence of the minimal detectable concentration difference on the HoMS concentration is highest for SPECT, despite the low activated fraction of HoMS. The exponential relationship between the level of uncertainty and the HoMS concentration causes a relatively strong increase of the minimal detectable

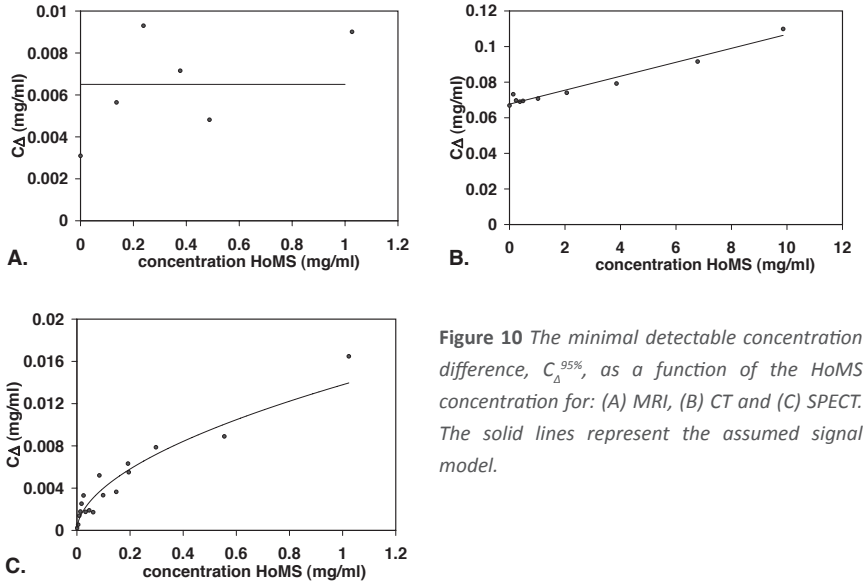

Figure 10 *The minimal detectable concentration difference, $C_{\Delta}^{95\%}$, as a function of the HoMS concentration for: (A) MRI, (B) CT and (C) SPECT. The solid lines represent the assumed signal model.*

concentration difference in the low concentration region, where both MRI and CT present a constant level of uncertainty in the low concentration region, leading to a constant minimal detectable concentration difference.

If C_1 is taken equal to zero, $C_{\Delta}^{p}(0^+)$ represents the absolute minimal detectable concentration. A one-sided t-test is used to determine $C_{\Delta}^{p}(0^+)$. $C_{\Delta}^{p}(0^+)$ is calculated using the level of uncertainty at a HoMS concentration close to zero. For a 95% level of confidence, the absolute minimal detectable concentration is

$$C_{\Delta}^{95\%}(0^+) = 1.65\sqrt{2} \cdot u_C / \sqrt{n} \qquad [11]$$

For MRI the absolute minimal detectable concentration is calculated to be $C_{\Delta}^{95\%}(0^+)$ = 0.0055 mg/ml, for CT $C_{\Delta}^{95\%}(0^+)$ = 0.057 mg/ml and for SPECT $C_{\Delta}^{95\%}(0^+)$ = 0.00054 mg/ml. Table 3 summarizes these results as well as the corresponding levels of uncertainty and size of VOI.

Table 3 *VOI expressed in number of pixels, level of uncertainty and the corresponding absolute minimal detectable concentration, $C_{\Delta}^{95\%}(0^+)$, of HoMS, for MRI, CT and SPECT. Equal VOI's were used for the different modalities.*

Modality	VOI, [voxels]	$u_c(0^+)$, [mg/ml]	$C_{\Delta}^{95\%}(0^+)$, [mg/ml]
MRI	*200*	*0.0332*	*0.0055*
CT	*2280*	*0.673*	*0.057*
SPECT	*32*	*0.00093*	*0.00054*

5. Factors affecting the sensitivityand detection limmits

In the previous section, the performance of MRI, CT and SPECT was characterized for a specific contrast agent, specific equipment, specific scan protocols, specific experimental conditions (SKE) and a specific diagnostic task. These findings will now be taken as a starting point for an overview of the factors affecting the sensitivity and detection limits of MRI, CT and SPECT for multimodal agents in general. In this, emphasis will be put on factors that must be taken into account when extrapolating our findings to other diagnostic tasks, other agents, other experimental conditions, and other scan protocols.

General aspects

In general terms, the possibility to detect a lesion depends on the contrast of the lesion with the surrounding tissue and the signal-to-noise ratio (SNR) in the image. Therefore, it is important to maximize contrast and limit image noise without degrading image resolution substantially. Although MR and CT imaging can be performed without the administration of contrast agents, lesion detection often strongly benefits from the use of contrast agents, both in disease diagnosis and treatment (80-83). Contrast between the lesion and the surrounding tissue is improved by a high tumor-to-background ratio of the contrast agent. High resolution measurements could also increase contrast by decreasing partial volume effects (84-86). This is most important when the size of the lesions to be detected is on the order of the voxel size. However, an increase in image resolution (accompanied by a decreased voxel size) inevitably leads to a decrease in SNR, since signal intensity is directly proportional to voxel volume whereas background noise is not. Especially in the case of low contrast detectability, which is the focus of this review, this might lead to a loss of detectability, since low SNR makes an object more susceptible to image noise (74, 87). Therefore, a high sensitivity of the imaging modality for the agent is of great importance. On the other hand, an increase in resolution results in more pixels covering the lesion. Since detectability depends on both signal uncertainty and the number of pixels covering the lesion, which are related, as shown in Eq. [11] in Section 4, both effects counteract each other. Therefore, in general, improving the image resolution enhances lesion detection mainly by decreasing partial volume effects.

Next to contrast and SNR, lesion detection is influenced by the homogeneity of the background as well. A non-uniform background in the image will hamper detection of a lesion. The homogeneity of the background depends on the tissue to be imaged as well as the imaging modality used. MRI and X-ray CT both show

the diagnostic agent in an anatomical reference image, which is advantageous for localization but may be hampering detectability. In nuclear imaging techniques such as SPECT, no endogenous signal is present. These imaging techniques only visualize the tracer in a background with signal intensity close to zero, dependent on the tumor-to-background ratio. This simplifies the detection of the agent, but lacks the possibility of accurate localization of the contrast agent relative to the patient's anatomy.

In summary, a tradeoff has to be made by the investigator between several parameters such as contrast, spatial and temporal resolution and SNR (Figure 11) prior to the actual imaging procedure in order to maximize low contrast detectability. Such tradeoffs are applicable for a detection task in all three imaging modalities currently investigated. Several other imaging modality specific aspects that have to be considered prior to imaging are discussed below.

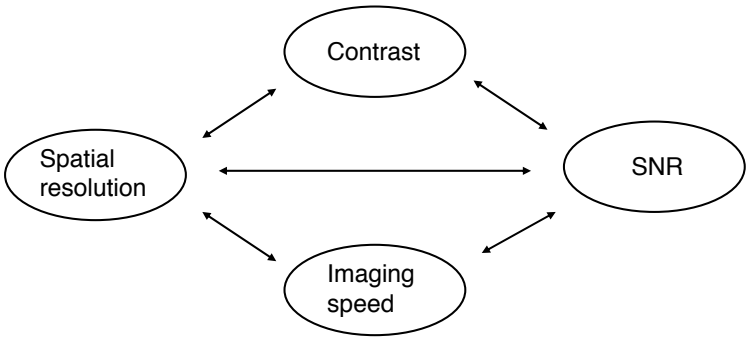

Figure 1**1.** *Lesion detection is determined by contrast and SNR, which are dependent on each other as well as on spatial resolution and imaging time. The complex interdependence forces the investigator to compromise, guided by the task at hand.*

MRI

Factors that can be chosen during MRI experiments influencing the performance of MRI include hardware related aspects such as magnetic field strength, the type of receive coil and the diagnostic agent, but also the choice of imaging sequence and imaging parameters such as the number of averages and the image resolution. Moreover, different possibilities exist in MRI to create contrast in an image based on differences in relaxation times (T_1, T_2, T_2^*), proton density (ρ_0), diffusion coefficient, chemical exchange rate, etc. The existence of potential contrast mechanisms depends on the agent's magnetic properties. The property of interest can be emphasized by an appropriately designed pulse sequence,

which was a T_2^*-weighted sequence in the case of our HoMS experiments. The sensitivity and the lower limits of detection of HoMS as a diagnostic agent were investigated in our phantom experiments. The most important aspects influencing both sensitivity and detection limit are highlighted below, taking HoMS as a starting point.

Holmium-loaded microspheres

The sensitivity and detection limits of MRI were determined for the case of HoMS. One should bear in mind, however, that the results that were obtained relate to HoMS of a particular size distribution (20-50 µm), weight percentage (17 %) of holmium and activated fraction (1.38 ppm). The influence of the level of activation is negligible for MRI. However, other properties can strongly influence the outcome of the results. For instance, a higher weight percentage would increase the volume susceptibility of HoMS and therefore the sensitivity, which will lead to a lower absolute minimal detectable concentration. Differently sized microspheres incorporating contrast agent may be expected to invoke additional contrast mechanisms, caused for instance by diffusion effects (65, 88). The influence on sensitivity depends on the actual size of the microspheres. Dependence between the size of the microsphere and the sensitivity was confirmed by in-vitro experiments for several contrast agents including HoMS. An optimum size was determined depending on both weight percentage of holmium in HoMS and magnetic field strength. Table 4 summarizes the considerations of this paragraph.

Table 4 *The influence of an increase in particle size, weight percentage or activated fraction of HoMS and field strength on sensitivity and detectability of MRI for a fixed quantity (mg) of HoMS.*

Performance measure	Particle size ↑	Weight percentage ↑	Activated fraction ↑	Field strength ↑
Sensitivity	↑/↓	↑	_	↑
Detectability	↑/↓	↑	_	↑

Signal known exactly conditions

The specific conditions during the phantom experiments included a sample with homogeneous HoMS distribution of known size and position in a homogeneous background, according to signal-known-exactly conditions. SKE conditions were chosen to allow straightforward comparison between imaging modalities. For MRI, it was shown that the spatial distribution and the degree of clustering of a T_2^* contrast agent has a profound effect on the relaxivity and thus on the sensitivity of MRI for the contrast agent (89-91). It is known from animal studies using

rabbits and pigs that selective administration of HoMS to the liver results in a strongly inhomogeneous distribution caused by clustering in the arterial tree (23, 24). Locally, this causes high concentrations of HoMS, leading to signal voids and nonlinear behavior of the sensitivity, placing an upper limit to the quantifiable HoMS concentration with MRI (24). The calibration curve would not apply to such high concentrations, causing the determination of the sensitivity and detection limits of HoMS to be inaccurate. To prevent such unclear influences of additional variables the experiments of this review were conducted under SKE conditions.

An important drawback of the used experimental settings is the fact that it leads to a distribution of HoMS in a homogeneous background, which is not the case in-vivo. The low background variability has a positive effect on the minimal detectable concentration. The inhomogeneous background in patients causes tissue variability induced noise, hampering low contrast detectability. Therefore, the determined minimal detectable concentration can not simply be extrapolated to clinical situations, but is useful for comparative purposes.

SNR and detectability in MRI

Lesion detection is determined by the contrast of the lesion with the surrounding tissue and the SNR in the image, as mentioned before. In MRI, specific mechanisms are responsible for the generation of both contrast and SNR. The choices made by the investigator concerning hardware related aspects as well as the imaging settings have a profound effect on the performance of the agent, in this case HoMS. Important imaging parameters directly influencing the SNR include the voxel volume, the number of signal averages and pulse sequence design. Other important aspects are the choices of receive coil and magnetic field strength. The influence on SNR and detectability of these aspects, as well the possible contrast mechanisms, is clarified in more detail in this Section.

Receive coil

The sensitivity of the receive coil to detect the MR signal is defined by its receive field (63). The receive field depends on the type and size of the receive coil. The experiments conducted to investigate the performance for HoMS were done using a quadrature birdcage coil, which is known for its high SNR. In general, the better the coil encompasses a given sample, expressed by the coil filling factor, the higher the signal intensity received by the coil. Nowadays, a lot of research is done in the area of coil design and multiple coils covering the area of interest, which resulted in smart techniques such as sensitivity encoding (SENSE) that are used to shorten imaging time, increase resolution or increase SNR (92-94). Especially higher SNR is beneficial for lesion detection tasks, resulting in a higher diagnostic quality (95).

Contrast mechanisms

It is important to realize that the signal in MRI is not originating from the contrast agent, but from the water protons in the object. The use of MR contrast agents is based on the ability of a contrast agent to disturb MR signal formation and induce local signal changes. During the use of HoMS as an MR contrast agent, for instance, the ability to induce magnetic field inhomogeneities causing signal voids in a T_2*-weighted image is exploited. Other MR contrast agents make use of alternative mechanisms to affect the magnetic relaxation properties of the protons in the surrounding water. These magnetic relaxation properties determine the time dependence of the MR signal. The dependence of the MR signal on timing parameters and tissue properties is shown for a basic gradient echo experiment:

$$S \propto \rho_0 (1 - e^{-T_R/T_1}) e^{-T_E/T_2^*} \qquad [11]$$

where TR represents the repetition time and TE the echo time. By changing these timing parameters the investigator can optimize the contrast between tissues with different relaxation properties. T_1 and T_2^* (or T_2) represent the spin-lattice relaxation time and the spin-spin relaxation time, respectively. In general, the value of T_1 is at least one order of magnitude larger than the value of T_2. The tissue relaxation properties as well as their ratio may be altered considerably in the presence of paramagnetic or super-paramagnetic agents. The enhancement of the tissue relaxation rate in the presence of these (super-) paramagnetic agents is caused by the high magnetic susceptibility, the number of unpaired electrons and the electronic relaxation time of these agents (96). Dedicated imaging sequences designed to highlight the differences in relaxation properties are employed to create optimal contrast in the MR image, as was done for HoMS.

A recent development in MRI concerning the detection of small amounts of contrast agents is the use of 'positive' contrast mechanisms, firstly introduced as the white marker phenomenon and used for tracking of endovascular devices by Seppenwoolde et al. (97). These techniques utilize local magnetic field inhomogeneities, introduced by a difference in magnetic susceptibility between the agent and the surrounding, to enhance the signal in a suppressed background. Since these methods aim to suppress the background signal, contrast agent detection is less hampered by the inhomogeneity of the background. It is possible to distinguish between signal voids created by the contrast agent and from sources that cause weaker field perturbations. T_2^* contrast agents, normally introducing negative contrast (signal voids), are most suitable for this method since they cause local magnetic field inhomogeneities. Different positive contrast

techniques have been introduced to utilize the magnetic field disturbances, based on the use of a dephasing gradient (97-99) or spectrally selective excitation pulses (100).

Another promising research topic in MRI is fluorine (^{19}F) imaging, which is a positive contrast technique as well. In fluorine imaging, targeted probes labelled with ^{19}F can be imaged with conventional MR scanners and imaging techniques, tuned to the specific resonance frequencies of ^{19}F in stead of the resonance frequencies of protons. Since there are no endogenous ^{19}F atoms present in the body, no background signal will be present, leading to local hot spots (positive contrast), which can be overlaid on conventional anatomical proton images acquired in the same imaging session, allowing accurate localization of the contrast agent (101, 102). The use of higher magnetic field strengths, leading to a higher SNR and sensitivity, makes fluorine imaging attractive.

Field strength

The main static magnetic field used in clinical MRI nowadays varies between 0.5 T and 3 T. The field strength in the typical clinical liver scan protocol used was 1.5 T. Despite the fact that this is the most widely used field strength to investigate hepatic lesions (80, 103, 104), the trend in MR imaging is to use higher field strengths (105, 106), clinically towards 7 T. According to MR physics, one can expect the signal to exhibit quadratic growth with the field strength (63, 93). In MRI experiments using a magnetic field strength above 0.5 T, the noise shows a linear dependence on field strength, resulting in a linearly increasing SNR with increasing field strength (63, 107). This higher intrinsic SNR can be used to increase resolution or decrease acquisition times. It is this increase of SNR, spatial or temporal resolution with higher field strength that accounts for the interest in higher field imaging in MRI.

Field strength and contrast mechanisms

Contrast agent sensitivity is influenced by magnetic field strength since it has a pronounced effect on contrast generating mechanisms (108). For HoMS, predominantly a T_2^*-contrast agent, higher field strengths lead to a higher r_2^* relaxivity, increasing the sensitivity. The influence of increasing field strength on T_2^*-contrast agent detection threshold results from the increased sensitivity and increased SNR efficiency at higher field strength, leading to a lowering of the contrast agent detection limit. Since the mechanisms of T_2 and T_2* relaxation are alike, except for the rewinding of signal loss caused by static field inhomogeneities in T_2 relaxation, the influence of higher field strength on T_2 relaxation is a similar to that on T_2*, but less pronounced.

At higher field strengths r_1 relaxivity is decreased. Rinck et al. presented relations between field strength, contrast agent dose and induced contrast for gadolinium based contrast agents (108). They showed a nonlinear decreasing relaxivity with increasing field strength and an increasing contrast between target tissue and surrounding tissue. This was confirmed by several other studies on lesion detection, presenting that the administration of a T_1-shortening contrast agent produced higher contrast between tumor and normal tissue at high field strengths (3T) than at low field strengths (1.5T) (109, 110). One should keep in mind that contrast in an image between several tissue types is dependent on many imaging parameters, set according to the task at hand.

Alternative MR contrast agents

A wide range of MR contrast agents for detection and characterization of hepatic lesions has been developed in the past decade. The MR contrast agents used most often are based on the paramagnetic gadolinium ion (Gd^{3+}) (111), super-paramagnetic iron oxide (SPIO) particles and ultra small super-paramagnetic iron oxide (USPIO) particles (Fe^{2+} and/or Fe^{3+}) (112, 113) and manganese (Mn^{2+}) (114, 115), as summarized in Table 5 (83). Other elements that have been investigated for the use as a MR contrast agent include dysprosium (37, 40), holmium (24, 37) and europium (37), all coupled to macromolecules. All these contrast agents have a pronounced effect on the signal intensity of a T_1-, T_2-, or T_2*-weighted image.

Table 5 *MRI contrast agents used for liver imaging with predominant contrast mechanisms.*

Agent	ion	Contrast mechanism
HoMS	Ho^{3+}	T_2*
Iron oxide	Fe^{2+}, Fe^{3+}	T_1, T_2, T_2*
Gadolinium chelates	Gd^{3+}	T_1
Manganese chelates	Mn^{2+}	T_1

T_2 contrast agents

The shortening of T_2 relaxation times by contrast agents is caused by their influence on spin-spin relaxation. Iron oxide based contrast agents are frequently used T_2 shortening contrast agents since their influence on spin-spin relaxation is large, resulting in effective contrast generation. SPIO's and USPIO's have shown their diagnostic value as a T_2 contrast agent, and have been reported to play an important role in the therapeutic decision making for patients with hepatic malignancies (103, 104, 116-118).

T_2^* contrast agents

The effect of the induced field inhomogeneity by T_2 contrast agents is partly undone by the imaging sequences used in T_2-weighted imaging. Other than in T_2-weighted imaging sequences, T_2^*-weighted sequences fully exploit the capacity of contrast agents to induce signal voids. In such a situation, the observed spin-spin relaxation is dramatically increased and the transverse relaxation is characterized by the T_2^* relaxation time constant. Iron oxide based contrast agent have strong T_2^* effects and have shown their diagnostic value in lesion detection (103, 117). The contrast agent used in our experiments, HoMS, exploits the same principle to induce contrast (24).

T_1 contrast agents Gadolinium is the most frequently used T_1 contrast agent in the clinic. Mostly, the Gd^{3+} ion is incorporated in a larger molecule using a chelate such as DTPA or DOTA and can be incorporated in a liposomal bilayer (14, 119). The efficiency of the contrast agent can be enhanced by modifications to the surface of the gadolinium-loaded particles to alter interaction with protons (120). Since gadolinium chelates can be linked to all sorts of macromolecules, it is an attractive contrast agent for multimodal imaging (14, 48, 49).

In the detection and characterization of liver metastases gadolinium chelates are used extensively as a contrast agent and have proven to have a profound diagnostic value (80, 104, 116). A lot of research is done investigating the efficiency of gadolinium-based contrast agents in MRI compared to the efficiency of contrast enhanced CT in the detection of hepatic malignancies. In most of these studies, MRI was moderately superior to state-of-the-art CT in detection and characterization of hepatic lesions (3, 121, 122).

Another group of T_1 shortening contrast agents is based on the Mn^{+2} ion. It was shown that manganese based contrast agents improved detection and characterization of hepatic lesions (123, 124). Others have shown that manganese-enhanced MRI can be used to image neuronal activity in the brain by monitoring calcium channel activity (125).

CT

Sensitivity and detection limits of CT were determined for the case of HoMS utilizing specific experimental conditions. In this section the influence of specific issues and the choices made concerning the experimental conditions on sensitivity and detection limits of CT for HoMS as a contrast agent are discussed. Firstly, the influences of the material properties of HoMS are discussed, followed by the importance of the choice of experimental conditions. More general considerations concerning SNR and detectability in X-ray CT imaging such as tube settings, contrast generation, spatial resolution and reconstruction filters

and algorithms are brought to the attention. Especially their influence on SNR is explained since most factors that can be set by the investigator influence lesion detection by influencing the SNR of the image. The contrast generated by the diagnostic agent used mainly depends on the type and the concentration of the diagnostic agent. Therefore, a short overview of alternative CT contrast agents will end this section.

Holmium-loaded microspheres

The physical property that is actually measured in X-ray CT is the attenuation coefficient of the object under investigation, as mentioned before. HoMS with a certain size distribution, weight percentage and activated fraction has shown a linear relationship between attenuation coefficient and concentration. This relationship, denoted as the sensitivity, depends mainly on the relative amount of the element holmium in HoMS because holmium causes attenuation of X-rays since it possesses a high mass attenuation coefficient, caused by the high atomic weight and relatively high k-edge. Therefore, the sensitivity and detection limit of HoMS depend on the weight percentage of holmium in HoMS. Since the weight percentage of HoMS may vary with the size of the microspheres, the size distribution could influence the sensitivity as well, be it indirectly. The activated fraction of HoMS has negligible influence on the mass attenuation coefficient and therefore no significant influence on the sensitivity of CT for HoMS. Table (6) summarizes the influences of several physical properties of HoMS on the sensitivity and detection limits of CT for HoMS.

Signal known exactly conditions

The SKE conditions used in the HoMS performance tests provide a clear situation in which sensitivity and detection limits could be investigated. Attenuation of X-rays by the perspex phantom simulated attenuation by a patient, albeit simplified. The homogeneous distribution of HoMS in the sample does not influence the mechanism responsible for contrast generation, as it does in MRI. A linear relationship is to be expected between signal attenuation and HoMS concentration, no matter how high it is. This implies that the upper limit of detection is not dependent on the imaging system in X-ray CT imaging.

SNR and detectability in X-ray CT imaging

The level of uncertainty in CT images acts as a limiting factor in detectability tasks. In the experimental setup used to investigate a sample with a homogeneous distribution of HoMS, noise applies to the variation of the signal intensity distribution in a VOI within the sample. The possible sources of the signal uncertainty in CT include system noise, round-off errors, quantum noise and

tissue noise (69, 126). Influences or errors originating from the system itself (system noise) and from data handling (digital noise) are negligible with state-of-the-art CT scanner. The main sources of noise present are quantum noise and tissue noise. Quantum noise, or photon noise, is caused by the inherent random variations in the number of transmitted and detected X-ray quanta. This uncertainty is purely statistical in origin and leads to Poisson counting statistics (71). To reduce quantum noise, a relatively high number of incident X-ray quanta needs to be recorded, requiring CT system efficiency to be as high as possible. System efficiency is mainly determined by the type of detector (xenon or ceramic) and the geometric efficiency (collimation).

Tissue noise or structural noise, caused by variations in X-ray attenuation coefficient in the sample, is negligible in a true homogeneous sample such as a water bath. Although tissue noise is no 'real' type of noise since the variation is intrinsic to the object itself, it is mentioned, as it may influence lesion detection. In the situation of a sample containing a homogeneous HoMS suspension, signal uncertainty did increase slightly with increasing HoMS concentration, which may be caused by what is described here as "tissue" noise. Comparable situations are to be expected in a biodistribution in a patient, leading to a similar increase of signal uncertainty (23, 24). Such signal uncertainties contribute to the total signal uncertainty and influence lesion detection. Other aspects influencing the SNR in CT imaging include X-ray tube settings, image resolution, filtering and the reconstruction algorithm. These factors are chosen by the investigator and are discussed in following subsections.

X-ray tube settings

The tube settings used during the acquisition of the HoMS calibration curve, according to the clinical liver protocol, included a peak tube voltage of 120 kV and a tube current of 200 mA, which are both intermediate values. On most CT scanners, the peak tube voltage can be set from 80 to 140 kV and the tube current from 10 to 375 mA (69). An important variable to be set by the investigator that influences detectability is the mAs value. The mAs value is determined by the tube current and the scan time per imaging slice and is related to the patient dose per volume of tissue (127-129). In a clinical situation, the patient dose is kept as low as possible, to minimize radiation damage, while maintaining the needed image quality. Since tube settings determine both patient dose and image quality, a tradeoff has to be made. Increasing the mAs value increases the number of X-ray quanta to be emitted and detected, increasing the SNR and consequently the CNR (130). Since high SNR and CNR positively influence the low contrast detectability, increasing the mAs value is an option to lower the detection limit (130), at the cost of an elevated patient dose.

The sensitivity of CT for a contrast agent can be increased by decreasing the peak tube voltage, since the mass attenuation coefficient increases with decreasing X-ray energy (43, 131, 132). This introduces an inverse relationship between contrast and X-ray energy (132, 133), which was observed for HoMS as well. Increasing the tube voltage, however, results in more and higher energy X-ray quanta to be detected, increasing the SNR. The CNR, determining low contrast detectability, depends on the combined effect of tube voltage and tube current on the SNR and the sensitivity of the diagnostic agent on contrast generation, as summarized in Table 6 (134). Dependent on the task at hand, a tradeoff has to be made by the investigator, considering SNR, CNR and patient dose, while choosing the X-ray tube settings.

Table 6 *The influence of an increase in particle size, weight percentage or activated fraction of HoMS and tube settings on sensitivity and detectability of X-ray CT for a fixed amount (in mg) of HoMS.*

Performance measure	Particle size ↑	Weight percentage ↑	Activated fraction ↑	Tube voltage ↑	Tube current time product (mAs) ↑
Sensitivity	_	↑	_	↓	_
Detectability	_	↑	_	↓/↑	↑

Spatial resolution

In our experiments, we used multi-slice spiral CT to acquire multiple slices per X-ray tube rotation. Multi-slice spiral CT allows the investigator to retrospectively select the filter width and type and define the effective slice width and thus also the image noise level and spatial resolution in the z-direction (69). The reconstruction increment can be chosen arbitrarily to determine the overlap of adjacent reconstructed slices, to adapt the level of partial volume effects (135).

While low contrast detectability of small objects in CT is mainly dominated by the resolution of the system and limited by partial volume effects, detection of larger objects is predominantly dominated by the noise in the image (87). In the case of the used clinical scan protocol and experimental setup, the area (3.56 cm^2) covering the HoMS samples in the scan plane was large in comparison to the in-plane resolution (sub-millimeter), leading to a negligible influence of partial volume effects in the scan plane. The choice of cylindrically shaped sample tubes, positioned perpendicular to the imaging plane, eliminated partial volume effects in the z-direction, since the sample completely covered the slice thickness. In a different situation, in which a lesion does not fully cover the entire slice, partial volume effects may decrease contrast and hamper lesion detection.

Smaller slice thicknesses have shown improved detection rates in such cases (84, 136). However, others groups have reported a worse detection rate with decreasing slice thickness, indicating the task dependency of the issue (137, 138). Thin-section scanning reduces coverage and increases image noise. To cover the same 3D volume a longer scan time is needed resulting in increased patient dose which might be undesirable. To acquire the same CNR one has to increase patient dose, and, therefore, lesion detection becomes dose-dependent. Another option in spiral CT to overcome partial volume effects is to reconstruct overlapping slices in the z-direction, which compensates for partial volume effects and positively influences lesion detection as well (135, 139).

Filtering and image reconstruction

Image reconstruction is accomplished using filtered back-projection (FBP). The type of convolution kernel (or filter) during reconstruction has a profound effect on the in plane image resolution and noise level and can be chosen according to the task at hand. A relatively high resolution is obtained using a 'sharp' or 'hard' kernel, also called edge enhancement. The downside of a hard kernel is that it is accompanied by an increase in pixel noise. Such kernels can therefore be recommended only in situations with high CNR. A 'smoothing' or 'soft' kernel is used preferably in a low contrast situation, decreasing the resolution, but also the noise level, improving low contrast detectability. This is the type of convolution kernel used in the experiments conducted to investigate the performance of HoMS as a contrast agent. Currently, novel filtering techniques are designed to improve low-contrast detectability by reducing the noise in the image without loss of resolution (140, 141). In addition statistical reconstruction methods are under development for CT, that improve SNR, resolution and quantitative accuracy (142-146).

Alternative X-ray CT contrast agents

In X-ray imaging, only one mechanism is available to generate contrast, based on the attenuation of incident radiation by a radiopaque agent. The sensitivity of the agent is determined by the mass attenuation coefficient, which depends on the energy of the X-rays and the atomic number of the agent, as stressed before in Section 3. The performance of HoMS as a CT contrast agent was investigated and showed a relatively high sensitivity, as presented in Sections 3 and Section 4. The reason for this increased sensitivity finds its origin in the high atomic number of holmium (atomic number = 67, k-edge = 55.6 keV) and the fact that the k-edge matches well with the energy spectrum produced during CT scanning, wherein the peak in intensity of the X-ray spectrum occurs at about 50 keV. Both these aspects positively influence X-ray attenuation.

In the last decade, several other elements of the group of lanthanides, such as gadolinium, dysprosium and ytterbium, which have a relatively high atomic number and matching k-edge, were investigated for their potential as X-ray CT contrast agents (Table 7) (16, 41-43, 143, 147-149). However, the most used contrast agents for years in X-ray CT imaging are iodine-based (atomic number= 53, k-edge = 33keV) (81, 150, 151). The sensitivities of X-ray CT to gadolinium and ytterbium were reported to be higher compared to the sensitivity to iodine, based on the attenuation in HU per mg agent per ml at a tube voltage of 120 kV (42, 43). The same is valid for the element holmium in HoMS, as was confirmed recently.

The most widely used non-iodine-based CT contrast agents are gadolinium-based contrast agents. These agents are well tolerated and are a good alternative for patients suffering from contrast medium-induced nephropathy (152-156). Gadolinium-based contrast agents have been used for several purposes including angiography (156, 157), vascular interventions (158) and to detect hepatic lesions (42, 149).

Table 7 Alternative X-ray CT contrast agents with corresponding atomic numbers and k-edge.

Element	Atomic number	k-edge (keV)
Iodine	*53*	*33*
Gadolinium	*64*	*50*
Terbium	*65*	*52*
Dysprosium	*66*	*54*
Holmium	*67*	*56*
Ytterbium	*70*	*61*

SPECT

The high intrinsic sensitivity of SPECT as known from literature (18, 35) was demonstrated in the case of HoMS as well. However, a drawback of clinical SPECT is the inherently low spatial resolution compared to MRI and even lower compared to CT. Limiting noise is of major importance during detectability tasks in SPECT imaging. Contrary to CT, the projection counts are relatively low; therefore, when filtered back-projection (FBP) is used, low-pass filtering is needed to reduce the noise. Alternative reconstruction algorithms include a large variety of statistical iterative reconstruction methods that can significantly increase the SNR over FBP algorithms, particularly in noisy situations (159, 160). The choice of filtering and reconstruction algorithm partly determines the signal uncertainty and as

a consequence the low contrast detectability. Apart from noise-issues, images are also degraded by attenuation of the photon flux, by detector and collimator blurring, by the detection of photons scattered in the object, and by septal penetration in the collimator septa. Correction methods have been developed that compensate for these effects by accurately modeling the image degrading effects during (statistical) iterative reconstruction (159-161). The latter class of algorithms not only lead to higher resolution and better quantitative accuracy, but also to a significant increase of SNR.

In the case of activated HoMS, Ho-166 specific issues with regard to the spectrum and associated photon penetration and scatter tend to decrease image quality even more (21). These aspects influence sensitivity and detection limits of SPECT for HoMS, as is reviewed in this section.

Holmium-loaded microspheres

HoMS with a certain size distribution, weight fraction and activated fraction of Ho-166 were studied. The signal intensity in SPECT showed a linear relationship with the concentration of Ho-166 in activated HoMS. In other words, for a fixed amount of HoMS, the sensitivity of SPECT is linearly dependent on the activated fraction of HoMS. An activated fraction of 1.38 ppm was used during the SPECT experiments, which is approximately four orders of magnitude lower than the activated fraction that is typically used for most diagnostic tracers in nuclear medicine, and therefore disadvantageous for the sensitivity of SPECT for HoMS. However, such diagnostic tracers are not multimodal and are optimized for nuclear imaging purposes. Increasing the activated fraction of a fixed amount (in mg) of HoMS leads to a proportional increase of the sensitivity and correspondingly to a decreased limit of detection. The size of HoMS only has an indirect effect on the sensitivity by its influence on the weight fraction of holmium present in the HoMS. A higher weight percentage of holmium in HoMS at equal activated fraction results in a proportional increase of total activity and therefore increases the sensitivity (see Table 8).

One of the main problems specifically encountered during SPECT imaging

Table 8 *The influence of an increase in particle size, weight percentage, activated fraction of HoMS and system efficiency and the use of correction methods on sensitivity and detectability SPECT for a fixed quantity (in mg) of HoMS.*

Performance measure	Particle size ↑	Weight percentage ↑	Activated fraction ↑	System efficiency ↑	Advanced correction methods
Sensitivity	_	↑	↑	↑	↑
Detectability	_	↑	↑	↑	↑

of HoMS is caused by down-scatter in the detector and collimator originating from higher energy photons in the MeV-range, Bremsstrahlung in the phantom or patient and the contribution of lead fluorescence into the Ho-166 energy window originating from the lead collimator (21, 162). These factors are Ho-166 specific and result in signal intensities measured outside the area where the radionuclide is present, increasing signal uncertainty and hampering the detection of low contrast tumors.

Signal known exactly conditions

The use of SKE conditions in the SPECT performance tests have similar motivations and advantages as they have in CT performance tests of HoMS. Attenuation of γ-rays in a patient's body is simulated by the physical phantom surrounding the sample. Knowledge of the exact location and quantity of activated HoMS in the SPECT experiments according to SKE conditions simplifies the interpretation of the determined radionuclide distribution. The homogeneous distribution of HoMS in the sample does not influence the mechanisms responsible for signal generation, albeit within limits. The detection of the γ-rays may be influenced by very high concentrations of the radionuclide, since dead time effects caused by local saturation of the detector elements may introduce nonlinear behavior between radionuclide concentration and detected signal intensity. This may introduce an upper limit of the local concentration that can be determined reliably using a calibration curve. In the low concentration region dead time effects are not present and SKE conditions facilitate the determination of the sensitivity and the lower detection limit.

SNR and detectability in SPECT imaging

The SNR in SPECT imaging depends on many parameters and has a direct influence on lesion detectability. The considerations concerning quantum noise explained for X-ray CT apply to SPECT as well since the decay of the studied radionuclide is a random process and follows Poisson statistics. Quantum noise is decreased by an increase of the total number of detected quanta, which can be accomplished by a higher concentration of activated HoMS, a higher activated fraction or by increasing the imaging time per projection. Aspects that are strictly taken no noise (photons scattered in the object and collimator, septal penetration, lead fluorescence in the collimator and detector blurring) degrade image quality by added background counts. This consequently leads to a decreased contrast and image resolution in the reconstructed image. For convenience these types of signal variation are denoted as signal uncertainty in this section. These aspects influence SNR, CNR and lesion detection as is explained in this section.

System efficiency

As pointed out before, the projection counts in SPECT are relatively low. High system efficiency is therefore of great importance. System efficiency is defined as the ratio between detected and transmitted γ-rays. The main aspects influencing system efficiency are detection efficiency, detector geometry, energy window settings, efficiency of the collimator and the type of radionuclide. The detection efficiency and detector geometry can not be influenced by the investigator and depend on the type and thickness of the detector crystal and the number of detectors making up the entire system (71). The thickness of the detector crystal influences the intrinsic spatial resolution as well, introducing a tradeoff between detection efficiency and spatial resolution (163).

The additional high energy (MeV range) γ-rays emitted by Ho-166 that cause down-scatter in the detector and collimator introduce specific considerations concerning the imaging settings. A 15% wide energy window was set around the Ho-166 photopeak at 81 keV. To decrease the contribution of down-scattered γ-rays the width of the energy window was reduced. This however decreased the number of detected γ-rays, lowering the system efficiency. The choice of collimator is determined by the specific radionuclide, as it influences system efficiency and image quality as well.

Collimation & spatial resolution

Since most clinical SPECT scanners have an in-plane spatial resolution of about 1 to 2 cm, which is roughly the size of the lesions to be detected, partial volume effects hamper lesion detection (163). In a low contrast detection task, which is the task at hand, partial volume effects are even more destructive. Low spatial resolution is mainly caused by collimator blurring as well as other radiation physics related phenomena such as detector blurring, septal penetration and (down-) scatter (164). Detector blurring is determined by the intrinsic resolution of the gamma camera. The weakest link in the gamma camera system concerning spatial resolution is in general the collimator. The type of collimator has a direct influence on SNR, spatial resolution and the level of signal variability caused by septal penetration and collimator scatter (165-167). Therefore, the choice to be made by the investigator which collimator to use is determined by a tradeoff between these aspects, taking into account the task at hand. This optimal choice will depend on the reconstruction algorithm used (168).

A medium energy general purpose (MEGP) collimator was chosen to investigate the performance of HoMS as a SPECT agent. This choice was made to keep septal penetration and collimator blurring to a minimum without lowering SNR too much. Septal penetration is limited by increasing the septal thickness or

length. For the case of activated HoMS emitting higher energy γ-rays lowering septal penetration is desirable. The downside is a decrease of detection efficiency and consequently SNR, because fewer γ-rays reach the detector. Collimator blurring is determined by the shape, length and diameter of the collimator holes (71). Again, adapting the collimator towards less blurring, increasing the spatial resolution, leads to a decrease in SNR (165). These considerations have led to the choice of a MEGP collimator.

Contrast

Image contrast in SPECT refers to differences in intensity in parts of the image corresponding to different concentrations of radionuclide. In a detection task, it is the contrast relative to the signal uncertainty in the image that determines whether a signal is detectable. In a realistic bio-distribution contrast is determined by the selective uptake of the radionuclide in the lesion compared to the concentration in the background tissue, known as the tumor-to-background ratio. In the phantom setup the activated HoMS concentration in the sample was varied while the background did not contain HoMS, theoretically leading to a TBR of infinity, which positively influences low contrast detectability.

Physical aspects of SPECT imaging deteriorate contrast by partial volume effects and background counting rate. Partial volume effects are mainly caused by a poor detector and collimator response. The background counting rate is mainly caused by septal penetration (169, 170) and scatter. In the case of HoMS, both these aspects strongly contribute to background counting rates, since HoMS emit high energy photons.

Image quality and contrast are increased by methods correcting for attenuation, scatter and collimator response (resolution recovery) (167). Such methods increase resolution and decrease background counting rates, resulting in improved low contrast detectability.

Filtering and image reconstruction

Possible reconstruction algorithms include filtered back-projection and iterative reconstruction. When FBP is used, low-pass filtering is often required to reduce the noise before image reconstruction. Currently, a trend is seen towards iterative reconstruction methods in clinical SPECT. In research, iterative reconstruction methods are often combined with correction methods for attenuation (171-173), scatter (160, 173-176) and resolution recovery (173, 177-179). Such methods generally increase SNR, contrast, quantitative accuracy and resolution (161, 174, 177-181). When resolution recovery is implemented more iterations result in a better resolution and less background activity at the cost of SNR (181, 182). In such cases low-pass post-filtering is required to increase SNR while maintaining

improved resolution (183). As an alternative to filtering, Bayesian reconstruction methods (184) that incorporate smoothness constraints may be utilized.

Just recently a scatter correction method specifically for Ho-166 SPECT was developed, that deals with the image degrading aspects caused by high energy photons (21). This allows quantitative SPECT with Ho-166 to be performed. However, iterative reconstruction without correction for attenuation, detector blurring and scatter was used to investigate the sensitivity and detection limits of HoMS, according to the standard clinical protocol.

Alternative diagnostic agents for SPECT

In SPECT imaging, many different radionuclides are used. The most common goals assessed using radiolabeling include determination the biodistribution of drugs and monitor blood flow or metabolism in specific organs (185). This large variety of possible radionuclides has several reasons. Each radionuclide has its own advantages and disadvantages, related to the unique energy spectrum, the half-life, labeling possibilities of the radionuclide and therapeutic considerations. Not every radionuclide can be labeled to any biologically important compound. Labeling is necessary to be able to image several specific physiological processes in vivo. The use of HoMS in internal radiation therapy does not require labeling as HoMS are administered locally and embolize in the target tissue.

The unique energy spectrum of a radionuclide is of great importance. Ideally, the energy spectrum consists of one photopeak in the energy range 100-300 keV. In this energy range the detector efficiency is highest. Additionally, higher energy γ-rays cause all kind of disturbances such as septal penetration, down-scatter and Brehmsstrahlung, as is the case for Ho-166.

Several radionuclides that have a combined gamma and beta emission such as ^{133}Sm and $^{186/188}$Re are used for treatment of bone metastases. These isotopes are attached to EDTMP (ethylenediaminetetramethylenephosphonic acid) and HEDP (1,1-hydroxyethylidene diphosphonate), respectively. These radio pharmaceuticals selectively accumulate and bind to hydroxyapetite crystals in skeletal tissue (186, 187). Another example of such an isotope is ^{177}Lu that is labelled to somatostatin analogs which can be used for treatment of neuroendocrine tumors (188, 189).

5 Summary and conclusions

In the first part of this review, physical phantom experiments were presented that enable a comparative evaluation of the sensitivity and detection limits of clinical MRI, CT and SPECT for what may now be concluded to be a truly

multimodal diagnostic agent, holmium-loaded microspheres. The findings of these experiments are summarized in Table 9 in a qualitative manner.

Table **9** *Comparison of the performance measures and imaging properties of MRI, X-ray CT and SPECT for activated HoMS (1.38 ppm).*

Performance measures	MRI	X-ray CT	SPECT
Sensitivity	+/-	--	++
Detectability	+/-	-	++
Spatial resolution	+	++	--
Temporal resolution	+	++	--
Anatomical reference	++	++	--

Despite the low activated fraction of HoMS, SPECT shows the highest sensitivity and the lowest detection limit, followed by MRI and CT, respectively. The temporal and spatial resolution are the highest for CT, followed by MRI and SPECT. Concerning "monomodal" diagnostic agents, one should bear in mind that these agents are optimized for a particular imaging modality and task. In comparison with such agents, HoMS is a therapeutic agent for intra-arterial radiation therapy in the first place and was not optimized to operate as a multimodal diagnostic agent.

In the second part of this review, the findings of the performed experiments were taken as a starting point for a discussion of the factors affecting the sensitivity and detection limits of MRI, CT and SPECT for multimodal agents in general. In this, emphasis was put on the factors that must be taken into account when interpreting the results of the performance evaluation of MRI, CT and SPECT for HoMS. The wide range of factors influencing sensitivity and detection limits suggests that predicting exact results may be very difficult.

Caution should be exercised when extrapolating the specific findings for HoMS to other diagnostic tasks, other contrast agents, other experimental conditions, and other scan protocols. Therefore, in such cases specific comparisons of the type illustrated for holmium may be necessary to evaluate the situation at hand.

In conclusion, we believe that important knowledge of multimodal imaging can be gained from an in depth study on the performance of a particular multimodal diagnostic agent like presented here. Not only gives it new insights in the particular agent itself, it also provides an overview of the factors affecting multimodal imaging in general. This review will aid anyone working in the field of multimodal imaging in determining what aspects are of importance for the task at hand and why.

Acknowledgements

We would like to thank Remmert de Roos for his technical assistence with the design and manufacturing of the phantoms. This work was supported by the Technology Foundation STW (UGT 6069).

References

1. Hori M, Murakami T, Kim T, Tomoda K, Nakamura H. CT Scan and MRI in the Differentiation of Liver Tumors. Dig Dis **2004**;22(1):39-55.
2. Noguchi Y, Murakami T, Kim T, Hori M, Osuga K, Kawata S, Kumano S, Okada A, Sugiura T, Nakamura H. Detection of hepatocellular carcinoma: comparison of dynamic MR imaging with dynamic double arterial phase helical CT. AJR Am J Roentgenol **2003**;180(2):455-460.
3. Semelka RC, Martin DR, Balci C, Lance T. Focal liver lesions: comparison of dual-phase CT and multisequence multiplanar MR imaging including dynamic gadolinium enhancement. J Magn Reson Imaging **2001**;13(3):397-401.
4. Blankenberg FG, Strauss HW. Nuclear medicine applications in molecular imaging. J Magn Reson Imaging **2002**;16(4):352-361.
5. Gabriel M, Hausler F, Bale R, Moncayo R, Decristoforo C, Kovacs P, Virgolini I. Image fusion analysis of (99m)Tc-HYNIC-Tyr(3)-octreotide SPECT and diagnostic CT using an immobilisation device with external markers in patients with endocrine tumours. Eur J Nucl Med Mol Imaging **2005**.
6. Chen GT, Pelizzari CA, Levin DN. Image correlation in oncology. Important Adv Oncol **1990**;131-141.
7. Bocher M, Balan A, Krausz Y, Shrem Y, Lonn A, Wilk M, Chisin R. Gamma camera-mounted anatomical X-ray tomography: technology, system characteristics and first images. Eur J Nucl Med **2000**;27(6):619-627.
8. Fahrig R, Butts K, Wen Z, Saunders R, Kee ST, Sze DY, Daniel BL, Laerum F, Pelc NJ. Truly hybrid interventional MR/X-ray system: investigation of in vivo applications. Acad Radiol **2001**;8(12):1200-1207.
9. Fahrig R, Butts K, Rowlands JA, Saunders R, Stanton J, Stevens GM, Daniel BL, Wen Z, Ergun DL, Pelc NJ. A truly hybrid interventional MR/X-ray system: feasibility demonstration. J Magn Reson Imaging **2001**;13(2):294-300.
10. Ganguly A, Wen Z, Daniel BL, Butts K, Kee ST, Rieke V, Do HM, Pelc NJ, Fahrig R. Truly hybrid X-ray/MR imaging: toward a streamlined clinical system. Acad Radiol **2005**;12(9):1167-1177.
11. Hasegawa BH, Wong KH, Iwata K, Barber WC, Hwang AB, Sakdinawat AE, Ramaswamy M, Price DC, Hawkins RA. Dual-modality imaging of cancer with SPECT/CT. Technol Cancer Res Treat **2002**;1(6):449-458.
12. Townsend DW, Beyer T. A combined PET/CT scanner: the path to true image fusion. Br J Radiol **2002**;75 Spec No:S24-S30.
13. Townsend DW. From 3-D positron emission tomography to 3-D positron emission tomography/computed tomography: what did we learn? Mol Imaging Biol **2004**;6(5):275-290.
14. Mulder WJ, Strijkers GJ, Griffioen AW, van BL, Molema G, Storm G, Koning GA, Nicolay K. A liposomal system for contrast-enhanced magnetic resonance imaging of molecular targets. Bioconjug Chem **2004**;15(4):799-806.
15. Zheng J, Perkins G, Kirilova A, Allen C, Jaffray DA. Multimodal contrast agent for combined computed tomography and magnetic resonance imaging applications. Invest Radiol **2006**;41(3):339-348.

16. Zielhuis SW, Nijsen JF, Seppenwoolde JH, Zonnenberg BA, Bakker CJ, Hennink WE, van Rijk PP, van het Schip AD. Lanthanide bearing microparticulate systems for multi-modality imaging and targeted therapy of cancer. Curr Med Chem Anti -Canc Agents **2005**;5(3):303-313.
17. Pietrzyk U, Herholz K, Schuster A, von Stockhausen HM, Lucht H, Heiss WD. Clinical applications of registration and fusion of multimodality brain images from PET, SPECT, CT, and MRI. Eur J Radiol **1996**;21(3):174-182.
18. Meikle SR, Kench P, Kassiou M, Banati RB. Small animal SPECT and its place in the matrix of molecular imaging technologies. Phys Med Biol **2005**;50(22):R45-R61.
19. Grosu AL, Weber WA, Franz M, Stark S, Piert M, Thamm R, Gumprecht H, Schwaiger M, Molls M, Nieder C. Reirradiation of recurrent high-grade gliomas using amino acid PET (SPECT)/CT/MRI image fusion to determine gross tumor volume for stereotactic fractionated radiotherapy. Int J Radiat Oncol Biol Phys **2005**;63(2):511-519.
20. Winkelmann S, Schaeffter T, Eggers H, Doessel O. Simultaneous imaging and R_2* mapping using a radial multi-gradient-echo (rMGE) sequence. J Magn Reson Imaging **2006**;In press.
21. Wit de TC, Xiao J, Nijsen JFW, van het Schip AD, Staelens S, van Rijk P.P., Beekman FJ. Hybrid scatter correction for quantitative Holmium-166 SPECT. Phys Med Biol **2006**.
22. Wolf GL. Delivery of diagnostic agents: achievements and challenges. Adv Drug Deliv Rev **1999**;37(1-3):1-12.
23. Nijsen JF, Seppenwoolde JH, Havenith T, Bos C, Bakker CJ, van het Schip AD. Liver tumors: MR imaging of radioactive holmium microspheres--phantom and rabbit study. Radiology **2004**;231(2):491-499.
24. Seppenwoolde JH, Nijsen JF, Bartels LW, Zielhuis SW, van het Schip AD, Bakker CJ. Internal radiation therapy of liver tumors: qualitative and quantitative magnetic resonance imaging of the biodistribution of holmium-loaded microspheres in animal models. Magn Reson Med **2005**;53(1):76-84.
25. Nijsen JF, van het Schip AD, Hennink WE, Rook DW, van Rijk PP, de Klerk JM. Advances in nuclear oncology: microspheres for internal radionuclide therapy of liver tumours. Curr Med Chem **2002**;9(1):73-82.
26. Mulder WJ, Strijkers GJ, van Tilborg GA, Griffioen AW, Nicolay K. Lipid-based nanoparticles for contrast-enhanced MRI and molecular imaging. NMR Biomed **2006**;19(1):142-164.
27. Bulte JW. Intracellular endosomal magnetic labeling of cells. Methods Mol Med **2006**;124:419-439.
28. Bulte JW, Kraitchman DL. Monitoring cell therapy using iron oxide MR contrast agents. Curr Pharm Biotechnol **2004**;5(6):567-584.
29. Mastrobattista E, Koning GA, Storm G. Immunoliposomes for the targeted delivery of antitumor drugs. Adv Drug Deliv Rev **1999**;40(1-2):103-127.
30. Sinha VR, Goyal V, Bhinge JR, Mittal BR, Trehan A. Diagnostic microspheres: an overview. Crit Rev Ther Drug Carrier Syst **2003**;20(6):431-460.
31. Massoud TF, Gambhir SS. Molecular imaging in living subjects: seeing fundamental biological processes in a new light. Genes Dev **2003**;17(5):545-580.

32. Bulte JW, Kraitchman DL. Iron oxide MR contrast agents for molecular and cellular imaging. NMR Biomed **2004**;17(7):484-499.
33. Weissleder R, Mahmood U. Molecular imaging. Radiology **2001**;219(2):316-333.
34. Weissleder R. Scaling down imaging: molecular mapping of cancer in mice. Nat Rev Cancer **2002**;2(1):11-18.
35. Cherry SR. In vivo molecular and genomic imaging: new challenges for imaging physics. Phys Med Biol **2004**;49(3):R13-R48.
36. Kraitchman DL, Tatsumi M, Gilson WD, Ishimori T, Kedziorek D, Walczak P, Segars WP, Chen HH, Fritzges D, Izbudak I, Young RG, Marcelino M, Pittenger MF, Solaiyappan M, Boston RC, Tsui BM, Wahl RL, Bulte JW. Dynamic imaging of allogeneic mesenchymal stem cells trafficking to myocardial infarction. Circulation **2005**;112(10):1451-1461.
37. Fossheim S, Johansson C, Fahlvik AK, Grace D, Klaveness J. Lanthanide-based susceptibility contrast agents: assessment of the magnetic properties. Magn Reson Med **1996**;35(2):201-206.
38. Thunus L, Lejeune R. Overview of transition metal and lanthanide complexes as diagnostic tools. Coordination Chemistry Reviews **1999**;184:125-155.
39. Miyamoto A, Okimoto H, Shinohara H, Shibamoto Y. Development of water-soluble metallofullerenes as X-ray contrast media. Eur Radiol **2005**;1-4.
40. Bulte JW, Wu C, Brechbiel MW, Brooks RA, Vymazal J, Holla M, Frank JA. Dysprosium-DOTA-PAMAM dendrimers as macromolecular T2 contrast agents. Preparation and relaxometry. Invest Radiol **1998**;33(11):841-845.
41. Krause W, Schuhmann-Giampieri G, Bauer M, Press WR, Muschick P. Ytterbium- and dysprosium-EOB-DTPA. A new prototype of liver-specific contrast agents for computed tomography. Invest Radiol **1996**;31(8):502-511.
42. Schmitz SA, Wagner S, Schuhmann-Giampieri G, Krause W, Bollow M, Wolf KJ. Gd-EOB-DTPA and Yb-EOB-DTPA: two prototypic contrast media for CT detection of liver lesions in dogs. Radiology **1997**;205(2):361-366.
43. Zwicker C, Hering M, Langer R. Computed tomography with iodine-free contrast media. Eur Radiol **1997**;7(7):1123-1126.
44. Kwekkeboom DJ, Bakker WH, Kam BL, Teunissen JJ, Kooij PP, de Herder WW, Feelders RA, van Eijck CH, de JM, Srinivasan A, Erion JL, Krenning EP. Treatment of patients with gastro-entero-pancreatic (GEP) tumours with the novel radiolabelled somatostatin analogue [177Lu-DOTA(0),Tyr3]octreotate. Eur J Nucl Med Mol Imaging **2003**;30(3):417-422.
45. Mumper RJ, Ryo UY, Jay M. Neutron-activated holmium-166-poly (L-lactic acid) microspheres: a potential agent for the internal radiation therapy of hepatic tumors. J Nucl Med **1991**;32(11):2139-2143.
46. Nijsen JF, Zonnenberg BA, Woittiez JR, Rook DW, Swildens-van W, I, van Rijk PP, van het Schip AD. Holmium-166 poly lactic acid microspheres applicable for intra-arterial radionuclide therapy of hepatic malignancies: effects of preparation and neutron activation techniques. Eur J Nucl Med **1999**;26(7):699-704.
47. Rajendran JG, Eary JF, Bensinger W, Durack LD, Vernon C, Fritzberg A. High-dose 166Ho-DOTMP in myeloablative treatment of multiple myeloma: pharmacokinetics, biodistribution, and absorbed dose estimation. J Nucl Med **2002**;43(10):1383-1390.

48. McDonald MA, Watkin KL. Small particulate gadolinium oxide and gadolinium oxide albumin microspheres as multimodal contrast and therapeutic agents. Invest Radiol **2003**;38(6):305-310.
49. Watkin KL, McDonald MA. Multi-modal contrast agents: a first step. Acad Radiol **2002**;9 Suppl 2:S285-S289.
50. Gennari L, Doci R, Mazzaferro V, Colella G, Montalto F, Regalia E. Hepatic resection for hepatocellular carcinoma. J Surg Oncol Suppl **1993**;3:62-66.
51. Okuda K, Ohtsuki T, Obata H, Tomimatsu M, Okazaki N, Hasegawa H, Nakajima Y, Ohnishi K. Natural history of hepatocellular carcinoma and prognosis in relation to treatment. Study of 850 patients. Cancer **1985**;56(4):918-928.
52. Cochrane AM, Murray-Lyon IM, Brinkley DM, Williams R. Quadruple chemotherapy versus radiotherapy in treatment of primary hepatocellular carcinoma. Cancer **1977**;40(2):609-614.
53. Emami B, Lyman J, Brown A, Coia L, Goitein M, Munzenrider JE, Shank B, Solin LJ, Wesson M. Tolerance of normal tissue to therapeutic irradiation. Int J Radiat Oncol Biol Phys **1991**;21(1):109-122.
54. Falkson G, Moertel CG, Lavin P, Pretorius FJ, Carbone PP. Chemotherapy studies in primary liver cancer: a prospective randomized clinical trial. Cancer **1978**;42(5):2149-2156.
55. Patt YZ, Claghorn L, Charnsangavej C, Soski M, Cleary K, Mavligit GM. Hepatocellular carcinoma. A retrospective analysis of treatments to manage disease confined to the liver. Cancer **1988**;61(9):1884-1888.
56. Ehrhardt GJ, Day DE. Therapeutic use of 90Y microspheres. Int J Rad Appl Instrum B **1987**;14(3):233-242.
57. Nijsen JF, van Steenbergen MJ, Kooijman H, Talsma H, Kroon-Batenburg LM, van de WM, van Rijk PP, De WA, Van Schip AD, Hennink WE. Characterization of poly(L-lactic acid) microspheres loaded with holmium acetylacetonate. Biomaterials **2001**;22(22):3073-3081.
58. Nijsen JF, van het Schip AD, van Steenbergen MJ, Zielhuis SW, Kroon-Batenburg LM, van de WM, van Rijk PP, Hennink WE. Influence of neutron irradiation on holmium acetylacetonate loaded poly(L-lactic acid) microspheres. Biomaterials **2002**;23(8):1831-1839.
59. Nijsen JF, Rook D, Brandt C, Meijer R, Dullens H, Zonnenberg B, de KJ, van RP, Hennink W, van het SF. Targeting of liver tumour in rats by selective delivery of holmium-166 loaded microspheres: a biodistribution study. Eur J Nucl Med **2001**;28(6):743-749.
60. Lau WY, Ho S, Leung TW, Chan M, Ho R, Johnson PJ, Li AK. Selective internal radiation therapy for nonresectable hepatocellular carcinoma with intraarterial infusion of 90yttrium microspheres. Int J Radiat Oncol Biol Phys **1998**;40(3):583-592.
61. Ho S, Lau WY, Leung TW, Chan M, Chan KW, Lee WY, Johnson PJ, Li AK. Tumour-to-normal uptake ratio of 90Y microspheres in hepatic cancer assessed with 99Tcm macroaggregated albumin. Br J Radiol **1997**;70(836):823-828.
62. Sarfaraz M, Kennedy AS, Cao ZJ, Sackett GD, Yu CX, Lodge MA, Murthy R, Line BR, Van Echo DA. Physical aspects of yttrium-90 microsphere therapy for nonresectable hepatic tumors. Med Phys **2003**;30(2):199-203.
63. Haacke EM, Brown RW, Thompson MR, Venkatesan R. Magnetic Resonance Imaging. Physical Principles and Sequence Design. New York: John Wiley & Sons, Inc.; 1999.

64. [Anonymous]. Handbook of Chemistry and Physics. 84 ed. London, UK: CRC press; 2000.
65. Yablonskiy DA, Haacke EM. Theory of NMR signal behavior in magnetically inhomogeneous tissues: the static dephasing regime. Magn Reson Med **1994**;32(6):749-763.
66. Hornak JP. The basics of MRI. Rochester, New York: 1996.
67. Dahnke H, Schaeffter T. Limits of detection of SPIO at 3.0 T using T2 relaxometry. Magn Reson Med **2005**;53(5):1202-1206.
68. Hounsfield GN. Computerized transverse axial scanning (tomography): Part I. Description of system. 1973. Br J Radiol **1995**;68(815):H166-H172.
69. Kalender WA. Computed Tomography. Munich: Publicis MCD Verlag; 2000.
70. Prokop M, Galanski M. Computed tomography of the body. 2003.
71. Cherry SR, Sorensen JA, Phelps ME. Physics in Nuclear Medicine. 3rd ed. Philadelphia: Saunders, Elsevier Science; 2003.
72. Wernick MN, Aarsvold JN. Emission tomography. San Diego: Elsevier Science; 2004.
73. Albert Rose. The Sensitivity of the Human Eye on an Absolute Scale. J Opt Soc Am **1948**;38(2):196-208.
74. Constable RT, Henkelman RM. Contrast, resolution, and detectability in MR imaging. J Comput Assist Tomogr **1991**;15(2):297-303.
75. Park S, Clarkson E, Kupinski MA, Barrett HH. Efficiency of the human observer detecting random signals in random backgrounds. J Opt Soc Am A Opt Image Sci Vis **2005**;22(1):3-16.
76. Suess C, Kalender WA, Coman JM. New low-contrast resolution phantoms for computed tomography. Med Phys **1999**;26(2):296-302.
77. Thijssen JM, van Wijk MC, Cuypers MH. Performance testing of medical echo/Doppler equipment. Eur J Ultrasound **2002**;15(3):151-164.
78. Thomas MD, Bailey DL, Livieratos L. A dual modality approach to quantitative quality control in emission tomography. Phys Med Biol **2005**;50(15):N187-N194.
79. Baldoc C, Lepage M, Back SA, Murry PJ, Jayasekera PM, Porter D, Kron T. Dose resolution in radiotherapy polymer gel dosimetry: effect of echo spacing in MRI pulse sequence. Phys Med Biol **2001**;46(2):449-460.
80. Bluemke DA, Sahani D, Amendola M, Balzer T, Breuer J, Brown JJ, Casalino DD, Davis PL, Francis IR, Krinsky G, Lee FT, Jr., Lu D, Paulson EK, Schwartz LH, Siegelman ES, Small WC, Weber TM, Welber A, Shamsi K. Efficacy and safety of MR imaging with liver-specific contrast agent: U.S. multicenter phase III study. Radiology **2005**;237(1):89-98.
81. Hanninen EL, Vogl TJ, Felfe R, Pegios W, Balzer J, Clauss W, Felix R. Detection of focal liver lesions at biphasic spiral CT: randomized double-blind study of the effect of iodine concentration in contrast materials. Radiology **2000**;216(2):403-409.
82. Krause W. Delivery of diagnostic agents in computed tomography. Adv Drug Deliv Rev **1999**;37(1-3):159-173.
83. Semelka RC, Helmberger TKG. Contrast agents for MR imaging of the liver. Radiology **2001**;218(1):27-38.
84. Fischbach F, Knollmann F, Griesshaber V, Freund T, Akkol E, Felix R. Detection of pulmonary nodules by multislice computed tomography: improved detection rate with reduced slice thickness. Eur Radiol **2003**;13(10):2378-2383.

85. Shapiro EM, Skrtic S, Koretsky AP. Sizing it up: cellular MRI using micron-sized iron oxide particles. Magn Reson Med **2005**;53(2):329-338.
86. Heyn C, Bowen CV, Rutt BK, Foster PJ. Detection threshold of single SPIO-labeled cells with FIESTA. Magn Reson Med **2005**;53(2):312-320.
87. Cohen G, DiBianca FA. The use of contrast -- detail -- dose evaluation of image quality in a computed tomographic scanner. J Comput Assist Tomogr **1979**;3(2):189-195.
88. Yung KT. Empirical models of transverse relaxation for spherical magnetic perturbers. Magn Reson Imaging **2003**;21(5):451-463.
89. Fahlvik AK, Holtz E, Klaveness J. Relaxation efficacy of paramagnetic and superparamagnetic microspheres in liver and spleen. Magn Reson Imaging **1990**;8(4):363-369.
90. Tanimoto A, Pouliquen D, Kreft BP, Stark DD. Effects of spatial distribution on proton relaxation enhancement by particulate iron oxide. J Magn Reson Imaging **1994**;4(5):653-657.
91. Tanimoto A, Oshio K, Suematsu M, Pouliquen D, Stark DD. Relaxation effects of clustered particles. J Magn Reson Imaging **2001**;14(1):72-77.
92. Pruessmann KP, Weiger M, Scheidegger MB, Boesiger P. SENSE: sensitivity encoding for fast MRI. Magn Reson Med **1999**;42(5):952-962.
93. Wiesinger F, Van de Moortele PF, Adriany G, De ZN, Ugurbil K, Pruessmann KP. Potential and feasibility of parallel MRI at high field. NMR Biomed **2006**;19(3):368-378.
94. Tsao J, Boesiger P, Pruessmann KP. k-t BLAST and k-t SENSE: dynamic MRI with high frame rate exploiting spatiotemporal correlations. Magn Reson Med **2003**;50(5):1031-1042.
95. Kim YK, Kim CS, Kwak HS, Lee JM. Three-dimensional dynamic liver MR imaging using sensitivity encoding for detection of hepatocellular carcinomas: comparison with superparamagnetic iron oxide-enhanced mr imaging. J Magn Reson Imaging **2004**;20(5):826-837.
96. Schwert DD, Davis PL, Richardson N. Non-Gadolinium-Based MRI Contrast Agents. Topics in Current Chemistry **2002**;221:165-199.
97. Seppenwoolde JH, Viergever MA, Bakker CJ. Passive tracking exploiting local signal conservation: the white marker phenomenon. Magn Reson Med **2003**;50(4):784-790.
98. Bakker CJ, Seppenwoolde JH, Vincken KL. Dephased MRI. Magn Reson Med **2006**;55(1):92-97.
99. Mani V, Briley-Saebo KC, Itskovich VV, Samber DD, Fayad ZA. Gradient echo acquisition for superparamagnetic particles with positive contrast (GRASP): sequence characterization in membrane and glass superparamagnetic iron oxide phantoms at 1.5T and 3T. Magn Reson Med **2006**;55(1):126-135.
100. Cunningham CH, Arai T, Yang PC, McConnell MV, Pauly JM, Conolly SM. Positive contrast magnetic resonance imaging of cells labeled with magnetic nanoparticles. Magn Reson Med **2005**;53(5):999-1005.
101. Ahrens ET, Flores R, Xu H, Morel PA. In vivo imaging platform for tracking immunotherapeutic cells. Nat Biotechnol **2005**;23(8):983-987.
102. Bulte JW. Hot spot MRI emerges from the background. Nat Biotechnol **2005**;23(8):945-946.
103. Kanematsu M, Itoh K, Matsuo M, Maetani Y, Ametani F, Kondo H, Kato H, Hoshi H. Malignant hepatic tumor detection with ferumoxides-enhanced MR imaging with a 1.5-T system: comparison of four imaging pulse sequences. J Magn Reson Imaging **2001**;13(2):249-257.

104. Takahama K, Amano Y, Hayashi H, Ishihara M, Kumazaki T. Detection and characterization of focal liver lesions using superparamagnetic iron oxide-enhanced magnetic resonance imaging: comparison between ferumoxides-enhanced T1-weighted imaging and delayed-phase gadolinium-enhanced T1-weighted imaging. Abdom Imaging **2003**;28(4):525-530.
105. Baudendistel KT, Heverhagen JT, Knopp MV. [Clinical MR at 3 Tesla: current status]. Radiologe **2004**;44(1):11-18.
106. Zech CJ, Schoenberg SO, Herrmann KA, Dietrich O, Menzel MI, Lanz T, Wallnofer A, Helmberger T, Reiser MF. [Modern visualization of the liver with MRT. Current trends and future perspectives]. Radiologe **2004**;44(12):1160-1169.
107. Edelstein WA, Glover GH, Hardy CJ, Redington RW. The intrinsic signal-to-noise ratio in NMR imaging. Magn Reson Med **1986**;3(4):604-618.
108. Rinck PA, Muller RN. Field strength and dose dependence of contrast enhancement by gadolinium-based MR contrast agents. Eur Radiol **1999**;9(5):998-1004.
109. Krautmacher C, Willinek WA, Tschampa HJ, Born M, Traber F, Gieseke J, Textor HJ, Schild HH, Kuhl CK. Brain tumors: full- and half-dose contrast-enhanced MR imaging at 3.0 T compared with 1.5 T--Initial Experience. Radiology **2005**;237(3):1014-1019.
110. Nobauer-Huhmann IM, Ba-Ssalamah A, Mlynarik V, Barth M, Schoggl A, Heimberger K, Matula C, Fog A, Kaider A, Trattnig S. Magnetic resonance imaging contrast enhancement of brain tumors at 3 tesla versus 1.5 tesla. Invest Radiol **2002**;37(3):114-119.
111. Tilcock C, Unger E, Cullis P, Macdougall P. Liposomal Gd-Dtpa - Preparation and Characterization of Relaxivity. Radiology **1989**;171(1):77-80.
112. Weissleder R, Elizondo G, Wittenberg J, Rabito CA, Bengele HH, Josephson L. Ultrasmall superparamagnetic iron oxide: characterization of a new class of contrast agents for MR imaging. Radiology **1990**;175(2):489-493.
113. Weissleder R, Bogdanov A, Neuwelt EA, Papisov M. Long-Circulating Iron-Oxides for Mr-Imaging. Advanced Drug Delivery Reviews **1995**;16(2-3):321-334.
114. Koenig SH, Brown RD, Kurland R, Ohki S. Relaxitivity and Binding of Mn-2+ Ions in Solutions of Phosphatidylserine Vesicles. Magnetic Resonance in Medicine **1988**;7(2):133-142.
115. Aime S, Anelli L, Botta M, Brocchetta M, Canton S, Fedeli F, Gianolio E, Terreno E. Relaxometric evaluation of novel manganese(II) complexes for application as contrast agents in magnetic resonance imaging. J Biol Inorg Chem **2002**;7(1-2):58-67.
116. Limanond P, Raman SS, Sayre J, Lu DS. Comparison of dynamic gadolinium-enhanced and ferumoxides-enhanced MRI of the liver on high- and low-field scanners. J Magn Reson Imaging **2004**;20(4):640-647.
117. Tanimoto A, Kuribayashi S. Application of superparamagnetic iron oxide to imaging of hepatocellular carcinoma. Eur J Radiol **2006**.
118. Yamashita Y, Morishita S, Awai K, Kawanaka K. Imaging of the liver by helical CT and MR imaging. Intervirology **2004**;47(3-5):125-133.
119. Chan KW, Barra S, Botta M, Wong WT. Novel gadolinium(III) polyaminocarboxylate macrocyclic complexes as potential magnetic resonance imaging contrast agents. J Inorg Biochem **2004**;98(5):677-682.

120. Trubetskoy VS, Cannillo JA, Milshtein A, Wolf GL, Torchilin VP. Controlled delivery of Gd-containing liposomes to lymph nodes: surface modification may enhance MRI contrast properties. Magn Reson Imaging **1995**;13(1):31-37.
121. Semelka RC, Worawattanakul S, Kelekis NL, John G, Woosley JT, Graham M, Cance WG. Liver lesion detection, characterization, and effect on patient management: comparison of single-phase spiral CT and current MR techniques. J Magn Reson Imaging **1997**;7(6):1040-1047.
122. Yamashita Y, Mitsuzaki K, Yi T, Ogata I, Nishiharu T, Urata J, Takahashi M. Small hepatocellular carcinoma in patients with chronic liver damage: prospective comparison of detection with dynamic MR imaging and helical CT of the whole liver. Radiology **1996**;200(1):79-84.
123. Liou J, Lee JK, Borrello JA, Brown JJ. Differentiation of hepatomas from nonhepatomatous masses: use of MnDPDP-enhanced MR images. Magn Reson Imaging **1994**;12(1):71-79.
124. Oudkerk M, Torres CG, Song B, Konig M, Grimm J, Fernandez-Cuadrado J, Op de BB, Marquardt M, van DP, de Groot JC. Characterization of liver lesions with mangafodipir trisodium-enhanced MR imaging: multicenter study comparing MR and dual-phase spiral CT. Radiology **2002**;223(2):517-524.
125. Pautler RG. Biological applications of manganese-enhanced magnetic resonance imaging. Methods Mol Med **2006**;124:365-386.
126. McCullough EC. Factors affecting the use of quantitative information from a CT scanner. Radiology **1977**;124(1):99-107.
127. Frush DP, Slack CC, Hollingsworth CL, Bisset GS, Donnelly LF, Hsieh J, Lavin-Wensell T, Mayo JR. Computer-simulated radiation dose reduction for abdominal multidetector CT of pediatric patients. AJR Am J Roentgenol **2002**;179(5):1107-1113.
128. Hamberg LM, Rhea JT, Hunter GJ, Thrall JH. Multi-detector row CT: radiation dose characteristics. Radiology **2003**;226(3):762-772.
129. Nickoloff EL, Dutta AK, Lu ZF. Influence of phantom diameter, kVp and scan mode upon computed tomography dose index. Med Phys **2003**;30(3):395-402.
130. Haaga JR, Miraldi F, MacIntyre W, LiPuma JP, Bryan PJ, Wiesen E. The effect of mAs variation upon computed tomography image quality as evaluated by in vivo and in vitro studies. Radiology **1981**;138(2):449-454.
131. Funama Y, Awai K, Nakayama Y, Kakei K, Nagasue N, Shimamura M, Sato N, Sultana S, Morishita S, Yamashita Y. Radiation dose reduction without degradation of low-contrast detectability at abdominal multisection CT with a low-tube voltage technique: phantom study. Radiology **2005**;237(3):905-910.
132. Nakayama Y, Awai K, Funama Y, Hatemura M, Imuta M, Nakaura T, Ryu D, Morishita S, Sultana S, Sato N, Yamashita Y. Abdominal CT with low tube voltage: preliminary observations about radiation dose, contrast enhancement, image quality, and noise. Radiology **2005**;237(3):945-951.
133. Prokop M. Multislice CT: technical principles and future trends. Eur Radiol **2003**;13 Suppl 5:M3-13.
134. Tanaka C, Ueguchi T, Shimosegawa E, Sasaki N, Johkoh T, Nakamura H, Hatazawa J. Effect of CT acquisition parameters in the detection of subtle hypoattenuation in acute cerebral infarction: a phantom study. AJNR Am J Neuroradiol **2006**;27(1):40-45.

135. Kalender WA, Polacin A, Suss C. A comparison of conventional and spiral CT: an experimental study on the detection of spherical lesions. J Comput Assist Tomogr **1994**;18(2):167-176.
136. Weg N, Scheer MR, Gabor MP. Liver lesions: improved detection with dual-detector-array CT and routine 2.5-mm thin collimation. Radiology **1998**;209(2):417-426.
137. Abdelmoumene A, Chevallier P, Chalaron M, Schneider F, Verdun FR, Frascarolo P, Meuli R, Schnyder P, Denys A. Detection of liver metastases under 2 cm: comparison of different acquisition protocols in four row multidetector-CT (MDCT). Eur Radiol **2005**;15(9):1881-1887.
138. Verdun FR, Denys A, Valley JF, Schnyder P, Meuli RA. Detection of low-contrast objects: experimental comparison of single- and multi-detector row CT with a phantom. Radiology **2002**;223(2):426-431.
139. Fuchs T, Krause J, Schaller S, Flohr T, Kalender WA. Spiral interpolation algorithms for multislice spiral CT--part II: measurement and evaluation of slice sensitivity profiles and noise at a clinical multislice system. IEEE Trans Med Imaging **2000**;19(9):835-847.
140. Funama Y, Awai K, Miyazaki O, Nakayama Y, Goto T, Omi Y, Shimonobo T, Liu D, Yamashita Y, Hori S. Improvement of low-contrast detectability in low-dose hepatic multidetector computed tomography using a novel adaptive filter: evaluation with a computer-simulated liver including tumors. Invest Radiol **2006**;41(1):1-7.
141. Kalra MK, Maher MM, Blake MA, Lucey BC, Karau K, Toth TL, Avinash G, Halpern EF, Saini S. Detection and characterization of lesions on low-radiation-dose abdominal CT images postprocessed with noise reduction filters. Radiology **2004**;232(3):791-797.
142. Beekman FJ, Kamphuis C. Ordered subset reconstruction for x-ray CT. Phys Med Biol **2001**;46(7):1835-1844.
143. Zbijewski W, Beekman FJ. Efficient Monte Carlo based scatter artifact reduction in cone-beam micro-CT. IEEE Trans Med Imaging **2006**;25(7):817-827.
144. Nuyts J, De MB, Dupont P, Defrise M, Suetens P, Mortelmans L. Iterative reconstruction for helical CT: a simulation study. Phys Med Biol **1998**;43(4):729-737.
145. Zbijewski W, Beekman FJ. Characterization and suppression of edge and aliasing artefacts in iterative x-ray CT reconstruction. Phys Med Biol **2004**;49(1):145-157.
146. Kole JS, Beekman FJ. Evaluation of the ordered subset convex algorithm for cone-beam CT. Phys Med Biol **2005**;50(4):613-623.
147. Krause W, Mahler M, Hanke B, Milius W, Kaufmann J, Rogalla P, Hamm B. Dy-EOB-DTPA: tolerance and pharmacokinetics in healthy volunteers and preliminary liver imaging in patients. Invest Radiol **2001**;36(8):431-444.
148. Krause W, Handreke K, Schuhmann-Giampieri G, Rupp K. Efficacy of the iodine-free computed tomography liver contrast agent, Dy-EOB-DTPA, in comparison with a conventional iodinated agent in normal and in tumor-bearing rabbits. Invest Radiol **2002**;37(5):241-247.
149. Schmitz SA, Wagner S, Schuhmann-Giampieri G, Krause W, Wolf KJ. A prototype liver-specific contrast medium for CT: preclinical evaluation of gadoxetic acid disodium, or Gd-EOB-DTPA. Radiology **1997**;202(2):407-412.
150. Awai K, Inoue M, Yagyu Y, Watanabe M, Sano T, Nin S, Koike R, Nishimura Y, Yamashita Y. Moderate versus high concentration of contrast material for aortic and hepatic enhancement and tumor-to-liver contrast at multi-detector row CT. Radiology **2004**;233(3):682-688.

151. Marchiano A, Spreafico C, Lanocita R, Frigerio L, Di TG, Patelli G, Garbagnati F, Heiman F, Taroni P, Damascelli B. Does iodine concentration affect the diagnostic efficacy of biphasic spiral CT in patients with hepatocellular carcinoma? Abdom Imaging **2005**;30(3):274-280.
152. Goldstein HA, Kashanian FK, Blumetti RF, Holyoak WL, Hugo FP, Blumenfield DM. Safety assessment of gadopentetate dimeglumine in U.S. clinical trials. Radiology **1990**;174(1):17-23.
153. Albrecht T, Dawson P. Gadolinium-DTPA as X-ray contrast medium in clinical studies. Br J Radiol **2000**;73(872):878-882.
154. Niendorf HP, Haustein J, Cornelius I, Alhassan A, Clauss W. Safety of gadolinium-DTPA: extended clinical experience. Magn Reson Med **1991**;22(2):222-228.
155. Prince MR, Arnoldus C, Frisoli JK. Nephrotoxicity of high-dose gadolinium compared with iodinated contrast. J Magn Reson Imaging **1996**;6(1):162-166.
156. Spinosa DJ, Kaufmann JA, Hartwell GD. Gadolinium chelates in angiography and interventional radiology: a useful alternative to iodinated contrast media for angiography. Radiology **2002**;223(2):319-325.
157. Bae KT, McDermott R, Gierada DS, Heiken JP, Nolte MA, Takahashi N, Hong C. Gadolinium-enhanced computed tomography angiography in multi-detector row computed tomography: initial observations. Acad Radiol **2004**;11(1):61-68.
158. Kaufman JA, Geller SC, Waltman AC. Renal insufficiency: gadopentetate dimeglumine as a radiographic contrast agent during peripheral vascular interventional procedures. Radiology **1996**;198(2):579-581.
159. Hutton BF, Hudson HM, Beekman FJ. A clinical perspective of accelerated statistical reconstruction. Eur J Nucl Med **1997**;24(7):797-808.
160. Tsui BM, Frey EC, LaCroix KJ, Lalush DS, Mccartney WH, King MA, Gullberg GT. Quantitative myocardial perfusion SPECT. J Nucl Cardiol **1998**;5(5):507-522.
161. Beekman FJ, Kamphuis C, King MA, van Rijk PP, Viergever MA. Improvement of image resolution and quantitative accuracy in clinical Single Photon Emission Computed Tomography. Comput Med Imaging Graph **2001**;25(2):135-146.
162. Bayouth JE, Macey DJ. Quantitative Imaging of Ho-166 with An Anger Camera. Physics in Medicine and Biology **1994**;39(2):265-279.
163. Meikle SR, Eberl S, Iida H. Instrumentation and methodology for quantitative pre-clinical imaging studies. Curr Pharm Des **2001**;7(18):1945-1966.
164. Frey EC, Tsui BM, Gullberg GT. Improved estimation of the detector response function for converging beam collimators. Phys Med Biol **1998**;43(4):941-950.
165. Formiconi AR. Collimators. Q J Nucl Med **2002**;46(1):8-15.
166. Moore SC, Kouris K, Cullum I. Collimator design for single photon emission tomography. Eur J Nucl Med **1992**;19(2):138-150.
167. Moore SC, Foley KM, El FG. Collimator optimization for detection and quantitation tasks: application to gallium-67 imaging. IEEE Trans Med Imaging **2005**;24(10):1347-1356.
168. Lau YH, Hutton BF, Beekman FJ. Choice of collimator for cardiac SPET when resolution compensation is included in iterative reconstruction. Eur J Nucl Med **2001**;28(1):39-47.
169. Muehllehner G, Luig H. Septal penetration in scintillation camera collimators. Phys Med Biol **1973**;18(6):855-862.

170. Smith MF, Jaszczak RJ. A rotating parallel hole collimator for high resolution imaging of medium energy radionuclides. Ieee Transactions on Nuclear Science **1998**;45(4):2102-2112.
171. Ogawa K, Takagi Y, Kubo A, Hashimoto S, Sannmiya T, Okano Y, Morozumi T, Nakajima M, Yuta S. [An attenuation correction method of single photon emission computed tomography using gamma ray transmission CT]. Kaku Igaku **1985**;22(4):477-490.
172. Tsui BM, Gullberg GT, Edgerton ER, Ballard JG, Perry JR, Mccartney WH, Berg J. Correction of nonuniform attenuation in cardiac SPECT imaging. J Nucl Med **1989**;30(4):497-507.
173. Beekman FJ, de Jong HW, van Geloven S. Efficient fully 3-D iterative SPECT reconstruction with Monte Carlo-based scatter compensation. IEEE Trans Med Imaging **2002**;21(8):867-877.
174. Beekman FJ, Kamphuis C, Viergever MA. Improved SPECT quantitation using fully three-dimensional iterative spatially variant scatter response compensation. Ieee Transactions on Medical Imaging **1996**;15(4):491-499.
175. Beekman FJ, Kamphuis C, Frey EC. Scatter compensation methods in 3D iterative SPECT reconstruction: a simulation study. Phys Med Biol **1997**;42(8):1619-1632.
176. Hutton BF, Osiecki A, Meikle SR. Transmission-based scatter correction of 180 degrees myocardial single-photon emission tomographic studies. Eur J Nucl Med **1996**;23(10):1300-1308.
177. Kamphuis C, Beekman FJ, Viergever MA. Evaluation of OS-EM vs ML-EM for 1D, 2D and fully 3D SPECT reconstruction. Ieee Transactions on Nuclear Science **1996**;43(3):2018-2024.
178. Tsui BMW, Frey EC, Zhao X, Lalush DS, Johnston RE, Mccartney WH. The Importance and Implementation of Accurate 3D Compensation Methods for Quantitative Spect. Physics in Medicine and Biology **1994**;39(3):509-530.
179. Zeng GL, Gullberg GT, Tsui BMW, Terry JA. 3-Dimensional Iterative Reconstruction Algorithms with Attenuation and Geometric Point Response Correction. Ieee Transactions on Nuclear Science **1991**;38(2):693-702.
180. Kamphuis C, Beekman FJ, van Rijk PP, Viergever MA. Duel matrix ordered subsets reconstruction for accelerated 3D scatter compensation in single-photon emission tomography. European Journal of Nuclear Medicine **1998**;25(1):8-18.
181. Seo Y, Wong KH, Sun M, Franc BL, Hawkins RA, Hasegawa BH. Correction of photon attenuation and collimator response for a body-contouring SPECT/CT imaging system. J Nucl Med **2005**;46(5):868-877.
182. Brambilla M, Cannillo B, Dominietto M, Leva L, Secco C, Inglese E. Characterization of ordered-subsets expectation maximization with 3D post-reconstruction Gauss filtering and comparison with filtered backprojection in 99mTc SPECT. Ann Nucl Med **2005**;19(2):75-82.
183. Beekman FJ, Slijpen ET, Niessen WJ. Selection of task-dependent diffusion filters for the post-processing of SPECT images. Phys Med Biol **1998**;43(6):1713-1730.
184. Leahy RM, Qi JY. Statistical approaches in quantitative positron emission tomography. Statistics and Computing **2000**;10(2):147-165.
185. Bhatnagar A, Hustinx R, Alavi A. Nuclear imaging methods for non-invasive drug monitoring. Adv Drug Deliv Rev **2000**;41(1):41-54.

186. Finlay IG, Mason MD, Shelley M. Radioisotopes for the palliation of metastatic bone cancer: a systematic review. Lancet Oncol **2005**;6(6):392-400.
187. Lam MG, de Klerk JM, van Rijk PP. 186Re-HEDP for metastatic bone pain in breast cancer patients. Eur J Nucl Med Mol Imaging **2004**;31 Suppl 1:S162-S170.
188. de JM, Breeman WA, Valkema R, Bernard BF, Krenning EP. Combination radionuclide therapy using 177Lu- and 90Y-labeled somatostatin analogs. J Nucl Med **2005**;46 Suppl 1:13S-17S.
189. Teunissen JJ, Kwekkeboom DJ, Krenning EP. Staging and treatment of differentiated thyroid carcinoma with radiolabeled somatostatin analogs. Trends Endocrinol Metab **2006**;17(1):19-25.

Chapter 3

W. Bult, P.R. Seevinck, G.C. Krijger, T. Visser, L.M.J. Kroon-Batenburg, C.J.G. Bakker, W.E. Hennink, A.D. van het Schip, J.F.W. Nijsen

Based on: Pharmaceutical Research 2009;26(6):1371-8.

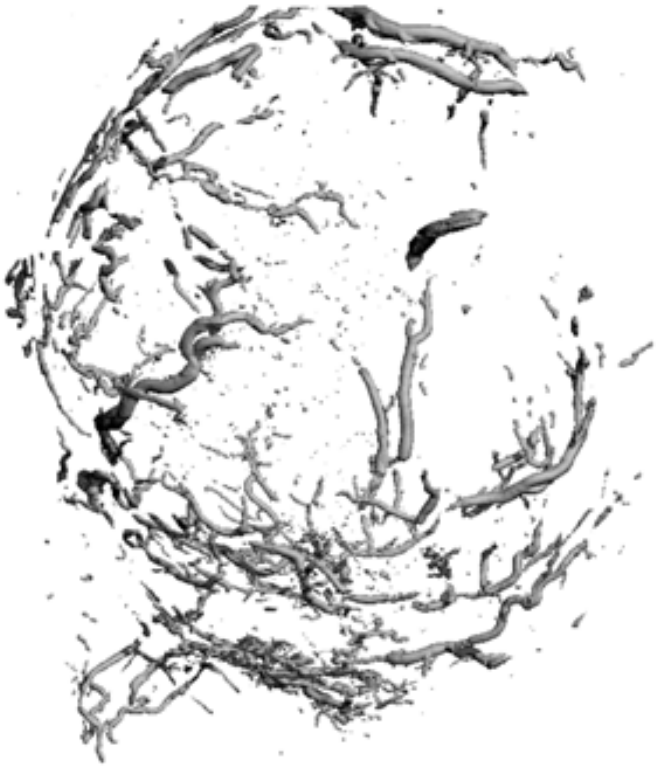

Microspheres with ultrahigh holmium content for radioablation of malignancies: preparation and multimodality characterization

Abstract

Purpose

The aim of this study was to develop and characterize microspheres with an ultrahigh holmium content to increase specific activity and enhance multimodal diagnostic properties for magnetic resonance imaging (MRI) and x-ray computed tomography (CT).

Methods

Holmium acetylacetonate (HoAcAc) microspheres were prepared by solvent evaporation, using HoAcAc crystals as the sole ingredient. HoAcAc-MS were characterized using light and scanning electron microscopy, coulter counter and titrimetry. Diagnostic sensitivity of MRI and CT were investigated quantitatively in vitro and qualitatively in an ex vivo rabbit liver.

Results

HoAcAc-MS with an increased holmium load of 45 % (*w/w*) were prepared. The highly-loaded HoAcAc-MS displayed a smooth surface, which was not significantly influenced by 6 hours of neutron bombardment. Due to the increased holmium load, the radioactivity per sphere after neutron bombardment strongly increased, possibly boosting therapeutic efficacy. The strongly enhanced diagnostic sensitivity allowed for the detection of microgram amounts of microspheres in liver tissue using MRI and CT.

Conclusions

Stable HoAcAc microspheres with ultra high holmium content were prepared. The increased specific activity makes the microspheres suitable for radioablation of tumors by intratumoral injections. The increased diagnostic sensitivity potentially allows transcatheter radioembolization treatment planning by image-guided biodistribution assessment.

Introduction

Worldwide, primary liver cancer is the sixth most common cancer, and each year over 600,000 new cases are presented. A limited number of patients is eligible for surgical resection (partial hepatectomy or liver transplantation), limiting the five year survival rate to only 3-5% (1, 2). The use of systemic chemotherapy has been proven ineffective, however recently a survival benefit of several months has been reported for the oral multikinase inhibitor sorafenib (3).

The liver is also a common site of metastasis, and more than 50% of patients with primary malignancies will develop hepatic metastases. A very common type of cancer to metastasize solely to the liver is colorectal carcinoma. Each year over 1,000,000 new cases of colorectal cancer are presented and the mortality is approximately 500,000 patients per year. Five year survival of patients in the developed world with colorectal cancer is approximately 55%, with main prognostic factors being the extent of lymphatic spread, the number and resectability of liver metastases (1, 2). Surgical resection, considered to be the only curative treatment option, is only eligible in 10 to 20% of patients (4). Currently applied chemotherapy protocols (e.g. FOLFOX or FOLFORI, 5-fluorouracil/leucovorin combined with oxaliplatin or irrinotecan, respectively, in combination with the angiogenesis inhibitor bevacizumab) are associated with a survival of patients with unresectable liver metastases of nearly two years (5, 6).

Intra-arterial radioembolization with radioactive microspheres (glass- or resin-based) containing the high-energy beta emitter yttrium-90 (^{90}Y) is currently increasingly applied in patients with unresectable hepatic malignancies. This ^{90}Y radioembolization treatment has shown high response rates, both in a salvage setting and as a first-line treatment option (7, 8). However, the lack of (quantitative) imaging options for ^{90}Y (9) prevents accurate treatment planning prior to transcatheter radioembolization, which is necessary to assure a favorable dose distribution in each individual patient. This led to the development of holmium-166 loaded poly (L-lactic acid) (^{166}Ho-PLLA) microspheres, since ^{166}Ho emits gamma rays and beta particles that can be used for nuclear imaging and therapy, respectively (10-12). Moreover, holmium is highly paramagnetic and has a high linear attenuation coefficient allowing for visualization by magnetic resonance imaging (MRI) and X-ray computed tomography (CT), respectively (13, 14). Currently, quantitative SPECT is the method of choice for transcatheter radioembolization treatment planning with ^{166}Ho-PLLA-MS (11, 15). However, in the near future, particularly MRI is expected to become important in transcatheter radioembolization treatment planning and microsphere deposition, due to its superior soft tissue contrast, high image resolution, quantitative possibilities and

capabilities to provide real-time feedback during administration of holmium-loaded microspheres (15-18). For these applications, as well as for biodistribution prediction using a small tracer dose, an increased diagnostic sensitivity would be favorable.

Not all patients suffering from unresectable liver metastases are eligible for intra-arterial transcatheter radioembolization. In patients who have been heavily pretreated with bevacizumab or cetuximab, for example, the tumor feeding vessels may be too feeble for the microspheres to be deposited peri- and endotumorally (19). Efficacy may also be diminished in patients with hypovascular liver tumors. Furthermore, patients with portal vein thrombosis are excluded from treatment with resin microspheres (20). Those patients, with a limited number of unresectable hepatic tumors not eligible for transcatheter radioembolization, are potential candidates for intratumoral injections of radioactive microspheres. This approach has been explored in patients with liver tumors using ^{90}Y glass microspheres, showing a response rate in 90% of patients (21). Direct intratumoral injection requires small deposits of radioactive microspheres in compact tumor tissue, limiting the overall injection volume to 0.1–0.3 ml (21, 22). Consequently, the amount of activity per injection should be very high, which may be accomplished by the use of microspheres with a high holmium load.

In this paper, the preparation of microspheres with ultra high holmium load will be addressed. Size distribution, holmium content and surface characteristics are investigated, as well as the possible influence of neutron irradiation on microsphere's integrity. Furthermore, the therapeutic and diagnostic potential of the prepared microspheres will be explored, by investigating the specific activity and MRI and CT imaging characteristics. Finally, the implementation of microspheres with an ultrahigh holmium load for direct intratumoral injection and transcatheter radioembolization treatment planning will be discussed from a clinical perspective.

Materials and methods

Materials

All chemicals are commercially available and were used as obtained. Acetylacetone, 2,4-pentanedione (AcAc; >99.9%), ammoniumhydroxide (NH_4OH; 29.3% in water), chloroform (HPLC-grade), phosphorus pentoxide (Sicapent®), polyvinyl alcohol (PVA, average MW 30,000 – 70,000) and Pluronic F68® ($PEO_{100}PPO_{65}PEO_{100}$; MW 9,840-14,600) were purchased from Sigma Aldrich (Steinheim, Germany).

Holmium CertiPUR ICP standard and hexamethylentetramine were purchased from Merck (Darmstadt, Germany). Seakem LE Agarose was purchased from Lonza (Basel, Switzerland). Holmium (III) chloride hexahydrate ($HoCl_3.6H_20$; 99.95%) was purchased from Metall Rare Earth Ltd (Shenzhen, China).

Preparation of HoAcAc microspheres

The holmium acetylacetonate microspheres (HoAcAc-MS) were prepared using a solvent evaporation process. Holmium acetylacetonate crystals were prepared as previously described by Nijsen et al. (10). HoAcAc crystals were dissolved in chloroform (186 g, 5.5% *(w/w)*) and emulsified in an aqueous PVA solution (1 l, 2 % *(w/w)*). The chloroform/water emulsion was continuously stirred at a preset stirring speed (300-500 rpm). To evaporate chloroform, the mixture was thermostated at 25°C and a constant flow of nitrogen (12 l min^{-1}) was applied. After 40 hours of evaporation the formed microspheres were collected by centrifugation and washed five times with water. The washed microspheres were sieved using an electronic sieve vibrator, (EMS 755) and ultrasonic processor (UDS 751; Topaz GmbH, Dresden, Germany) as described by Zielhuis et al. (23). The microspheres were dried at room temperature for 24 hours, followed by drying at 50°C for 48 hours.

Size distribution, holmium content and surface characteristics

The size distribution of the sieved fractions and dried fractions was determined using a Coulter counter (Multisizer 3, Beckman Coulter, Mijdrecht, The Netherlands), equipped with an orifice of 100 µm. The holmium content of the microspheres was determined by complexometric titration with EDTA as described by Zielhuis et al. (23), and Inductively Coupled Plasma Optical Emission spectroscopy (ICP OES). Samples were measured at three different wavelengths (339.898, 345.600 and 347.426 nm) in an Optima 4300 CV (PerkinElmer; Norwalk, USA). SEM micrographs were acquired using a FEI PHENOM (FEI Company, Eindhoven, The Netherlands) electron microscope. Samples were mounted on an aluminum stub, and coated with a Pt layer of 6 nm.

Neutron activation

Neutron activation was performed in the pneumatic rabbit system operational at a research reactor facility (Department of Radiation, Radionuclides and Reactors, Delft University of Technology, Delft, The Netherlands). Samples were irradiated for three or six hours with a thermal neutron flux of 5×10^{12} n cm^{-2} s^{-1}. The radioactive ^{166}Ho was left to decay for one month, to ensure safe handling of HoAcAc microspheres.

Multimodality imaging characteristics

To determine the sensitivity of MRI and CT for the HoAcAc microspheres, phantom experiments were carried out. The phantom used to determine MRI and CT sensitivity consisted of agarose (2 % (*w/w*)) gel samples in plastic tubes (diameter 10 mm, length 100 mm), in which HoAcAc-MS were homogeneously dispersed with the following loadings [0.0; 0.5; 0.9; 1.9; 3.8] in mg/ml agarose, in duplicate. MR imaging was performed using a 1.5 T clinical MR scanner (Intera, Philips Medical Systems, Best, The Netherlands). To determine the r_2* relaxivity, which represents the MR sensitivity of the HoAcAc microspheres, a time series of transverse images was acquired using a multiple gradient echo sequence with 15 echoes, a first echo time of 2.0 ms, echo spacing of 1.39 ms, repetition time of 500 ms, a field of view (FOV) of 128 mm, a voxel size of 1x1x5 mm, two signal averages and a 60° flip angle. Monoexponential signal decay was assumed. Using the relation $R_2^*=R_2^*(0) + r_2^* \times$ [HoAcAc-MS], in which R_2^* is the relaxation rate, $R_2^*(0)$ the baseline relaxation rate and [HoAcAc-MS] the concentration HoAcAc-MS, the r_2* relaxivity in s^{-1} mg^{-1} ml was determined (14).

Quantitative X-ray CT imaging was performed on a clinical 64 slice CT scanner (Brilliance, Philips Medical Systems, Best, The Netherlands). The sample tubes were positioned co-axially to the main axis of the scanner. Imaging parameters included a FOV of 200x200 mm2, matrix = 256x256, slice thickness of 1 mm. X-ray tube voltage was varied between 80, 120 and 140 kV and a tube current of 200 mA was used. Using the methods described in reference (14), a linear regression curve was constructed to determine the sensitivity of X-ray CT for HoAcAc microspheres in Hounsfield units (HU) per mg/ml (14).

A second agarose gel phantom was constructed for qualitative imaging. This gel consisted of 2 % (*w/w*) agarose, with pockets for the administration of a suspension of HoAcAc microspheres to obtain depots of 1 µg to 1 mg. The imaging parameters were similar to the imaging parameters as mentioned before, except for the slice thickness used in MR imaging, which was set to 1 mm.

To mimic potential in vivo imaging applications, depots of HoAcAc microspheres were injected in an ex vivo rabbit liver. The excised liver was flushed with water, and placed in an aqueous solution containing $MnCl_2$ (19.2 mg/L), to reduce the relaxation time of the water. Fifty microlitre of a suspension of HoAcAc microspheres was administered to the liver, to obtain depots of 1, 5 and 10 µg microspheres. The imaging parameters were similar to the imaging parameters mentioned before. For the MR images displayed in Figure 3A, D, E and F an echo time of 20 ms was used.

Results and discussion

Size distribution, holmium content and surface characteristics

HoAcAc microspheres were obtained using HoAcAc crystals as the sole ingredient, without PLLA as a matrix forming polymer. The size distribution and surface morphology of the microspheres were characterized using Coulter Counter, light microscopy and scanning electron microscopy (SEM), both before and after neutron activation. The particle size distribution was rather broad, from 5 to 40 µm, with an average microsphere size of 15 µm when the microspheres were prepared at 500 rpm. The average particle size could be tailored by altering the stirring rate during emulsifying and increased from 15 µm at 500 rpm to 20 µm at 400 rpm and 26 µm at 300 rpm. The size distribution should be narrow to control the biodistribution of the microspheres and to reduce possible shunting of small microspheres to non-target organs after administration. Therefore, a sieving step is necessary to obtain a more confined size distribution. More than 93 % of the microspheres had a size between 15 – 20 µm after sieving. No changes in microsphere size distribution were observed after neutron activation, which is an indication that radiation damage was absent. Light and scanning electron microscopy showed that spherical particles with a smooth surface were formed (Figure 1A and B). Neither surface damage nor agglomeration was observed after neutron activation of the microspheres. After neutron activation for 3 or even 6 hours, the surface of the microspheres only showed small crevices and no fragments were present (Figure 1C). This, in combination with the size distribution results, indicates that the microspheres are resistant to neutron irradiation.

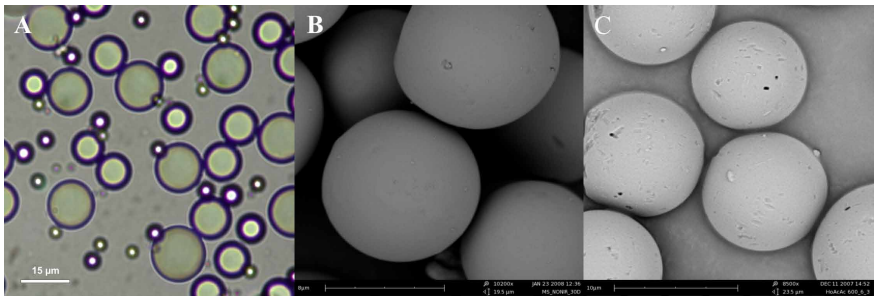

Figure 1 *A) Light micrograph of HoAcAc microspheres before sieving (mean size 15 µm), B) scanning electron micrograph of non activated HoAcAc-MS and C) scanning alectron micrograph of HoAcAc-MS after 6h of neutron activation.*

The holmium content of the HoAcAc microspheres, as determined by complexometric titration and ICP OES was found to be 45.0 ± 0.5 % (*w/w*), which is a factor 2.6 higher than the holmium content of the Ho-PLLA-MS (17.0 % (*w/w*)). The density of the HoAcAc microspheres (1.90 g/ml) was higher than the density of Ho-PLLA-MS (1.4 g/ml) as well. The substantially higher holmium load for the Ho-PLLA microspheres resulted in a strong increase in radioactivity per mg microspheres, which increased from 29 MBq/mg for Ho-PLLA microspheres (11) to 76 MBq/mg for HoAcAc microspheres (6 h neutron activation; thermal neutron flux of 5 x 10^{12} n cm^{-2} s^{-1}). Clinical results after intratumoral injection of ^{90}Y glass microspheres showed that 74 MBq ^{90}Y is sufficient to evoke a tumoricidal effect on a tumor of 3 cm (21). The injected volume of the microsphere suspension to such a tumor is limited to typically 0.1–0.3 ml (22). Based on the radiation characteristics of ^{166}Ho and ^{90}Y it can be calculated that a tumoricidal dose of ^{166}Ho activity (230 MBq per 3 mg) can be delivered in this volume using HoAcAc microspheres for intratumoral administration (11).

Multimodality imaging characteristics

The diagnostic sensitivity of MRI and CT for HoAcAc-MS was investigated. The obtained R_2^* relaxation rate map and a representative X-ray CT reconstructed image of the HoAcAc-MS dilution series are shown in Figure 2A and C. Linear MRI and CT calibration curves are shown in Figure 2B and D.

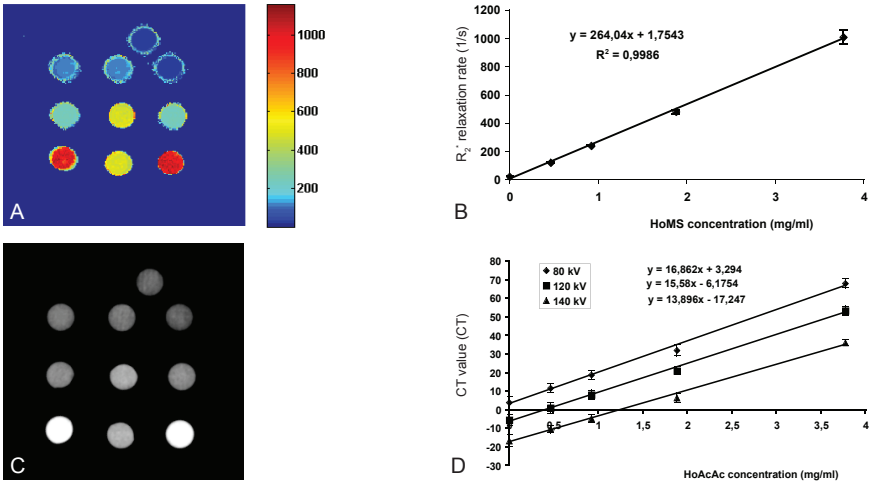

Figure 2 *A) Calculated R_2* relaxation rate map of the HoAcAc-MS dilution series in duplicate, containing [0.0; 0.5; 0.9; 1.9; 3.8] mg/ml agarose. B) R_2* calibration curve, the slope of which represents the MR sensitivity, expressed by the r_2* relaxivity. C) CT reconstruction image of the HoAcAc-MS dilution series. D) CT calibration curves acquired at varying tube energies (80, 120, 140 kV), of which the slopes represent the diagnostic sensitivity of CT for HoAcAc-MS (For color figure see addendum).*

The resulting r_2* relaxivity of the HoAcAc microspheres with a holmium load of 45 % (*w/w*), was 264 ± 5.7 s^{-1} mg^{-1} ml, which is a factor 2.8 higher than the r_2* value of the Ho-PLLA microspheres with a holmium load of 17 % (*w/w*) (92 ± 3.2 s^{-1} mg^{-1} ml) (24). The increased r_2* relaxivity represents an enhanced sensitivity of MRI for the HoAcAc microspheres, as compared to Ho-PLLA microspheres.

Quantitative CT imaging of the agarose phantom resulted in a mass attenuation coefficient at 120 kV of 15.6 HU mg^{-1} ml for HoAcAc-MS, which is a factor 2.3 higher as compared to the mass attenuation coefficient of Ho-PLLA microspheres at 120 kV, which was 6.7 HU mg^{-1} ml (14). The increased sensitivity of CT, like the increased sensitivity of MRI for the HoAcAc microspheres, can be attributed to the increase in holmium content.

Table 1 summarizes relevant characteristics of conventional Ho-PLLA-MS and HoAcAc-MS.

Table 1 *Summary of results: holmium load, specific activity, MR sensitivity and CT sensitivity given for the conventional HoPLLA-MS and the HoAcAc-MS.*

Type of microsphere	*Holmium load (%)*	*Specific activity [Mbq/mg]*	*MRI sensitivity at 1.5T [s^{-1} mg^{-1} ml]*	*CT sensitivity at 120kV [HU mg-1 ml]*
HoPLLA	*17*	*29*	*92*	*6.7*
HoAcAc	*45*	*76*	*264*	*15.6*

To demonstrate the feasibility of visualization of microgram amounts of HoAcAc microspheres using MRI and CT, decreasing amounts of HoAcAc microspheres (1 mg to 1µg) in clusters were imaged in vitro as well as in a rabbit liver ex-vivo. The enhanced r_2* relaxivity of the HoAcAc microspheres enabled detection of 1 µg of HoAcAc microspheres in the agarose gel phantom (Figure 3A). The same setup was used for CT measurements, in which clusters as small as 50 µg HoAcAc-MS could still be detected (Figure 3B and 3C). Depots of 1, 5 and 10 µg HoAcAc microspheres were investigated in an excised rabbit liver (Figure 3D). A minimum clustersize of 5 µg HoAcAc-MS in liver tissue was detectable with MRI (Figure 3E and 3F).

Unlike ^{90}Y microspheres, which lack the MR imaging possibilities, very small amounts of HoAcAc-MS can be detected using MRI. The high MR sensitivity of HoAcAc-MS brings MR image-based biodistribution prediction, using small tracer doses, one step closer. The linear relation between the local concentration and both MR and CT signal enables image based quantification (14, 16, 17). Furthermore, the detection of microgram amounts of HoAcAc microspheres

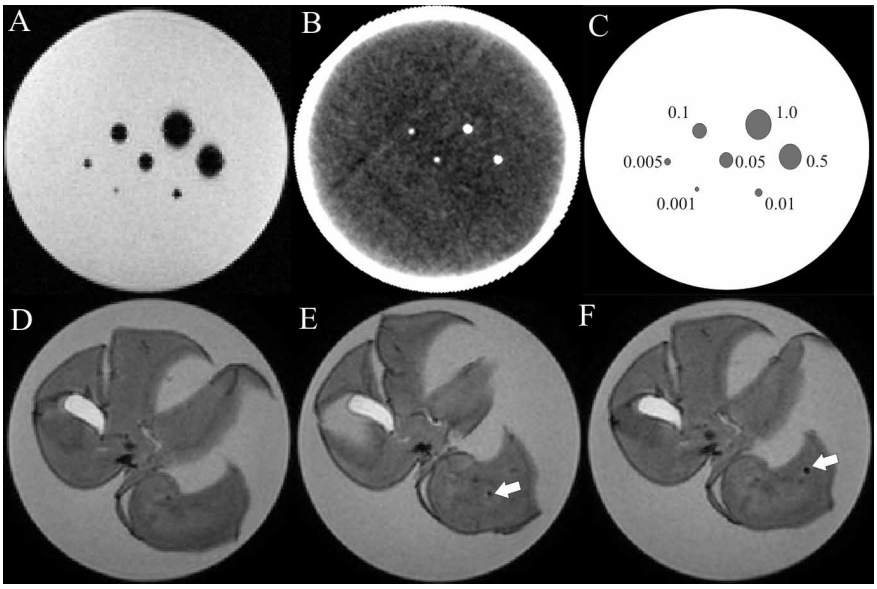

Figure 3 *A) Gradient echo MRI image of agarose phantom with different depots of HoAcAc microspheres, B) CT image of agarose phantom with different depots of HoAcAc microspheres, C) schematic representation of agarose phantom with different depots of HoAcAc microspheres, including the amount of microspheres in milligram, D) MRI image of rabbit liver before administration of HoAcAc microspheres, E) MRI image of rabbit liver after administration of 5 µg HoAcAc microspheres, indicated by arrow, F) MRI image of rabbit liver after administration of 10 µg HoAcAc microspheres, indicated by arrow. An echo time of 20 ms was used in images A, D, E and F.*

enables MR image-guided administration of the particles, both for transcatheter and direct intratumoral injections, facilitating accurate delivery of HoAcAc-MS to the tumor, whilst refraining healthy tissue from radiation damage(18). Interestingly, the MR imaging characteristics of holmium-loaded microspheres are independent of radioactivity, allowing tracking of the microspheres long after ^{166}Ho has decayed using MRI as well, enabling noninvasive investigation of the in vivo fate of the microspheres after transcatheter delivery or intratumoral injection of HoAcAc-MS.

Clinical perspective

The two currently available ^{90}Y microspheres are glass-based (Therasphere®, MDS Nordion, Kanata, Canada) and resin-based (SIR-Spheres®, SIRTeX Medical Ltd., Sydney, Australia). The glass microspheres have a very high specific activity (2.5 kBq/microsphere), and are registered as a Humanitarian Use Device by the FDA for use in radiation treatment or neoadjuvant to surgery or transplantation in patients with unresectable hepatocellular carcinoma (25). The resin based

microspheres have a relatively low specific activity 40 Bq/sphere, and were granted premarket approval by the FDA in 2002 (25).

With regard to the transcatheter approach, the HoAcAc microspheres are a good candidate for treatment of patients with hypovascular liver malignancies. This is due to the high specific activity of the ^{166}HoAcAc microspheres, which is in the range of the specific activity of the glass ^{90}Y microspheres. The obvious advantages of the ^{166}HoAcAc microspheres as compared to the glass ^{90}Y microspheres lie in the multimodal imaging opportunities, allowing accurate treatment planning, image-guided delivery, biodistribution assessment and follow-up. Moreover, the high specific activity of the ^{166}HoAcAc microspheres will allow for the delivery of a tumoricidal dose through intratumoral injections. This approach is thought to be applicable not only in patients with liver malignancies, but also in patients with solid tumors in other organs, e.g. brain, kidney and lungs.

Before a phase I clinical study is allowed to be conducted, several issues need to be addressed. First the pharmaceutical quality needs to be investigated, e.g. stability testing. Secondly, the *in vivo* toxicity needs to be assessed. The toxicity is expected to be minor, since holmium is a relatively non toxic metal (26). Finally, the therapeutic efficacy of the ^{166}HoAcAc microspheres needs to be evaluated in tumor bearing animals.

Conclusion

The present study demonstrates that microspheres with an ultra high holmium content can be prepared from HoAcAc crystals as the sole starting material, without the use of a polymeric matrix. The prepared microspheres have a smooth surface and are resistant to neutron irradiation with a thermal neutron flux (5 x 10^{12} n cm^{-2} s^{-1}). The mean particle size can be tailored for different tumor treatment approaches by adapting the processing parameters. The size increased from 15 to 26 µm when lowering the stirring rate from 500 to 300 rpm during emulsifying. The HoAcAc microspheres have an unexpectedly high holmium content of 45 % (*w/w*), which is higher than the starting material and substantially higher when compared to the Ho-PLLA microspheres (17 % (*w/w*)). The increased holmium content led to a 2.6 fold increase in specific activity, allowing for tumoricidal radioactive doses in small volumes necessary for direct intratumoral injection. Additionally, the increased holmium content strongly increased diagnostic sensitivity of MRI and X-ray CT, enabling detection of microgram amounts of microspheres in liver tissue facilitating image-guided drug delivery. Moreover, the linear relation between both MR and CT signal and the HoAcAc-MS concentration enables quantitative biodistribution assessment for transcatheter radioembolization treatment planning.

References

1. Kamangar F, Dores GM, Anderson WF. Patterns of cancer incidence, mortality, and prevalence across five continents: defining priorities to reduce cancer disparities in different geographic regions of the world. J Clin Oncol **2006**;24(14):2137-2150.
2. Parkin DM, Bray FI, Devesa SS. Cancer burden in the year 2000. The global picture. Eur J Cancer **2001**;37 Suppl 8:S4-66.
3. Llovet JM, Bruix J. Molecular targeted therapies in hepatocellular carcinoma. Hepatology **2008**;48(4):1312-1327.
4. Vibert E, Canedo L, Adam R. Strategies to treat primary unresectable colorectal liver metastases. Semin Oncol **2005**;32(6 Suppl 8):33-39.
5. Hochster HS, Hart LL, Ramanathan RK, Childs BH, Hainsworth JD, Cohn AL, Wong L, Fehrenbacher L, Abubakr Y, Saif MW, Schwartzberg L, Hedrick E. Safety and efficacy of oxaliplatin and fluoropyrimidine regimens with or without bevacizumab as first-line treatment of metastatic colorectal cancer: results of the TREE Study. J Clin Oncol **2008**;26(21):3523-3529.
6. Zuckerman DS, Clark JW. Systemic therapy for metastatic colorectal cancer: current questions. Cancer **2008**;112(9):1879-1891.
7. van Hazel G, Blackwell A, Anderson J, Price D, Moroz P, Bower G, Cardaci G, Gray B. Randomised phase 2 trial of SIR-Spheres plus fluorouracil/leucovorin chemotherapy versus fluorouracil/leucovorin chemotherapy alone in advanced colorectal cancer. J Surg Oncol **2004**;88(2):78-85.
8. Vente MAD, Wondergem M, van der Tweel I, van den Bosch MAAJ, Zonnenberg BA, Lam MGEH, van het Schip AD, Nijsen JFW. Yttrium-90 microsphere radioembolization for the treatment of liver malignancies: a structured meta-analysis. Eur Radiol **2008**.
9. Gupta T, Virmani S, Neidt TM, Szolc-Kowalska B, Sato KT, Ryu RK, Lewandowski RJ, Gates VL, Woloschak GE, Salem R, Omary RA, Larson AC. MR Tracking of Iron-labeled Glass Radioembolization Microspheres during Transcatheter Delivery to Rabbit VX2 Liver Tumors: Feasibility Study. Radiology **2008**;249(3):845-854.
10. Nijsen JFW, Zonnenberg BA, Woittiez JR, Rook DW, Swildens-van Woudenberg IA, van Rijk PP, van het Schip AD. Holmium-166 poly lactic acid microspheres applicable for intra-arterial radionuclide therapy of hepatic malignancies: effects of preparation and neutron activation techniques. Eur J Nucl Med **1999**;26(7):699-704.
11. Vente MAD, Nijsen JFW, de Wit TC, Seppenwoolde JH, Krijger GC, Seevinck PR, Huisman A, Zonnenberg BA, Van den Ingh TSGAM, van het Schip AD. Clinical effects of transcatheter hepatic arterial embolization with holmium-166 poly(L: -lactic acid) microspheres in healthy pigs. Eur J Nucl Med Mol Imaging **2008**;35(7):1259-1271.
12. Zielhuis SW, Nijsen JFW, Seppenwoolde JH, Bakker CJG, Krijger GC, Dullens HF, Zonnenberg BA, van Rijk PP, Hennink WE, van het Schip AD. Long-term toxicity of holmium-loaded poly(L-lactic acid) microspheres in rats. Biomaterials **2007**;28(31):4591-4599.
13. Fossheim S, Johansson C, Fahlvik AK, Grace D, Klaveness J. Lanthanide-based susceptibility contrast agents: assessment of the magnetic properties. Magn Reson Med **1996**;35(2):201-206.

14. Seevinck PR, Seppenwoolde JH, de Wit TC, Nijsen JF, Beekman FJ, van het Schip AD, Bakker CJ. Factors affecting the sensitivity and detection limits of MRI, CT, and SPECT for multimodal diagnostic and therapeutic agents. Anticancer Agents Med Chem **2007**;7(3):317-334.
15. de Wit TC, Xiao J, Nijsen JF, van het Schip FD, Staelens SG, van Rijk PP, Beekman FJ. Hybrid scatter correction applied to quantitative holmium-166 SPECT. Phys Med Biol **2006**;51(19):4773-4787.
16. Seevinck PR, Seppenwoolde JH, Zwanenburg JJM, Nijsen JFW, Bakker CJG. FID Sampling Superior to Spin-Echo Sampling for T-2*-Based Quantification of Holmium-Loaded Microspheres: Theory and Experiment. Magn Reson Med **2008**;60(6):1466-1476.
17. Seppenwoolde JH, Nijsen JF, Bartels LW, Zielhuis SW, van het Schip AD, Bakker CJ. Internal radiation therapy of liver tumors: qualitative and quantitative magnetic resonance imaging of the biodistribution of holmium-loaded microspheres in animal models. Magn Reson Med **2005**;53(1):76-84.
18. Seppenwoolde JH, Bartels LW, van der WR, Nijsen JF, van het Schip AD, Bakker CJ. Fully MR-guided hepatic artery catheterization for selective drug delivery: a feasibility study in pigs. J Magn Reson Imaging **2006**;23(2):123-129.
19. [Anonymous]. Dosimetry Update. Emerging trends in radioembolisation using microspheres: clinical workshop, Chicago, IL, 4-5 May 2007; **2007**.
20. Kulik LM, Carr BI, Mulcahy MF, Lewandowski RJ, Atassi B, Ryu RK, Sato KT, Benson A, III, Nemcek AA, Jr., Gates VL, Abecassis M, Omary RA, Salem R. Safety and efficacy of 90Y radiotherapy for hepatocellular carcinoma with and without portal vein thrombosis. Hepatology **2008**;47(1):71-81.
21. Tian JH, Xu BX, Zhang JM, Dong BW, Liang P, Wang XD. Ultrasound-guided internal radiotherapy using yttrium-90-glass microspheres for liver malignancies. J Nucl Med **1996**;37(6):958-963.
22. Lin WY, Tsai SC, Hsieh JF, Wang SJ. Effects of 90Y-microspheres on liver tumors: comparison of intratumoral injection method and intra-arterial injection method. J Nucl Med **2000**;41(11):1892-1897.
23. Zielhuis SW, Nijsen JFW, Figueiredo R, Feddes B, Vredenberg AM, van het Schip AD, Hennink WE. Surface characteristics of holmium-loaded poly(l-lactic acid) microspheres. Biomaterials **2005**;26(8):925-932.
24. Nijsen JFW, Seppenwoolde JH, Havenith T, Bos C, Bakker CJG, van het Schip AD. Liver tumors: MR imaging of radioactive holmium microspheres--phantom and rabbit study. Radiology **2004**;231(2):491-499.
25. Vente MAD, Hobbelink MGG, van het Schip AD, Zonnenberg BA, Nijsen JFW. Radionuclide liver cancer therapies: from concept to current clinical status. Anticancer Agents Med Chem **2007**;7(4):441-459.
26. Arvela P. Toxicity of rare-earths. Prog Pharmacol **1979**;2:73-113.

Chapter 4

P.R. Seevinck, L. Mulder, J.F.W. Nijsen, M.A.D. Vente, M.A.A.J. van den Bosch, C.J.G. Bakker

Submitted

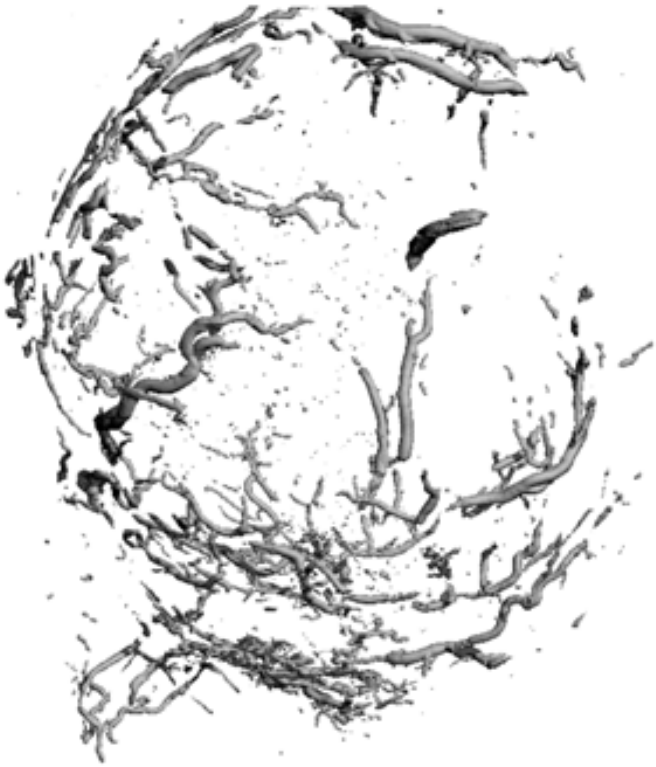

Quantitative 3D microCT imaging of holmium-166 microspheres in a rabbit liver tumor model after transarterial radioemoblization

Abstract

In this article micro-computed tomography (microCT) was explored on its capabilities to qualitatively and quantitatively assess the 3D distribution of holmium-166 loaded poly(L-lactic acid) microspheres (^{166}Ho-PLLA-MS) on a microscopic level in vitro and in tumorous tissue after hepatic arterial radioembolization of a VX2 tumor in a rabbit liver. In vitro experiments were conducted in agarose gel phantoms and were validated by light microscopy, demonstrating reliable and accurate detection of single Ho-PLLA-MS. MicroCT of VX2 tumor-bearing liver tissue revealed that the microspheres mainly lodged in the highly vascularized periphery of the tumor. An extremely heterogeneous distribution was observed, with arterioles containing elongated aggregates of thousands of microspheres over a distance of several millimeters, as well as arterioles with only few microspheres, which was confirmed by histological examinations. The total amount of clustered microspheres in the tumor as assessed by microCT was in good agreement with the low background gamma counter, with a 4.4 % underestimation and a tumor to liver ratio of 4.9. Detailed three-dimensional analysis of the cluster population revealed a highly skewed volume distribution towards small volumes. Half of the clusters contained less than five microspheres; however, these clusters contained less than 10% of all microspheres in the tumor. The largest 14 microsphere aggregates accounted for 50% of the total cluster volume, with clusters containing at least 10,000 microspheres. As opposed to conventional microsphere biodistribution analysis using 2D light micrographs, the presented results demonstrate that microCT does enable 3D quantitative and qualitative biodistribution assessment of Ho-PLLA-MS after hepatic arterial radioembolization, providing valuable insight on microsphere lodging in the neovasculature of the tumor, and potentially allowing 3D dose calculations for treatment optimization.

Introduction

Internal radiation therapy with radioactive microspheres has proven to be an effective treatment option for patients with hepatic malignancies, resulting in a significant increase of median survival in patients with liver malignancies (1-4). The importance of detailed knowledge of microsphere biodistribution (5-7) and radiation dose distribution (8-10) in the liver for radioembolization treatment optimization has been acknowledged long ago and has been studied since. The purpose of radioembolization is to deliver a high radiation dose to the tumorous tissue while minimizing exposure to healthy liver parenchyma (8-12), which is accomplished by exploiting the predominance of arterial blood supply to liver tumors and of portal blood supply to normal parenchyma (13, 14).

A major drawback of the currently used microspheres for radioembolization, ^{90}Y-microspheres (^{90}Y-MS), is the lack of high quality imaging possibilities, preventing direct biodistribution assessment, accurate dosimetry and real-time feedback during microsphere infusion. Microscopically, biodistribution assessment (5, 6) and dose calculations (8-10) of ^{90}Y-MS in animal models and human explanted livers have been performed in 2D using light micrographs of 10-µm biopsy sections obtained every 200-250 µm. 3D analysis was facilitated by stacking of 2D images, while discarding most of the tissue volume (6, 8-10). Fox et al. stated that this methodology did not compromise dose calculations (8). However, others hypothesized that a real 3D microsphere biodistribution would be preferable for realistic 3D biodistribution assessment (6) and dose estimation (15). Furthermore, real 3D data may provide detailed insight in important biophysical and vascular changes induced by tumor growth and neovascularization (13, 14) and their influence on microsphere biodistribution (5, 6, 10). The inability to image ^{90}Y-MS prohibits further investigation of these issues.

Poly(L-lactic acid) microspheres loaded with holmium-166 (^{166}Ho-PLLA-MS) proposed for internal radiation therapy of liver malignancies (16, 17) constitute an attractive alternative for ^{90}Y-MS, owing to their mulitimodal imaging possibilities (12, 18-22) and favorable radiation characteristics, which allow for nuclear imaging and therapy (12, 23, 24). Quantitative SPECT of ^{166}Ho-PLLA-MS has been developed and was applied in pigs to perform preprocedural biodistribution assessment in order to predict therapeutic dose distributions and extrahepatic shunting (18, 23, 25). Furthermore, holmium is highly paramagnetic and has a high linear attenuation coefficient and can therefore be visualised by MR imaging and X-ray computed tomography (CT) imaging, respectively, enabling imaging of radioactive as well as of non-radioactive microspheres evenly well in a clinical setting (19, 21, 24). As a consequence, Ho-PLLA-MS allow real-time MR-guided

transcatheter selective delivery (22) and quantitative MR-based biodistribution assessment (20, 21). However, the limited image resolution of the mentioned clinical imaging modalities prevents Ho-PLLA-MS biodistribution assessment on a microscopic scale. For similar reasons as mentioned for ^{90}Y microspheres, high resolution 3D data of the Ho-PLLA-MS biodistribution in liver tissue would be extremely valuable.

The purpose of this study was to investigate the feasibility to qualitatively and quantitatively assess the 3D intrahepatic distribution of ^{166}Ho-PLLA-MS using micro-computed tomography (microCT) after transarterial radioembolization. The paper consists of two parts; 1) an in vitro study, investigating the capabilities of microCT for detection and quantification of Ho-PLLA-MS; 2) an ex vivo study, depicting and quantifying the 3D biodistribution of Ho-PLLA-MS in a Vx2 tumor-bearing rabbit liver on a microscopic scale after in vivo transarterial radioembolization.

Materials and methods

In vitro experiments

Holmium-loaded poly(L-lactic acid) microspheres were prepared as previously described, resulting in microspheres with a density of 1.4 g/ml and size distribution of 20-50 µm after sieving (17). The mean diameter and holmium content were 26.4 µm and 18.2%, respectively. Theoretically, the number of microspheres per unit mass is $74 \bullet 10^3$ Ho-PLLA-MS per mg, based on density and diameter.

Determination of the number of Ho-PLLA-MS per unit mass

The number of microspheres per unit mass was determined experimentally in an agarose gel suspension using light microscopy and microCT. Samples of agarose gel (2% w/w) containing different concentrations of homogeneously suspended Ho-PLLA-MS (1-15 mg/ml) were deposited (in duplo) on a microscope graticulate counting slide with a section thickness of 100 µm and a square grid to enable counting of particles in a known volume. Light micrographs were acquired and analyzed to relate the number of microspheres to the Ho-PLLA-MS concentration, providing a regression curve. For microCT, a wider Ho-PLLA-MS concentration range (1-30 mg/ml) was investigated. The Ho-PLLA-MS suspensions were brought into cylindrical vials (diameter = 1 cm, length = 5 cm) suitable for microCT imaging. The slope of the acquired regression curves is a measure of the number of microspheres per unit mass. Furthermore, the feasibility to detect single Ho-PLLA-MS with microCT was investigated qualitatively by comparison of light micrographs with microCT images of the same 100-µm thick gel sample containing Ho-PLLA-MS.

Optimization of the threshold value

Prior to analysis of microCT data, an optimal segmentation threshold value was determined, using data of homogeneously suspended Ho-PLLA-MS, to differentiate high-intensity noise pixels from actual microspheres. Pixel values above the segmentation threshold value were regarded as being (part of) a holmium microsphere or cluster. The threshold value was chosen such that the contribution of noise to the segmented volume was minimized while maintaining a mean particle size as close as possible to the actual microsphere diameter.

Quantitative microCT imaging of Ho-PLLA-MS dilution series

A second regression curve was determined, to enable quantification of clustered Ho-PLLA-MS instead of homogeneously distributed Ho-PLLA-MS. This curve, the density calibration curve, relates the CT-value of the Ho-PLLA-MS gel suspension in Hounsfield units (HU) to the Ho-PLLA-MS concentration [Ho-PLLA-MS], providing the mass attenuation coefficient $\mu_{m,Ho\text{-}PLLA\text{-}MS}$ in HU·mg^{-1}·ml. Using the mass attenuation coefficient, a local increase in CT value can be related to the Ho-PLLA-MS concentration according to [Ho-PLLA-MS] = $\Delta CT[HU]/\mu_{m,Ho\text{-}PLLA\text{-}MS}$. The microCT voxel volume was varied (10, 18, 36, 74 µm) prior to image reconstruction to investigate its influence on the standard deviation of the microCT signal.

Rabbit experiment

Animal model A healthy New Zealand White rabbit weighing 3800g was obtained from a certified supplier (Harlan, Horst, Netherlands). The experimental protocol was in agreement with the local applicable Dutch law, "Wet op dierproeven" (art. 9, 1977) and the European Convention guidelines (86/609/EC). Approval was obtained of the ethical committee for animal experiments of the University Medical Center Utrecht, Utrecht, The Netherlands (FDC/DEC/GNK nr. 99042).

Vx2 tumor implantation and ^{166}Ho-PLLA-MS infusion

After premedication with methadone (1 mg/kg) IV and acepromazine (1 mg/kg) IV, general anesthesia was induced by fentanyl (0.15 mg/ml)/fluanisone (10 mg/ml) and maintained by inhalation of halothane (2%) in N_2O/O_2 (1:1). A laparotomy was performed to implant a small sample (~2 mm) of VX2 tumor in the liver (lobus sinister lateralis) by injection with an 18G Abbocath-T®. When the tumor had reached a diameter of >20mm, as was monitored by ultrasound, a second laparotomy was performed in order to administer 50 mg of ^{166}Ho-PLLA-MS (601 Mbq ^{166}Ho). Prior to microsphere infusion, the celiac artery was ligated. The gastroduodenal artery was cannulated with a 24G Abbocath-T® to administer the microspheres, which were suspended in a saline solution containing 0.1% methy-

lene blue to visualize possible backflow. After microsphere infusion, the gastroduodenal artery was sealed with tissue glue to restore arterial hepatic circulation. The administration system was measured for activity pre- and post-injection to calculate the injected dose. In order to determine the spatial distribution macroscopically, nuclear images of the rabbit were acquired in vivo two days post administration of ^{166}Ho-PLLA-MS using a dual-head γ-camera (Vertex-MCD, ADAC, Milpitas, CA, USA).

Harvesting of tissue samples The rabbit was sacrificed four weeks after ^{166}Ho-PLLA-MS administration by an overdose of sodium pentobarbitone (100-200 mg/kg) IV, and the liver was excised. MRI was performed of the ex vivo rabbit liver for qualitative depiction of the presence of Ho-PLLA-MS in the liver using a 1.5T clinical MR scanner (Achieva, Philips Healthcare, Best, The Netherlands). T_2^*-weighted gradient echo images, sensitive for the depiction of Ho-PLLA-MS, and T_1-weighted spin echo images, providing anatomical reference, were acquired as described previously (21). The entire primary tumor was harvested based on the MR images. The sample was immersed in formalin in a custom-made perspex cylindrical container with a diameter of 3.5 cm and a length of 7.3 cm suitable for microCT imaging.

Biodistribution assessment and Ho-PLLA-MS quantification

MicroCT images of the tumor sample were acquired according to the protocol described in the next section. Analysis was done using different segmentation thresholds, enabling to focus on differently sized microsphere aggregates. Using the segmented volume, V_s, which contain (clusters of) Ho-PLLA-MS, and the mass attenuation coefficient of Ho-PLLA-MS as determined from the density calibration curve, the total amount of Ho-PLLA-MS in mg present in the segmented volume was determined according to the following relation: $\text{Ho-PLLA-MS[mg]} = V_s * \Delta CT / \mu_{m,\text{Ho-PLLA-MS}}$. Furthermore, 3D cluster analysis was performed, investigating the size and number of clusters. Results were shown in histograms plotting the number of clusters against the cluster volume.

The total amount of ^{166}Ho-PLLA-MS instilled in the rabbit liver and in the excised tumor sample was determined retrospectively using a low-background gamma counter (Nuclear Chicago, Chicago, IL, USA). The activity of the metastable ^{166m}Ho isotope, ($T_{1/2}$ = 1,200 y), which is co-generated during neutron activation of ^{165}Ho, was related to the initial amount of ^{166}Ho activity and used to calculate the amount of Ho-PLLA-MS in the entire liver and in the tumor tissue sample, providing the tumor to liver ratio.

Histopathologic evaluation, the conventional 2D gold standard, was performed. Tumor tissue samples were embedded in paraffin and sectioned in 4-µm

thick slices and stained by using hematoxylin-eosin (HE). Micrographs were made to inspect HE stained sections qualitatively using a 40x magnification.

MicroCT imaging protocol

Three dimensional high-resolution images were acquired of all Ho-PLLA-MS gel samples as well as of the tumor sample using a microCT system (µCT 40, Scanco Medical AG., Basserdorf, Switserland). The CT scanner consists of a cone beam x-ray source with rotating sample and a 2048x64 element CCD detector. The analysis was performed with a peak tube voltage of 45 kV, resulting in an effective X-ray energy of 24 keV. Total acquisition time was 15 hour for the tumor sample and varied between one and six hours for the agarose gel samples. The standard Feldkamp algorithm was used for image reconstruction of isotropic voxels. In vitro microCT data was reconstructed with varying voxel sizes (10, 18, 36, 74 µm), liver tissue data was reconstructed with a voxel size of 18 µm. The maximum sample size to be inserted in the microCT scanner was limited to a cylinder with a diameter of 3.5 cm and a length of 7.5 cm.

Results

In vitro experiments

Determination of the amount of Ho-PLLA-MS per unit mass

The number of Ho-PLLA-MS as a function of the Ho-PLLA-MS concentration was determined experimentally by analyzing light micrographs of 100-µm thick gel samples containing varying Ho-PLLA-MS concentrations (Figure 1) and by analyzing 3D microCT data obtained from Ho-PLLA-MS dilution series in agarose gel. The obtained regression curves are shown in Figure 2a and 2b, both displaying highly correlated (r^2=0.99) linear relations between the detected number of Ho-PLLA-MS and the Ho-PLLA-MS concentration. A slope of 71,857 and 78,578 was found for light microscopy data and microCT data, respectively, representing the number of microspheres per mg. Those values are close to the theoretical value of 74,141 calculated using a density of 1.4 mg/ml and average particle diameter of 26.4 µm.

Optimization of the threshold value

An optimal threshold value was determined such that the contribution of noise to the segmented volume was minimized while maintaining a mean particle size as close as possible to the actual microsphere diameter (26.4 µm). Figure 3a shows that the contribution of noise to the volume fraction strongly decreases with increasing threshold values and demonstrates a plateau close to 0 ppm at thresh-

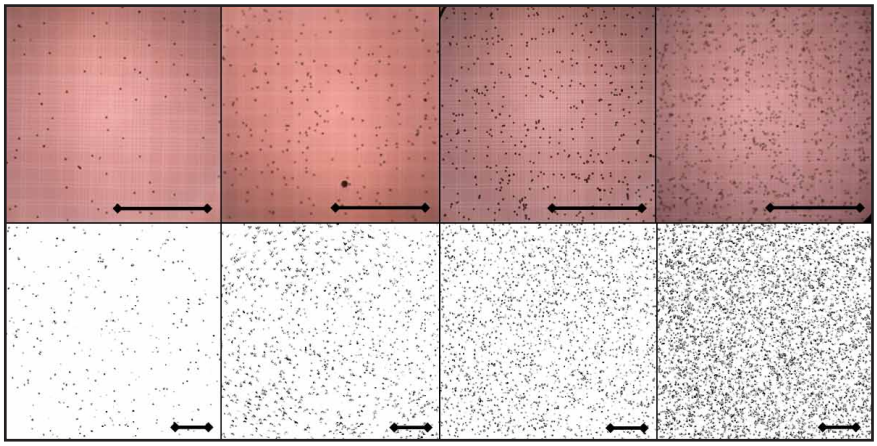

Figure 1 *top row: Light micrographs (magnification 40x) of Ho-PLLA-MS dilution series on a microscope graticulate counting slide, slab thickness = 100 µm. Ho-PLLA-MS concentrations: 1.0, 3.9, 7.0 and 14.2 mg/ml. bottom row: MicroCT images of the Ho-PLLA-MS dilution series. Ho-PLLA-MS concentrations: 1.0, 3.8, 7.6 and 16.6 mg/ml. Bars represent 1 mm.*

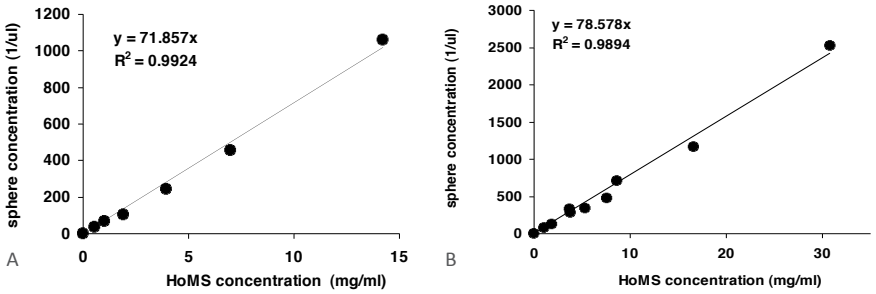

Figure 2 *Regression curves of the number of Ho-PLLA-MS as a function of Ho-PLLA-MS concentration, determined using a) light microscopy and b) microCT imaging.*

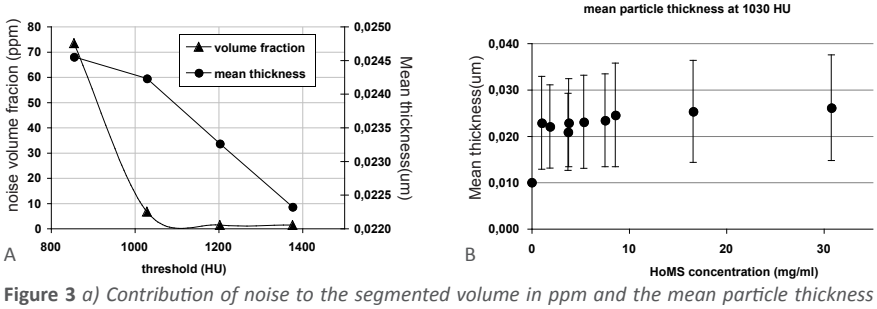

Figure 3 *a) Contribution of noise to the segmented volume in ppm and the mean particle thickness plotted against the segmentation threshold. b) Mean particle diameter plotted for against Ho-PLLA-MS concentrations in agarose gel, determined at the optimal segementation threshold of 1030 HU.*

old values above 1100 HU. The particle's mean diameter strongly decreases with threshold values larger than 1000 HU (Figure 3a). Therefore, a threshold value of 1030 HU was chosen, which resulted in a constant microsphere diameter of 24 µm at varying Ho-PLLA-MS concentrations (Figure 3b).

Quantitative imaging of Ho-PLLA-MS dilution series

Figure 4a. depicts the density calibration curve, relating the density of the Ho-PLLA-MS gel suspensions and the Ho-PLLA-MS concentration for different reconstructed voxel sizes. The slope of the calibration curves, determined for voxel sizes of 10, 18, 36 and 74 µm was 10.2, 10.6, 8.9 and 9.5 HU/mg/ml, representing the sensitivity of the method. A relatively large standard deviation compared to the slope of the curve was observed, as shown in Figure 4b, which increased with increasing concentration.

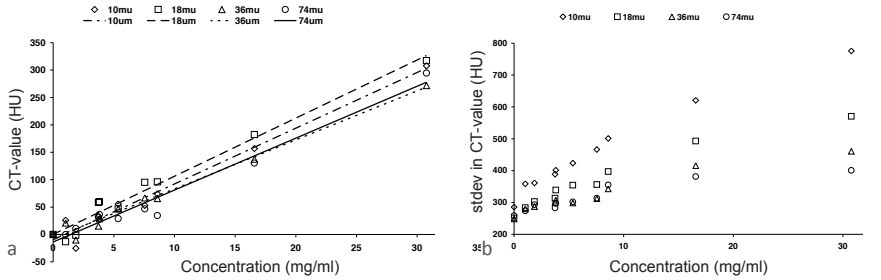

Figure 4 *a) Density calibration curves, relating the density of the Ho-PLLA-MS gel suspensions and the Ho-PLLA-MS concentration assessed using voxel sizes of 10, 18, 36 and 74 µm. b) Standard deviation as a function of Ho-PLLA-MS concentration for the different voxel sizes. A relatively large standard deviation is shown, which is already apparent in the agarose gel without Ho-PLLA-MS and which is larger for smaller voxel sizes.*

Single particle detection

Detection of single Ho-PLLA-MS by microCT was qualitatively assessed using a segmentation threshold of 1030 HU. Comparison with light micrographs showed an excellent correspondence between both imaging modalities. Each particle detected using microCT was identified on the light microscopy image as a microsphere. Furthermore, no individual Ho-PLLA-MS were missed by the microCT, however, Ho-PLLA-MS located close to each other were depicted as one larger particle in several cases.

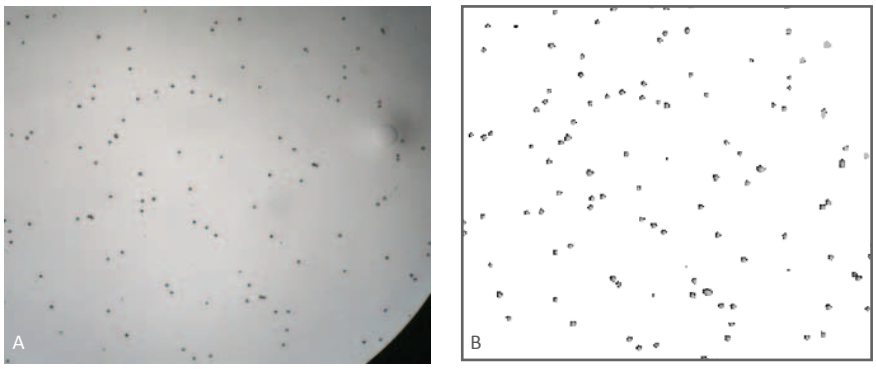

Figure 5 *a) Light micrograph of agarose gel sample containing Ho-PLLA-MS b) Thresholded microCT of the same agarose gel sample.*

Rabbit experiment

Intra-arterial administration of ^{166}Ho-PLLA-MS into the hepatic artery of a Vx2 tumor-bearing rabbit was performed successfully. The complete dose of 49.6 mg of ^{166}Ho-PLLA-MS (601 Mbq) was administered to the liver via the hepatic artery. No backflow was observed during the administration procedure. A heterogeneous distribution of the activity was observed on the scintigraphic image acquired in vivo (Figure 6a), clearly showing a hotspot surrounded by a region with lower activity. This was confirmed on a T_2^*-weighted MR image of the ex-vivo liver, showing decreased signal intensity in the locations containing Ho-PLLA-MS (Figure 6c

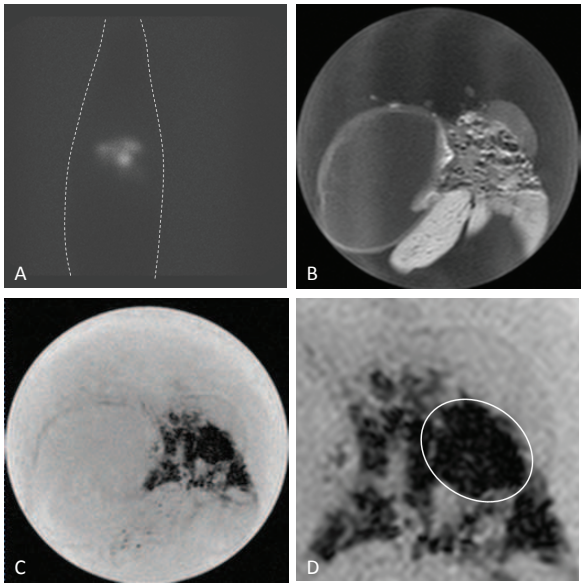

Figure 6 *a) γ-Scintigraphy of the tumor-bearing rabbit acquired in vivo, demonstrating a heterogeneous distribution of ^{166}Ho-PLLA-MS, probably located in the in the liver. b) T1-weighted spin echo image of the excised liver, clearly depicting anatomy. c) T_2^*-weighted gradient echo image, depicting the region containing Ho-PLLA-MS in black. d) Enlarged view of the T_2^*-weighted gradient echo image. The region of the tumor that was excised for microCT analysis is encircled.*

and 6d). Figure 6d depicts the liver tumor and the region (encircled) that was excised to be analyzed using microCT.

Qualitative analysis

MicroCT clearly depicted the heterogeneous distribution of Ho-PLLA-MS in the liver tissue (Figure 7). When applying the optimized segmentation threshold of 1030 HU, small clusters of Ho-PLLA-MS as well as large cylinder-shaped aggregates were shown (Figure 7a). Cluster diameters up to 500 µm where observed. Increasing the segmentation threshold caused many (small clusters of) Ho-PLLA-MS not to be shown (Figure 7b and 7c), while preserving depiction of the larger Ho-PLLA-MS clusters. Projections at different angles (Figure 7d and 7e) demonstrated that Ho-PLLA-MS predominantly lodged in the highly vascularized periphery of the tumor, in a similar fashion as was predicted and schematically depicted in Figure 7f.

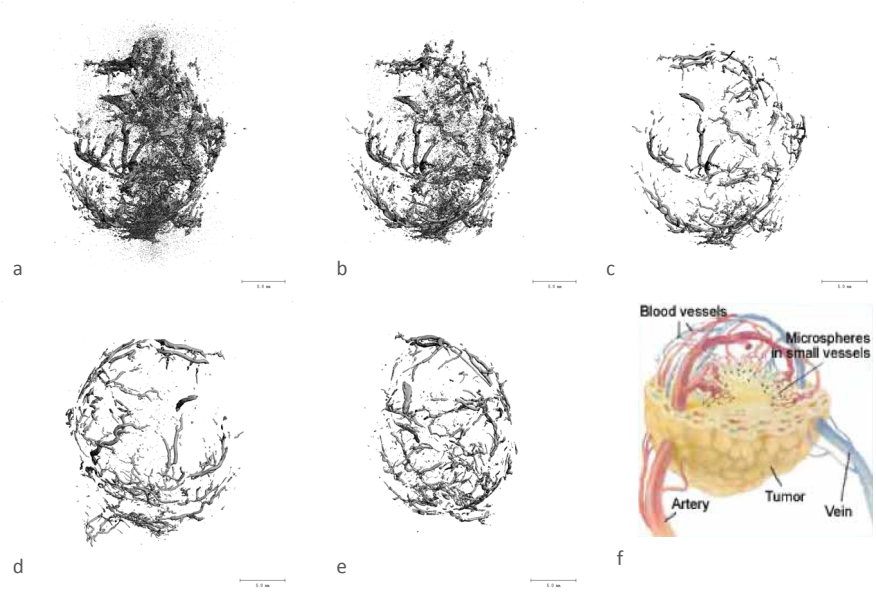

Figure 7 *Projections of high resolution (18 µm) 3D microCT reconstructions of Ho-PLLA-MS lodging in the periphery of the tumor at different threshold values and projection angles. The bar in the lower right corner denotes 5 mm. a) At the optimized threshold value of 1030 HU, single microspheres were depicted as well as large clusters. Increasing the segmentation threshold to b) 1203 HU and c) 1377 HU, decreases the number of small clusters that are depicted. Projections at different angles (d, e) clearly demonstrate that Ho-PLLA-MS predominantly lodged in the periphery of the tumor. f) A schematic drawing of the arterial and venous blood flow in the periphery of a tumor, demonstrating the embolization process (http://www.nordion.com/therasphere).*

Figure 8 shows an enlarged view of the Ho-PLLA-MS biodistribution in the periphery of the tumor. Small side branches can be observed, originating from the larger elongated clusters. As compared to large spherical clusters, elongated structures and branching clusters more effectively occupy the entire volume of the vascularized tumor tissue. Furthermore, intermitted longitudinal microsphere aggregates were observed as well, as delineated by the black lines in Figure 8. Although anatomical confirmation lacks in the microCT images, these intermitted clusters may be assumed to be located in arterioles. This suggests that blood flow is not hampered by these small clusters during intra-arterial microsphere administration, and that embolization of arterioles is a gradual process.

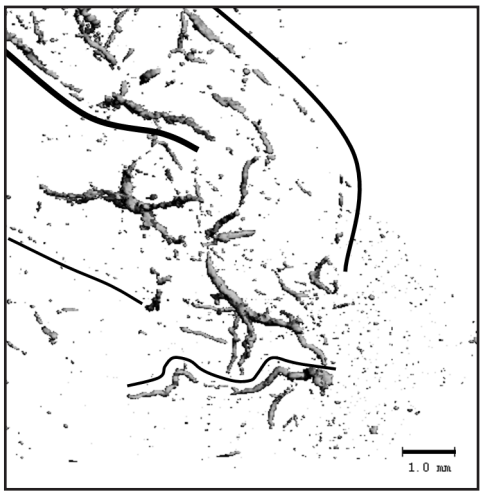

Figure 8 *Enlarged view of the Ho-PLLA-MS biodistribution in the periphery of the tumor. Black lines denote intermitted longitudinal microsphere clustering, which are hypothesized to be partly embolized arterioles.*

Histological analysis

Histological examination of the liver tissue showed many small and a few larger aggregates of microspheres. Figure 9a and 9b depict an elongated cluster of hundreds of Ho-PLLA-MS located in an artery, which was sectioned almost parallel to its axis. It may be assumed that this Ho-PLLA-MS aggregation contains several hundreds of microspheres, resulting in the elongated clusters as observed using the microCT imaging technique. The small clusters and single Ho-PLLA-MS were mainly located close to the tumor tissue, sometimes embedded in connective tissue. No cell nucleus was seen in most cells in liver tissue and tumor tissue indicating necrosis.

Figure 9**c** shows three slices sectioned at 80 µm apart, depicting an artery containing several Ho-PLLA-MS embedded in the arterial wall. These images demonstrate that Ho-PLLA-MS do not only lodge end-arteriolar, but in stead may

also settle in arterioles, without completely embolizing them. Similar findings were obtained on microCT images, as shown by the intermitted longitudinal microsphere aggregates.

Quantitative analysis

Data obtained by the background γ-counter revealed that 40.8% of total activity administered to the liver was located in the tumor, which represented 20.2 mg of

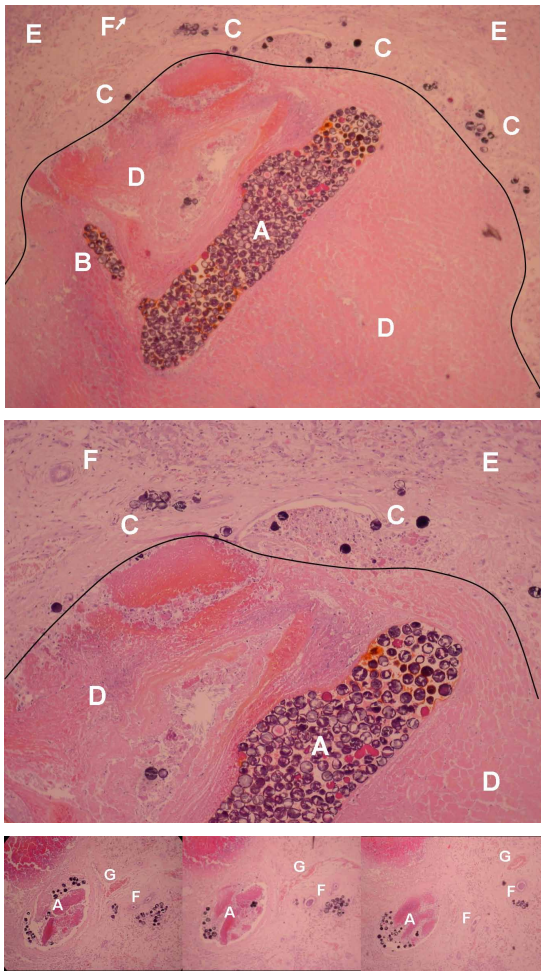

Figure 9 *Light micrographs of HE-stained 4-µm thick liver tissue sections after radioembolization with ^{166}Ho-PLLA-MS (original magnification, x40). a) Liver tissue section depicting: (A) a large Ho-PLLA-MS cluster longitudinally stacked in an arteriole, (B) a small side branch arteriole containing Ho-PLLA-MS, (C) connective tissue with small Ho-PLLA-MS clusters and single Ho-PLLA-MS, (D) necrotic liver tissue, (E) tumor tissue, (F) bile duct. b) Enlarged view of image a). c) Three slices sectioned at 80 µm apart, showing an arteriole (A) with several Ho-PLLA-MS, indicating intermitted longitudinal microsphere clustering. Also shown are blood vessels (H) belonging to the portal system and bile ducts (G) (For color figure see addendum).*

^{166}Ho-PLLA-MS. Assuming that the residual part of the ^{166}Ho-PLLA-MS were homogeneously distributed over the remaining part of the liver, and using the weight of the total liver and the tumor, which were 140.2 g and 17.1 g respectively, a tumor-to liver ratio of 4.9 was calculated. In reality, this ratio is higher, since in most nor-

mal liver parenchyma very low concentrations of ^{166}Ho-PLLA-MS were present.

Quantitative microCT analysis of tumor and liver tissue data was performed using four different segmentation thresholds (855; 1030; 1203; 1377 in HU) on data with an 18-µm voxel size. A segmentation threshold of 1030 HU was considered the optimal value, as determined in the in vitro study. At this threshold, a segmented volume of 63.8 mm^3 with an average density of 3458 HU was determined. Taking into account an average liver tissue density of 246 HU, a total amount of Ho-PLLA-MS in the tumor of 19.3 mg was determined, which is in good agreement with the amount determined using the data obtained with the low background γ-counter (4.4% underestimation). Increasing the segmentation threshold resulted in a lower segmented volume and higher average density, providing a smaller total amount of Ho-PLLA-MS. This was expected since the relatively low-intensity single microspheres and small clusters were excluded by increasing the segmentation threshold. Results are summarized in Table 1.

Table 1 *CT sensitivity in HU mg^{-1} ml, segmented volume in mm^3, density of the segmented volume in HU and total amount of Ho-PLLA-MS in mg, for different segmentation threshold values, as determined for the tumor sample.*

Segmentation threshold [HU]	855	1030	1203	1377
CT sensitivity [HU mg^{-1} ml]	*10.18*	*10.62*	*8.95*	*9.47*
Segmented volume [mm^3]	*83.6*	*63.8*	*53.2*	*46.4*
Density segmented Volume [HU]	*2881*	*3458*	*3913*	*4294*
Average Ho-PLLA-MS density [mg/ml]	*248*	*302*	*345*	*381*

Cluster analysis

The high-resolution microCT data enabled detailed three-dimensional cluster analysis. The volume distribution of the cluster population was skewed towards small volumes, as shown by Figure 10a and 10b. Cluster volumes, which were expressed in multiples of the volume of a single microsphere, varied between 1 and over 10000 in the analyzed sample (Figure 10b). These clusters are not fully occupied by microspheres, as may be concluded from the average Ho-PLLA-MS density as was shown in Table 1. However, clusters of tens of thousands of microspheres will readily be present. Figure 10a shows that clusters of only a few microspheres are most abundant. It was calculated that half of the clusters consisted of five microspheres or less. However, those clusters contributed less than 10% to the total amount of Ho-PLLA-MS in the tumor. Furthermore, the 14 largest clusters contained over 50% of the total amount of Ho-PLLA-MS, as shown by the cumulative volume percentage presented in Figure 10c.

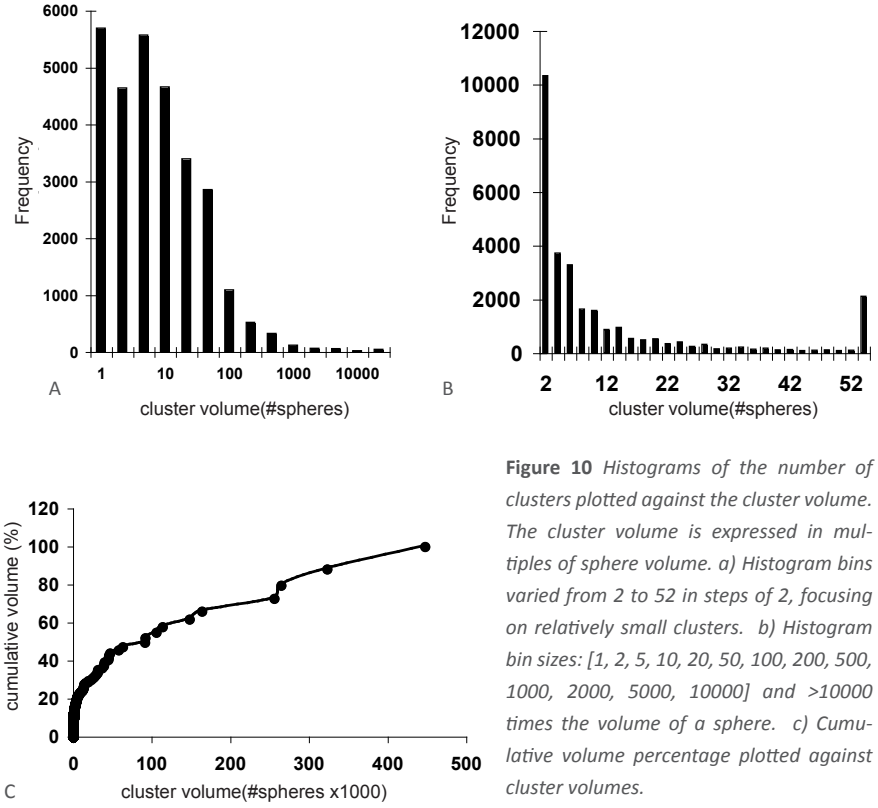

Figure 10 *Histograms of the number of clusters plotted against the cluster volume. The cluster volume is expressed in multiples of sphere volume. a) Histogram bins varied from 2 to 52 in steps of 2, focusing on relatively small clusters. b) Histogram bin sizes: [1, 2, 5, 10, 20, 50, 100, 200, 500, 1000, 2000, 5000, 10000] and >10000 times the volume of a sphere. c) Cumulative volume percentage plotted against cluster volumes.*

Discussion and conclusions

In this paper, microCT was applied to investigate the 3D distribution of Ho-PLLA-MS in great detail in an agarose gel matrix and in tumor-bearing rabbit liver tissue after in vivo transarterial radioembolization. In vitro experiments demonstrated that single Ho-PLLA-MS can readily be detected using microCT, as was validated by light micrographs. Quantification of the amount of Ho-PLLA-MS by counting individual Ho-PLLA-MS was shown to be feasible up to a concentration of 30 mg/ml, and when homogeneously suspended. To quantify the amount of Ho-PLLA-MS when aggregated into clusters, an alternative method was proposed. Based on a predefined segmentation threshold, the volume occupied by aggregated Ho-PLLA-MS was determined. By relating the average CT-value in HU to the local Ho-PLLA-MS density, using the mass attenuation coefficient $\mu_{m,\text{Ho-PLLA-MS}}$, the total amount of Ho-PLLA-MS could be determined. A segmentation threshold of 1030HU was determined to be optimal, to minimize the influence of noise while maximizing sensitivity. This may seem very high, however, it must be noted that

the CT-values values as observed for microCT are not representative for clinical CT, since much lower tube voltages are used during microCT, leading to different linear attenuation coefficients and CT-values for certain tissue types.

Quantitative microCT was applied successfully to determine the amount of Ho-PLLA-MS in the excised liver tumor sample. A total amount of 19.3 mg was estimated to be located in the tumor, as compared to 20.2 mg determined using a dose calibrator. Varying the segmentation threshold between 855 and 1377 HU only caused relatively small variations in estimated amount of Ho-PLLA-MS from 20.8 mg to 17.7 mg, indicating the robustness of the quantification method with respect to the segmentation threshold.

Qualitatively, microCT images depicted a heterogeneous distribution of Ho-PLLA-MS in the tumor tissue. Ho-PLLA-MS predominantly lodged in the highly vascularized periphery of the tumor, in agreement with previously reported observations (5, 6, 10). Large elongated microsphere accumulations of several millimeters long and up to 500 µm in diameter were observed in the periphery of the tumor. Although similar diameters were reported by Pillai et al., who called these accumulations 'superclusters' (5), the conventional 2D analysis prevented the identification of elongated aggregates of microspheres. Several smaller side branches were observed on microCT images as well, together constituting a network encapsulating the sphere-shaped tumor, with smaller clusters in between. This was in agreement with the 2D histological sections presented in Figure 9a, depicting large elongated microsphere aggregates with small clusters and single microspheres in the periphery of the tumor tissue.

Pillai et al. concluded that increasing the amount of administered microspheres mainly increased cluster size, without increasing the number of clusters (5). We found indications pointing in the same direction, based on microCT data and histological examinations. Figure 8 shows a microCT image presenting elongated but intermitted microsphere aggregates, indicating that arterioles gradually home microspheres, without instantaneous occlusion of a small part of the vessel. Histological examination of three slices sectioned 80 µm apart demonstrated a single artery at three different locations containing several microspheres, which did not occlude the artery. It may be assumed that blood flow was not seriously compromised. Increasing the amount of microspheres would gradually lead to occlusion of these arteries, eventually resulting in completely embolized vessels as demonstrated on both microCT (Figure 8) and histology (Figure 9). Similar observation were done on MR images by Seppenwoolde et al. who administered several doses of Ho-PLLA-MS successively and did not see significant changes in biodistribution as compared to the first administered dose (21).

Three dimensional cluster analysis showed a highly skewed cluster volume distribution towards small cluster volumes and revealed that half of the clusters consisted of five microspheres or less. Similar distributions were reported previously by Pillai et al. and Campbell et al. (5, 6), although in these studies 2D cluster analysis was performed on slices sectioned every 200 µm. However, microCT data also revealed that half of all microspheres present in the sample were aggregated in the 14 largest clusters. These large aggregates formed elongated and branching structures, as was shown by the microCT images (Figure 7 and 8), and as was confirmed by histology (Figure 9). The extent of the longitudinal microsphere aggregates could not be determined using 2D histological analysis. These observations may have important implications for dose calculations, as was already hypothesized by Zavgorodni (15). We suggest, based on the presented microCT data, that the statement by Fox et al. that 2D analysis of histological section taken every 200 µm would not compromise dose calculations (8), should be reconsidered. More research is needed to investigate the implications of the particular biodistribution found using microCT on dose calculations.

A highly relevant aspect in transcatheter radioembolization of hepatic malignancies is the influence of the amount of microspheres administered on treatment efficacy (4, 26, 27). Differences in biodistribution, degree of clustering and dose distribution may be expected, for example, between the two types of clinically used ^{90}Y microspheres, since standard doses of 5 GBq in 4 million spheres (glass microspheres) and 2-3 Gbq in 50 million spheres (resin microspheres) are used (4, 10). The differences in tumor response between the two types of microspheres, according to a meta-analysis recently published (4), may possibly be explained using detailed knowledge of microsphere biodistribution and microdosimetry obtained from high resolution 3D microCT data. We suggest that it would be interesting to analyze the biodistribution of the high-density glass microspheres using microCT, perform microdosimetry and compare results with our findings, to optimize the number of microspheres to be used.

All observations involving microsphere biodistribution were based on the distribution of Ho-PLLA-MS after radioembolization of a single Vx2 tumor implanted in a rabbit liver. Although this model has often been used to investigate biodistribution assessment and microdosimetry after hepatic arterial radioembolization with radioactive microspheres, translating results obtained in animal models to humans should always be done with great care.

In conclusion, as opposed to conventional 2D microsphere distribution analysis, the presented results demonstrate that microCT enables 3D quantitative and qualitative biodistribution assessment of Ho-PLLA-MS after hepatic arterial radioembolization, providing valuable insight on microsphere lodging in the neovasculature of the tumor, and potentially allowing 3D dose calculations for treatment optimization.

References

1. Kennedy AS, Coldwell D, Nutting C, Murthy R, Wertman DE, Jr., Loehr SP, Overton C, Meranze S, Niedzwiecki J, Sailer S. Resin 90Y-microsphere brachytherapy for unresectable colorectal liver metastases: modern USA experience. Int J Radiat Oncol Biol Phys **2006**;65(2):412-425.
2. Salem R, Thurston KG. Radioembolization with yttrium-90 microspheres: a state-of-the-art brachytherapy treatment for primary and secondary liver malignancies: part 3: comprehensive literature review and future direction. J Vasc Interv Radiol **2006**;17(10):1571-1593.
3. Sato KT, Lewandowski RJ, Mulcahy MF, Atassi B, Ryu RK, Gates VL, Nemcek AA, Jr., Barakat O, Benson A, III, Mandal R, Talamonti M, Wong CY, Miller FH, Newman SB, Shaw JM, Thurston KG, Omary RA, Salem R. Unresectable chemorefractory liver metastases: radioembolization with 90Y microspheres--safety, efficacy, and survival. Radiology **2008**;247(2):507-515.
4. Vente MA, Wondergem M, van dT, I, van den Bosch MA, Zonnenberg BA, Lam MG, van Het Schip AD, Nijsen JF. Yttrium-90 microsphere radioembolization for the treatment of liver malignancies: a structured meta-analysis. Eur Radiol **2009**;19(4):951-959.
5. Pillai KM, McKeever PE, Knutsen CA, Terrio PA, Prieskorn DM, Ensminger WD. Microscopic analysis of arterial microsphere distribution in rabbit liver and hepatic VX2 tumor. Sel Cancer Ther **1991**;7(2):39-48.
6. Campbell AM, Bailey IH, Burton MA. Analysis of the distribution of intra-arterial microspheres in human liver following hepatic yttrium-90 microsphere therapy. Phys Med Biol **2000**;45(4):1023-1033.
7. Meade VM, Burton MA, Gray BN, Self GW. Distribution of different sized microspheres in experimental hepatic tumours. Eur J Cancer Clin Oncol **1987**;23(1):37-41.
8. Fox RA, Klemp PF, Egan G, Mina LL, Burton MA, Gray BN. Dose distribution following selective internal radiation therapy. Int J Radiat Oncol Biol Phys **1991**;21(2):463-467.
9. Campbell AM, Bailey IH, Burton MA. Tumour dosimetry in human liver following hepatic yttrium-90 microsphere therapy. Phys Med Biol **2001**;46(2):487-498.
10. Kennedy AS, Nutting C, Coldwell D, Gaiser J, Drachenberg C. Pathologic response and microdosimetry of (90)Y microspheres in man: review of four explanted whole livers. Int J Radiat Oncol Biol Phys **2004**;60(5):1552-1563.
11. Burton MA, Gray BN, Klemp PF, Kelleher DK, Hardy N. Selective internal radiation therapy: distribution of radiation in the liver. Eur J Cancer Clin Oncol **1989**;25(10):1487-1491.
12. Nijsen F, Rook D, Brandt C, Meijer R, Dullens H, Zonnenberg B, de KJ, van RP, Hennink W, van het SF. Targeting of liver tumour in rats by selective delivery of holmium-166 loaded microspheres: a biodistribution study. Eur J Nucl Med **2001**;28(6):743-749.
13. Bierman HR, Byron RL, Jr., Kelley KH, Grady A. Studies on the blood supply of tumors in man. III. Vascular patterns of the liver by hepatic arteriography in vivo. J Natl Cancer Inst **1951**;12(1):107-131.
14. Breedis C, Young G. The blood supply of neoplasms in the liver. Am J Pathol **1954**;30(5):969-977.
15. Zavgorodni SF. A model for dose estimation in therapy of liver with intraarterial microspheres. Phys Med Biol **1996**;41(11):2463-2480.

16. Mumper RJ, Ryo UY, Jay M. Neutron-activated holmium-166-poly (L-lactic acid) microspheres: a potential agent for the internal radiation therapy of hepatic tumors. J Nucl Med **1991**;32(11):2139-2143.
17. Nijsen JF, Zonnenberg BA, Woittiez JR, Rook DW, Swildens-van W, I, van Rijk PP, van Het Schip AD. Holmium-166 poly lactic acid microspheres applicable for intra-arterial radionuclide therapy of hepatic malignancies: effects of preparation and neutron activation techniques. Eur J Nucl Med **1999**;26(7):699-704.
18. de Wit TC, Xiao J, Nijsen JF, van het Schip FD, Staelens SG, van Rijk PP, Beekman FJ. Hybrid scatter correction applied to quantitative holmium-166 SPECT. Phys Med Biol **2006**;51(19):4773-4787.
19. Seevinck PR, Seppenwoolde JH, de Wit TC, Nijsen JF, Beekman FJ, van Het Schip AD, Bakker CJ. Factors affecting the sensitivity and detection limits of MRI, CT, and SPECT for multimodal diagnostic and therapeutic agents. Anticancer Agents Med Chem **2007**;7(3):317-334.
20. Seevinck PR, Seppenwoolde JH, Zwanenburg JJ, Nijsen JF, Bakker CJ. FID sampling superior to spin-echo sampling for T(2) (*)-based quantification of holmium-loaded microspheres: Theory and experiment. Magn Reson Med **2008**;60(6):1466-1476.
21. Seppenwoolde JH, Nijsen JF, Bartels LW, Zielhuis SW, van het Schip AD, Bakker CJ. Internal radiation therapy of liver tumors: qualitative and quantitative magnetic resonance imaging of the biodistribution of holmium-loaded microspheres in animal models. Magn Reson Med **2005**;53(1):76-84.
22. Seppenwoolde JH, Bartels LW, van der WR, Nijsen JF, van Het Schip AD, Bakker CJ. Fully MR-guided hepatic artery catheterization for selective drug delivery: a feasibility study in pigs. J Magn Reson Imaging **2006**;23(2):123-129.
23. Vente MA, Nijsen JF, de Wit TC, Seppenwoolde JH, Krijger GC, Seevinck PR, Huisman A, Zonnenberg BA, van d, I, van Het Schip AD. Clinical effects of transcatheter hepatic arterial embolization with holmium-166 poly(L: -lactic acid) microspheres in healthy pigs. Eur J Nucl Med Mol Imaging **2008**.
24. Nijsen JF, Seppenwoolde JH, Havenith T, Bos C, Bakker CJ, van Het Schip AD. Liver tumors: MR imaging of radioactive holmium microspheres--phantom and rabbit study. Radiology **2004**;231(2):491-499.
25. Vente MAD. Preclinical studies on holmium-166 poly (L-lactic acis) microspheres for hepatic arterial radioembolization [dissertation]. Utrecht University, The Netherlands; **2009**.
26. Popperl G, Helmberger T, Munzing W, Schmid R, Jacobs TF, Tatsch K. Selective internal radiation therapy with SIR-Spheres in patients with nonresectable liver tumors. Cancer Biother Radiopharm **2005**;20(2):200-208.
27. Sato K, Lewandowski RJ, Bui JT, Omary R, Hunter RD, Kulik L, Mulcahy M, Liu D, Chrisman H, Resnick S, Nemcek AA, Jr., Vogelzang R, Salem R. Treatment of unresectable primary and metastatic liver cancer with yttrium-90 microspheres (TheraSphere): assessment of hepatic arterial embolization. Cardiovasc Intervent Radiol **2006**;29(4):522-529.

Chapter 5

P.R. Seevinck, G.Varma, H. de Leeuw, J. Senegas, T. Schaeffter, C.J.G. Bakker

In Proceedings of the 17th Annual Meeting of ISMRM, Honolulu, USA 2009

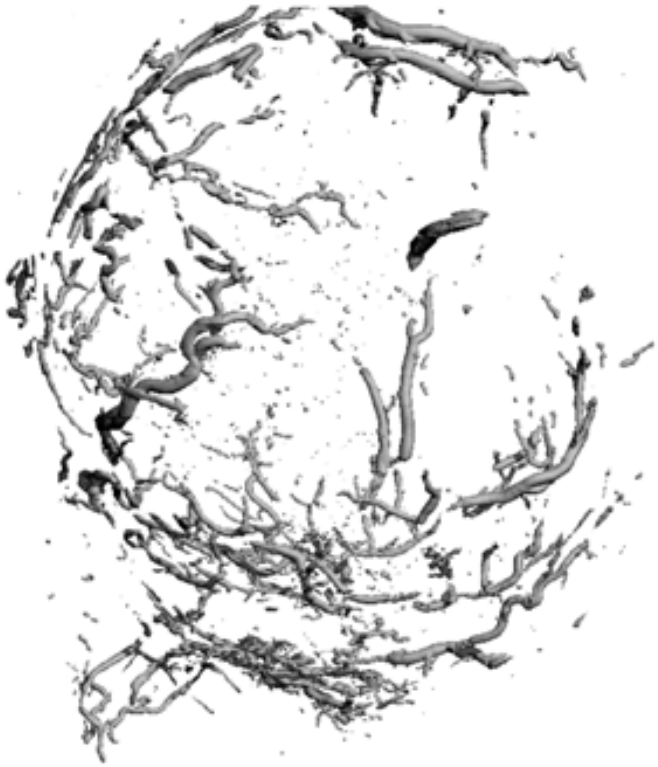

Selective depiction of holmium-loaded microspheres using susceptibility gradient mapping (SGM): initial experience in animal models

Abstract

Purpose

To investigate the potential of susceptibility gradient mapping (SGM) to selectively depict holmium-loaded microspheres (HoMS) in the presence of background magnetic field inhomogeneities.

Materials and Methods

Susceptibility gradient (SG) maps are calculated by determining the local echo shift using a short-term Fourier transform. The echo shift, which is related to the susceptibility gradient, is depicted in the SG map. Selective depiction of spatially-oriented magnetic field gradients was investigated qualitatively by determining 1D, 2D and 3D SG maps. Furthermore, SGM was applied to ex vivo rabbit liver data and in vivo pig liver data after intra-arterial administration of HoMS. Results were compared to conventional T_2^* weighted images and T_2^* maps.

Results

SGM was demonstrated to allow selective depiction of spatially-oriented field gradients with positive contrast. By applying 2D SGM, it was possible to distinguish macroscopic field gradients from local, HoMS-induced magnetic field distortions. Conventional T_2^* contrast was unable to discriminate signal voids induced by both types of magnetic field distortion. Furthermore, increasing the echo time increased the conspicuity of HoMS on susceptibility gradient maps.

Conclusion

SGM successfully depicted HoMS with positive contrast in the liver of animal models in the presence of background field gradients, induced by tissue-air interfaces. By discarding the macroscopic spatially-oriented field gradients the local HoMS induced magnetic field distortions can be highlighted selectively.

Introduction

To successfully apply radioembolization with holmium-166 loaded microspheres (^{166}HoMS), which is a promising treatment option for both unresectable liver metastases and hepatocellular carcinoma (1, 2), image-based treatment planning is essential. The highly paramagnetic nature of holmium makes HoMS an ideal T_2^* contrast agent. The local magnetic field distortions induced in the vicinity of HoMS when placed in a strong external magnetic field, cause dephasing and lead to signal loss (1, 3, 4). In previous animal studies on radioembolization of hepatic malignancies, MR imaging was demonstrated to enable real-time monitoring of transcatheter HoMS administration (5) and MR-based quantification (3, 4). However, the presence of macroscopic field inhomogeneities due to air-tissue interfaces in the vicinity of the liver severely complicated selective depiction of HoMS depositions when using conventional T_2^* contrast, since both macroscopic field inhomogeneities and local magnetic field distortions due to the presence of HoMS cause negative contrast on MR magnitude images.

It has been suggested that alternative imaging approaches, which generate positive contrast or hyperintensities, may improve selective depiction of paramagnetically labeled contrast agents or particulates such as HoMS (6). In the past few years several positive contrast technique have been proposed, including white marker imaging (7) and GRASP (8), which both are gradient compensation techniques, and techniques that exploit spectrally selective excitation of off-resonant spins (9) or pre-saturate on-resonant spins (10). These positive contrast generating imaging methods need dedicated MR pulse sequences or adaptations to conventional imaging techniques. Furthermore, the mentioned techniques require knowledge of the expected frequency shifts to optimize specific imaging parameters. A recently proposed alternative to generate positive contrast is susceptibility gradient mapping (SGM) (11), which is a post-processing technique applicable to complex data acquired with a conventional gradient echo imaging sequences. Previously, SGM was shown to successfully depict iron-labeled C6 glioma cells with positive contrast in vivo in a rat tumor model (6, 11).

In this work, we investigate the potential of SGM for the selective depiction of HoMS with positive contrast in the presence of macroscopic field inhomogeneities. The theory behind SGM will shortly be summarized. Susceptibility gradient (SG) maps will be derived from complex data obtained with conventional gradient echo experiments. By way of phantom experiments, the use of 1D, 2D and 3D SG maps to either emphasize or discard directional information obtained with SGM will be explored qualitatively. Initial experiences with SGM on data obtained from ex vivo rabbit liver containing HoMS and from in vivo pig liver after transcatheter

radioembolization with HoMS will be presented. The influence of the echo time on positive contrast generation will be shown, demonstrating its influence on the sensitivity of SGM. Finally, SGM will be discussed in the context of sensitivity and specificity and in relation to a recently proposed post-processing methodology, phase gradient mapping (12, 13).

Methods

Susceptibility gradient mapping

In susceptibility gradient mapping, local magnetic field gradients are exploited to generate positive contrast in the vicinity of the magnetic perturber. The influence on frequency encoding of an object with a susceptibility difference with its surrounding, causing a local field distortion, can be divided into two phenomena

First, the local field gradients superimpose upon the applied frequency encoding gradient, causing a disturbed and nonlinear frequency-position relation, which leads to a geometrical distortion parallel to the direction of the imaging gradient.

Second, the time instance at which rephasing has fully balanced dephasing experiences a shift, since the magnitude of the rephasing gradient changed by the superimposed local field gradient, and consequently differed from the dephasing gradient. Therefore, an echo shift in k-space may be expected, which represents a position dependent phase term in image space that manifests itself as signal dephasing after integration over the voxel volume. In the imaging equation of a 1D gradient echo experiment, describing the signal that is acquired during application of the imaging gadient, both phenomena can be identified. The 1D imaging equation can be written in terms of t'(t'=t-TE):

$$S(t') = \sum_{n=0}^{N-1} \rho(n \cdot \Delta x) \cdot \exp[-i2\pi\gamma G_x^{im} \cdot n \cdot \Delta x \cdot t'] \times \exp[-i2\pi\gamma G_x^{sus} n \cdot \Delta x \cdot (t'+TE)] \quad [1]$$

with t the time from the excitation pulse, TE the echo time, G^{im} the imaging gradient, G^{sus} the spatially varying field gradient due to the presence of a magnetized object, ρ(n Δx) the spin density and Δx the pixel size. Eq. [1] can be reformulated to separate geometrical distortions, related to scaling of the k-space variable, as shown in the first exponent of Eq. [2], and a position dependent phase term, leading to an echo shift, which is represented by the second exponential of Eq. [2].

$$S(t') = \sum_{n=0}^{N-1} \rho(n \cdot \Delta x) \cdot \exp[-i2\pi\gamma G_x^{im} \cdot t' \cdot (1 + \frac{G_x^{sus}}{G_x^{im}}) \cdot n \cdot \Delta x] \times \exp[-i2\pi\gamma G_x^{sus} \cdot TE \cdot n \cdot \Delta x] \quad [2]$$

The echo is created when the phases induced by G^{sus} completely cancel out G^{im}, which occurs when (11):

$$m = -\frac{G_x^{sus} \cdot TE}{(G_x^{im} + G_x^{sus}) \cdot \tau_x} \quad [3]$$

where τ_x is the sampling interval. The parameter m represents the local echo shift in terms of multitudes of the sampling interval τ_x, or in terms of k-space intervals, when considered in the time domain or in the frequency domain, respectively. In SGM, m is determined using a short-term Fourier transform, as described by Dahnke et al. (11). The method utilizes a sliding window in image space to determine the echo shift for each voxel separately in a low resolution k-space. Consequently, the resolution of the SG map is degraded.

As can be concluded from Eq. [3], the echo shift increases when G^{sus} or TE increases. Therefore, the obtained SG map depicts locations with high G^{sus} with hyperintense signal, while areas with low G^{sus} are suppressed. Since the echo time is linearly related to m, TE may be adapted to influence the magnitude of m, and thus the sensitivity of SGM. However, it is unclear how this influences error measures in SGM. By calculating the parameter m in three dimensions, a 3D echo shift vector is derived, enabling the calculation of SG maps for any arbitrary direction. Furthermore, one can choose to discard a specific direction by depicting a 2D SG map, or emphasize a single direction by depicting a 1D SG map. The 2D and 3D SG maps are calculated by taking the magnitude of the 2D or 3D vector according to $m_{x,y} = \sqrt{(m_x^2 + m_y^2)}$ and $m_{x,y,z} = \sqrt{(m_x^2 + m_y^2 + m_z^2)}$.

Experimental setup and data acquisition

Ex vivo experiment

Up to 40mg of highly-loaded HoMS (14) were administered in steps of 10 mg into the hepatic artery of an excised rabbit liver (15, 16). After each administration multi-gradient echo acquisitions were performed using multi-slice imaging with the following imaging parameters: TR/TE_1/ΔTE = 500/1.36/1.11, flip angle = 50°, 3 echoes, FOV = 128x128x44mm, scan matrix = 128x128x11, BW_{read} = 1314 Hz, on a 3T system (Achieva, Philips Healthcare, Best, The Netherlands).

Phantom experiment

The potential to selectively depict spatially-oriented magnetic field gradients using SGM was qualitatively explored using a phantom setup. A cylindrical phantom filled with agarose gel (2% w/w), doped with 16.6 mM Ho(III) leading to a susceptibility equal to 0 ppm, and a glass cylinder ($d\chi$ = -10 ppm) positioned in the center of the cylindrical phantom was used (17). The phantom was positioned perpendicular to the main magnetic field to induce spatially-varying but known magnetic field gradients (12). Imaging parameters were TR/TE/flip = 8.2/3.8/10°, FOV = 128x128x64, scan matrix = 128x128x64, BW_{read} = 893 Hz, and B_0 = 3T.

In vivo experiment

Radioembolization with ^{166}HoMS was performed in a healthy pig, as described in detail in by Vente et al. (2). To summarize, 600 mg of ^{166}HoMS were administered via a catheter into the hepatic artery of a pig. MRI was performed on a 1.5T system (Achieva, Philips Healthcare, Best, The Netherlands) using a 3D multi-gradient echo sequence with the following imaging parameters: TR/TE_1/ΔTE = 25/2.2/1.4, flip angle = 25°, 15 echoes, BW_{read} = 570 Hz, FOV = 320x256x136 mm, scan matrix = 208x149x68 applying breath-hold.

Results

Ex vivo experiment

SGM successfully depicted the distribution of HoMS in the ex vivo rabbit liver with positive contrast (Figure 1.)

Qualitatively, a good agreement was observed between the distribution of positive contrast as depicted by SGM and the negative contrast observed in T_2^*-weigthed images. Increasing the echo time from 1.4 ms to 3.6 ms clearly resulted in an increased conspicuity of the HoMS, as shown in the second row of Figure 1. For the small dose of 10 mg, the increased positive contrast obtained by increasing TE improved the HoMS conspicuity while providing a realistic image, however, for a higher dose of 40mg, the shorter echo time turned out to be favorable in order to keep the positive contrast of HoMS more local and in accordance with the negative contrast in T_2^*.

Phantom experiment

To qualitatively explore the potential to selectively depict spatially-oriented magnetic field gradients, 1D SG maps were derived. Figure 2 demonstrates that 1D SG maps selectively depicted echo shift along the x and y direction induced by the glass cylinder, which was oriented perpendicular to B_0. By selecting the

z-direction in which no field distortions were expected outside the cylinder, susceptibility gradients in the x and y direction were successfully discarded, leading to an absence of positive contrast in the 1D SG map of the z-direction. The 3D SG map depicted the 3D echo shift vector combining x, y and z echo shifts in one image, which resembles a summation of the individual 1D SG maps.

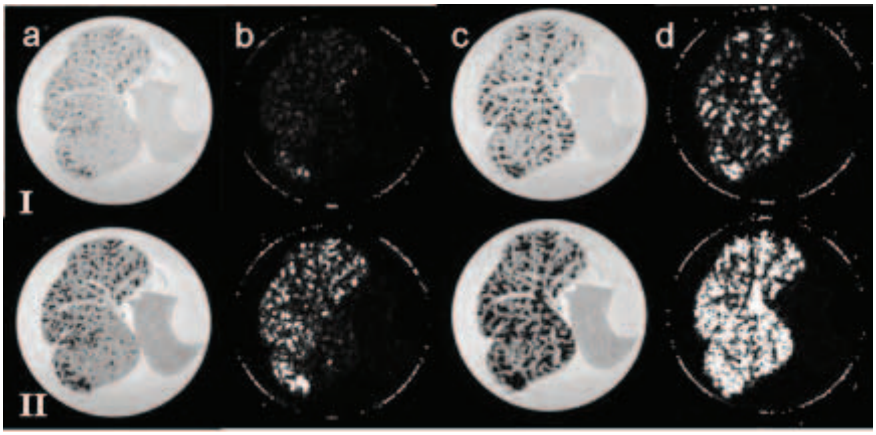

Figure 1 *T_2*-w images and 2D SG maps of an ex vivo rabbit liver after successive administrations of HoMS, 10 mg (a, b) and 40 mg (c, d). Row I represents the 1st echo, row II the 3rd echo, with echo times of 1.4 ms and 3.6 ms, respectively.*

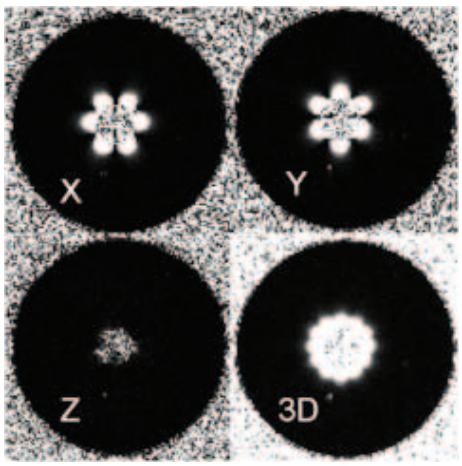

Figure 2 *SG maps of the agarose gel phantom containing a glass cylinder, positioned perpendicular to B_0. 1D SG maps of the echo shift in x and y direction depict hyperintense patterns. The 1D SG map of the echo shift in the z-direction does not show a hyperintensity. The 3D SG map shows a hyperintense pattern resembling a summation of the 1D SG maps belonging to the x-direction and y-direction.*

In vivo pig experiment

Coronal images of the abdomen of the pig are shown in Figure 3, with the liver delineated in red. SGM clearly depicted the distribution of HoMS in the liver. Similar distributions were shown by the 2D SGM (Figure 3b) and T_2^*-weighted images (Figure 3a) as verified by the overlay in blue in Figure 3c. The presence of air in the abdomen and in the lungs introduced magnetic field inhomogeneities which resulted in positive contrast in the abdomen and the lungs and showed that SGM cannot distinguish between different origins of susceptibility. When comparing SGM to the R_2^* map (Figure 3d), a similar pattern of positive contrast and high R_2^* was observed in the liver. However, the R_2^* map showed high values close to the tissue-air interface between liver and lung, due to macroscopic field inhomogeneities caused by the air in the lungs (Figure 3d, white arrows). The 2D SG map, in which the feet-head direction was chosen to be discarded, was insensitive to these macroscopic field inhomogeneities. As a result, no positive contrast was depicted in this area, while maintaining the depiction of isotropic field variations due to the presence of HoMS as shown in Figure 3b and c. At longer echo times, the regions with positive contrast increased, as can be observed when comparing the upper and lower row of images in Figure 3. An observation that needs further investigation is the depiction of water-fat interfaces by SGM.

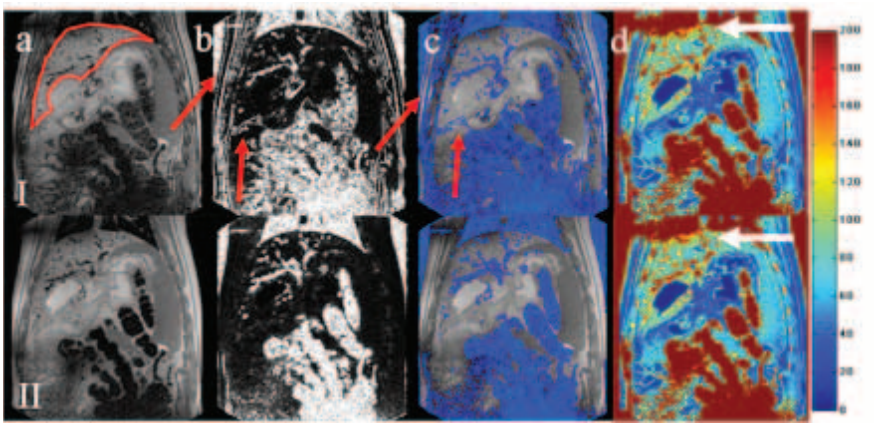

Figure 3 *In vivo coronal images of a pig liver, after administration of 600 mg of HoMS, obtained using a 3D multiple gradient echo scan in breath-hold. Row I represents the 1st echo, row II the 3rd echo. a) T_2^*-w images, with the liver delineated in red. b) 2D SG maps of the left-right and through-plane echo shift, discarding the feet-head direction. c) SG maps in blue overlaid on the T_2^*-w images. d) R_2^* maps. Red arrows indicate positive contrast generation at water-fat interfaces. White arrows indicate the influence of macrospcopic magnetic field inhomogeneities on the R_2^* value, in the vicinity of the tissue-air interface between liver and lung (For color figure see addendum).*

This is shown in Figure 3.I b and c, stressed by the red arrows for an image acquired with an out-of-phase echo time (TE = 2.3 ms at 1.5T). This enhancement was not observed in Figure 3II, which was acquired at an echo time (TE = 5.0 ms) close to in-phase, suggesting that either the phase effects or the partial volume effects due to tissue-fat interfaces may lead to positive contrast in SGM.

Discussion and conclusions

SGM was demonstrated to provide detailed qualitative depiction of HoMS in liver tissue ex vivo and in vivo in animal models after transcatheter HoMS administration. Longer echo times can be chosen to increase positive contrast due to an increase of the underlying echo shift. This echo time dependency may be used to optimize positive contrast in areas with different concentrations of contrast agent, i.e. longer echo times for low concentrations and shorter echo times for higher concentrations. Although SGM is not sensitive to the origin of the induced echo shift, exploiting directional information by calculating 1D or 2D SG maps was demonstrated to allow exclusion of macroscopic echo shifts along certain directions. This enables discriminating between T_2^* effects induced by paramagnetic substances (local $d\chi$) and due to macroscopic field inhomogeneities, which tend to create anisotropic susceptibility gradients.

SGM utilizes a short term fourier transform in image space to derive a low resolution k-space in which the echo shift is determined. This causes the image resolution to be degraded as compared to the original data. Since the parameter m which is determined by SGM is actually proportional to echo time and field gradient (11), we suggest that simply calculating the phase gradient would be a more intuitive approach to determine the echo shift. Interestingly, since we are left with a physical quantity then, it is easier to put the findings in perspective. Furthermore, direct calculation of phase gradient maps allows estimation and analysis of error measures, which is not possible when applying the methodology used by Dahnke et al (11). The main advantage of SGM over conventional phase gradient determination is the fact that SGM is not affected by phase wraps, since the determination of the echo shift is performed in the frequency domain. Conventional methods determining the phase require some unwrapping algorithm which may be error-prone. However, recently a method was proposed, phase gradient mapping (PGM) (12), which actually derives the phase derivative directly. When determined analytically using the complex data (13), resolution is maintained, error analysis is possible and phase unwrapping is unnecessary. Further investigation will be required to compare SGM and PGM and to be able to value both methods on their advantages and disadvantages.

References

1. Nijsen JF, Seppenwoolde JH, Havenith T, Bos C, Bakker CJ, van het Schip AD. Liver tumors: MR imaging of radioactive holmium microspheres--phantom and rabbit study. Radiology **2004**;231(2):491-499.
2. Vente MA, Nijsen JF, de Wit TC, Seppenwoolde JH, Krijger GC, Seevinck PR, Huisman A, Zonnenberg BA, van d, I, van het Schip AD. Clinical effects of transcatheter hepatic arterial embolization with holmium-166 poly(L: -lactic acid) microspheres in healthy pigs. Eur J Nucl Med Mol Imaging **2008**.
3. Seevinck PR, Seppenwoolde JH, Zwanenburg JJ, Nijsen JF, Bakker CJ. FID sampling superior to spin-echo sampling for T(2) (*)-based quantification of holmium-loaded microspheres: Theory and experiment. Magn Reson Med **2008**;60(6):1466-1476.
4. Seppenwoolde JH, Nijsen JF, Bartels LW, Zielhuis SW, van het Schip AD, Bakker CJ. Internal radiation therapy of liver tumors: qualitative and quantitative magnetic resonance imaging of the biodistribution of holmium-loaded microspheres in animal models. Magn Reson Med **2005**;53(1):76-84.
5. Seppenwoolde JH, Bartels LW, van der WR, Nijsen JF, van het Schip AD, Bakker CJ. Fully MR-guided hepatic artery catheterization for selective drug delivery: a feasibility study in pigs. J Magn Reson Imaging **2006**;23(2):123-129.
6. Liu W, Dahnke H, Jordan EK, Schaeffter T, Frank JA. In vivo MRI using positive-contrast techniques in detection of cells labeled with superparamagnetic iron oxide nanoparticles. NMR Biomed **2008**;21(3):242-250.
7. Seppenwoolde JH, Viergever MA, Bakker CJ. Passive tracking exploiting local signal conservation: the white marker phenomenon. Magn Reson Med **2003**;50(4):784-790.
8. Mani V, Briley-Saebo KC, Itskovich VV, Samber DD, Fayad ZA. Gradient echo acquisition for superparamagnetic particles with positive contrast (GRASP): sequence characterization in membrane and glass superparamagnetic iron oxide phantoms at 1.5T and 3T. Magn Reson Med **2006**;55(1):126-135.
9. Cunningham CH, Arai T, Yang PC, McConnell MV, Pauly JM, Conolly SM. Positive contrast magnetic resonance imaging of cells labeled with magnetic nanoparticles. Magn Reson Med **2005**;53(5):999-1005.
10. Stuber M, Gilson WD, Schar M, Kedziorek DA, Hofmann LV, Shah S, Vonken EJ, Bulte JW, Kraitchman DL. Positive contrast visualization of iron oxide-labeled stem cells using inversion-recovery with ON-resonant water suppression (IRON). Magn Reson Med **2007**;58(5):1072-1077.
11. Dahnke H, Liu W, Herzka D, Frank JA, Schaeffter T. Susceptibility gradient mapping (SGM): a new postprocessing method for positive contrast generation applied to superparamagnetic iron oxide particle (SPIO)-labeled cells. Magn Reson Med **2008**;60(3):595-603.
12. Bakker CJ, de LH, Vincken KL, Vonken EJ, Hendrikse J. Phase gradient mapping as an aid in the analysis of object-induced and system-related phase perturbations in MRI. Phys Med Biol **2008**;53(18):N349-N358.

13. Leeuw de H, Seevinck PR, Maat van de GH, Bakker CJG. High resolution phase gradient mapping as a tool for the detection and analysis of local field disturbances. In Proceedings of the 17th Annual Meeting of ISMRM, Honolulu, USA **2009**.
14. Bult W, Seevinck PR, Krijger GC, Visser T, Kroon-Batenburg LM, Bakker CJ, Hennink WE, van het Schip AD, Nijsen JF. Microspheres with ultrahigh holmium content for radioablation of malignancies. Pharm Res **2009**;26(6):1371-1378.
15. Seevinck PR, Bult W, Nijsen JFW, Vente MAD, Roos de R, Schip van het AD, Bakker CJG. Highly-loaded holmium microspheres for test dose detection and biodistribution prediction in internal radiation therapy of liver malignancies. In Proceedings of the 16th Annual Meeting of ISMRM, Toronto, Canada **2008**.
16. Seevinck PR, Varma G, Leeuw de H, Senegas T, Schaeffter T, Bakker CJG. Selective depiction of holmium-loaded microspheres using susceptibility gradient mapping (SGM): initial experience in animal models. In Proceedings of the 17th Annual Meeting of ISMRM, Honolulu, USA **2009**.
17. Bakker CJ, de RR. Concerning the preparation and use of substances with a magnetic susceptibility equal to the magnetic susceptibility of air. Magn Reson Med **2006**;56(5):1107-1113.

Chapter 6

P.R. Seevinck, Hendrik de Leeuw, C. Bos, and C.J.G. Bakker

Subitted

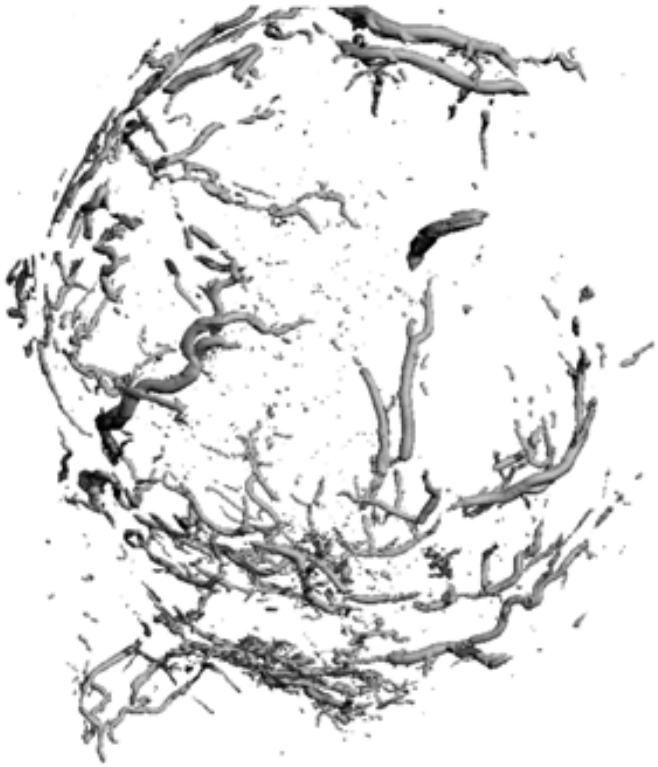

Highly localized positive contrast of small paramagnetic objects using 3D center-out RAdial Sampling with Off-resonance Reception (RASOR)

Abstract

In this paper we present a 3D imaging technique, applying RAdial Sampling with Off-resonance Reception (RASOR), to accurately depict and localize small paramagnetic objects with high positive contrast while suppressing long T_2^* components. The RASOR imaging technique is a fully frequency encoded 3D ultrashort TE (UTE) center-out acquisition method, which utilizes a large excitation bandwidth and off-resonance reception. By manually introducing an offset, Δf_0, to the central reception frequency (f_0), optimized for the paramagnetic object to be visualized, the magnetic field disturbance causing the typical radial signal pile in 3D center-out sampling can be compensated for, resulting in a hyperintense signal at the exact location of the small paramagnetic object. This was demonstrated both theoretically and using 1D time domain simulations. Experimental verification was done with a gel phantom containing three paramagnetic objects with very different geometry, viz., subvoxel stainless steel spheres, paramagnetic brachytherapy seeds and a puncture needle. In all cases, RASOR was shown to generate high positive contrast exactly at the location of the magnetized object, as confirmed by X-ray computed tomography (CT).

Introduction

Accurate depiction and localization of small (super-)paramagnetic objects with MRI, such as paramagnetic markers (1-3), endovascular coils (4-6) and stents (4, 6-8), brachytherapy seeds (9, 10), biopsy needles (11-14) and clusters of magnetically labeled cells (15) or microspheres (16), has been a challenge since the advent of MRI (17, 18). The strong magnetic field gradients in the vicinity of the magnetized objects lead to intravoxel dephasing and extreme shortening of T_2^*. Hence, T_2^* weighted gradient echo imaging can be applied to generate negative contrast (19). Although a sensitive contrast mechanism, the size and shape of the susceptibility artifact in T_2^*-weighted images is most often not representative for the object, and the negative contrast is non-specific. To increase conspicuity, several positive contrast techniques have been developed in the past few years, which most often exploit the off resonance precession frequency present in the vicinity of the perturber (white marker imaging (2), GRASP (20), frequency selective excitation (21), IRON (22), SGM (23)). These methods successfully generate positive contrast while suppressing long T_2^* components or on-resonant spins. Similar as observed with gradient echo imaging, though, the location and shape of the hyperintensities do often not match with the location and shape of the magnetic perturber (24). Instead, the magnetic field disturbance in the vicinity of the paramagnetic object is highlighted, showing either one or several smaller hyperintensities (2, 21-24). So to our opinion, the challenge of accurate localization and depiction of small magnetized objects has not been satisfactorily resolved as yet.

In this paper we present a 3D imaging technique, applying RAdial Sampling with Off-resonance Reception (RASOR), to accurately depict and localize small paramagnetic objects with high positive contrast while suppressing long T_2^* components. The RASOR imaging technique is a fully frequency encoded 3D ultrashort TE (UTE) center-out acquisition method (25), which utilizes a large excitation bandwidth and off-resonance reception. By manually introducing an offset, Δf_0, to the central reception frequency (f_0), optimized for the paramagnetic object to be visualized, the magnetic field disturbance causing the typical radial signal pile in 3D center-out sampling can be compensated for, resulting in a hyperintense signal at the exact location of the small paramagnetic object. When required, long T_2^* suppression will be accomplished by subtraction of a second echo (25, 26).

To gain a better understanding of the underlying principles enabling the generation of highly localized positive contrast when applying RASOR, the influence of a magnetized object on spatial encoding with 3D radial center-

out sampling will first be investigated both theoretically and using 1D time domain simulations. Next, the applicability and versatility of the method will be demonstrated experimentally on a gel phantom containing three paramagnetic objects with very different geometry, viz, subvoxel stainless steel spheres, paramagnetic brachytherapy seeds and a puncture needle. The influence of the objects' geometry and susceptibility on the optimal value of Δf_0 to generate localized positive contrast will be studied. Finally, geometric accuracy of the RASOR method is evaluated both quantitatively and qualitatively, using computed tomography (CT) as the gold standard.

Theory

Image distortions near dipolar magnetic field perturbations in radial sampling

Dipolar magnetic field distribution

The dipolar magnetic field perturbation $\Delta B_z(r, \varphi_p, \theta_p)$ of a paramagnetic sphere with a bulk magnetic susceptibility difference $\Delta\chi$ with its surrounding and radius *a* can be described by Eq. [1], in which B_0 is the field strength and *r* and φ_p designate spherical coordinates with respect to the sphere's center and B_0 (see Figure 1).

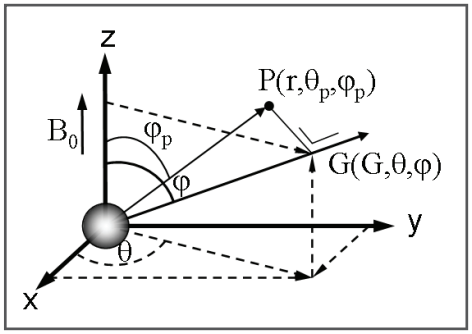

Figure 1 *Definition of the spherical coordinate system with respect to the center of a magnetized sphere. The position of a point P in 3D space is specified by the radial distance r from the center of the coordinate system, the inclination angle φ_p with respect to the z-axis and the azimuthal angle θ_p with respect to the x-axis. Similarly, the radially varying read out gradient vector can be described using G, φ and θ.*

$$\Delta B_z(r,\varphi_p,\theta_p) = \frac{\Delta\chi B_0}{3}\left(\frac{a}{r}\right)^3\left(3Cos^2\varphi_p - 1\right) \qquad [1]$$

From Equation 1 it can be deducted that the dipolar field disturbance caused by a spherical susceptibility perturber is point symmetric with respect to its center and that the field disturbance is independent of the azimuthal angle θ.

Three dimensional radial sampling

The 3D imaging equation in spherical coordinates can be written as

$$s(k,\varphi,\theta) = \int_0^{2\pi} d\theta_p \int_0^{\pi} d\varphi_p \int_0^{\infty} dr\, r^2 \sin\varphi_p \rho(r,\varphi_p,\theta_p) e^{-i2\pi\, W_{3D} kr} \qquad [2]$$

with the inclination angle φ and the azimuthal angle θ with respect to the z and x-axis, respectively, as schematically shown in Figure 1, and using $\vec{k}\cdot\vec{r} = W_{3D}(\theta,\theta_p,\varphi,\varphi_p)kr$. Thermal relaxation is incorporated in the effective spin density ρ(r, φ_p, θ_p). W_{3D}(θ, θ_p, φ, φ_p) represent a 3D geometrical weighting factor in which the subscript p characterizes a point in image space. The physical meaning of W_{3D} is a mapping of the position vector $\vec{r}$ of point P onto the radial read-out gradient vector $\vec{G}$ (See Figure 1). A complete derivation of Eq. [2] can be found in Appendix I.

A local dipolar field distortion ΔB_z(r, φ_p, θ_p) located at the center (*r=0*) of the spherical coordinate system is introduced (Figure 1). By writing k in terms of γ, G and t'(t'=t-TE) and after reordering the exponential terms to separate t' and TE (see Figure 2 for definition of t' and TE), the influence of the local field distortion on signal dephasing and spatial encoding can be recognized separately, as demonstrated in Eq. [3].

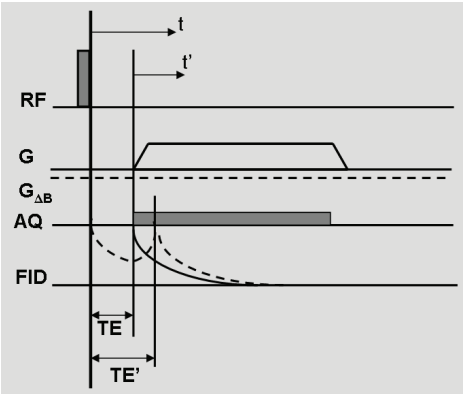

Figure 2 *Schematic representation of the ultrashort TE imaging sequence. The presence of a magnetized sphere with susceptibility Δχ, locally introducing a static magnetic field disturbance, ΔB, is represented by an additional, time invariant gradient, $G_{\Delta B}$ on the read gradient axis. The presence of $G_{\Delta B}$ locally changes the read gradient, leading to an echo shift from TE to TE', as schematically shown by the dashed line. The time t' with respect to the actual echo formation is defined as t'=t-TE.*

$$s(t',G,\varphi,\theta) = \int_0^{2\pi} d\theta_p \int_0^{\pi} d\varphi_p \int_0^{\infty} dr\, r^2 \sin\varphi_p \rho(r,\varphi_p,\theta_p) \times e^{-i\gamma G\, W_{3D}(r+\Delta B_z(r,\varphi_p,\theta_p))/(G\, W_{3D}))t'} e^{-i\gamma\ \Delta B_z(r,\varphi_p,\theta_p)TE} \qquad [3]$$

The second exponential term, which is dependent on the echo time TE and the field distortion ΔB_z(r, φ_p, θ_p), represents a local echo shift in k-space which is manifested as dephasing in image space (27). Eq [3] shows that minimizing TE, as

is done in UTE imaging, will therefore minimize the echo shift and consequently intravoxel signal dephasing. The first exponential term represents a scaling of the k-space variable, which causes a geometrical distortion in image space. Since geometrical distortions are induced in the direction parallel to the read gradient, the typical geometrical distortion observed in 3D radial sampling can be described by a pattern of replicated objects in all radial directions, which in some cases resembles a radial smear. This has been demonstrated in literature for a B_0 inhomogeneity, which resulted in a radial point spread function (28, 29).

Geometrical distortion of a susceptibility perturbation in radial sampling

To gain insight in the geometrical distortion caused by a dipolar magnetic field distortion located at the center of the imaging volume, we consider a 1D experiment.

The geometrical weighting factor as defined for the 3D imaging equation in spherical coordinates reduces to unity in a 1D experiment, since the directions of the read gradient and the position vector of P are parallel. The 1D imaging equation may then be written as:

$$s(t',G) = \int_0^\infty dr\ \rho(r) e^{-i\gamma G\ (r+\Delta B(r)/G)t'} e^{-i\gamma\ \Delta B(r)TE} \qquad [4]$$

The first term in Eq. [4] is independent of the echo time TE and represents scaling of the k-space variable, which leads to a geometrical distortion in image space according to

$$r' \equiv r + \Delta B(r)/G = r/\lambda(r) \qquad [5]$$

with r' the spatial variable in the distorted image and $G_{\Delta B}(r) = d/dr\ (\Delta B(r))$ the local field gradient induced by the magnetic field distortion, leading to $\lambda(r) = G/(G + G_{\Delta B}(r))$. Here $\lambda(r)$ represents the spatially dependent dilation factor (28), characterizing both smearing and shifting of signal intensity. For a constant $G_{\Delta B}(r)$, the relation between the distorted and undistorted image can be described by

$$\rho'(r) = \lambda\rho(\lambda r) \qquad [6]$$

with $\rho'(r)$ and $\rho(r)$ the distorted and undistorted spin density, respectively. The signal intensity of a particular voxel will be smeared out when $|\lambda|<1$ and piled up when $|\lambda|>1$.

Center out sampling

Center out sampling causes a line in k-space to be acquired with both positive and negative read-out gradients. Therefore, for half of the acquired sample points, $\lambda < 1$, and for the other half $\lambda > 1$. In image space, a point symmetric magnetic field distortion consequently causes a symmetrical distortion with respect to the origin of the field distortion. In other words, for a spherical subvoxel susceptibility perturber a radial hyperintensity around the center of the perturber may be expected in a 2D plane perpendicular to B_0.

Off-resonance reception

The influence of a magnetic field distortion $\Delta B(r)$ on the local precession frequency may be expressed using the larmor equation: $\Delta f_{larmor}(r)=\gamma/2\pi \cdot \Delta B(r)$. Hence, manually changing the f_0 reception frequency may be regarded as imposing an offset to the magnetic field, yielding the following expression for the total field distortion: $\Delta B(r)_{total} = \Delta B(r)+\Delta f_0 \cdot 2\pi/\gamma$. By introducing an offset Δf_0 of opposite sign, magnetic field distortions caused by paramagnetic perturbers can be balanced. Optimization of Δf_0 causes the radial hyperintensity to become a hyperintense spot at the location of the susceptibility perturber. The optimized value of Δf_0 can be determined using the acquisition BW per pixel and the number of pixels the positive contrast was shifted away from the actual location of the perturber, i.e. $\Delta f_0 = n \cdot BW_{pix}$, with $BW_{pix} = \gamma/2\pi \cdot d_{pix} \cdot G$ in [Hz/pix], n the number of pixels to be shifted for gradient balancing and d_{pix} the size of a pixel. By incorporating $\Delta B(r)_{total}$ in Eq [4], the 1D imaging equation becomes

$$s(t',G) = \int_0^\infty dr\ \rho(r) e^{-i\gamma G\ (r+(\Delta B(r)+\Delta f_0 \cdot 2\pi/\gamma)/G)t'} e^{-i\gamma\ (\Delta B(r)+\Delta f_0 \cdot 2\pi/\gamma)TE} \qquad [7]$$

Introducing an f_0 offset, however, will apply to the entire image, resulting in a radial smear in the entire image, as mentioned before. This is of no concern in the presented application, since the objective was to apply long T_2^* suppression to null the signal in the entire image, while highlighting short T_2^* components at the location of the susceptibility perturber. In this way, selective highly localized positive contrast will be accomplished.

Methods

Simulations

Radial center-out k-space sampling was simulated in 1D both perpendicular and parallel to B_0 to investigate the typical geometrical distortions associated with UTE RASOR imaging of a strongly magnetized sphere. Since the dipolar

magnetic field distortion induced by a magnetized sphere is point symmetric, a profile in the transversal plane (perpendicular to B_0) crossing the magnetized sphere is representative for any profile in the transversal plane. Simulations were performed in Mathematica (Wolfram Research, USA), by implementing Eq [7], using center-out sampling scheme with a positive read gradient for the positive k values and a negative read gradient for the negative k values, followed by a Fourier transform. For comparison conventional acquisitions with either a positive or negative read gradient were simulated as well. A super-sampling factor of 10 was used to take into account intravoxel dephasing. The dipolar magnetic field perturbation of the inclusion was calculated using Eq. [1] with $\Delta\chi$ = 4000ppm and a = 0.25 mm. The R_2 of the medium was set to R_2=30 s^{-1}. A B_0 field strength of 3T was used. Other parameters included FOV = 128mm; imaging matrix = 128 and TE/ΔTE=0.08/3.0ms. The read gradient was set at 24 mT/m, leading to BW_{pix}~1 kHz/pix.

MRI experiments

Stainless steel spheres

Two agarose gel (2%) phantoms were made, doped with 32 mg/ml $MnCl_2$ to adapt the R_1 relaxation rate. The first phantom (A) contained one stainless steel sphere (radius a = 0.25mm) and was used to investigate two phenomena; first, the specific artifact associated with 3D UTE RASOR of a subvoxel magnetized sphere; second, the influence of varying the value of Δf_0. The second phantom (B) contained five stainless steel spheres and was used to investigate the geometrical accuracy. X-ray CT was used as a gold standard to compare UTE RASOR with. A 64-slice clinical CT scanner (Brilliance, Philips Healthcare, Best, The Netherlands) was used with a tube voltage of 120 kV and reconstructed voxel size = 0.2578x0.2578x0.5 mm. MR imaging experiments were done on a 3T system (Achieva, Philips Healthcare, Best, The Netherlands) with the following imaging parameters: FOV = 128 mm; scan matrix = 128^3; NSA = 1; flip angle = 8° and a read-out bandwidth such that BW_{pix} = 1020 Hz per pixel. Volume excitation was done using a hard, non-selective RF block pulse, resulting in a large excitation bandwidth BW_{ex}~40 kHz centered around f_0. Timing parameters were; TR/ΔTE=5.0/1.5ms with 2 echoes, scan time=2:43 minutes. Phantom A was scanned using a sense headcoil with TE_1=0.15ms. Δf_0 offsets between 0 and -4.0 kHz were applied, which correspond to zero to minus four times the BW_{pix}. Phantom B was scanned using a surface coil with TE_1=0.08ms. An optimized frequency offset Δf_0=-2.0 kHz was applied.

Brachytherapy seeds

An agarose gel phantom was made as previously described, containing four brachytherapy seeds (0.8x4.5mm), positioned two by two roughly at an angle of 90°. The phantom was positioned in such a way that two seeds were aligned with B_0 and two were perpendicular to B_0. UTE RASOR imaging was performed as described for phantom B to accurately depict and localize the brachytherapy seeds. An optimized frequency offset of Δf_0=-1.0 kHz was used to generate localized positive contrast. MR data was compared qualitatively to X-ray CT data.

MRI coaxial puncture needle

The depiction of an MRI coaxial puncture needle (Somatex®, diameter 18G~1.2 mm) with UTE RASOR was investigated in an agarose gel phantom. To allow localization of the needle and needle tip a stainless steel sphere (0.5mm) was inserted in the phantom close to the tip of the needle. The phantom was positioned such that the needle was perpendicular to B_0. UTE RASOR imaging was performed as described for phantom B. An optimized f_0 offset of Δf_0=-2.0 kHz was used to generate localized positive contrast. MR data was compared qualitatively to X-ray CT data.

Results

Simulations

1D Simulations of a subvoxel magnetized sphere perpendicular to B_0 showed that, when using an ultrashort TE, signal pile up was observed on one side of the magnetized sphere, leaving a signal void on the other side of the magnetized sphere (Figure 3b). The location of hyper- and hypointensity depended on the sign of the read gradient (Figure 3b, 3c). Center-out sampling caused the hyperintensity to be located on both sides of the magnetized perturber, creating a signal void exactly at the location of the magnetized sphere (Figure 3d). At a longer echo time signal decay is observed in the vicinity of the magnetized sphere due to intravoxel dephasing (Figure 3e). Therefore, subtraction of the longer echo time signal profile from the ultrashort TE signal profile provided signal pile up on both sides of the magnetized sphere, while suppressing the background signal (Figure 3f). When applying an optimized f_0 offset, the hyperintensities 'merged', creating high positive contrast at the location of magnetized sphere (Figure 3g). Again, the background signal was suppressed by subtraction of a later echo (Figure 3h).

Image profiles parallel to B_0 (Figure 4), crossing the positive magnetic field lobes of the dipolar field disturbance, showed similar behavior compared to

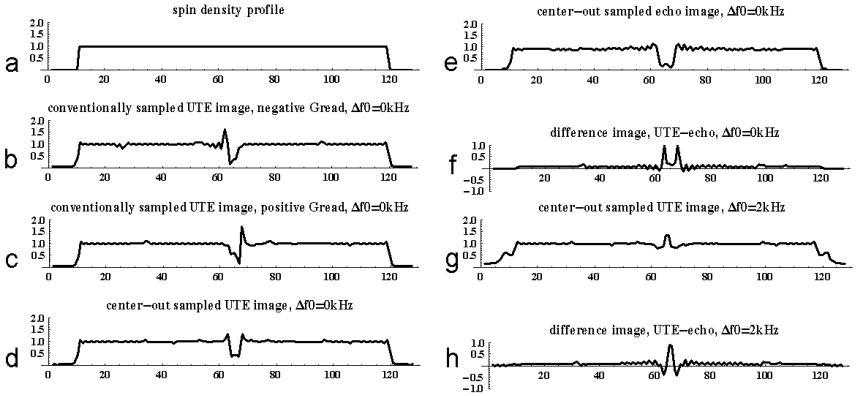

Figure 3 *Magnitude image profiles obtained with 1D simulations, perpendicular to B_0: object profile (a), UTE with positive read gradient (b), UTE with negative read gradient (c), UTE with center-out sampling (d), Echo signal at 3ms with center-out sampling (e), difference image of UTE minus echo (f), center-out sampling with Δf_0 = 2 kHz (g), difference image of UTE minus 2nd echo with Δf_0 = 2 kHz (h).*

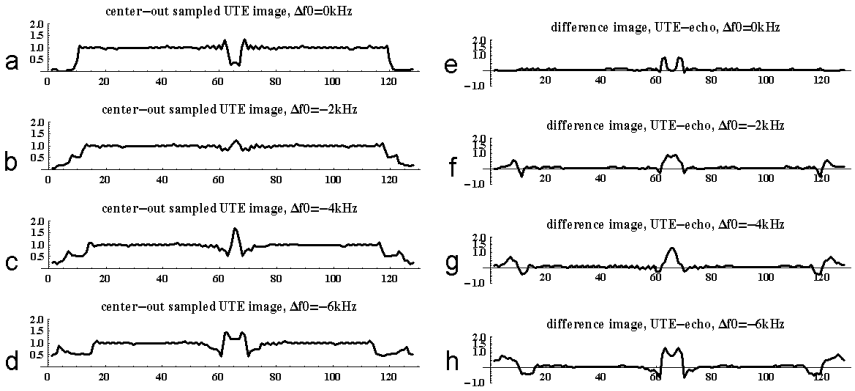

Figure 4 *Magnitude UTE image profiles obtained with 1D simulations, parallel to B_0; with center-out sampling with Δf_0 = [0, -2, -4, -6] in kHz (a-d); corresponding difference images of UTE minus echo (3ms), with Δf_0 = [0, -2, -4, -6] in kHz (e-h).*

the profiles perpendicular to B_0 (Figure 3), involving negative magnetic field disturbances. This demonstrated that during center-out sampling, the sign of the magnetic field distortion did not influence the geometrical distortion, as long as the magnetic field distortion was symmetrical. However, a wider signal void was observed for the 1D simulation parallel to B_0 (Figure 3d and 4a), which was due to the fact that the absolute magnitude of the positive field lobes of a dipolar magnetic field distortion is twice as high as compared to the negative ring-like magnetic field lobe surrounding the center of the dipolar field distortion (see Eq. 1.).

Increasing Δf_0 over the range [0, -2, -4, -6] in kHz , clearly demonstrated that the signal pile up originally located on both sides of the magnetized sphere (Figure 4a, 4e) first move towards each other (Figure 4b, 4f) and then move apart again (Figure 4d, 4h). The value of Δf_0 necessary to exactly compensate for the field distortion and generate high localized positive contrast (Figure 4c, 4g) was twice as high (2kHz vs -4kHz) and of opposite sign for the simulations parallel to B_0.

MR experiments

Geometrical distortion of a susceptibility perturbation in radial sampling

Spherical signal pile up surrounding the signal void was observed at the location of the magnetized stainless steel sphere, when applying 3D center-out radial UTE imaging (Figure 5a). At longer echo times the hyperintense ring disappeared due to dephasing, as depicted for the transverse plane perpendicular to B_0 (Figure 5b). Subtraction of the echo image from the UTE image successfully suppressed the long T_2^* components, while highlighting the hyperintense ring.

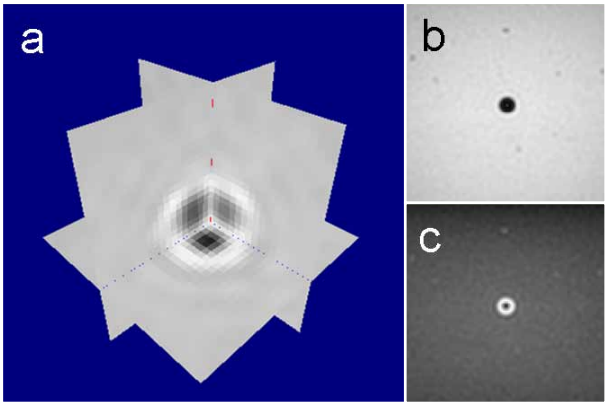

Figure 5 *Orthogonal views (a) of a magnetized sphere in 3D UTE imaging. Echo image at TE = 1.5ms (b) and difference images of UTE minus echo (c).*

Off-resonance reception

The influence off-resonance reception is demonstrated by manually varying the reception frequency offset Δf_0=[0, -2.0, -4.0] in kHz. Figure 6 shows transversal and coronal images obtained using the 3D UTE RASOR imaging technique with varying Δf_0. Similar to what was observed in the 1D simulations, the spherical hyperintensity first converged when increasing the absolute value of Δf_0 and formed a local hyperintensity exactly at the location of the magnetized sphere (Figure 6b and e). A further increase of the absolute value of Δf_0 resulted in a radial divergence again. At the edges of the agarose gel phantom, the effect of

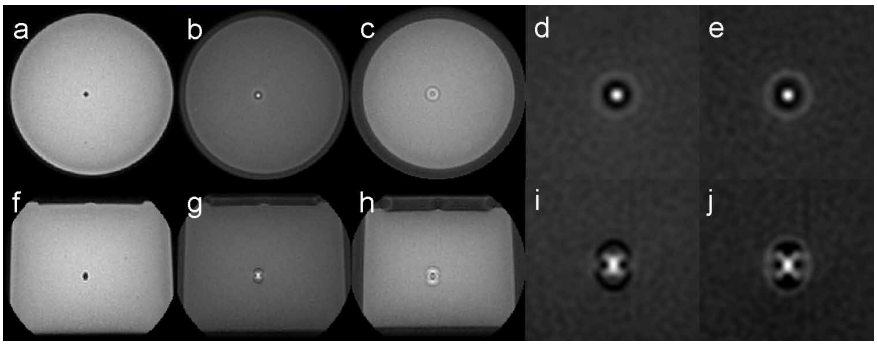

Figure 6 *Transversal (a, b, c, d, e) and coronal (d, e, f, g, h) images obtained using 3D UTE RASOR imaging with Δf_0 varied between 0 (a, f), -2.0 kHz (b, g, d, i, e, j) and -4.0 kHz (c, h) pixels. Zoomed in RASOR UTE images (d, i) and difference images (e, j) are shown as well for Δf_0. = 2.0 kHz.*

the radial image replication associated with RASOR can be observed (Figure 6 b, c, g and h). The diameter of the actual agarose gel phantom decreased by the number of pixels equal to the reception frequency offset in pixels. However, at the same time, a larger circular object is depicted with the roughly half intensity of the original object, but a diameter which increased by the number of pixels equal to reception frequency offset in pixels. Similar patterns were observed in the image profiles of the 1D simulations (Figure 3g, 4b, 4c, 4d).

A detailed look at UTE RASOR images shows that perpendicular to B_0 a single hyperintensity is shown (Figure 6d, e), whereas in a plane parallel to B_0 (i, j), a cross-like structure is seen, with the highest intensity in the center. Subtraction of the echo image from the UTE RASOR image provided good long T_2^* suppression, which becomes particularly clear in the intensity profiles of the transversal plane as depicted in Figure 7.

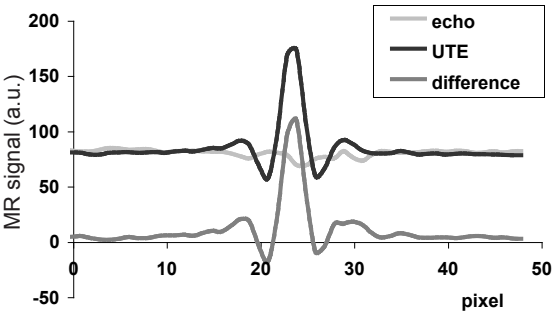

Figure 7 *Intensity profiles of MR images obtained perpendicular to B_0 using 3D UTE RASOR imaging with Δf_0=-2.0 kHz. UTE image profile (black), echo image profile (light gray) and difference image (UTE-echo) profile (dark gray).*

Localization accuracy

Very good agreement was observed qualitatively when comparing maximum intensity projections (MIP's) of coronal and transversal UTE RASOR MR images and CT images of phantom B, as depicted in Figure 8. After 3D rigid registration a mean error of 0.89±0.30 mm (mean±sd) was found, which is less than the image resolution of 1 mm used for MRI.

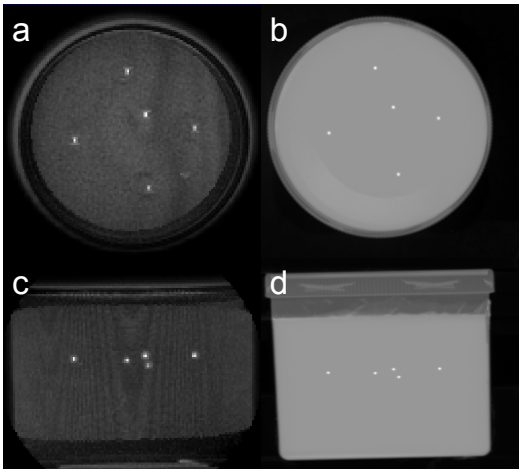

Figure 8 *Coronal (a) and transversal (c) MIP UTE RASOR images with Δf_0= 2.0 kHz (b, c) pixels. Coronal (b) and transversal (d) gold standard MIP x-ray CT images.*

Brachytherapy seeds

Brachytherapy seeds were accurately depicted with positive contrast using the UTE RASOR imaging technique, applying a frequency offset of Δf_0=-1.0 kHz. Interestingly, the orientation of brachy seeds positioned both parallel as well as perpendicular to B_0 was easily resolved, without the need for dedicated segmentation algorithms. Such information is crucial for detailed post-implantation dosimetry, which currently needs either x-ray radiography or CT imaging (9, 30). The CT images depicted the brachytherapy seeds with high intensity, however, streaking artifacts compromise the accuracy of the shape the brachy seeds were depicted with, in a similar way as observed in literature (31).

MRI coaxial puncture needle

The puncture needle was successfully depicted with high conspicuity using the UTE RASOR technique with an f_0 offset of Δf_0=-2.0 kHz, when oriented perpendicular to the main magnetic field. When oriented parallel to B_0, the tip of the needle was depicted with high positive contrast as well, however, the shaft was depicted with much lower conspicuity. In both orientations the stainless steel

sphere was depicted with high positive contrast as well. The location, orientation and shape of the puncture needle with respect to the stainless steel sphere as visualized with UTE RASOR imaging showed very good qualitative comparison with the X-ray CT images.

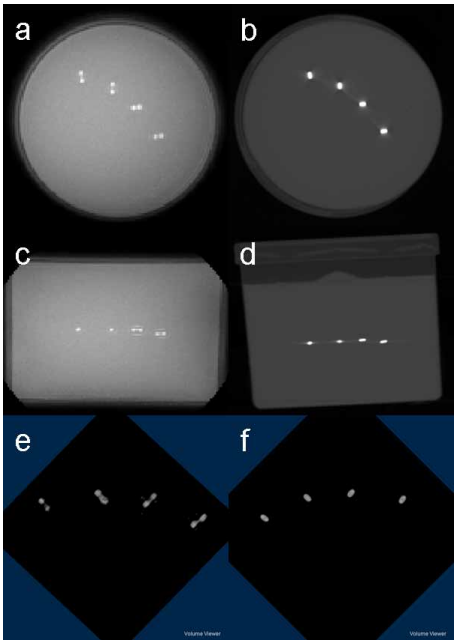

Figure 9 *Coronal (a, d) and transversal (b, e) MIP UTE RASOR images (a, b, c) and MIP CT images (d, e, f) of brachytherapy seeds. Angulated volume renderings are depicted to demonstrate accurate delineation of the brachytherapy seeds, independent on orientation with respect to* B_0 *(c).*

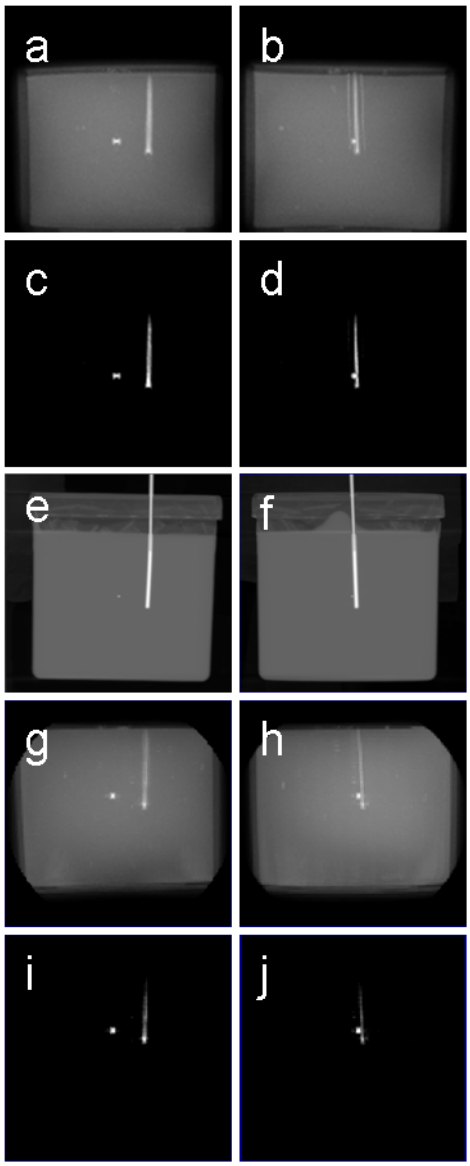

Figure 10 *Depiction of puncture needle in agarose gel using the UTE RASOR method, compared with X-ray CT images. The needle was oriented perpendicular to B_0 in images a-d, and parallel in images g-j. A stainless steel sphere was placed close to the needle tip as a reference. Transversal (a and c) and coronal (b and d) MIP UTE RASOR images depict the needle and sphere with high positive contrast, closely resembling the CT images. When oriented parallel to B_0, the shaft of the needle was depicted with much lower conspicuity, whereas the tip of the needle was depicted with high positive contrast. Volume renderings selectively depict the needle and stainless steel sphere (c, d, i, j).*

Discussion

This paper presents a method to accurately localize and depict small paramagnetic objects with high positive contrast while, when desired, suppressing long T_2^* components. The technique utilizes radial sampling with off-resonance reception, RASOR, incorporated in a fully frequency encoded 3D ultrashort TE center-out acquisition method. The success of the method can be attributed to

a combination of factors, together exploiting the underlying principles generally causing geometrical distortions and signal voids near magnetized objects in frequency encoding techniques.

Firstly, a hard, non-selective RF block pulse is used, which generates a large excitation bandwidth to excite the entire spin ensemble in the volume of interest. This is important, since in the vicinity of (super-)paramagnetic objects at clinical field strengths of 1.5T and higher, frequency offsets of several kHz are readily found (32). When using conventional RF excitation pulses with a limited bandwidth of a few kHz at maximum, signal voids are expected near the magnetized objects due to the large off-resonance precession frequencies in these areas, which will not be excited (32). Furthermore, by using a non-selective excitation pulse in combination with a fully frequency encoded 3D acquisition method, slice selection is omitted, which is generally severely affected by strong local magnetic field variations, resulting in distorted excitation profiles that cause through-plane slice distortions (11, 32, 33).

Secondly, radial sampling of k-space is applied, which is crucial in the presented technique. Due to the fact that signal mismapping in frequency encoding is always parallel to the read gradient, the used sampling scheme causes a radial signal pile up in the vicinity of a small magnetized object, the center of gravity of which coincides with the center of the magnetized object (29). By applying an optimized frequency offset during signal reception, the signal mismapping can be compensated for, leading to a summation of the radial signal pile up exactly at the location of the small magnetized object, locally generating high positive contrast. The hyperintense signal can therefore become much higher than would be expected from the actual spin density at the location of the magnetized object.

Thirdly, ultrashort echo times are used, which minimize subvoxel dephasing at locations with high magnetic field gradients in the vicinity of the magnetized objects. Geometrical distortions and signal pile-up, however, are independent of echo time and are in fact exploited in UTE RASOR imaging to generate high positive contrast. In a later gradient echo image, with longer TE, the blooming effect of intravoxel dephasing overshadows the hyperintensities at the locations of the magnetized object (13). Hence, by subtraction of a later gradient echo from a UTE image, the hyperintensities are left unaffected while effectively suppressing long T_2^* components. Furthermore, subtraction of a later echo reduces macroscopic signal variations related to B_0 and B_1 field inhomogeneities, facilitating threshold based segmentation of the object of interest.

The broad applicability of the RASOR method was demonstrated by accurately depicting three types of paramagnetic objects with very different geometry and susceptibility, with highly localized positive contrast. Subvoxel stainless steel spheres were located with subvoxel accuracy, as compared to X-ray CT images. Brachytherapy seeds were accurately depicted, easily resolving the orientation of the individual brachytherapy seeds, irrespective of their orientation with respect to B_0, which is of major importance for post-implant dosimetry (9). Currently, in prostate brachytherapy, X-ray CT is used to accurately locate the seeds, while MRI is used to delineate the prostate, requiring multimodal image registration prior to post-implant dosimetry (9, 30). The presented methodology may facilitate a much easier fully MR-based dosimetry procedure. Finally, a puncture needle was accurately depicted with high positive contrast, both perpendicular and parallel to B_0, which may facilitate accurate MR-guided biopsies and radiofrequency or cryoablation (11, 34).

Each object, with its unique shape and susceptibility, requires optimization of the f_0 offset, which was done on a trial and error basis in this paper. However, when a specific object is to be visualized, it will be possible to determine the optimal value of Δf_0 prior to imaging. Its value is a function of several object properties and imaging parameters, including the object's susceptibility and shape, image resolution and read gradient strength. Furthermore, both positive and negative Δf_0 values may be used, to either balance positive or negative magnetic field distortions introduced by the magnetized object. Specificity may be increased by exploiting these options to tune the receive offset specifically for the objects under investigation.

The presented imaging methodology has some limitations. First, the concept of off-resonance reception influences the entire image, and not just the area in close proximity of the magnetized object. As mentioned briefly in the theory section, RASOR introduces a radial replication of the entire object, which may be appreciated as a radial smear, and is expected to compromise the anatomical image. In the present work, however, the objective was to generate highly localized positive contrast while suppressing long T_2^* background signal by subtraction of a later echo. The suboptimal anatomical images (UTE and echo) prior to subtraction may therefore be regarded as a bonus.

Second, the magnetic field distortion induced by the paramagnetic object to be imaged depends on the orientation with respect to the B_0 direction. For spherical objects this is of no concern, but for different shapes it is. Therefore, the optimized value of Δf_0 may vary for different orientations. The extent of this limitation should be investigated for each specific object, since it will vary among

objects. For the brachytherapy seeds, for instance, it was observed to be of minor importance. For the puncture needle, however, a clear difference in conspicuity was observed when oriented parallel or perpendicular to B_0.

Third, the proposed method applies to relatively small objects. To accurately depict larger objects such as metallic implants, commonly used in knee and hip arthroplasty, SE based imaging sequences are often preferred, since signal loss due to intravoxel dephasing can be reduced to a minimum by applying a 180° refocusing pulse (4, 17). However, geometrical distortions will still be present, as well as partial excitation near implants due to the limited bandwidth of conventional excitation pulses. Recently, specific imaging sequences have been proposed to address these difficulties and to correct for in-plane and through slice distortions. Based on principles such as view-angle-tilting, additional through-slice encoding and selective excitation and reception (SEMAC (33), MAVRIC (32)) these methods were shown to strongly suppress geometrical distortions in the vicinity of the large metallic implants, enabling imaging near metallic implants. The aim of the imaging method presented in this paper, however, was to accurately depict small paramagnetic objects with high positive contrast while suppressing background signal. Therefore, the RASOR technique may be regarded as a complementary imaging technique to SEMAC and MAVRIC.

When comparing RASOR to other positive contrast techniques, the most important difference is the location at which the positive contrast is obtained. RASOR is unique in that it enables positive contrast generation exactly at the location of the small paramagnetic object. Since most other positive contrast techniques exploit either the off resonance precession frequency or the high field gradients in the vicinity of the perturber, the positive contrast is typically generated in the vicinity of the perturber, as was demonstrated in literature for white marker imaging (2, 24), GRASP (20), frequency selective excitation (21), IRON (22, 24) and SGM (23, 24). When imaging small paramagnetic objects, therefore, RASOR will be the only method that will yield a realistic geometrical representation.

In conclusion, the concept of off-resonance reception in combination with radial sampling, as applied in the presented RASOR imaging technique, successfully exploits the ever-present magnetic field distortions in the vicinity of small magnetized objects placed in a B_0 field, by generating high positive contrast exactly at the location of the magnetized object, while suppressing background signal.

Appendix

Derivation of the 3D imaging equation in spherical coordinates

The influence of a spherical subvoxel susceptibility deviation on spatial encoding and signal dephasing in 3D radial sampling can be used more easily to demonstrate by the 3D imaging equation in spherical coordinates. Therefore, it is deduced from the cartesian form in this appendix. In 3D carthesian k-space sampling, the signal obtained in the presence of three orthogonal gradients after a nonselective excitation pulse may be written as the 3D Fourier transform

$$s(\vec{k}) = \int d^3 r \rho(\vec{r}) e^{-i2\pi \vec{k}\cdot\vec{r}} \qquad [A1]$$

$$s(k_x, k_y, k_z) = \iiint dx dy dz \ \rho(x, y, z) e^{-i2\pi(k_x x + k_y y + k_z z)} \qquad [A2]$$

In 3D radial k-space sampling, k-space is encoded radially over a sphere (kooshball) by applying an angulated read gradient $\vec{G}$ with magnitude $G = \sqrt{G_x^2 + G_y^2 + G_z^2}$ at an angle defined by the inclination angle φ and the azimuthal angle θ with respect to the z and x-axis, respectively. The angles φ and θ may be defined as $\theta = \tan^{-1}(G_y/G_x)$ and $\varphi = \tan^{-1}(\sqrt{G_x^2 + G_y^2}/G_z)$. Using $\vec{k} = \gamma \vec{G} t'$ with $k = \sqrt{k_x^2 + k_y^2 + k_z^2}$, such that $k_x = k\sin(\varphi)\cos(\theta)$, $k_y = k\sin(\varphi)\sin(\theta)$ and $k_z = k\cos(\varphi)$, the 3D imaging equation in its spherical coordinates may be written as follows

$$s(k, \varphi, \theta) = \iiint dx dy dz \ \rho(x, y, z) \times e^{-i2\pi k(x\sin(\varphi)\cos(\theta) + y\sin(\varphi)\sin(\theta) + z\cos(\varphi))} \qquad [A3]$$

By expressing the coordinates of a point P(x, y, z) in image space in spherical coordinates (P(r, φ_p, θ_p)), Eq. [A3] can be completely written in spherical coordinates

$$s(k, \varphi, \theta) = \int_0^{2\pi} d\theta_p \int_0^{\pi} d\varphi_p \int_0^{\infty} dr \, r^2 \sin\varphi_p \rho(r, \varphi_p, \theta_p) e^{-i2\pi \vec{k}\cdot\vec{r}} \qquad [A4]$$

The dot product $\vec{k}\cdot\vec{r}$ in Eq. [A4] represents a mapping of the position vector $\vec{r}$ onto the radial read-out gradient vector $\vec{G}$ since this is parallel to $\vec{k}$ (see Figure 1). Using $x = r\sin(\varphi_p)\cos(\theta_p)$, $y = r\sin(\varphi_p)\sin(\theta_p)$ and $z = r\cos(\varphi_p)$ with $r = \sqrt{x^2 + y^2 + z^2}$, the dot product $\vec{k}\cdot\vec{r}$ can be written as follows $\vec{k}\cdot\vec{r} = W_{3D}(\theta, \theta_p, \varphi, \varphi_p) kr$ with $W_{3D}(\theta, \theta_p, \varphi, \varphi_p) = (\sin(\varphi)\cos(\theta)\sin(\varphi_p)\cos(\theta_p) + \sin(\varphi)\sin(\theta)\sin(\varphi_p)\sin(\theta_p) + \cos(\varphi)\cos(\varphi_p))$

Using the 3D geometrical weighting factor $W_{3D}(\theta, \theta_p, \varphi, \varphi_p)$ and Eq. [A4], the 3D imaging equation in spherical coordinates form becomes

$$s(k,\varphi,\theta) = \int_0^{2\pi} d\theta_p \int_0^{\pi} d\varphi_p \int_0^{\infty} dr\, r^2 \sin\varphi_p \rho(r,\varphi_p,\theta_p) e^{-i2\pi\, W_{3D} kr} \qquad [A5]$$

References

1. van der Weide R, Bakker CJ, Viergever MA. Localization of intravascular devices with paramagnetic markers in MR images. IEEE Trans Med Imaging **2001**;20(10):1061-1071.
2. Seppenwoolde JH, Viergever MA, Bakker CJ. Passive tracking exploiting local signal conservation: the white marker phenomenon. Magn Reson Med **2003**;50(4):784-790.
3. Huisman HJ, Futterer JJ, van Lin EN, Welmers A, Scheenen TW, van Dalen JA, Visser AG, Witjes JA, Barentsz JO. Prostate cancer: precision of integrating functional MR imaging with radiation therapy treatment by using fiducial gold markers. Radiology **2005**;236(1):311-317.
4. Lauer UA, Graf H, Berger A, Claussen CD, Schick F. Radio frequency versus susceptibility effects of small conductive implants--a systematic MRI study on aneurysm clips at 1.5 and 3 T. Magn Reson Imaging **2005**;23(4):563-569.
5. Shellock FG, Gounis M, Wakhloo A. Detachable coil for cerebral aneurysms: in vitro evaluation of magnetic field interactions, heating, and artifacts at 3T. AJNR Am J Neuroradiol **2005**;26(2):363-366.
6. Teitelbaum GP, Bradley WG, Jr., Klein BD. MR imaging artifacts, ferromagnetism, and magnetic torque of intravascular filters, stents, and coils. Radiology **1988**;166(3):657-664.
7. Bartels LW, Smits HF, Bakker CJ, Viergever MA. MR imaging of vascular stents: effects of susceptibility, flow, and radiofrequency eddy currents. J Vasc Interv Radiol **2001**;12(3):365-371.
8. Vonken EJ, Schar M, Stuber M. Positive contrast visualization of nitinol devices using susceptibility gradient mapping. Magn Reson Med **2008**;60(3):588-594.
9. Miquel ME, Rhode KS, Acher PL, Macdougall ND, Blackall J, Gaston RP, Hegde S, Morris SL, Beaney R, Deehan C, Popert R, Keevil SF. Using combined x-ray and MR imaging for prostate I-125 post-implant dosimetry: phantom validation and preliminary patient work. Phys Med Biol **2006**;51(5):1129-1137.
10. Moerland MA, Wijrdeman HK, Beersma R, Bakker CJ, Battermann JJ. Evaluation of permanent I-125 prostate implants using radiography and magnetic resonance imaging. Int J Radiat Oncol Biol Phys **1997**;37(4):927-933.
11. Butts K, Pauly JM, Daniel BL, Kee S, Norbash AM. Management of biopsy needle artifacts: techniques for RF-refocused MRI. J Magn Reson Imaging **1999**;9(4):586-595.
12. Sinha S, Sinha U, Lufkin R, Hanafee W. Pulse sequence optimization for use with a biopsy needle in MRI. Magn Reson Imaging **1989**;7(5):575-579.
13. Glowinski A, Adam G, Bucker A, van VJ, Gunther RW. A perspective on needle artifacts in MRI: an electromagnetic model for experimentally separating susceptibility effects. IEEE Trans Med Imaging **2000**;19(12):1248-1252.
14. Muller-Bierl B, Graf H, Lauer U, Steidle G, Schick F. Numerical modeling of needle tip artifacts in MR gradient echo imaging. Med Phys **2004**;31(3):579-587.
15. Weissleder R, Cheng HC, Bogdanova A, Bogdanov A, Jr. Magnetically labeled cells can be detected by MR imaging. J Magn Reson Imaging **1997**;7(1):258-263.
16. Seppenwoolde JH, Nijsen JF, Bartels LW, Zielhuis SW, van het Schip AD, Bakker CJ. Internal radiation therapy of liver tumors: qualitative and quantitative magnetic resonance imaging of the biodistribution of holmium-loaded microspheres in animal models. Magn Reson Med **2005**;53(1):76-84.

17. Ludeke KM, Roschmann P, Tischler R. Susceptibility artefacts in NMR imaging. Magn Reson Imaging **1985**;3(4):329-343.
18. Reichenbach JR, Venkatesan R, Yablonskiy DA, Thompson MR, Lai S, Haacke EM. Theory and application of static field inhomogeneity effects in gradient-echo imaging. J Magn Reson Imaging **1997**;7(2):266-279.
19. Bos C, Viergever MA, Bakker CJ. On the artifact of a subvoxel susceptibility deviation in spoiled gradient-echo imaging. Magn Reson Med **2003**;50(2):400-404.
20. Mani V, Briley-Saebo KC, Itskovich VV, Samber DD, Fayad ZA. Gradient echo acquisition for superparamagnetic particles with positive contrast (GRASP): sequence characterization in membrane and glass superparamagnetic iron oxide phantoms at 1.5T and 3T. Magn Reson Med **2006**;55(1):126-135.
21. Cunningham CH, Arai T, Yang PC, McConnell MV, Pauly JM, Conolly SM. Positive contrast magnetic resonance imaging of cells labeled with magnetic nanoparticles. Magn Reson Med **2005**;53(5):999-1005.
22. Stuber M, Gilson WD, Schar M, Kedziorek DA, Hofmann LV, Shah S, Vonken EJ, Bulte JW, Kraitchman DL. Positive contrast visualization of iron oxide-labeled stem cells using inversion-recovery with ON-resonant water suppression (IRON). Magn Reson Med **2007**;58(5):1072-1077.
23. Dahnke H, Liu W, Herzka D, Frank JA, Schaeffter T. Susceptibility gradient mapping (SGM): a new postprocessing method for positive contrast generation applied to superparamagnetic iron oxide particle (SPIO)-labeled cells. Magn Reson Med **2008**;60(3):595-603.
24. Liu W, Dahnke H, Jordan EK, Schaeffter T, Frank JA. In vivo MRI using positive-contrast techniques in detection of cells labeled with superparamagnetic iron oxide nanoparticles. NMR Biomed **2008**;21(3):242-250.
25. Rahmer J, Blume U, Bornert P. Selective 3D ultrashort TE imaging: comparison of "dual-echo" acquisition and magnetization preparation for improving short-T 2 contrast. MAGMA **2007**;20(2):83-92.
26. Seevinck PR, Bos C, Bakker CJ. High positive contrast generation of a subvoxel susceptibility deviation using ultrashort TE (UTE) radial center-out imaging at 3T. In Proceedings of the 17th Annual Meeting of ISMRM, Honolulu, USA **2009**.
27. Bakker CJ, Seppenwoolde JH, Vincken KL. Dephased MRI. Magn Reson Med **2006**;55(1):92-97.
28. Haacke EM, Brown RW, Thompson MR, Venkatesan R. Magnetic Resonance Imaging. Physical Principles and Sequence Design. New York: John Wiley & Sons, Inc.; 1999.
29. Lauzon ML, Rutt BK. Effects of polar sampling in k-space. Magn Reson Med **1996**;36(6):940-949.
30. Acher P, Rhode K, Morris S, Gaya A, Miquel M, Popert R, Tham I, Nichol J, McLeish K, Deehan C, Dasgupta P, Beaney R, Keevil SF. Comparison of combined x-ray radiography and magnetic resonance (XMR) imaging-versus computed tomography-based dosimetry for the evaluation of permanent prostate brachytherapy implants. Int J Radiat Oncol Biol Phys **2008**;71(5):1518-1525.
31. Orio PF, III, Tutar IB, Narayanan S, Arthurs S, Cho PS, Kim Y, Merrick G, Wallner KE. Intraoperative ultrasound-fluoroscopy fusion can enhance prostate brachytherapy quality. Int J Radiat Oncol Biol Phys **2007**;69(1):302-307.

32. Koch KM, Lorbiecki JE, Hinks RS, King KF. A multispectral three-dimensional acquisition technique for imaging near metal implants. Magn Reson Med **2009**;61(2):381-390.
33. Lu W, Pauly KB, Gold GE, Pauly JM, Hargreaves BA. SEMAC: Slice encoding for metal artifact correction in MRI. Magn Reson Med **2009**.
34. Clasen S, Pereira PL. Magnetic resonance guidance for radiofrequency ablation of liver tumors. J Magn Reson Imaging **2008**;27(2):421-433.

Chapter 7

P.R. Seevinck, J.H. Seppenwoolde, J.J.M. Zwanenburg, J.F.W. Nijsen, C.J.G. Bakker

Magnetic Resonance in Mediciine 2008:60:1466-1476

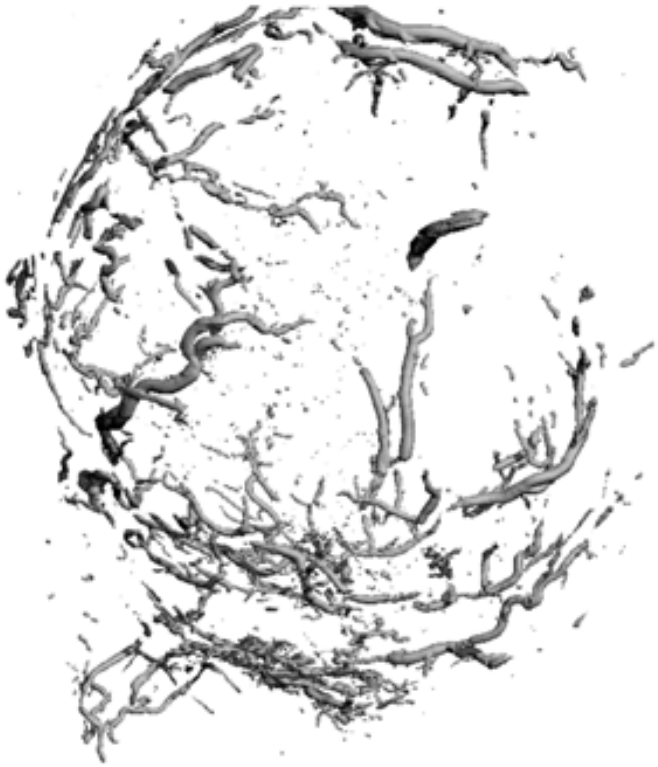

FID sampling superior to spin echo sampling for T_2^*-based quantification of holmium-loaded microspheres: Theory and experiment

Abstract

This work demonstrates both theoretically and experimentally that multiple gradient echo sampling of the FID (MGEFID) is superior to MGE sampling of the spin echo (MGESE) for T_2^*-based quantification of holmium-loaded microspheres (HoMS). An interleaved sampling strategy was applied to characterize the MR signal behavior of FID and SE signals of gels and perfused rabbit livers containing HoMS in great detail. Diffusion sensitivity was demonstrated for MGESE sampling, resulting in nonexponential signal decay on both sides of the SE peak and in an underestimation of the HoMS concentration. Other than MGESE sampling, MGEFID sampling was demonstrated to be insensitive to diffusion, to exhibit exponential signal decay and to allow accurate T_2^*-based quantification of HoMS. Furthermore, a fit procedure extending the upper limit of quantifiable R_2^* relaxation rates to at least 1500 s^{-1} was proposed. With this post-processing step incorporated, MGEFID was shown to correctly estimate the integral amount of inhomogeneously distributed HoMS in liver tissue, up to a clinically relevant limit. All experimental findings could be explained with the theory of NMR signal behavior in magnetically inhomogeneous tissues. HoMS were shown to satisfy the static dephasing regime when investigated with MGEFID and to violate the static dephasing conditions for MGESE at longer echo times typically used in SE.

Introduction

Local radiation therapy with neutron-activated holmium-loaded microspheres (HoMS) is a novel and promising treatment technique for both unresectable liver metastases and hepatocellular carcinoma (1, 2). In embolization therapies with radioactive microspheres, accurate assessment and quantification of the biodistribution is of major importance for treatment planning, dosimetry and follow up (1). Since holmium (a lanthanide like gadolinium) is strongly paramagnetic, it can be detected by magnetic resonance imaging (MRI) (3, 4). Previously, excellent high resolution images of the biodistribution of HoMS in the liver were obtained with T_2^*-weighted imaging in pigs and rabbits (1, 3). A highly inhomogeneous distribution of HoMS was revealed with local concentrations of at least 15 mg/g at an average concentration of about 0.6 mg/g liver tissue (3). These findings imply that a wide range of concentration dependent T_2^* values may be expected, varying from 40 ms in native liver tissue to sub-millisecond T_2^* values for the highest HoMS concentrations, which makes HoMS quantification based on T_2^* relaxometry a difficult task. Subsequent attempts to quantify the biodistribution of HoMS using T_2^* relaxometry were less successful and yielded a strong underestimation of the integral injected dose, which increased for larger amounts of HoMS (3). In these initial studies, T_2^* relaxometry was done with a conventional multiple gradient echo spin echo (MGESE) sampling scheme (3, 5) under the assumption of monoexponential signal decay and negligible diffusion effects, i.e. the static dephasing (SD) regime (6). MGESE was preferred rather than sampling of the free induction decay (MGEFID) because inclusion of the central spin echo peak was expected to enable a better determination of higher R_2^* relaxation rates (3, 7).

In this study, we aim to demonstrate both theoretically and experimentally that MGEFID is superior to MGESE for quantification of the highly inhomogeneous distribution of HoMS as seen in the liver. The theory of NMR signal behavior in magnetically inhomogeneous systems will be applied to predict the transverse relaxation regime (6) of the spin-sphere system under investigation and will be compared to our experimental findings. MR experiments will be done with gels and ex vivo perfused rabbit livers to show that the underestimation of the total amount of HoMS, as previously reported (3), can be attributed to the increased diffusion sensitivity associated with MGESE sampling and is strongly reduced by sampling of the FID. An interleaved acquisition scheme will be used to densely sample the FID and SE signals, allowing detailed characterization of the signal behavior of the FID and SE (8). By varying the echo time of the SE as well as the sample temperature, it will be demonstrated that the damped nonexponential

signal decay as observed in MGESE originates from diffusion effects, indicating the violation of the SD conditions. MGEFID sampling of the same spin-sphere system will be shown to be insensitive to diffusion, in accordance with the SD regime. Furthermore, we show that the upper limit of quantifiable R_2^* relaxation rates can be extended to at least 1500 s^{-1} by using a fit procedure in which the initial amplitude of the decay curve (S_0 at t=0 ms) is estimated from the decay curve of noninvolved tissue. With this post-processing step incorporated, MGEFID is shown to correctly estimate the integral amount of HoMS present in the tissue of interest, up to a clinically relevant limit. In the discussion, the differences in signal behavior and relaxation regime as observed for HoMS in gel or liver tissue when investigated with MGEFID and MGESE sampling strategies, are explained with the theory of NMR signal behavior in magnetically inhomogeneous systems(6). In addition, the findings are placed into a wider perspective and it is that similar signal behavior may be expected for other spin-sphere systems incorporating micron-sized paramagnetic particles, such as compartmentalized superparamagnetic particles as observed in ironoxide (USPIO) labeled cells.

Theory

Herein we briefly summarize the theory of NMR signal behavior in magnetically inhomogeneous systems, as proposed by Yablonskiy and Haacke (6), and apply it to the HoMS system under investigation. This theory describes the signal behavior of a spin-sphere system in the static dephasing (SD) regime, meaning that diffusion phenomena may be ignored because signal dephasing due to susceptibility-induced field inhomogeneities has occurred before molecular diffusion averages out the phases accumulated by different nuclear magnetic moments (9). In this regime, the size and strength of the magnetic perturbers induce a strong and large enough outer-sphere dipolar field such that diffusional motion is relatively small and has a minimal effect on NMR signal decay, as was confirmed by Monte Carlo simulations (10-13) and by analytical models (13, 14). Yablonskiy and Haacke formulated a static dephasing regime criterion in Eq. [24] of their work (6) which can be rewritten in terms of the characteristic diffusion time τ_D and the characteristic frequency $\delta\omega$ of the spin-sphere system under investigation:

$$\delta\omega \cdot \tau_D >> 6 \cdot \varsigma^{-1/3} \qquad [1]$$

Here $\tau_D=R_0^2/D$ is in the order of the time it takes to diffuse a distance comparable with the magnetic perturber's diameter and $\delta\omega=\gamma \cdot B_{eq}$ ($B_{eq}=\Delta\chi \cdot B_0/3$), which characterizes the change in nuclear precession in the equatorial magnetic

field of the perturber. R_0 is the particle's radius, D the diffusion coefficient and ς the volume fraction of the particles. Applying eq. [1] to HoMS in liver tissue using the following parameters: $\gamma=2\pi\cdot42.576\cdot10^6$ rad/s/T, $\Delta\chi$=800 ppm, B_0=1.5T, R_0=15µm and D_{tissue}=1 (µm)^2/ms leads to a left-hand side ($\delta\omega\cdot\tau_D$) of Eq. [1] of two to three orders of magnitude larger than the right-hand side for volume fractions between 0.0007 and 0.0014 (corresponding to HoMS concentrations between 1 and 20 mg/ml). Therefore, it can be concluded that HoMS in liver tissue satisfy the SD criterion, as was previously stated (3).

NMR signal model for the SD regime

The MR signal decay for gradient echo experiments of magnetically inhomogeneous systems in the SD regime is generally modeled using the well known empirical expression as described in Eq. [2], implying monoexponential signal behavior (6, 12).

$$S(TE) = S(0)\exp(-R_2^* \cdot TE) \qquad [2]$$

Here R_2^* represents the effective transverse relaxation rate. In a more advanced model presented by Yablonskiy, however, nonexponential signal decay was predicted during a certain time period for both FID and SE experiments in the SD regime (9). It was demonstrated that the MR signal behavior can be divided into two distinct regions; a region of quadratic exponential signal decay, the short time scale, immediately after the onset of the FID ($t<1.5\cdot t_c$) and on either sides of TE_{SE} for a SE experiment ($|t-TE_{SE}|<1.5\cdot t_c$) and a region of linear exponential (monoexponential) signal decay, the long time scale, which is valid when $t>1.5\cdot t_c$ for a FID experiment and ($|t-TE_{SE}|>1.5\cdot t_c$) for a SE experiment (9). In this definition t_c represents the characteristic time:

$$t_c = (\eta \cdot \pi \cdot \gamma \cdot \Delta\chi \cdot B_0)^{-1} \qquad [3]$$

Here η is a numerical coefficient which is equal to 2/9√3 for spherical objects (in SI units). According to Eq. [2a] and [2b] in the work of Yablonskiy (9), the MR signal decay for a FID experiment can then be described as follows for both regions

$$S(t) = S(0)\cdot\exp(-\lambda\cdot\varsigma\cdot(t/t_c)^2 - R_2\cdot t) \qquad for \quad t<1.5\cdot t_c \qquad [4]$$

$$S(t) = S(0)\cdot\exp(\varsigma)\cdot\exp(-R_2^*\cdot t) \qquad for \quad t>1.5\cdot t_c \qquad [5]$$

Here λ solely depends on the system geometry (9). Similar equations can be described for the signal decay following a SE with respect to the echo time of the spin echo. For HoMS the characteristic time t_c was estimated to be 0.0077ms using Eq. [3]. Hence, we can ignore quadratic exponential signal decay as described by Eq. [4] and expect signal decay to occur by a linear exponential as described by Eq. [5]. The effective transverse relaxation rate R_2^* is defined as R_2+R_2', and since R_2', the additional irreversible contribution of spin-spin relaxation, is considered to be small in the SD regime (11, 15), as was confirmed for HoMS previously (r_2=1.14 $s^{-1}mg^{-1}ml$ (3)), it may be expected that $R_2^*\approx R_2'$. R_2', the reversible contribution due to local field inhomogeneities introduced by magnetic perturbers, is predicted by Yablonskiy and Haacke in Eq. [58] of their work (6) as follows

$$R_2' = \varsigma / t_c = \varsigma \cdot \eta \cdot \pi \cdot \gamma \cdot \Delta\chi \cdot B_0 \qquad [6]$$

For a HoMS suspension the increase of R_2' due an increase of the HoMS concentration of 1 mg/ml (ς=0.00071) can be estimated to be 91.8 s^{-1},using Eq. [6].

SD regime for SE experiments

Although considered to be generally applicable, the SD criterion in Eq. [1] is only valid for a FID experiment. For a SE experiment an additional, less known criterion should be met to satisfy SD conditions, which is given in Eq. [32] in the work of Yablonskiy (9). Using Eq. [6], this SD criterion specific for SE experiments can be rewritten as follows:

$$TE_{SE} << TE_c = 2.9(\tau_D \cdot t_c^2 / \varsigma)^{1/3} \qquad [7]$$

Here TE_{SE} represents the echo time of the SE experiment and TE_c the critical echo time. From this criterion, it becomes clear that the validity of the SD regime in a SE experiment is not only dependent on the spin-sphere system itself, as it is for a FID experiment, but also on the pulse sequence timing parameters of the SE experiment. Applying Eq. [7] to different HoMS concentrations (1, 10 and 20 mg/ml) in liver tissue (D_{tissue}=1 $(\mu m)^2/ms$) gives a critical echo time of 7.8 ms, 3.6ms and 2.9ms, respectively. For HoMS suspended in an agarose gel matrix with a higher diffusion coefficient even smaller values for the TE_c are found (Eq. [7]). To satisfy the SD conditions, the TE_{SE} should be much smaller than those values, which is not the case in conventional SE experiments. Therefore, the HoMS system under investigation may be expected to act in different transverse relaxation regime and to exhibit different NMR signal behavior when subjected to MGEFID as compared to MGESE sampling.

Methods

Phantom preparations

Holmium-loaded microspheres

Holmium-loaded microspheres were prepared as described by Nijsen et al. (16), resulting in HoMS with a density of 1.4 g/ml, size distribution of 20-50 µm (mean diameter 30 µm) after sieving and a reproducible holmium content of 17% ± 0.6% by weight.

HoMS gel phantom

A HoMS dilution series of homogeneously suspended HoMS ranging from 0-14.9 mg/ml in a 2% agarose solution was prepared. To adapt the MR relaxation properties of the native gel to liver tissue, manganese-chloride (32 mg/ml $MnCl_2.4H_2O$) was added. Samples were sealed in tubes and placed in a cylindrical phantom setup filled with the native gel. A diameter to length ratio of the sample tubes of ten was chosen to secure a homogeneous field distribution through-plane halfway along the sample tubes.

Perfused rabbit liver model

Four excised rabbit livers were stored in saline after removing the blood volume. Prior to imaging, the hepatic artery of each liver was cannulated using a small injection tube. Known amounts of HoMS (20-120 mg) were administered to the livers using the injection tube during continuous perfusion of the liver with saline. In three livers three successive doses were given, in one liver two doses were given. After each administration quantitative imaging was performed using MGEFID and MGESE sampling.

Data acquisition

MR imaging experiments were performed on a clinical 1.5 T MR scanner (Achieva, Philips Medical Systems, Best, The Netherlands). In all gel phantom experiments the cylindrical phantom setup was placed in the center of the magnet with the main axis of the sample tubes parallel to the external magnetic field B_0.

Sampling strategies

R_2^* relaxometry was done applying two different sampling strategies, which are shown in Figure 1. In the first strategy, the 'true' FID signal immediately following excitation was sampled using multiple gradient echoes, to which we refer as MGEFID sampling. This method is identical to the initial part of the gradient echo sampling of FID and Echo (GESFIDE) method proposed by Ma and Wehrli (17). In the second method, the decaying part of the SE signal including the SE

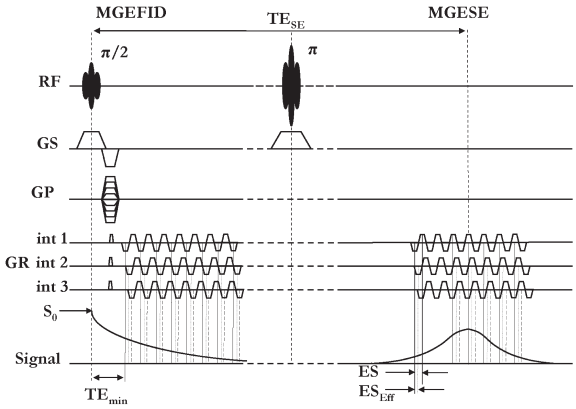

Figure 1 *Schematic structure of the MGEFID and MGESE. The left part of the scheme displays the MGEFID sampling strategy. Immediate sampling of the MR signal following the π/2 radio frequency (RF) excitation pulse is prohibited by the presence of the slice select (GS) and phase encoding gradients (GP), introducing a minimal echo time (TEmin). The minimal echo time is reduced as much as possible to sample signal decay of fast decaying MR signals prior to complete dephasing. Even and odd echoes are acquired using an EPI read gradient (GR) with removed phase encoding blips. Each acquired echo is used to fill the k-space of a separate image, belonging to the specific echo time. The effective echo spacing (ES_{Eff}) is reduced by shifting the complete EPI read-out train, which is demonstrated for three interleaves, allowing detailed characterization of the MR signal decay model. The right part of the scheme illustrates the MGESE sampling strategy, which is combined with multiple gradient echo shifting to reduce ES_{Eff} in a similar fashion as explained for MGEFID. The inclusion of the SE peak in the sampling scheme was thought to allow signal sampling of fast decaying signals which could not be sampled with conventional MGEFID sampling.*

peak, is sampled using multiple gradient echoes, to which we refer as MGESE sampling. This sampling strategy closely resembles the gradient echo sampling of SE (GESSE) method proposed by Yablonskiy and Haacke (5). Both the MGEFID and MGESE sampling strategies utilize an EPI readout train with removed phase encoding blip, sampling both even and odd echoes. In this way gradient echo images with equidistant echo times are acquired.

Ultradense sampling

To decrease the minimal echo spacing and allow detailed signal decay characterization we adopted a method involving gradient echo shifting (18). In this method the complete imaging sequence is repeated N times in an interleaved fashion, meanwhile shifting the gradient readout train and acquisition window over N consecutive sub-millisecond intervals. Figure 1 demonstrates the shift in time of the complete readout train for three interleaves. Altogether, this results in N+1 images separated by an effective echo spacing (ES_{Eff}) of the interleaved

imaging sequence of ES_{Eff}=ES/N. An arbitrary small ES_{Eff} can be acquired using this interleaved acquisition scheme at the cost of total scan duration. When applied in combination with multiple gradient echo sampling strategies, interleaved multiple gradient echo of FID (iMGEFID) and interleaved multiple gradient echo spin echo (iMGESE) sampling provide ultradensely sampled FID and SE signals enabling detailed characterization of the signal decay of FID and SE signals (8).

Diffusion sensitivity

The possible influence of diffusion on the effective transverse relaxation rate R_2^* was investigated by conducting two types of experiments. First, the echo time of the spin echo (TE_{SE}) in the MGESE sampling strategy was systematically varied. The following values for TE_{SE} were used for the gel phantom experiment: 26.0ms; 13.9ms and 8.2ms, and for the ex vivo rabbit liver experiment 35.0ms, 26.0ms; 13.9ms and 8.2ms. For MGEFID the smallest possible echo time was used, which was 2.1 ms. Second, the temperature of the HoMS gel phantom was varied while keeping TE_{SE} constant (26.0 ms) to directly alter the diffusion coefficient (12, 19). Cooling was done in a fridge and heating using warm tap water. Temperatures were monitored before and directly after imaging. The mean sample temperatures during imaging were 11°C, 23°C and 36°C with a maximum variation of 2°C in time. Diffusion sensitivity was investigated by observation of the signal decay behavior and by determination of the r_2^* relaxivity of MGEFID and MGESE data at the different temperatures.

Imaging parameters

Ultradense sampling was applied using ten interleaves (N=10), resulting in an ES_{eff} of 0.14 ms. To keep imaging times reasonable when ultradense sampling was applied, only one slice was imaged. For quantitative imaging of ex vivo rabbit livers multislice acquisitions were conducted to cover the livers, in combination with conventional sampling (N=0). The number of gradient echoes used was fifteen for iMGEFID and between seven and fifteen for iMGESE, dependent on TE_{SE}. For smaller TE_{SE} fewer echoes were fitted in the iMGESE imaging sequence. Those and other imaging parameters of the MR experiments are summarized in Table 1.

Data analysis

Data analysis was performed in Matlab R7.0 (The MathWorks, Natick, USA). MGE images belonging to odd and even echoes were separated prior to analysis.

Table 1 *MR imaging parameters of gel phantom experiments and ex vivo liver experiments.*

	HoMS gel phantom		Ex vivo rabbit liver			
Parameters	iMGEFID	iMGESE	MGEFID	MGESE	iMGEFID	iMGESE
Matrix	120x160	120x160	177x256	177x256	120x160	120x160
FOV (mm)	160x160	160x160	256x256	256x256	160x160	160x160
Slice (mm)	10	10	4	4	5	5
Num of slices	1	1	9	9	1	1
NSA	1	1	2	2	2	1
Flip (˚)	90˚	90 ˚	90˚	90˚	25˚	90˚
Interleaves	10	10	1	1	10	10
Echoes	15	7-15	15	15	15	7-15
TE_{min} (ms)	2.54	-	2.11	-	2.54	-
TE_{SE}(ms)	-	8.2;13.9; 26	-	30.8	-	8.2; 13.9; 26; 35
ES (ms)	1.42	1.42	1.55	1.55	1.30	1.30
ES_{Eff} (ms)	0.14	0.14	1.55	1.55	0.13	0.13
TR (ms)	500	500	350	500	24	500
Scantime (min)	10:02	10:02	1:15	3:35	0:49	10.02

T_2^* relaxometry

Effective transverse relaxation rates R_2^* were determined pixelwise using a linear weighted least squares (WLS) fitting algorithm on multiple gradient echo data of the HoMS gel phantom and the ex vivo rabbit livers. For all data a monoexponential signal decay model was assumed. For MGESE data only the decaying part of the SE signal was used for T_2^* relaxometry. In case of nonexponential signal decay, sample points close to the SE peak were excluded from analysis. The possible influence of Rician distributed noise on the amplitude of the magnitude signal (20) was prevented by excluding data with an SNR<2 from the analysis. HoMS calibration curves were made for both iMGEFID and iMGESE sampling strategies using the average R_2^* value of each HoMS concentration, determined in a ROI (80 pixels) in the HoMS sample in the gel phantom. Four calibration curves were made, one for the iMGEFID data and three for the iMGESE data (one for each TE_{SE}). Using linear least squares fitting on these calibration curves the HoMS relaxivity r_2^* was determined. Because the calibration curve was nonlinear in MGESE data, the relaxivity was determined twice for each calibration curve; once

in a low concentration range (0-4 mg/ml) and once in a high concentration range (4-13 mg/ml). For the ex vivo rabbit livers with HoMS administered R_2^* maps were determined using MGEFID and MGESE data in a similar way as described for the gel phantom.

T_2^* relaxometry using the amplitude of S_0

High concentrations of HoMS lead to sub-millisecond T_2^* values and signal decay that is so fast that conventional MGE techniques can not adequately sample the signal decay using regular gradient echo times (TE~2ms). This problem was overcome in MGESE sampling, where the inclusion of the SE peak allowed signal sampling and quantification of high concentrations of HoMS. For MGEFID, the initial amplitude of the MR signal of the tissue of interest immediately following excitation, $S_{0,}$ was used. S_0 was determined in a region without HoMS or with a low HoMS concentration in which R_2^* was well defined so that $S_{0,est}$ could be easily estimated using the following monoexponential relation: $S(t)=S_{0,est}.e^{-t.R2^*}$. Then, the value of $S_{0,est}$ was incorporated as the first data point belonging to t=0ms in the MGEFID data allowing the estimation of R_2^* using the WLS fitting algorithm. Only pixels with an initial SNR<10 were subjected to this fit procedure. To prevent a large influence of noise to the R_2^* value to be determined in pixels with a high R_2^* and low initial SNR (SNR<2), the value of the first measured data point of these pixels, belonging to TE_{min}, is set to SNR=2 in the fitting algorithm. This puts a limit on the maximum R_2^* value to be possibly determined to $R_{2\,max}^*=\ln(SNR_{S0,est}/2)/TE_{min}$, which is on the order of $R_{2\,max}^*$~1500 s^{-1}, dependent on the SNR of the image and TE_{min}.

Determination of the total amount of HoMS

The integral amount of HoMS present in the ex vivo rabbit livers was estimated as follows. First, the liver was manually segmented in high contrast TSE images. Then, R_2^* maps were determined as described previously. A baseline $R_2^*(0)$ value was determined in a region in the liver that contained no HoMS on visual inspection. Using the relation $R_2^*(Ho)=R_2^*(0)+r_{2\,HoMS}^*.[HoMS]$ the R_2^* values in regions containing HoMS ($R_2^*(Ho)$) were determined (3). Here $r_{2\,HoMS}^*$ is the r_2^* relaxivity of HoMS as determined with MGEFID. This value is considered the 'true' r_2^* relaxivity, since MGEFID of HoMS was demonstrated to satisfy the SD regime implying that the diffusive effect is negligible and the relaxation solely comes from phase dispersion due to static field inhomogeneities created by the presence of HoMS. Pixelwise analysis of the entire liver finally provided maps representing the local HoMS concentration ([HoMS]) in each voxel, which after multiplication by the voxel volume and summation over all liver voxels provided the total amount of HoMS in the liver.

HoMS susceptometry

The volume susceptibility of HoMS, which is needed to predict the validity of the SD regime using Eq. [1], was determined using the phase information of the MGEFID experiments. The phase (φ in rad) of HoMS sample tubes oriented co-axially with the external magnetic field was linearly related to the difference in volume susceptibility (Δχ in ppm) and echo time using the relation $\varphi=\gamma\ \Delta\chi\ B_0\ TE(3\cos^2\theta-1)/6$, leading to $\Delta\chi=3\varphi/(\gamma\ B_0\ TE)$ for θ equal to 0. When calculating the theoretical volume susceptibility using Curie's law a value of 823 ppm can be found for the HoMS material (3).

Results

HoMS gel phantom

MGEFID vs MGESE

Monoexponential signal behavior was observed for iMGEFID, as demonstrated by the linear relation between the log signal and the echo time (Figure 2a). Exploiting this relation the value of S_0 of the gel phantom was estimated (21) and depicted in Figure 2a at t=0ms. Similar values were found for S_0 when determined with different HoMS concentrations, as long as the R_2^* value of the specific HoMS concentration could be determined well. A deviation from monoexponential signal behavior was observed at longer echo times and low SNR, which may be associated with Rician distributed noise which is known to increase the magnitude amplitude at low SNR (20). The r_2^* relaxivity obtained from iMGEFID data was equal to 89.3±2.8 $sec^{-1}mg^{-1}ml$. The iMGESE data exhibited a more complex signal behavior, as demonstrated by the curve relating the log signal and echo time directly following the SE peak (TE_{SE}=26.0 ms) in Figure 2b. On both sides of the SE peak nonexponential signal decay was observed. A transition towards monoexponential signal decay was observed further away from the SE peak at longer echo times. Finally, at even longer echo times and low SNR the signal decay exhibited nonexponential signal behavior again, similar to the behavior observed for MGEFID.

Influence of the echo time

Reducing the TE_{SE} influenced the signal behavior of the SE in the HoMS gel phantom in three ways (Figure 3). First, the period that exhibited nonexponential signal decay decreased with decreasing TE_{SE}. Second, an increase of the R_2^* relaxation rates was observed for all HoMS concentrations with decreased TE_{SE}. Third, the amplitudes of the SE peaks belonging to the different HoMS concentrations tended to converge for shorter TE_{SE}. The calibration curves belonging to the HoMS

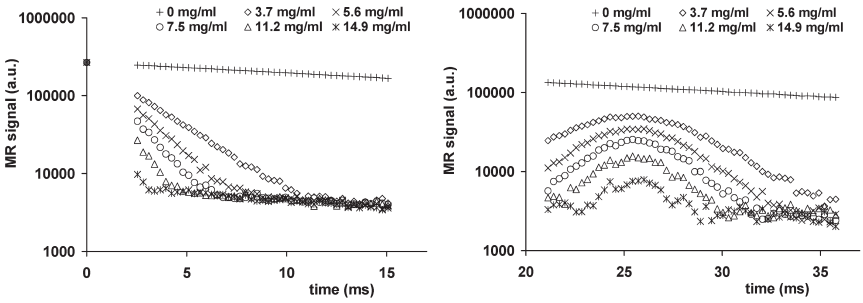

Figure 2 *Ultradensely sampled FID (a) and SE (b) modulus signals of the HoMS gel dilution series on a logarithmic scale. Sampling was done using the interleaved acquisition scheme with an effective echo spacing for odd echoes of 0.28ms. a) iMGEFID, minimal TE=2.5ms b) iMGESE, TE=26.0ms. Monoexponential signal behavior can be observed for iMGEFID signals as shown by the linearity between log MR signal and time. Using this linear relation the value of S0 can be estimated, as depicted at t=0ms in Fig. 2a. Nonexponential signal decay is demonstrated by iMGESE for all concentrations on both sides of the SE peak.*

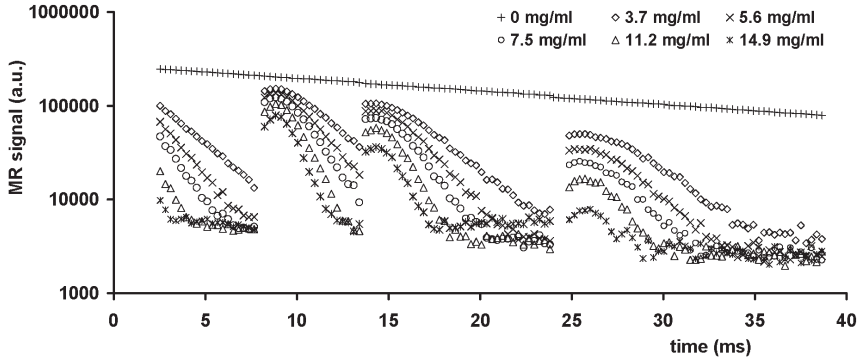

Figure 3 *Ultradensely sampled FID and SE modulus signals of the HoMS gel dilution series (0; 3.7 ; 5.6; 7.5; 11.2; 14.9 mg/ml) acquired in four separate experiments. For iMGESE three different echo times were used: TESE=8.2ms, TESE =13.9 and TESE =26.0ms. At high HoMS concentration nonexponential signal behavior is observed following the SE peak and at low SNR. Reducing TESE resulted in MR signal behavior resembling linear exponential decay, ultimately leading to monoexponential signal decay for iMGEFID.*

gel phantom determined with iMGEFID and iMGESE are presented in Figure 4. The calibration curve of HoMS acquired with iMGEFID demonstrated linear behavior over the entire concentration range. In the low concentration region the calibration curves of iMGEFID and iMGESE closely resembled, whereas at higher concentrations a decrease of the slope of the calibration curves of iMGESE was observed, with the lowest slope related to the longest TE_{SE}. Furthermore, the deviation from linearity occured at lower HoMS concentrations when longer

TE_{SE} were used. The r_2^* relaxivities of HoMS in the low concentration range were 90.0±0.9 $s^{-1}mg^{-1}ml$, 88.6±0.2 $s^{-1}mg^{-1}ml$, 82.8±2.2 $s^{-1}mg^{-1}ml$ and 73.2±5.1 $s^{-1}mg^{-1}ml$ for iMGEFID, $iMGESE_{TE=8.2}$, $iMGESE_{TE=13.8}$ and $iMGESE_{TE=26}$, respectively. In the high concentration range the r_2^* relaxivities were r_2^*=89.3±2.8 $s^{-1}mg^{-1}ml$, r_2^*=79.7±0.9 $s^{-1}mg^{-1}ml$, r_2^*=68.3±4.0 $s^{-1}mg^{-1}ml$, r_2^*=45.0±3.2 $s^{-1}mg^{-1}ml$, for iMGEFID, $iMGESE_{TE=8.2}$, $iMGESE_{TE=13.8}$ and $iMGESE_{TE=26}$, respectively.

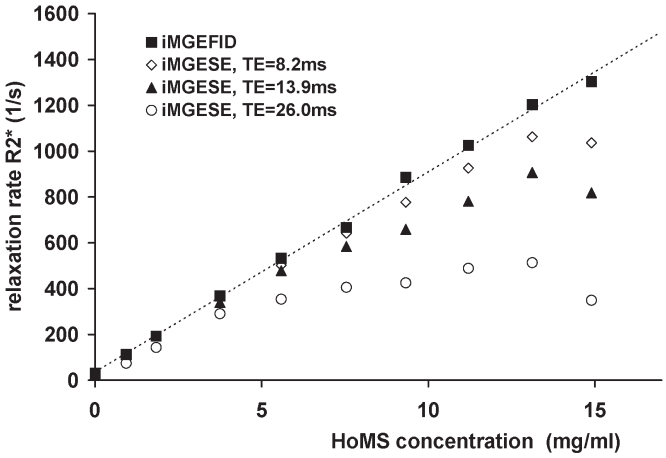

Figure 4 *Calibration curves of HoMS gel dilution series acquired with iMGEFID and iMGESE sampling schemes. For iMGESE sampling three different echo times were used: TESE=8.2ms, TESE=13.9 and TESE=26.0ms. The calibration curve belonging to iMGEFID demonstrates linear behavior over the entire concentration range, as indicated by the dotted straight line. At low concentrations the calibration curves of iMGEFID and iMGESE almost overlap, whereas at higher concentrations a decrease of the slope of the calibration curves of iMGESE is observed with the lowest slope related to the longest TESE. At the highest concentrations a decrease of the relaxation rates is demonstrated by the iMGESE data.*

Temperature dependence

Figure 5 shows the MR signal behavior of a HoMS gel sample ([HoMS]=3.7 mg/ml) acquired with both MGESE and MGEFID sampling strategies at three different temperatures (11°C; 23°C and 36°C). The presented signal behavior is representative for all HoMS concentrations. For MGEFID the signal behavior was nearly identical for all three temperatures, demonstrating monoexponential signal decay. The r_2^* relaxivity of HoMS determined with MGEFID were equal to 89.7±4.9 $s^{-1}mg^{-1}ml$, 90.6±4.1 $s^{-1}mg^{-1}ml$ and 93.7±5.3 $s^{-1}mg^{-1}ml$ for increasing temperatures. For MGESE, the effect of increasing the temperature was threefold. First, a further decrease of the SE peak was observed for increasing temperature. Second, an increase of the temperature caused the time period

of nonexponential signal decay to increase. Third, a decrease of the slope of the curve relating the log signal and TE_{SE} was observed, representing a decrease of the R_2^* relaxation rate (Figure 5). These observations were consistent for the entire concentration range of HoMS. The r_2^* relaxivities of HoMS determined with MGESE for increasing temperatures were 52.8±4.0 $s^{-1}mg^{-1}ml$, 45.7±1.6 $s^{-1}mg^{-1}ml$ and 32.0±2.2 $s^{-1}mg^{-1}ml$.

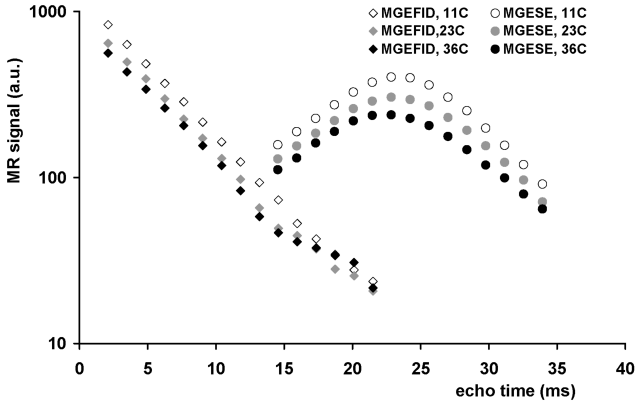

Figure 5 *The influence of diffusion on signal behavior of MGEFID and MGESE data investigated by varying the temperature (11; 23; 36 °C) of the HoMS gel dilution series. The signal behavior of the gel sample with a HoMS concentration of 3.7 mg/ml is shown. The MR signal (logarithmic scale) of MGEFID displays linear exponential behavior which is similar for samples at different temperatures. At lower signal values the MGEFID data deviate from exponential signal behavior, which may be caused by Rician distributed noise. MGESE data shows nonexponential signal behavior on both sides of the SE peak. For the higher temperature the slope is less steep, indicating a lower relaxation rate caused by an increase of diffusional motion associated with the higher sample temperature.*

HoMS susceptometry

Using the entire HoMS concentration range the volume susceptibility was determined which resulted in an average volume susceptibility of 0.58 ppm per mg/ml, which is equivalent to 829 ppm for the HoMS material.

Perfused liver model

Influence of the echo time

R_2^* maps of a rabbit liver with HoMS were derived from iMGEFID and iMGESE data and used to estimate the amount of HoMS present in an imaging slice. For iMGESE different echo times were used. Resulting R_2^* maps are shown in Figure 6, using different color scaling. In regions containing no or low concentrations of HoMS similar R_2^* values were found for iMGESE sampling with varying TE_{SE} and iMGEFID sampling.

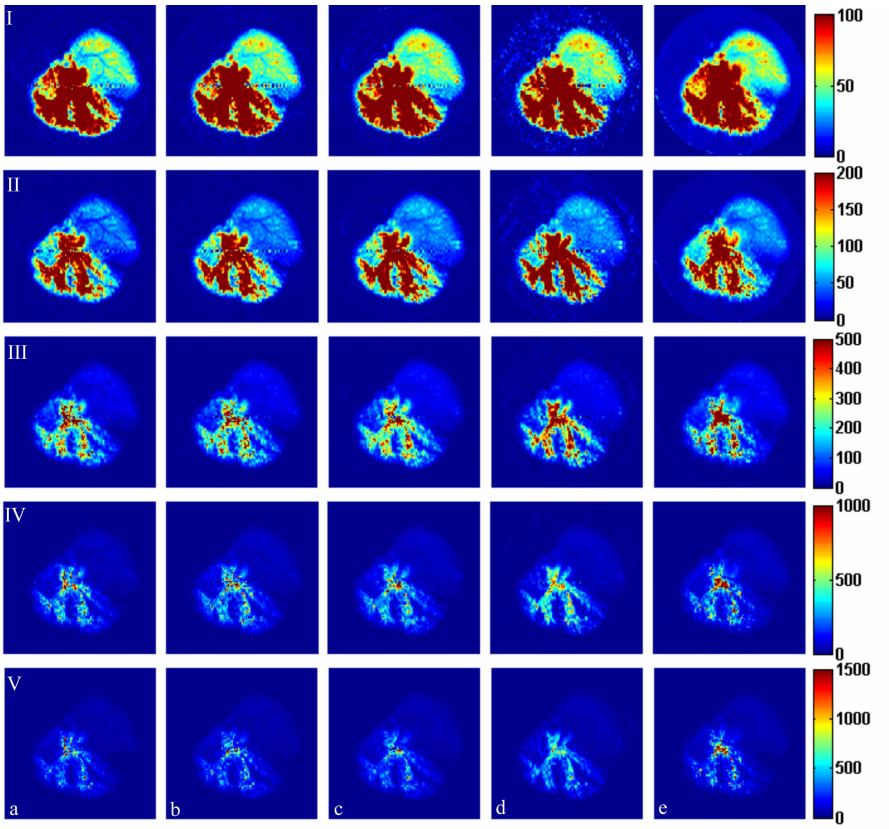

Figure 6 *R_2* maps of an excised rabbit liver with HoMS determined with iMGESE with different values for TE_{SE}; a) 35.0ms; b) 25.0ms; c) 13.9ms; d) 8.2ms and e) iMGEFID. Different color scaling is used in series I, II, III, IV and V, with maximum R_2* values in s^{-1} of 100, 200, 500, 1000 and 1500, respectively. Similar R_2* values were estimated in regions of liver tissue containing no or low concentrations of HoMS for both MGEFID and MGESE data, as shown in image series I and II. In regions containing high HoMS concentrations distinct differences are observed between iMGEFID and iMGESE data. The iMGEFID image (e) shows more pixels with a high R_2* values as shown in image series IV and V. Furthermore, the maximum R_2* value estimated with MGEFID is higher than the maximum R_2* value for MGESE and exceeds 1500 s^{-1} (For color figure see addendum).*

In regions containing high concentrations of HoMS lower R_2^* values were determined for all iMGESE experiments compared to MGEFID, decreasing with increasing TE_{SE}. For MGEFID experiments R_2^* values as high as 1500 s^{-1} were found. The total amount of HoMS present in this slice was estimated to be 43.8 mg, 43.7 mg, 37.5 mg, 33.6 mg and 30.1 mg for MGEFID and MGESE with TE_{SE} 8.2ms, 13.9ms, 26ms, and 35ms, respectively. This demonstrated an inverse relation between the estimated total amount of HoMS and the TE_{SE} for the (i)MGESE data.

In Figure 7 the estimated, total amount of HoMS administered to four excised and perfused rabbit livers is plotted against the total injected amount of HoMS. The underestimation as observed for the MGESE data was strongly reduced for all HoMS concentrations when using MGEFID. For administered doses of HoMS up to 70 mg the estimated and injected amounts of HoMS showed an excellent correspondence for MGEFID. At higher HoMS concentrations, however, a certain underestimation persisted.

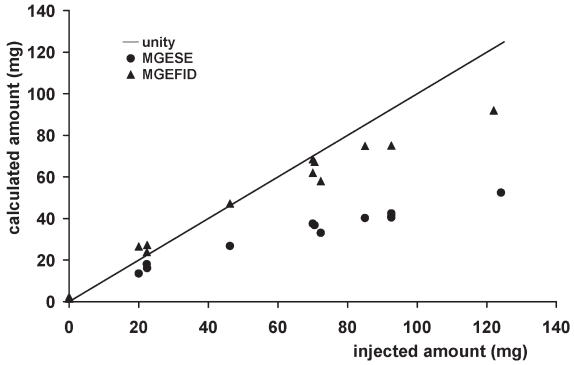

Figure 7 *Estimated versus injected amounts of HoMS in four excised and perfused rabbit livers, determined with MGEFID and MGESE sampling. Multiple successive injections were given followed by quantitative imaging. For administered doses of HoMS up to 70 mg the calculated and injected amounts of HoMS show a good correspondence. At higher HoMS concentrations an underestimation persisted.*

Discussion

MR signal behavior

The FID signals of the entire HoMS concentration range in the HoMS gel phantom showed monoexponential signal behavior (Figure 2a) for TE>2ms, as was predicted by the validity of the SD theory for MGEFID (Theory section). Recently, monoexponential signal decay was demonstrated for TE<2ms as well for HoMS suspended in agarose gel using ultrashort echo time imaging (21). The calibration curve acquired with iMGEFID showed linear behavior over the entire concentration range of HoMS as well (Figure 4). The transverse relaxivity of HoMS (r_2^*=89.3±2.8 $sec^{-1}mg^{-1}ml$) is in good correspondence with the literature (1, 4).

For MGESE, it has to be noticed that when the TE_{SE} is short enough so that Eq. 7 is satisfied, the system is expected to act according to the SD regime as well, meaning that the signal decay following the SE peak may be expected to be insensitive to diffusion providing an accurate estimate of the HoMS concentration.

However, for realistic values of TE_{SE}, the MR signal behavior of MGESE was expected to be sensitive to diffusion, because the SD regime criterion presented in Eq. [7] was violated. The MGESE experiments presented in this work confirmed these theoretical considerations. The signal behavior observed was nonexponential during a time period of several milliseconds on both sides of the SE peak. More specifically, both the time period of nonexponential signal behavior as well as the reduction of the SE peak as demonstrated by Figure 3 showed a dependence on the applied echo time during the SE experiment. Furthermore, the slope of the HoMS calibration curves and consequently the r_2^* relaxivity of HoMS was found to be dependent on the TE_{SE} (Figure 4). A strongly reduced r_2^* relaxivity of HoMS was observed for MGESE compared to MGEFID with an inverse relation between TE_{SE} and the r_2^* relaxivity of HoMS (Figure 4). Lastly, the MGESE calibration curves demonstrated nonlinear behavior. These experimental observations confirmed the theoretical prediction that the signal behavior of the HoMS system under investigation does not behave according to the SD regime when sampled with a MGESE strategy incorporating longer echo times, and is most likely influenced by diffusion.

As elaborated on in detail by Kennan et al. the conventional separation of contributions to transverse relaxation arising from static field effects and diffusion is not appropriate, since diffusive motion may induce averaging of the static field inhomogeneities, which causes a reduction of the decay rate in gradient echo images (11). It is this phenomenon that causes both the decrease of the SE peak as well as the damping of the T_2^* signal decay following the SE peak in MGESE sampling of the HoMS system. The longer echo times involved in MGESE sampling caused the average diffusion lengths of the water protons (diffusion length~$\sqrt{(D*TE_{SE})}$ (11)) through the dipolar field inhomogeneities at the moment of SE formation to increase. This increase of the average diffusion lengths leads to additional phase dispersion during SE formation (motional broadening). In a spin-sphere system close to static dephasing, additional phase dispersion at the moment of spin echo formation causes an increased signal loss as demonstrated by the lowered SE peak (Figure 3). For the multiple gradient echoes following the SE peak in a MGESE experiment, however, diffusing water protons through dipolar field inhomogeneities of HoMS, as opposed to static spins, caused averaging of the acquired phase, leading to damping of signal decay (motional narrowing) and consequently a decrease of the effective transverse relaxation rate (11, 13). For MGEFID sampling this was not observed because the average diffusion length of the moving spins was not sufficient to cause substantial averaging. The fact that the signal behavior of the FID differed from the signal behavior immediately

following the SE peak is a very important observation for quantitative purposes and confirms that a different relaxation regime may apply for a single spin-sphere system dependent on the pulse sequence timing parameters. The determination of the intrinsic relaxation rate R_2 using GESFIDE as proposed by Ma and Wehrli as well as the separation of R_2 and R_2' using GESSE as proposed by Yablonskiy et al. (5, 9, 22), both assuming the validity of the SD regime, may be complicated when the FID differs from the signal decay following the SE peak. The combination of a decreased R_2^* with an increased R_2 as observed for HoMS with MGESE sampling points in the direction of a different transverse relaxation model, viz. the slow diffusion regime (13, 14, 23).

Temperature dependence

The assumption that the echo time dependency of the MGESE sampling strategy originated from diffusion effects was confirmed by experiments in which the diffusion coefficient was directly changed by varying the temperature of the HoMS gel phantom, leading to an increase of the average diffusion length of the protons. In MGEFID experiments monoexponential signal decay was observed at all temperatures. The r_2^* relaxivity of HoMS did not significantly change with temperature, confirming the insensitivity of the MGEFID to diffusion in accordance with the SD regime. For MGESE, however, a deviation from exponential signal behavior was observed at all temperatures on both sides of the SE peak. The effect of increasing the temperature was twofold; a decrease of the SE peak and a decrease of the slope of the curve relating the log signal and TE_{SE}, which represented a decrease of the R_2^* relaxation rate (Figure 5). This was observed for all HoMS concentrations, ultimately leading to a decrease of the r_2^* relaxivity of HoMS with increasing temperature. These observations are in line with the phenomenon of signal decay damping caused by diffusion as explained in the previous section.

T_2^* relaxometry

A good correspondence is observed when comparing theoretically and experimentally determined R_2^* values for HoMS, which confirms that the HoMS system satisfies the SD condition for a MGEFID experiment. For a HoMS suspension of 1 mg/ml (ς=0.00071) the estimated increase of R_2^* (~R_2') according to Eq. [6] (assuming that the system satisfied the SD regime) is 91.8 s^{-1}, which closely resembles the experimentally determined value for HoMS using MGEFID for an increase of the HoMS concentration of 1 mg/ml: dR_2^*=89.3±2.8 s^{-1}. For a concentration of 14.9 mg/ml (ς=0.0106) an increase of the relaxation rate of dR_2^*=1377 s^{-1} was estimated according to Eq. [6]. At this concentration we

experimentally found an increase of the relaxation rate of dR_2^*=1303 s^{-1}. Notice that the calculated value is the theoretical maximum value of R_2' (6, 11). In case that the SD regime does not fully apply to this spin-sphere system, motional narrowing may cause a decrease of the R_2^* relaxation rate (11). This may account for the slightly lower value experimentally observed compared to the theoretically estimated value.

T_2^* relaxometry using the amplitude of S_0

Gradient echo times of conventional MGE sampling strategies are too long to adequately sample the fast signal decay associated with sub-millisecond T_2^* species (7), as introduced by high concentrations of HoMS (3). Hence, to quantify such high HoMS concentrations, we proposed the incorporation of the initial amplitude of the MR signal, S_0, in the fit procedure. Monoexponential signal decay was assumed in this method, which has been confirmed experimentally in this work. Since the time interval of quadratic exponential signal decay as predicted by the SD theory is only on the order of 0.01ms for HoMS, the assumption of monoexponential signal decay is acceptable. This implies that the amplitude of S_0 of tissue with and without HoMS may be expected to be similar, as long as the volume fraction is small, since S_0 scales with (1-ς) (6). Therefore, the value of S_0 estimated in a noninvolved region of the tissue of interest can be used for T_2^* relaxometry of both involved and noninvolved tissue in the region of interest. In Figure 2a the estimated value of $S_{0,est}$ is shown at t=0ms for the gel phantom, determined using the relation $S(t)=S_{0,est}.e^{-t.R2^*}$. This method was recently compared to quantitative ultrashort echo time imaging (qUTE), a method that allows echo times as short as 80 μs to image and quantify sub-millisecond T_2^* values (24). Similar results were found for the proposed method and qUTE when applied to T_2^* relaxometry of high concentrations of HoMS in gel and liver tissue, associated with very high relaxation rates (R_2^*>2000 s^{-1}). In this work, using a TE_{min}=2.1ms and a typical $SNR_{S0,est}$ equal to 60, the maximum R_2^* value possible to determine was on the order of $R_{2\ max}^* = \ln(SNR_{S0,est}/2)/TE_{min} = \ln(30)/0.0021 = 1620\ s^{-1}$.

HoMS quantification

Quantification of HoMS was done in both MGEFID and MGESE experiments using the true HoMS r_2^* relaxivity as determined with MGEFID. By doing so it is assumed that additional transverse relaxation is solely a result of dephasing due to static field inhomogeneities introduced by HoMS, which reduces the quantification problem to straightforward T_2^* relaxometry. For MGESE, however, the calibration curves appeared to be nonlinear, demonstrating similar r_2^* relaxivity as observed for MGEFID at low HoMS concentrations and short TE_{SE} and lower r_2^* relaxivity with increasing concentrations and TE_{SE} (Figure 4). The use of a nonlinear calibration

curve for quantification is problematic by definition and will always require compromises. The diffusion sensitivity of MGESE causes the calibration curve to be temperature dependent as well as dependent on the imaging parameters (TE_{SE}). Moreover, local changes in tissue diffusivity due to physiological changes in tumor tissue may require different HoMS r_2^* relaxivity values locally to allow accurate quantification, which would complicate the quantification problem in vivo even more. Therefore, a diffusion insensitive value was chosen for the HoMS r_2^* relaxivity to be used for T_2^*-based quantification.

The proposed fit algorithm for MGEFID sampling extended the upper limit of quantifiable R_2^* relaxation rates to at least 1620 s^{-1}, dependent on SNR and minimal TE (21). Using this procedure, MGEFID was shown to significantly reduce the underestimation of the integral amount of HoMS in a highly inhomogeneous biodistribution as observed in liver tissue when compared to MGESE based analysis (3). However, at the highest concentrations an underestimation is still observed (Figure 7). At these high concentrations clustering of particles may cause vessels to be completely filled leading to cylinder-shaped paramagnetic structures. The cylindrical shape induces sub-maximal signal loss compared to the spherical one and exhibits a geometrical dependency with respect to the B_0 field orientation, which may account for the underestimation still apparent (3, 6). Therefore, this geometrical dependence seriously complicates accurate T_2^* based quantification of the exact amount of HoMS. However, such high concentrations are not realistic knowing that on average 50 mg of HoMS are administered per 100g of liver tissue during HoMS radioembolization therapy (25), which corresponds to the weight of a rabbit liver. As shown in Figure 7. the currently used quantification methodology allowed accurate quantification of 50 mg of HoMS administered to a rabbit liver.

Relevance to (U)SPIO-labeled cells SPIO-labeled cells are generally considered to satisfy the SD criterion (15). As shown by simulations, a SPIO-labeled cell can be interpreted as a single entity with an average $\Delta\chi$ when observed from a region outside the cell (15, 26, 27). Since the diameter of the cells used for labeling are on the order of the diameter of holmium-loaded microspheres, similar signal behavior can be expected when the local magnetic dose ($LMD=\varsigma.\Delta\chi.B_0$) of a medium containing iron oxide-labeled cells is on the order of the LMD typical for holmium-loaded microspheres in a medium. The LMD of the cellular samples labeled with (U)SPIO's used by Bowen et al. varied between 0.7 and 16.9 µT (7-169 mG) at 4 Tesla, at volume fractions between 0.05% to 0.8%. Since the LMD of HoMS in the relevant concentration range of HoMS (1-20 mg/ml) varies between 0.86-17.1 µT at 1.5T, at volume fractions of 0.07% to 0.14% (Table II.), similar signal behavior may be expected as observed for HoMS. As a consequence,

one should be careful when quantifying ironoxide-labeled cells applying T2* relaxometry using MGESE sampling (7) or when separating R2 and R2' relaxation rate components using MGESE type of sequences (5, 9, 17).

In conclusion, MGEFID is the method of choice for T_2^*-based quantification of strongly inhomogeneous distributions of HoMS as observed in liver tissue. The challenges introduced by the relatively long minimal echo time as faced in conventional gradient echo imaging are successfully beaten using the proposed post-processing technique, incorporating the estimated value of S_0 in the fitting algorithm.

Furthermore, MGEFID sampling of HoMS was demonstrated by theory and experiment to satisfy in the SD regime, to exhibit exponential signal decay and to allow accurate T_2^*-based quantification of the total amount of HoMS present in a perfused rabbit liver model. MGESE sampling of the same HoMS system showed similar signal behavior for the shortest TE_{SE} used, however, in combination with longer echo times typically used in SE experiments, MGESE violated the SD criteria and exhibited diffusion sensitivity which caused nonexponential signal behavior and a strong underestimation of HoMS when used for T_2^*-based quantification. The difference in MR signal behavior between MGEFID and MGESE can be attributed to the fact that the validity of the SD regime in a SE experiment is not only dependent on the spin-sphere system itself, as it is for a FID experiment with its inherent short TE, but also on the pulse sequence timing parameters of the SE experiment.

Finally, we demonstrated on theoretical grounds that similar signal behavior as observed for HoMS may be expected for spin-sphere systems incorporating (U) SPIO labeled cells, which may complicate quantification of relaxation phenomena using R_2, R_2^* and R_2' relaxation rates in the presence of ironoxide-labeled cells, when investigated using MGESE strategies.

Acknowledgements

The authors would like to thank Remmert de Roos for technical assistance with the design and manufacturing of the gel phantoms. This work was supported by the Dutch Technology Foundation STW (06648).

References

1. Nijsen JF, Seppenwoolde JH, Havenith T, Bos C, Bakker CJ, van Het Schip AD. Liver tumors: MR imaging of radioactive holmium microspheres--phantom and rabbit study. Radiology **2004**;231(2):491-499.
2. Vente MA, Hobbelink MG, van Het Schip AD, Zonnenberg BA, Nijsen JF. Radionuclide liver cancer therapies: from concept to current clinical status. Anticancer Agents Med Chem **2007**;7(4):441-459.
3. Seppenwoolde JH, Nijsen JF, Bartels LW, Zielhuis SW, van Het Schip AD, Bakker CJ. Internal radiation therapy of liver tumors: qualitative and quantitative magnetic resonance imaging of the biodistribution of holmium-loaded microspheres in animal models. Magn Reson Med **2005**;53(1):76-84.
4. Seevinck PR, Seppenwoolde JH, de Wit TC, Nijsen JF, Beekman FJ, van Het Schip AD, Bakker CJ. Factors affecting the sensitivity and detection limits of MRI, CT, and SPECT for multimodal diagnostic and therapeutic agents. Anticancer Agents Med Chem **2007**;7(3):317-334.
5. Yablonskiy DA, Haacke EM. An MRI method for measuring T2 in the presence of static and RF magnetic field inhomogeneities. Magn Reson Med **1997**;37(6):872-876.
6. Yablonskiy DA, Haacke EM. Theory of NMR signal behavior in magnetically inhomogeneous tissues: the static dephasing regime. Magn Reson Med **1994**;32(6):749-763.
7. Lui W, Dahnke H, Lewis BK, Jordan EK, Banu N, Scheaffter T, Frank JA. Ultrasort T2* Relaxometry in iron labeled Tumors. In Proceedings of the 14th Annual Meeting of ISMRM, Seattle, Washington, USA, **2006**; p. 927.
8. Seevinck PR, Seppenwoolde J-H, Zwanenburg J, Bakker CJ. Ultradense sampling of FID and SE signals using an interleaved multiple gradient echo sequence for improved T2* mapping. In Proceedings of the 15th Annual Meeting of ISMRM, Berlin, Germany **2007**; p. 1786.
9. Yablonskiy DA. Quantitation of intrinsic magnetic susceptibility-related effects in a tissue matrix. Phantom study. Magn Reson Med **1998**;39(3):417-428.
10. Boxerman JL, Hamberg LM, Rosen BR, Weisskoff RM. MR contrast due to intravascular magnetic susceptibility perturbations. Magn Reson Med **1995**;34(4):555-566.
11. Kennan RP, Zhong J, Gore JC. Intravascular susceptibility contrast mechanisms in tissues. Magn Reson Med **1994**;31(1):9-21.
12. Weisskoff RM, Zuo CS, Boxerman JL, Rosen BR. Microscopic susceptibility variation and transverse relaxation: theory and experiment. Magn Reson Med **1994**;31(6):601-610.
13. Jensen JH, Chandra R. Strong field behavior of the NMR signal from magnetically heterogeneous tissues. Magn Reson Med **2000**;43(2):226-236.
14. Kiselev VG, Posse S. Analytical model of susceptibility-induced MR signal dephasing: effect of diffusion in a microvascular network. Magn Reson Med **1999**;41(3):499-509.
15. Bowen CV, Zhang X, Saab G, Gareau PJ, Rutt BK. Application of the static dephasing regime theory to superparamagnetic iron-oxide loaded cells. Magn Reson Med **2002**;48(1):52-61.
16. Nijsen JF, Zonnenberg BA, Woittiez JR, Rook DW, Swildens-van W, I, van Rijk PP, van Het Schip AD. Holmium-166 poly lactic acid microspheres applicable for intra-arterial radionuclide therapy of hepatic malignancies: effects of preparation and neutron activation techniques. Eur J Nucl Med **1999**;26(7):699-704.

17. Ma J, Wehrli FW. Method for image-based measurement of the reversible and irreversible contribution to the transverse-relaxation rate. J Magn Reson B **1996**;111(1):61-69.
18. Hilaire L, Wehrli FW, Song HK. High-speed spectroscopic imaging for cancellous bone marrow R(2)* mapping and lipid quantification. Magn Reson Imaging **2000**;18(7):777-786.
19. Le BD, Delannoy J, Levin RL. Temperature mapping with MR imaging of molecular diffusion: application to hyperthermia. Radiology **1989**;171(3):853-857.
20. Henkelman RM. Measurement of signal intensities in the presence of noise in MR images. Med Phys **1985**;12(2):232-233.
21. Seevinck PR, Bos C, Bakker CJ. Ultrashort T_2* relaxometry using conventional multiple gradient echo sampling with S0 fitting: validation with quantitative UTE (QUTE) imaging. In Proceedings of the 16th Annual Meeting of ISMRM, Toronto, Canada **2008**; p. 1419.
22. Yablonskiy DA, Reinus WR, Stark H, Haacke EM. Quantitation of T2' anisotropic effects on magnetic resonance bone mineral density measurement. Magn Reson Med **1997**;37(2):214-221.
23. Yung KT. Empirical models of transverse relaxation for spherical magnetic perturbers. Magn Reson Imaging **2003**;21(5):451-463.
24. Robson MD, Benjamin M, Gishen P, Bydder GM. Magnetic resonance imaging of the Achilles tendon using ultrashort TE (UTE) pulse sequences. Clin Radiol **2004**;59(8):727-735.
25. Vente MA, Nijsen JF, de Wit TC, Seppenwoolde JH, Krijger GC, Seevinck PR, Huisman A, Zonnenberg BA, van d, I, van Het Schip AD. Clinical effects of transcatheter hepatic arterial embolization with holmium-166 poly(L: -lactic acid) microspheres in healthy pigs. Eur J Nucl Med Mol Imaging **2008**.
26. Pintaske J, Mueller-Bierl B, Schick F. Numerical simulation of magnetic field distortions caused by cells loaded with SPIO nanoparticles. In Proceedings of the 14th Annual Meeting of ISMRM, Seattle, Washington, USA **2006**; p. 1811.
27. Ziener CH, Bauer WR, Jakob PM. Transverse relaxation of cells labeled with magnetic nanoparticles. Magn Reson Med **2005**;54(3):702-706.

Chapter 8

P.R. Seevinck, C. Bos, and C.J.G. Bakker

Submitted

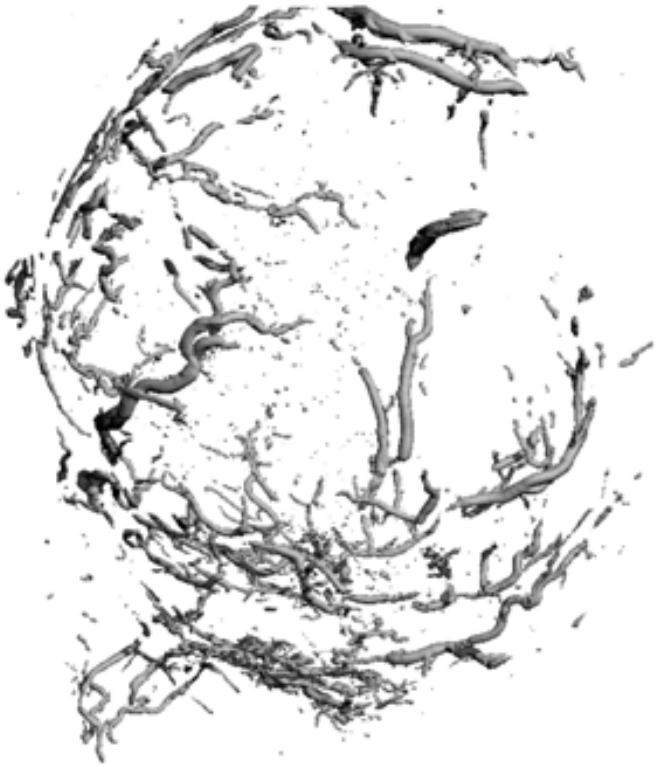

Ultrashort T_2^* relaxometry using conventional multiple gradient echo sampling with S_0 estimation: Validation with quantitative UTE (qUTE) imaging

Abstract

Purpose

To increase the upper limit of the detectable R_2^* range and hence the upper detection limit of the concentration of (super-) paramagnetic substances using multiple gradient echo sampling.

Materials and Methods

A post-processing method, S_0-fitting, was implemented to expand the detectable R_2^* range. S_0-fitting involves the incorporation of the estimated initial amplitude of the FID curve, S_0, in a monoexponential fitting algorithm. The method was applied to highly paramagnetic holmium loaded poly (L-lactic acid) microspheres (Ho-PLLA-MS) in vitro and ex vivo in rabbit livers. The accuracy and robustness of the S_0-fitting method were evaluated and results were compared qualitatively and quantitatively to R_2^* maps and regression curves obtained with quantitative ultrashort TE imaging (qUTE).

Results

Applying S_0-fitting dramatically increased the detectable R_2^* range as compared to conventional T_2^* relaxometry, up to 3000 s^{-1}. A good agreement was observed both quantitatively, for in vitro experiments, as well as qualitatively, for ex vivo rabbit liver experiments containing Ho-PLLA-MS, when validated with qUTE imaging. The influence of erroneously estimating S_0 was evaluated and demonstrated to be of minor concern.

Conclusions

S_0-fitting is a fast, robust and accurate post-processing method capable of estimating ultrahigh R_2^* values and, therefore, suitable for MR-based quantitative imaging of high concentrations of endogeneous and exogeneous (super-) paramagnetic substances. The method does not put any constraints on the MR pulse sequence as long as it is a MGE sampling scheme.

Introduction

An increased interest is observed in MR-based quantitative imaging of exogenous (super-) paramagnetic contrast agents, such as (U)SPIO's (1-4) and holmium loaded poly (L-lactic acid) microspheres (Ho-PLLA-MS) (5-7), as well as of endogenous (super-) paramagnetic substances, such as cardiac and hepatic iron depositions (i.e. hemosiderin and ferritin) in patients suffering from iron-overload diseases (8-12). Currently, the most widely accepted and employed imaging strategy for T_2^* relaxometry is multiple gradient echo (MGE) sampling of the free induction decay (FID). However, minimal echo times and intervals between successive gradient echoes in conventional MGE sampling schemes on clinical scanners are relatively long (~1ms). This limits the accuracy by which rapidly decaying signals can be sampled (4, 7, 9, 10) and complicates the quantification of high concentrations of paramagnetic substances, especially at higher magnetic field strengths. In practice, the upper limit of the detectable R_2^* ($R_2^*=1/T_2^*$) range and consequently of the detectable concentration of the paramagnetic substance is determined by the imaging parameters chosen, mainly by the minimal echo time (TE_{min}), the echo spacing (ES) (9, 13), and the parameters governing SNR.

To increase the upper limit of the detectable R_2^* range others investigated the use of dedicated imaging strategies capable of characterizing fast decaying MR signals. MGE sampling of spin echo (MGESE) was proposed since it allows sampling of a full echo and therefore the characterization of the entire SE signal decay time course (4, 7, 14). Recently, sampling of the decaying part of the SE by acquiring a series of shifted SE images was proposed as well, to characterize fast R_2^* decay (1). However, it was shown that diffusion may influence the signal decay time course of the SE in the presence of micron-sized strongly magnetized particles or cells, causing an increasing underestimation with increasing echo time, which makes accurate R_2^* based quantification of such particles or cells using a series of single SE error prone (1, 7, 15). A different imaging method initially proposed to depict high R_2 and R_2^* components is ultrashort echo time (UTE) imaging (16, 17). The reduced delay time between excitation and data acquisition characteristic for UTE imaging in combination with an interleaved acquisition scheme allows detailed assessment of the free induction decay (FID) of rapidly decaying components (18). This method, quantitative UTE (qUTE), was recently successfully applied to assess the distribution of paramagnetic Ho-PLLA-MS in vitro (5, 6). Although very suitable for in vitro and ex vivo validation studies, several aspects including the long scan times and the non-selective excitation typical for 3D UTE imaging make it less attractive for clinical practice.

In this paper, we present a post-processing strategy that expands the detectable R_2^* range and that provides an R_2^* estimate for all image voxels, irrespective of how fast the signal decays. The proposed method, S_0-fitting, is based on the incorporation of the estimated initial amplitude of the FID curve, S_0 (S at t=0ms), into the fitting algorithm. The method assumes monoexponential signal decay and uniform S_0 over the tissue of interest. S_0-fitting is applicable to any type of conventional MGE sampling strategy used for T_2^* relaxometry and does not put any constraints on the imaging sequence. Throughout this paper, the S_0-fitting method will be demonstrated for the particular case of Ho-PLLA-MS. First, monoexponentiality of signal decay introduced by Ho-PLLA-MS in an agarose gel phantom will be investigated using qUTE. Then, R_2^* regression curves obtained from conventional MGE data with and without S_0-fitting will be compared quantitatively to R_2^* regression curves obtained with qUTE. Next, the influence of the SNR on the detectable R_2^* range will be investigated. Finally, the accuracy and robustness of the S_0-fitting algorithm will be evaluated and results will be compared qualitatively and quantitatively to R_2^* maps and regression curves obtained with qUTE, both in vitro and in rabbit livers.

Methods

Phantom and specimen preparation

Ho-PLLA-MS gel phantom

Holmium loaded poly (L-lactic acid) microspheres (Ho-PLLA-MS) were prepared as described by Nijsen et al. (19), resulting in Ho-PLLA-MS with a density of 1.4 g/ml, size distribution of 20-50 µm (mean diameter 30 µm) after sieving. The holmium content of the Ho-PLLA-MS used in this work was 18.7% by weight. An agarose gel (2%) Ho-PLLA-MS dilution series with Ho-PLLA-MS concentrations ranging from 0 to 15 mg/ml was created, providing a wide range of R_2^* values. $MnCl_2.4H_2O$ was added to the native gel to increase the baseline R_2^* value ($R_{2\,gel}^*$~25 s^{-1}) to mimic liver tissue. Samples were sealed in tubes and placed parallel to the main magnetic field.

Ex vivo rabbit liver

An excised rabbit liver was stored in saline after removing the blood volume by extensive flushing. The hepatic artery was cannulated using a small injection tube. Qualitative MR imaging and R_2^* mapping was done prior to and after administration of 40 mg of Ho-PLLA-MS to the hepatic artery of an excised rabbit liver. After administration of Ho-PLLA-MS the liver was flushed extensively.

Data acquisition

MRI was performed on a 3T whole body scanner (Achieva, Philips Medical Systems, The Netherlands) using a birdcage headcoil. R_2^* estimation was done using three different MR imaging sequences, 1) conventional MGE sampling (cartesian) of FID, referred to as MGE sampling, 2) 3D ultrashort echo time (UTE) imaging with MGE (radial) sampling, referred to as UTE-MGE and 3) quantitative UTE (qUTE) sampling, which consists of a series UTE-MGE acquisitions in an interleaved fashion in which the entire read-out echo train is shifted systematically to ultra densely sample the decaying MR signal, as depicted schematically in Figure 1 (5, 6). The latter provides the most detailed signal characterization, however, at the cost of total acquisition time.

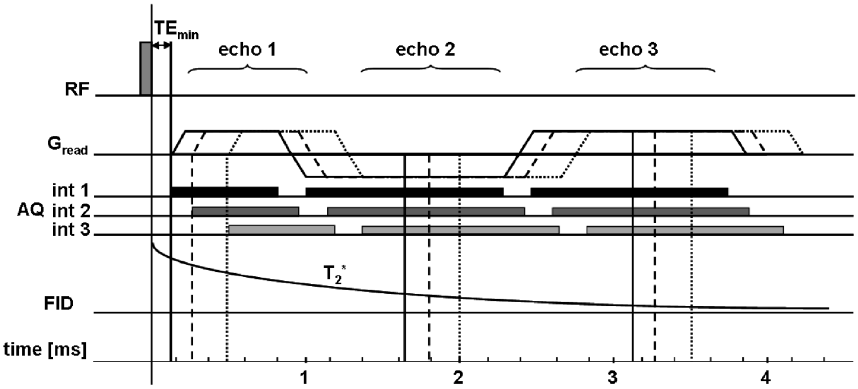

Figure 1 *3D qUTE sampling scheme, incorporating three gradient echoes and three interleaved acquisitions with shifted echo trains. The UTE acquisition (echo 1) is a half echo, the later echoes are full echoes. The echo time of the first echo is defined as the interval between the end of the RF excitation pulse and the beginning of the acquisition window. In this example, echo times of the three echoes of the first interleaved acquisition were 0.15 ms, 1.65 ms and 3.15 ms, resulting in an echo spacing of 1.50 ms. The complete second and third echo trains were shifted with respect to the first echo train over a time period of 0.15 ms and 0.35 ms, resulting in echo times of 0.3ms, 1.8ms, 3.3ms and 0.5ms, 2.0ms, 3.5ms, respectively. In practice, six interleaves were used, resulting in a densely sampled FID signal.*

Ho-PLLA-MS dilution gel phantom

To investigate FID signal behavior and to determine the r_2^* relaxivity of Ho-PLLA-MS, qUTE imaging was performed using an isotropic 3D radial sampling scheme with a FOV = 160^3 mm^3; scan matrix = 128^3; reconstruction matrix = 160^3; bandwidth per pixel = 867Hz and TR/ΔTE/flip = 13.5ms/1.5ms/10°. Seven gradient echoes were acquired. Six interleaves were applied with a minimal TE of, respectively, 0.15,

0.2, 0.3, 0.5, 0.8 and 1.2ms, allowing detailed assessment of the signal decay time course of fast decaying signals. Scan time of each interleave was 7 min, leading to a total scan time of 42 min.

The influence of the SNR on R_2^* estimation using both conventional weighted-least squares (WLS) fitting and S_0-fitting was investigated. For that purpose, 2D MGE sampling was performed with the following imaging parameters: FOV=160x160x5 mm^3; scan matrix=128^2; reconstruction matrix=160^2; bandwidth per pixel=867Hz and TR/TE_1/ΔTE/α = 35ms/1.43ms/1.20ms/35°. Fifteen gradient echoes were acquired. The SNR was systematically varied by changing the number of sample averages (NSA) over the range [1; 2; 4; 8; 16; 32]. The total scan time for NSA = 1 and NSA = 32 were 2.8 sec and 84.3 sec, respectively.

Ex vivo rabbit liver

MGE sampling was performed using a 3D acquisition scheme with FOV = 128x128x128 mm; scan matrix = 128x128x128; reconstruction matrix = 160^3, bandwidth per pixel = 867Hz and TR/TE_1/ΔTE/flip = 12.5ms/1.5ms/2.3ms/10°, acquiring five echoes without additional interleaves, resulting in a total scan time of 4 min 9 sec. Furthermore, UTE-MGE sampling was performed with similar FOV, scan matrix, reconstruction matrix and bandwidth per pixel as used for 3D MGE sampling. Imaging parameters included TR/TE_1/ΔTE/flip = 12.3ms/0.15ms/2.3ms/10°, acquiring five echoes without additional interleaves, resulting in a total scan time of 6 min 43 sec.

Data analysis

R_2^* estimation using conventional MGE data was done according to the following procedure. First, the noise (σ) of each magnitude image was determined in a region in the background, which was free from any residual signal on visual inspection, by determining the mean of the background (M_{BG}): $\sigma = M_{BG}/1.253$ (20). Then, for each image a SNR map was made according to SNR=S/σ. A monoexponential weighted least-squares (WLS) fitting algorithm, which weighs small and large signal amplitudes equally (21), was used to estimate R_2^* and S_0. A truncation model was used incorporating a threshold criterion to exclude longer echo time points with low SNR (SNR > 3 is included) (8) and prevent the influence of a Rician noise distribution in MR magnitude images at low SNR (22). In case that less than two data points fulfilled the truncation criterion, no R_2^* value was estimated. These pixels were assigned zero in the conventional R_2^* estimation algorithm.

To estimate R_2^* for pixels with very fast signal decay where conventional R_2^* estimation fails, S_0-fitting was applied, according to the following procedure. First, R_2^* maps were determined using conventional R_2^* estimation, providing reliable

R_2^* values in all areas without Ho-PLLA-MS. In these well-characterized areas the value of S_0 was estimated pixelwise by extrapolation of S to TE = 0 ms using the detemrined R_2^* value and assuming monoexponential signal decay. Next, all estimated values of S_0 were averaged per slice to provide one value for S_0 for each slice. In the problematic areas in which only one data point fulfilled the truncation criterion ($S(TE_{min})>3\sigma$ & $S(TE_2)<3\sigma$), the average S_0 value was used as the first data point, yielding an estimate of R_2^* equal to $R_2^* = \ln(S_0/S(TE_{min}))/TE_{min}$. In case that no data point fulfilled the truncation criterion ($S(TE_{min})<3\sigma$), a maximum R_2^* value was estimated and assigned to the particular pixel, according to $R_{2\ max}^* = \ln(S_0/3\sigma)/TE_{min}$. This procedure is summarized in Table 1.

Table 1 *R2* estimation procedures in for relatively slow, intermediate and fast decaying signals using conventional WLS fitting and/or S0 fitting.*

procedure	conventional fitting			S_0 fitting		
sign. decay	slow	intermediate	fast	slow	intermediate	fast
criterion	$S(TE_2)>3\sigma$	$S(TE_{min})>3\sigma$ & $S(TE_2)<3\sigma$	$S(TE_{min})<3\sigma$	$S(TE_2)>3\sigma$	$S(TE_{min})>3\sigma$ & $S(TE_2)<3\sigma$	$S(TE_{min})<3\sigma$
R_2^* estim.	WLS fitting	0 (nan)	0 (nan)	WLS fitting	$\ln(S_0/S(TE_{min}))/TE_{min}$	$\ln(S_0/3\sigma)/TE_{min}$

Ho-PLLA-MS dilution gel phantom

FID signal behavior and r_2^* relaxivity of Ho-PLLA-MS were investigated using mean ROI (225 pixels) data of the Ho-PLLA-MS dilution gel samples, acquired with qUTE, which was considered the gold standard. Pixelwise R_2^* estimation was done using MGE data with S_0-fitting and using UTE-MGE data with conventional WLS fitting. Resultant R_2^* values were displayed in regression curves and compared to the gold standard.

The robustness of the S_0-fitting algorithm was evaluated by exploring the influence of an erroneously estimated S_0 value on R_2^* estimation using S_0-fitting. With this goal in mind, the value of S_0 was varied systematically over a range of -25% to 25% relative to the actually determined value of S_0 prior to S_0-fitting. This dependence was investigated using the Ho-PLLA-MS gel dilution series for different acquisitions with varying SNR values (NSA = [2, 8, 32]). Results are shown in absolute R_2^* values and relative (in %) to the actual R_2^* values obtained with the correctly estimated S_0 value.

Ex vivo rabbit liver

R_2^* was estimated using conventional MGE data with and without S_0-fitting and

using UTE-MGE data acquired prior and post Ho-PLLA-MS administration. A difference R_2^* map was constructed by subtracting conventionally fitted and S_0-fitted R_2^* maps, so as to highlight areas with high R_2^* values which can not be characterized by the conventional WLS fitting algorithm. Furthermore, R_2^* maps obtained with S_0-fitting of MGE data were compared qualitatively to R_2^* maps obtained from UTE-MGE data.

Results

MR experiments: Ho-PLLA-MS dilution gel phantom

FID signal behavior

Densely sampled qUTE data (mean ROI data) was used to characterize the Ho-PLLA-MS induced signal decay in great detail over the entire MR signal range (from S_0 towards noise level). Monoexponential behavior was found as observed from the linear relation between log signal and echo time (Figure 2a) over a wide range of Ho-PLLA-MS concentrations ([1-15 mg/ml]) and a broad R_2^* range (25-3000 s^{-1}). A linear relation between R_2^* and Ho-PLLA-MS concentration was found as well (Figure 2b), representing an r_2^* relaxivity of 209 $s^{-1}.mg^{-1}.ml$ for Ho-PLLA-MS at 3T. Estimation of S_0 from these curves resulted in S_0=1341.1±64.7 a.u. (mean ± standard deviation), which means that the standard deviation of S_0 estimated for different samples was roughly 5% of the mean.

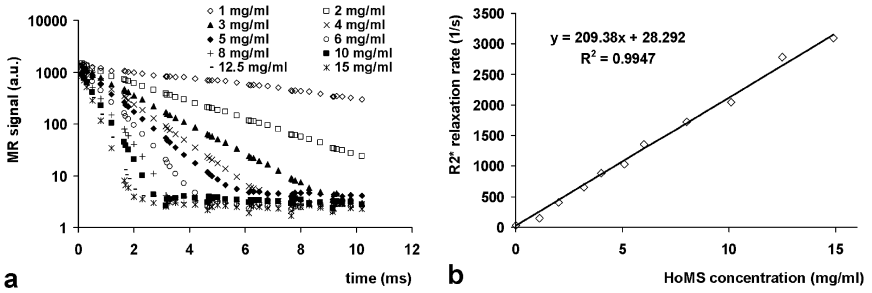

Figure 2 *a) Log MR signal (mean ROI) as a function of echo time for a range (1-15 mg/ml) of Ho-PLLA-MS homogeneously suspended in agarose gel. Data were acquired with a qUTE imaging sequence incorporating seven echoes with echo spacings of 1.5ms and six interleaves with first echo times of 0.15, 0.2, 0.3, 0.5, 0.8 and 1.2ms. A linear relation is observed for the log of the MR signal as a function of echo time for all echo times over the entire concentration range. b) A linear relation between R2* and Ho-PLLA-MS concentration is shown, representing an r2* relaxivity of 209 $s^{-1}.mg^{-1}.ml$ for Ho-PLLA-MS at 3T.*

The influence of SNR and S_0 fitting on R_2^* estimation

Both increasing SNR as well as applying S_0-fitting increased the upper value of the detectable R_2^* range. A maximum R_2^* value of about 1000 s^{-1} was characterized using conventional fitting of MGE data acquired with NSA = 1 (Figure 3a and 4a). Increasing the NSA from 1 to 32 led to increased SNR values of S_0 from 85 to 457, which was very close to the theoretically expected values (SNR α √NSA, see Table 2). The maximum R_2^* value increased from 1000 s^{-1} to about 1600 s^{-1} as a result of the increased SNR, which can be observed in the R_2^* map (Figure 3b) as well as in the regression curve (Figure 4a). A linear fit provided a Ho-PLLA-MS r_2^* relaxivity of 207 $s^{-1}.mg^{-1}.ml$ for pixelwise R_2^* estimation, which is similar to the r_2^* value determined using mean ROI data of a qUTE acquisition (r_2^* = 209 $sec^{-1}.ml^{-1}.mg.$). The standard deviation (sd) of the mean of the estimated R_2^* value increased with increasing Ho-PLLA-MS concentration and decreasing SNR (Figure 4b), which may be expected, since both lead to less data points available for exponential fitting.

Applying S_0-fitting on MGE data acquired with NSA = 1 and NSA =32 dramatically increased the estimated maximum detectable R_2^* value to about 2300 s^{-1} and 3000 s^{-1}, respectively (Figure 3c, 3d and 4c). A linear fit to the pixelwise analysed R_2^* values (NSA = 32) provided a Ho-PLLA-MS relaxivity of 201 $sec^{-1}.ml^{-1}.mg$. The sd of the mean of the estimated R_2^* value increased with increasing Ho-PLLA-MS concentration. However, the sd of the mean R_2^* value decreased for even higher Ho-PLLA-MS concentrations, due to the inclusion of S_0 in the fitting algorithm (Figure 4d). Since S_0 was a constant value, less variation in the estimated R_2^* value was expected. At even higher Ho-PLLA-MS concentrations the value $R_{2\ max}^*$ was assigned to an increasing number of pixels, which also causes less variation in the estimated R_2^* value in the gel samples.

Table 2 *Maximum estimated R_2^* value and theoretically expected and experimentally determined increase of SNR as a result of increasing NSA.*

NSA	SNR S_0	$R_{2\ max}^*$ (s^{-1}) (=$\ln(S_0/3\sigma)/TE_{min}$)	Experimentally determined increase in SNR	Theoretically expected increase in SNR (=sqrt(NSA))
1	85	2355	1.00	1.00
2	119	2592	1.40	1.41
4	169	2839	1.99	2.00
8	237	3077	2.79	2.83
16	337	3325	3.96	4.00
32	457	3539	5.38	5.66

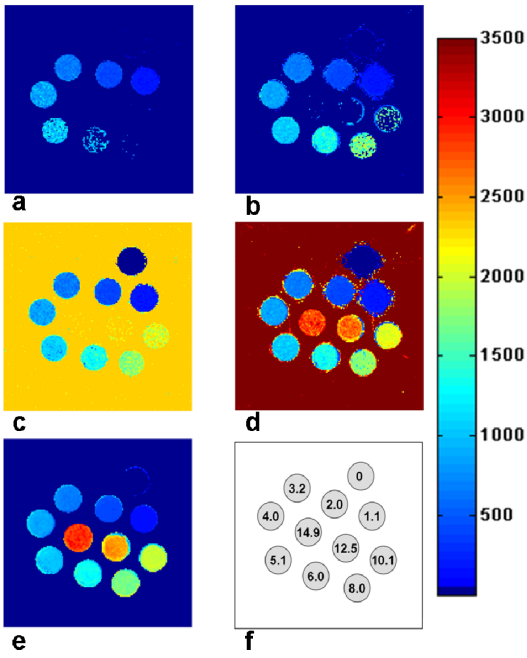

Figure 3 *R_2^* maps of the Ho-PLLA-MS dilution gel phantom determined with conventional R_2* estimation (a, b), with S_0-fitting (c, d) and using qUTE data (e). MGE data was acquired with low (a, c) and high SNR (b, d) by increasing the number of signal averages from 1 (a, c) to 32 (b, d). Increasing the SNR increased the detectable R_2^* range, both with conventional fitting (a, b) and with S_0-fitting (c, d). S_0-fitting dramatically increased the detectable R_2^* range compared to conventional WLS fitting (b, d). When using the S_0-fitting algorithm, the background was assigned the value of $R_{2\,max}^*$, as shown in c) and d). A good agreement is shown between the R_2^* map obtained from qUTE data and with high SNR data in combination with S_0-fitting (d, e). A schematic overview of the Ho-PLLA-MS concentrations in mg/ml is depicted in f) (For color figure see addendum).*

Pixelwise analyses of qUTE data provided an R_2^* map (Figure 3e) very similar to the R_2^* map obtained with S_0-fitting (Figure 3d). A Ho-PLLA-MS R_2^* relaxivity of 199 $s^{-1}.mg^{-1}.ml$ was determined using WLS fitting. The sd of the mean of the estimated R_2^* value showed a maximum value of 80 s^{-1} for higher Ho-PLLA-MS concentration which was less than half the sd observed for MGE data with and without S_0-fitting.

The influence of erroneous estimation of S_0 on R_2 estimation*

The influence of erroneously estimating S_0 on R_2* estimation using S_0-fitting was studied at different SNR values (SNR S_0 = [119, 237, 457]) by setting the NSA to 2, 8 and 32. Below R_2^* values of 1000 s^{-1}, erroneous estimation of S_0 had no influence on the estimated R_2^* value (Figure 5), due to the fact that S_0 was not utilized for R_2^* estimation, according to the criteria used in the S_0-fitting algorithm. For increasing R_2^*, changing the value of the S_0 led to a deviation of the estimated R_2^* value, which became apparent first at the lowest SNR (Figure 5d). The relative error in R_2^* first increased and at higher R_2^* values decreased again (Figure 5d). A variation of S_0 with -25% and +25% led to a deviation of the estimated R_2^* value of maximally -20% and +10% for NSA=2, -18% and +9% for NSA=8 and -15% and +8% for NSA=32, respectively.

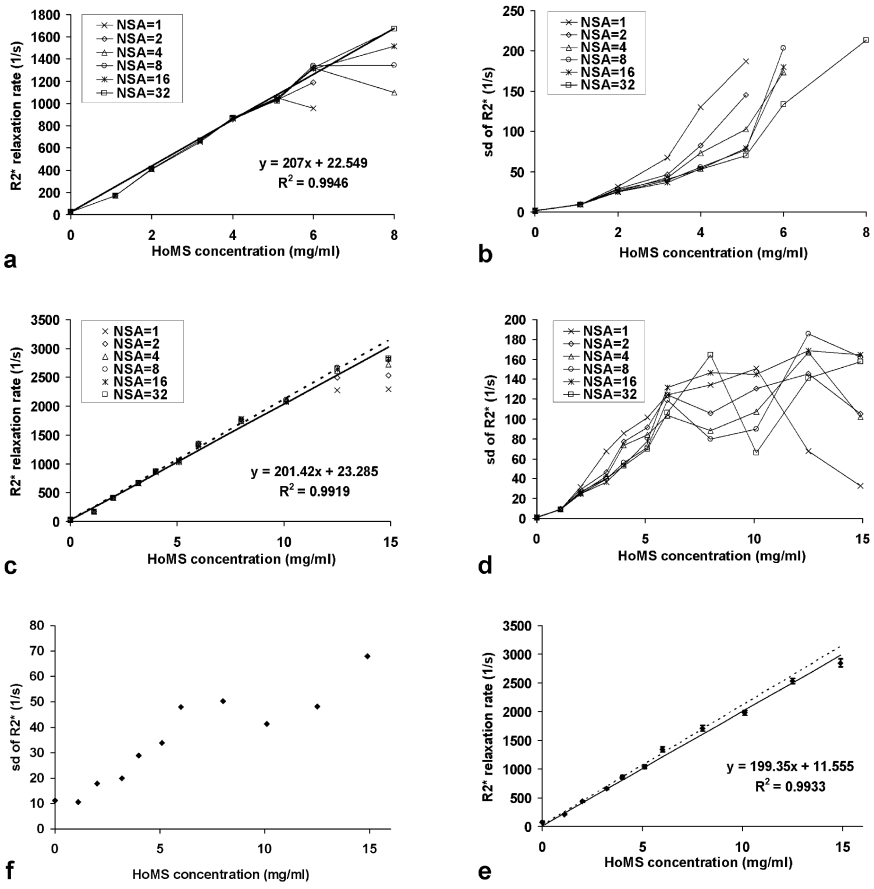

Figure 4 *R_2^* regression curves (a, c, e) showing a linear relation between R_2^* and Ho-PLLA-MS concentrations in agarose gel samples acquired using varying NSA (1, 2, 4, 8, 16, 32). Standard deviations of estimated R_2^* values are shown in b), d) and f). Regression curves obtained with conventional R_2^* estimation are shown in a), with S0-fitting on MGE data in c) and using qUTE data in e). The dotted lines in c) an e) represent the r_2^* relaxivity (= 209 $s^{-1}.mg^{-1}.ml$) as determined with qUTE ROI data (as presented in Figure 2).*

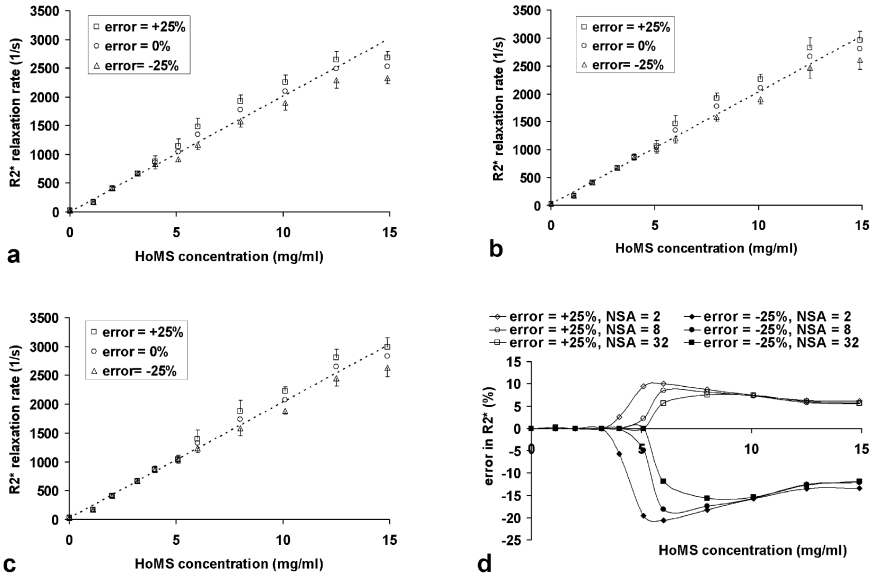

Figure 5 *The influence of erroneous estimating S_0 on R_2^* determination using S_0-fitting as a function of the Ho-PLLA-MS concentration is shown for different SNR values acquired with a) NSA=2, with b) NSA=8 and with c) NSA=32. The error in S_0 was set to -25%, 0% and +25% manually. The dotted lines in a), b) an c) represent the r_2^* relaxivity (= 201 $s^{-1}.mg^{-1}.ml$) as determined with S_0-fitting without S_0 error. The relative error in R_2^* for varying SNR as a function of the Ho-PLLA-MS concentration is shown in d).*

MR experiments: ex vivo rabbit liver

Pixelwise R_2^* estimation was done using MGE data with and without S_0-fitting and using UTE-MGE data acquired before and after administration of 40 mg of Ho-PLLA-MS to the ex vivo rabbit liver. Prior to Ho-PLLA-MS administration, constant signal intensity in the liver was shown by the first echo (at 1.5 ms) of the MGE image series (Figure 6a). The S_0 map (Figure 6b) and the R_2^* map (Figure 6c) also demonstrated fairly homogeneous signal intensity. After Ho-PLLA-MS administration, massive signal voids due to signal dephasing were observed at the locations where Ho-PLLA-MS was present (Figure 6d). A similar pattern was observed in the S_0 map (Figure 6e). On the UTE image (Figure 6i), signal dephasing was much less due to the very short echo time (0.15 ms); however, at the locations with very high concentrations the presence of Ho-PLLA-MS is still clearly visible by the lower signal intensity.

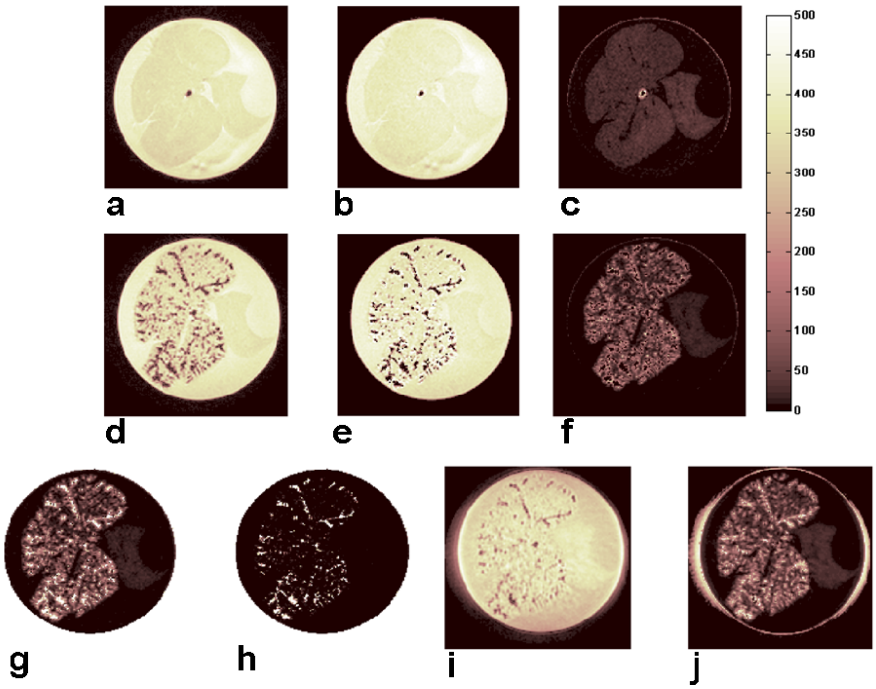

Figure 6 *First echo of a MGE series (a, d), S_0 (b, e) and R_2^* maps (c, f) of an ex vivo rabbit liver without Ho-PLLA-MS administered (a, b, c) and with 40 mg of Ho-PLLA-MS administered (d, e, f). Minimal echo time and echo spacing were 1.5 and 2.3 ms for MGE, respectively. Fairly homogeneous signal intensity in the liver is shown in the gradient echo image a), as well as in the S_0 map (b) and R_2^* map (c). The signal void in the center of the liver in a), b) and c) is a susceptibility artifact due to air in the catheter, which was located in the hepatic artery during imaging. The presence of Ho-PLLA-MS is clearly visible in the gradient echo image (d), as well as in the S_0 map (e). R_2^* estimation was not possible using a conventional R_2^* estimation, as shown by the signal voids in the R_2^* map (f). Applying S0-fitting did allow R_2^* estimation in these areas (g). The difference image between conventional fitting and S_0-fitting is depicted in h), mainly showing areas with very high R_2^*. A UTE image and corresponding R_2^* map is depicted in i) and j), respectively. Less signal dephasing is observed in the UTE image (TE=0.15ms) compared to the first echo of the MGE series (d), allowing R_2^* estimation using conventional WLS fitting, as shown in j). A good correspondence of the UTE-based R_2^* map (j) with the S_0-fitted R_2^* map (g) was observed.*

The influence of S_0 estimation on R_2^*maps

Regions containing relatively high concentrations of Ho-PLLA-MS, as concluded from UTE-MGE data, demonstrated a very low (<3σ) MR signal in the first gradient echo image of a MGE series. Therefore signal decay could not be characterized using conventional R_2^* estimation. These regions were depicted as black spots in Figure 5f, in which the maximum R_2^* values characterized were about 600 s^{-1}.

The R_2^* map determined using the S_0-fitting algorithm (Fig 6g,), showed a best estimate for all pixels, even for the problematic pixels demonstrating fast signal decay. The difference image between conventional fitting and S_0-fitting mainly highlighted regions with high R_2^* that could not be characterized by the conventional fitting algorithm (Figure 6h). A good correspondence was observed between the R_2^* map determined using the S_0-fitting algorithm and the R_2^* map obtained using the UTE-MGE data (Figure 6j).

Discussion

The potential of MRI to detect and quantify both endogenous and exogenous (super-) paramagnetic substances noninvasively is increasingly exploited in the last decade. However, high concentrations of these substances cause transverse signal decay to be so rapid that accurate signal characterization using conventional MGE sampling has become a difficult task, which is complicated even more by the trend to use higher magnetic field strengths. In this paper, a post-processing method was presented intended to expand the detectable R_2^* range towards higher values. The method, S_0-fitting, was demonstrated for the particular case of strongly paramagnetic Ho-PLLA-MS and evaluated on its accuracy, robustness and SNR dependenc S_0-fitting involves the estimation of S_0 to be incorporated in a monoexponential fitting algorithm. Estimation of S_0 of problematic areas was done using information obtained from well-characterized areas in the tissue of interest and was based on two assumptions. First, uniform S_0 over the tissue of interest was assumed, which will be discussed later in this paragraph. Second, monoexponential signal decay and linear relaxivity were assumed. For Ho-PLLA-MS, both monoexponential signal decay and linear relaxivity were demonstrated in vitro over a wide range of Ho-PLLA-MS concentrations ([1-15 mg/ml]) and a broad R_2^* range (25-3000 s^{-1}). To validate the S_0-fitting method, qUTE imaging was used; an interleaved radial MGE sampling strategy extremely useful for high R_2^* estimation due to its ultrashort echo times and sampling intervals (5, 6), providing densely sampled FID data. For Ho-PLLA-MS an r_2^* relaxivity of 209 $sec^{-1}.ml^{-1}.mg$ was obtained using mean ROI qUTE data and 199 $s^{-1}.mg^{-1}.ml$ (Figure 4e) for pixelwise analysed qUTE data. Pixelwise R_2^* estimation using conventional MGE data without S_0-fitting demonstrated monoexponential signal decay and linear relaxivity (r_2^* = 207 $s^{-1}.mg^{-1}.ml$) as well, however, on a smaller R_2^* range. S_0-fitting dramatically increased the detectable R_2^* range and provided a Ho-PLLA-MS relaxivity of r_2^* = 201 $s^{-1}.mg^{-1}.ml$ (Figure 4c), which was very similar to pixelwise qUTE analysis. R_2^* maps of ex vivo rabbit liver containing Ho-PLLA-MS calculated using conventional MGE data with and without S_0-fitting were compared

qualitatively to UTE-MGE R_2^* maps. R_2^* estimation using MGE data without S_0-fitting was unable to estimate R_2^* in areas with high Ho-PLLA-MS concentrations due to clustering. The S_0-fitting method, however, allowed R_2^* estimation in the entire tissue of interest and the estimated R_2^* map was in good agreement with the R_2^* maps estimated using UTE-MGE data.

The exponential fitting algorithm applied throughout this paper was based on a truncation model (8), incorporating a minimal threshold criterion to include data points to the fitting algorithm. This criterion was taken very strict, SNR>3, to prevent any influence of the Rician noise distribution of the MR magnitude signal at low SNR. At least two data points need to fulfill the threshold criterion to allow R_2^* estimation, otherwise R_2^* was set to zero. Less stringent criteria may seem to increase the detectable R_2^* range, however, it was shown in the literature that less stringent criteria may lead to an underestimation of the estimated R_2^* and will decrease the overall reliability of the R_2^*estimation (9). In this paper it was demonstrated that the upper limit of the detectable R_2^* range depends on the SNR of the first two data points. Increasing the NSA from 1 to 32 led to an increase of the upper limit of the detectable R_2^* range from 1000 s^{-1} to 1600 s^{-1}, respectively when using conventional R_2^* estimation. Similar observations were reported in literature, where the maximum detectable R_2^* value increased by decreasing the minimal echo time and the echo spacing, which are both indirect ways to increase the SNR of the first two data points (5, 6, 9, 17, 18).

To apply S_0-fitting, only a single measured data point needed to fulfill the threshold criterion, which was then used together with the estimated S_0 value to perform exponential fitting and R_2^* estimation. In case that signal decay was so rapid that even the first data point was below the SNR threshold, the value of $R_{2\,max}^*$ was assigned to the voxel. This calculated upper detection limit depended on the estimated value of S_0, the value of the threshold criterion (3σ) and the echo time of the first acquired sample point, TE_{min}, as was defined earlier (see Table 1: $R_{2\,max}^* = \ln(S_0/3\sigma)/TE_{min}$). For NSA equal to 1, 2 and 4, for example, the theoretically expected maximum R_2^* values were 2355 s^{-1}, 2592 s^{-1} and 2839 s^{-1} (Table 2), respectively, which is in good agreement with the experimentally determined upper detection limits of roughly 2300 s^{-1}, 2550 s^{-1} and 2730 s^{-1} (Figure 3c). For higher NSA values maximum R_2^* values close to 3000 s^{-1} were determined experimentally.

The influence of erroneously estimating S_0 on R_2^* estimation with S_0-fitting was investigated since it is known that S_0 uniformity in the tissue of interest, which is one of the main assumptions of the S_0-fitting algorithm, is likely to be violated due to inhomogeneous excitation and reception patterns. Although these effects

can be minimized using homogeneity correction methods, a variation in S_0 may still be expected. It was shown that underestimating S_0 caused a much smaller underestimation of R_2^* (Fig 5d). For example, an under- and overestimation of S_0 with 25% resulted in an under- and overestimation of R_2^* with -13% and +6%, respectively. Moreover, a 25% estimation error of S_0 is rather high; in this work a sd of 5% of the estimated mean S_0 value was found for agarose gel samples containing a wide range of Ho-PLLA-MS concentrations demonstrating a broad R_2^* range (25-3000 s^{-1}). Therefore, even smaller errors may be expected when using S_0-fitting for R_2^* estimation.

To further decrease the errors in R_2^* estimation as a result of under- and overestimation of S_0, the value of S_0 could be estimated pixelwise for the entire region of interest by fitting a smooth surface to the well-defined data points in each slice. In this way, local information of well-defined areas is taken into account when estimating S_0 in problematic areas.

As demonstrated in this work and in literature R_2^* estimation using conventional relaxometry applied to MGE images is often limited to R_2^* values below 1000 s^{-1}. This limits the maximum concentration of (super-) paramagnetic substances to which can be quantified image-based using MR. However, in several situations particularly the higher concentrations are of interest, for example to stage iron accumulation in iron-overload diseases (11, 12), in MR-based treatment planning, dosimetry and follow up of radioactive Ho-PLLA-MS in internal radiation therapy of liver malignancies (7, 23) and to quantitatively track the temporal and spatial migration of SPIO-labeled cells (1). Both methods proposed in literature intended to increase the detectable R_2^* range possess drawbacks. First, UTE based quantification methods are time-consuming and need non-selective excitation pulses. Second, characterization of R_2^* signal decay by sampling of the SE using either MGE (4, 7, 14, 24) or shifted SE (1) may be sensitive to diffusion due to the longer echo times typical for SE, leading to underestimation of the amount of paramagnetic substances present, as was shown recently (15). Lui et al observed an increasing underestimation of the amount of SPIO-labeled cells with increasing echo time, which may be well explained by the increasing diffusion sensitivity of their method with increasing echo time (1). Furthermore, the latter method only allows R_2^* estimation in case that R_2 is relatively low, which is the case in micron-sized paramagnetic particles such as Ho-PLLA-MS and clustered SPIO's in cells, however, which is violated for extracellular (U)SPIO (3). Finally, imaging times dramatically increase when applying shifted SE based techniques due to the longer repetition times and application of multiple interleaved acquisitions as was observed for qUTE as well (1). S_0-fitting may be extremely useful in providing

a best estimate of the total amount of paramagnetic substances in the cases just described, since it is based on MGE sampling of the FID, which makes it insensitive to diffusion, fast and generally applicable.

In conclusion, a post-processing method capable of estimation of ultrahigh R_2^* values is presented. The method does not put any constraints on the MR pulse sequence as long as it is a MGE sampling scheme, which makes it a fairly rapid quantification methodology. S_0-fitting is suitable for in vivo MR-based quantitative imaging of high concentrations of endogeneous (super-) paramagnetic substances such as cardiac and hepatic iron depositions in patients suffering from iron-overload diseases as well as of exogeneous paramagnetic contrast agents such as (U)SPIO's and holmium-loaded microspheres.

References

1. Liu W, Dahnke H, Rahmer J, Jordan EK, Frank JA. Ultrashort T2* relaxometry for quantitation of highly concentrated superparamagnetic iron oxide (SPIO) nanoparticle labeled cells. Magn Reson Med **2009**.
2. Dahnke H, Schaeffter T. Limits of detection of SPIO at 3.0 T using T2 relaxometry. Magn Reson Med **2005**;53(5):1202-1206.
3. Kuhlpeter R, Dahnke H, Matuszewski L, Persigehl T, von WA, Allkemper T, Heindel WL, Schaeffter T, Bremer C. R2 and R2* mapping for sensing cell-bound superparamagnetic nanoparticles: in vitro and murine in vivo testing. Radiology **2007**;245(2):449-457.
4. Lui W, Dahnke H, Lewis BK, Jordan EK, Banu N, Scheaffter T, Frank JA. Ultrashort T2* Relaxometry in iron labeled Tumors. In Proceedings of the 14th Annual Meeting of ISMRM, Seattle, Washington, USA, **2006**; p. 927.
5. Seevinck PR, Seppenwoolde J-H, Zwanenburg J, Bakker CJ. Ultradense sampling of FID and SE signals using an interleaved multiple gradient echo sequence for improved T2* mapping. In Proceedings of the 15th Annual Meeting of ISMRM, Berlin, Germany **2007**; p. 1786.
6. Seevinck PR, Bos C, Bakker CJ. Ultrashort T2* relaxometry using conventional multiple gradient echo sampling with S0 fitting: validation with quantitative UTE (QUTE) imaging. In Proceedings of the 16th Annual Meeting of ISMRM, Toronto, Canada **2008**; p. 1419.
7. Seppenwoolde JH, Nijsen JF, Bartels LW, Zielhuis SW, van Het Schip AD, Bakker CJ. Internal radiation therapy of liver tumors: qualitative and quantitative magnetic resonance imaging of the biodistribution of holmium-loaded microspheres in animal models. Magn Reson Med **2005**;53(1):76-84.
8. He T, Gatehouse PD, Kirk P, Mohiaddin RH, Pennell DJ, Firmin DN. Myocardial T(*)2 measurement in iron-overloaded thalassemia: An ex vivo study to investigate optimal methods of quantification. Magn Reson Med **2008**;60(2):350-356.
9. Ghugre NR, Enriquez CM, Coates TD, Nelson MD, Jr., Wood JC. Improved R2* measurements in myocardial iron overload. J Magn Reson Imaging **2006**;23(1):9-16.
10. Maris TG, Papakonstantinou O, Chatzimanoli V, Papadakis A, Pagonidis K, Papanikolaou N, Karantanas A, Gourtsoyiannis N. Myocardial and liver iron status using a fast T*2 quantitative MRI (T*2qMRI) technique. Magn Reson Med **2007**;57(4):742-753.
11. Anderson LJ, Holden S, Davis B, Prescott E, Charrier CC, Bunce NH, Firmin DN, Wonke B, Porter J, Walker JM, Pennell DJ. Cardiovascular T2-star (T2*) magnetic resonance for the early diagnosis of myocardial iron overload. Eur Heart J **2001**;22(23):2171-2179.
12. Wood JC, Enriquez C, Ghugre N, Tyzka JM, Carson S, Nelson MD, Coates TD. MRI R2 and R2* mapping accurately estimates hepatic iron concentration in transfusion-dependent thalassemia and sickle cell disease patients. Blood **2005**;106(4):1460-1465.
13. Song R, Song HK. Echo-spacing optimization for the simultaneous measurement of reversible (R2') and irreversible (R2) transverse relaxation rates. Magn Reson Imaging **2007**;25(1):63-68.

14. Gupta T, Virmani S, Neidt TM, Szolc-Kowalska B, Sato KT, Ryu RK, Lewandowski RJ, Gates VL, Woloschak GE, Salem R, Omary RA, Larson AC. MR Tracking of Iron-labeled Glass Radioembolization Microspheres during Transcatheter Delivery to Rabbit VX2 Liver Tumors: Feasibility Study. Radiology **2008**;249(3):845-854.
15. Seevinck PR, Seppenwoolde JH, Zwanenburg JJ, Nijsen JF, Bakker CJ. FID sampling superior to spin-echo sampling for T(2) (*)-based quantification of holmium-loaded microspheres: Theory and experiment. Magn Reson Med **2008**;60(6):1466-1476.
16. Robson MD, Gatehouse PD, Bydder M, Bydder GM. Magnetic resonance: an introduction to ultrashort TE (UTE) imaging. J Comput Assist Tomogr **2003**;27(6):825-846.
17. Robson MD, Benjamin M, Gishen P, Bydder GM. Magnetic resonance imaging of the Achilles tendon using ultrashort TE (UTE) pulse sequences. Clin Radiol **2004**;59(8):727-735.
18. Du J, Hamilton G, Takahashi A, Bydder M, Chung CB. Ultrashort echo time spectroscopic imaging (UTESI) of cortical bone. Magn Reson Med **2007**;58(5):1001-1009.
19. Nijsen JF, Zonnenberg BA, Woittiez JR, Rook DW, Swildens-van W, I, van Rijk PP, van Het Schip AD. Holmium-166 poly lactic acid microspheres applicable for intra-arterial radionuclide therapy of hepatic malignancies: effects of preparation and neutron activation techniques. Eur J Nucl Med **1999**;26(7):699-704.
20. Henkelman RM. Measurement of signal intensities in the presence of noise in MR images. Med Phys **1985**;12(2):232-233.
21. Wolfram.Mathworld. Wolfram.Mathworld. 2008.
22. Gudbjartsson H, Patz S. The Rician distribution of noisy MRI data. Magn Reson Med **1995**;34(6):910-914.
23. Nijsen JF, Seppenwoolde JH, Havenith T, Bos C, Bakker CJ, van Het Schip AD. Liver tumors: MR imaging of radioactive holmium microspheres--phantom and rabbit study. Radiology **2004**;231(2):491-499.
24. Schwenzer NF, Machann J, Haap MM, Martirosian P, Schraml C, Liebig G, Stefan N, Haring HU, Claussen CD, Fritsche A, Schick F. T2* relaxometry in liver, pancreas, and spleen in a healthy cohort of one hundred twenty-nine subjects-correlation with age, gender, and serum ferritin. Invest Radiol **2008**;43(12):854-860.

Chapter 9

P. R. Seevinck, K. L. Vincken, G. H. van de Maat, M.A. Viergever, and C. J.G. Bakker

Submitted

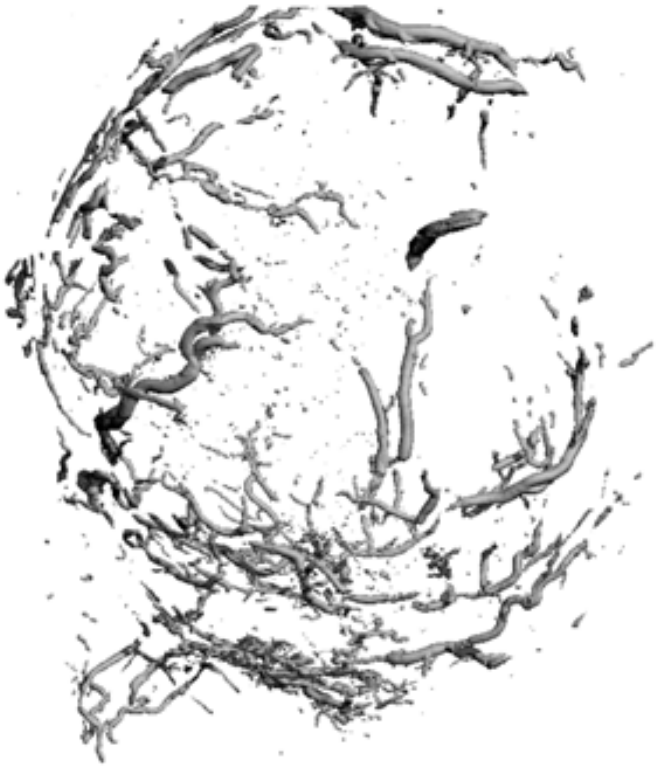

Predicting transverse relaxivity for MR-based quantification of strongly magnetized micron-sized particles or cells subjected to diffusion: theory, experiments and Monte Carlo simulations

Abstract

This paper demonstrated the feasibility to predict and quantify the signal decay time course of free induction decay (FID) and spin echo (SE) of diffusive media containing strongly magnetized impenetrable micron-sized particles by exploring and exploiting two well-known diffusion regimes, the static dephasing regime (SDR) and the strong field behavior (SFB). MR experiments and Monte Carlo simulations demonstrated that SDR and SFB enable accurate prediction of the signal decay time course of FID and SE when applied to a specific spin-sphere system, viz., holmium-loaded microspheres in an agarose gel matrix, while varying concentration, field strength and echo time. The applicability and restrictions of both theories were explored over a wide range of particle radii ($1\ \mu m < R < 100\ \mu m$) and susceptibility differences ($1\ ppm < \Delta\chi < 1000\ ppm$). MC simulations were used to validate SDR and SFB in predicting transverse relaxation and to verify their respective criteria of validity. Results suggest that by carefully choosing imaging and timing parameters, accurate prediction of signal decay as well as quantification of paramagnetic particles such as iron-labeled microspheres or cells and large endogenous iron accumulations is feasible using the either SDR or SFB, depending on the criteria of validity of both diffusion regimes.

Introduction

Quantitative magnetic resonance imaging of strongly magnetized micron-sized particles, clusters or cells in biological tissues has been studied since the advent of MRI (1-11). Some topical subjects include in vivo tracking of the spatiotemporal distribution of iron labeled cells with MRI to quantitatively assess cellular therapies, cell based tissue repair and cell viability (6, 7, 12-14). Furthermore, quantitative assessment of the biodistribution of (super-)paramagnetic microspheres, either labeled with holmium (8, 15) or iron (5), is currently being investigated for treatment planning of both chemo-embolization (16) and radioembolization (5, 8, 17) of hepatic malignancies. Another challenging application involves quantitative assessment of endogeneous super-paramagnetic particulate structures such as clustered ferritin in iron overload diseases (3).

Most often, MR-based quantification of (super-)paramagnetic cells, microspheres or clusters is accomplished by analyzing the NMR signal decay time course of Free Induction Decay (FID) or Spin Echo (SE) using T_2^* and T_2 relaxometry, respectively. Assuming monoexponential signal decay and linear transverse relaxivity allows voxel-based determination of the local concentration of the (super-)paramagnetic particles. This may seem a straightforward procedure at first sight, however, the abundance and versatility of relaxation theories presented in literature in the last two decades, aiming to model NMR signal formation in diffusive media containing strongly magnetized particles, demonstrates the complexity of the subject. An essential aspect to be aware of when deciding on which imaging strategy and relaxation model to apply in order to perform accurate quantitative imaging is the possible influence of diffusion on the signal decay time course (18, 19). The choice of diffusion regime is often made based on specific biophysical properties of the system under investigation, such as the diffusion coefficient (D), particle radius (R), susceptibility difference ($\Delta\chi$) and magnetic field strength (B_0). The two limiting cases, in which diffusion may either play a dominant or a negligible role, are known as motional narrowing regime (MNR) (1) and static dephasing regime (SDR) (20), respectively. Additionally, several intermediate diffusion regimes have been described in literature as well (21-24). Incorrect assumption of the validity of a diffusion regime may have a major impact on the outcome of the quantification procedure. For example, recently Liu et al. used a series of shifted SE images, to quantify high concentrations of iron-labeled cells in a rat tumor model and reported an underestimation of the R_2^* relaxation rate as compared to a FID based quantification method (7). Seppenwoolde et al. performed T_2^* relaxometry to estimate the local amount of holmium-loaded microspheres (HoMS) present in liver tissue using a Gradient

Echo Sampling of SE (GESSE (25)) sequence (15). In both cases an underestimation was observed. Due to the fact that both systems did satisfy the SDR, according to the well-known SDR criterion (20), the possible influence of diffusion was ignored. However, a thorough investigation of the literature could have revealed that for SE experiments, an additional, more strict criterion should be met for the static dephasing regime to apply (26). Therefore, the influence of diffusion, which may cause an underestimation in the mentioned situations (8), should not have been neglected beforehand.

These examples clearly illustrate the existing gap between relaxation theories, which aim to describe NMR signal behavior in magnetically heterogeneous systems, and clinical practice, in which these theories are applied for quantification using relaxometry. The rather esoteric character of many theoretical publications dealing with NMR signal behavior (1, 2, 4, 20, 21, 23) may be an important cause for the continued existence of this gap. Additionally, the versatility in terminology as well as the different unit systems applied by different groups, make comparison of the various theories and valuation for a specific application a challenge by itself. As a result, important findings presented in these theoretical investigations may be overlooked and remain unknown in clinical practice.

In this paper we aim to bridge the gap between theory and clinical practice by demonstrating how two relaxation theories may be interpreted and applied to predict and quantify the signal decay time course of FID and SE of diffusive media containing strongly magnetized micron-sized particles or cells. For this purpose, SDR and the theory of strong field behavior (SFB) were selected from the spectrum of diffusion regimes, based on their respective criteria of validity. It will be shown that by selecting a specific imaging strategy and dedicated imaging parameters, the investigator can choose to either suppress or emphasize specific biophysical phenomena to gain favorable circumstances for MR-based quantification. In order to demonstrate how the criteria of validity as proposed by SDR and SFB may be applied to predict transverse relaxation of the spin-sphere system under investigation and to facilitate accurate quantification, the following steps will be taken: First, both relaxation theories, SDR and SFB, will be presented, with an emphasis on their criteria of validity and on prediction of FID and SE signal behavior. Then, a representative spin-sphere system is chosen, viz. micron-sized paramagnetic holmium-loaded microspheres in an agarose gel matrix, to investigate NMR signal behavior of both FID and SE as a function of microsphere concentration, field strength and echo time. Experimental results will be used to validate the in house-built Monte Carlo simulation software. Once validated, Monte Carlo simulations, which are independent of criteria of validity, will be

performed over a wide and relevant range of microsphere radii and susceptibility differences, to investigate the predictive value of SDR and SFB and the correctness of their respective criteria of validity.

Theoretical background

The presence of paramagnetic particles in a strong magnetic field induces magnetic field variations, which leads to a loss of phase coherence in an aqueous medium, thereby causing intravoxel dephasing and signal loss in a FID experiment. The limiting case in which NMR signal decay is fully determined by static magnetic field variations and diffusion does not play a role is described by SDR (20). This type of signal loss, which may be regarded as a ceiling imposed on the increase of the transverse relaxation rate (R_2^*) due to the presence of the strongly magnetized particles (2), is reversible with respect to a 180° refocusing pulse in a SE experiment.

On the other hand, when spins experience different magnetic field strengths during the imaging experiment as a result of diffusive motion within an inhomogeneous magnetic field, averaging of stochastic phase modulation in space and time narrows the phase distribution while causing a loss of phase memory. This leads to a decrease of the transverse relaxation rate, R_2^*, observed during FID experiments and an increase of the transverse relaxation rate, R_2, observed during SE experiments (1, 8, 21-23). Accordingly, diffusion has a temporal damping effect on the influence of static magnetic field variations on the phase coherence of spins in the vicinity of strongly magnetized particles (8, 22).

Transverse relaxation theory: diffusion regimes

In this paper, it was chosen to investigate the FID and SE signal decay of a diffusive medium containing strongly magnetized impenetrable micron-sized spheres in perspective of the static dephasing regime (SDR) and the theory of strong field behavior (SFB). The latter may be interpreted as a diffusion regime dominated by SDR, however, possible influence of diffusion is taken into account (21). Therefore, this regime is sometimes called the slow diffusion regime (24). The validity of diffusion regimes is often characterized by two parameters: the characteristic diffusion time or correlation time, τ_D (or dynamic frequency scale, $\omega_D=1/\tau_D$), and the magnetic frequency scale, $\delta\omega$. The correlation time approximately represents the time required to diffuse past the magnetic perturber. The magnetic frequency scale characterizes the change in nuclear precession in the equatorial magnetic field of the perturber. For spherical objects, τ_D and $\delta\omega$ are defined as (1),

$$\tau_D = R^2 / D \quad [1]$$

$$\delta\omega = \gamma \cdot B_{eq} \quad [2]$$

with B_{eq}

$$B_{eq} = \Delta\chi \cdot B_0 / 3 \quad [3]$$

Based upon the relative magnitude of the dynamic frequency scale and the magnetic frequency scale, the relaxation behavior of a spin-sphere system can be categorized. In the following two sections, the NMR signal decay models and the criteria of validity of both SDR and SFB will be briefly outlined.

The static dephasing regime

The magnetically inhomogeneous systems under investigation contain relatively large and strongly magnetized particles and therefore satisfy the general SDR criterion ($\delta\omega\cdot\tau_D >> 1$), indicating that the influence of diffusion on the signal decay may be ignored. Particularly for spherical particles this criterion was stated more precisely to include the influence of the volume fraction ς (20):

$$(\delta\omega \cdot \tau_D) / (6 \cdot \varsigma^{-1/3}) >> 1 \quad [4]$$

Under SDR conditions, the NMR signal decay is determined by the frequency distribution in the volume of interest, also called the density of states (27). For a volume of interest containing one magnetized sphere, the density of states is determined by a single dipolar field distribution which is not Lorentzian, which means that the signal decay is not monoexponential (4, 27-29). However, for a random distribution of a large number of magnetized spheres within a voxel in a diffusive medium, some averaging over magnetization and dipole location may be expected, which yields an approximately Lorentzian phase distribution and hence monoexponential signal decay (4, 28, 30). The NMR signal decay of a FID experiment of magnetically inhomogeneous systems under SDR conditions can therefore be modeled using the following expression for the reduced signal $\widetilde{S}(t)$ (26):

$$\widetilde{S}(t) \propto \exp[\varsigma] \cdot \exp[-R_2^* \cdot t] \quad for \;\; t > 1.5 t_c \quad [5]$$

where R_2^* equals the sum of the increase of the intrinsic relaxation rate R_2 and the external relaxation rate R_2' due to static field effects, i.e., $R_2^* = R_2 + R_2'$. For SE experiments (26),

$$\widetilde{S}(t) \propto \exp[\varsigma] \cdot \exp[-R_{2\_}^{*} \cdot (t - TE)] \quad for \;\; TE/2 < t < TE - 1.5t_c \qquad [6]$$

$$\widetilde{S}(t) \propto \exp[\varsigma] \cdot \exp[-R_{2}^{*} \cdot (t - TE)] \quad for \;\; t > TE + 1.5t_c \qquad [7]$$

with $R_{2\_}^{*} = R_2 - R_2'$.

The characteristic time t_c, separates a region of quadratic exponential signal decay (short time scale) from a region with linear exponential signal decay (long time scale) and depends solely on the system's geometry (26):

$$t_c = (\eta \cdot \pi \cdot \gamma \cdot \Delta\chi \cdot B_0)^{-1} \qquad [8]$$

with η=2/(9√3) in SI units. When applied to strongly magnetized micron-sized particles such as HoMS and iron-labeled cells, t_c < 0.1ms (7, 8, 20), from which it can be concluded that the systems under investigation in this paper act in the long time scale as described by Equations [5-7]. Since the additional irreversible contribution of spin-spin relaxation due to the presence of the magnetized particles is considered to be negligible under SDR conditions (9, 22), it may be expected for a FID experiment that the transverse relaxation rate R_2^* of the reduced signal is equal to the reversible contribution, R_2'. Using the prediction for R_2' due to local field inhomogeneities introduced by magnetic perturbers as described by Yablonskiy and Haacke (20), the following expression for R_2^* is obtained

$$R_2^* \approx R_2' = \varsigma / t_c = \varsigma \cdot \eta \cdot \pi \cdot \gamma \cdot \Delta\chi \cdot B_0 \qquad [9]$$

When assuming a linear relation between R_2^* and particle concentration, the r_2^* relaxivity (in [$s^{-1}.mg^{-1}.ml$]) can be calculated using Eq. [9], by dividing R_2^* by the concentration:

$$r_2^*(\Delta\chi, B_0, \rho) \approx (\eta \cdot \pi \cdot \gamma \cdot \Delta\chi \cdot B_0)/\rho \qquad [10]$$

with ρ = C/ς, ρ the density of the particle material and C the particle's concentration. Although considered to be generally applicable, the SDR criterion in Eq. [4] is only sufficient for an FID experiment (26). For a SE experiment an additional, less known and more strict criterion should be met to satisfy SDR conditions, which is given in Eq. [32] in the work of Yablonskiy (26). Using Eq. [9], this SDR criterion specific for SE experiments can be rewritten as follows:

$$TE_{SE} << TE_c = 2.9(\tau_D \cdot t_c^2/\varsigma)^{1/3} \quad [11]$$

Here TE_{SE} represents the echo time of the SE experiment and TE_c the critical echo time. From this criterion, it becomes clear that the validity of the SDR in a SE experiment does not only depend on the spin-sphere system itself, as it does for a FID experiment, but also on the echo time of the SE experiment.

The strong field behavior

The theory of the strong field behavior (SFB), as proposed by Jensen and Chandra (21), predicts the behavior of the FID and SE signal decay time course of magnetically heterogeneous tissues and takes into account the possible influence of diffusion. SFB closely relates to SDR as proposed by Yablonskiy and Haacke (20) and the extended version by Kiselev and Posse (23) to include the influence of diffusion. The theory of the SFB predicts the reduced signal induced by the combined influence of static magnetic field inhomogeneities and diffusion, and takes into account the influence of the echo time on the validity of the theory. When applied to magnetized compact objects (e.g. microspheres, labeled cells) in a diffusive medium, the following length (L_1, L_2) and time scales (τ_0, τ_1, τ_2, τ_d) are defined to characterize the system and its criteria of validity:

$$L_1 = V_0^{1/3}; \quad L_2 = \left(\frac{V_0}{\varsigma}\right)^{1/3} \quad [12]$$

with V_0 the average object volume. The length L_1 reflects the average size of the objects, while L_2 reflects the average distance between the centers of adjacent objects.

$$\tau_1 = \frac{L_1^2}{D}; \quad \tau_2 = \frac{L_2^2}{D} \quad [13]$$

The time τ_1 is roughly the time it takes for a spin to diffuse past one of the magnetized objects, while τ_2 is roughly the time it takes for a spin to diffuse from the vicinity of one object to the vicinity of a neighboring object. Similar to SDR, SFB also defines a parameter incorporating the maximum magnitude of the magnetic field disturbances (in SI units):

$$\tau_0 = \frac{1}{\gamma|\Delta\chi|B_0} \quad [14]$$

Of principal importance in the SFB is the decay time τ_d, which represents the time t for a FID experiment (and TE_{SE} for a SE experiment), necessary for the

magnitude of the reduced signal $\widetilde{S}$ to change significantly from its initial value of 1. For a FID experiment, τ_d is defined as the solution to the equation

$$\left|\widetilde{S}(\tau_d)\right| = e^{-1} \qquad [15]$$

which means that $\tau_d = T_2^*$, in the case of monoexponential signal decay. For a SE experiments, a similar rationale yields $\tau_d = T_2$. For a spin-sphere system to behave according to SFB, the following, criterion should be met

$$\tau_d << \tau_1 \qquad [16]$$

A less strict criterion, which was reported to be sufficient as well, was obtained by replacing τ_1 by τ_2 in Eq. [16] (21). Eq. [15] and [16] imply that for SFB to apply, signal loss due to static dephasing should dominate dephasing due to dynamic effects. Since Eq. [15] implies that $\tau_d = T_2^*$ for FID, Eq. [16] can be rewritten as follows: $1/T_2^* = R_2^* >> 1/\tau_1$. This relation will be used in the RESULTS section.

When a magnetically inhomogeneous spin-sphere system fulfills SFB conditions, the magnitude of the reduced signal of FID and single SE signal decay can be described as follows (21):

$$\widetilde{S}(t) \approx \left|\exp[-\varsigma(k_1 - ik_2)t/\tau_0]\right| = \exp[-t \cdot k_1 \cdot \varsigma\gamma\Delta\chi B_0] \text{ for FID} \qquad [17]$$

$$\widetilde{S}(TE_{SE}) \approx \exp[-\varsigma \cdot k_3 (TE_{SE}{}^3/12\tau_0^2\tau_1)^{3/8}] \text{ for SE} \qquad [18]$$

with

$$k_1 = \eta \cdot \pi = 2\pi/(9\sqrt{3}) \approx 0.4031 \qquad [19]$$

$$k_2 \approx 0.0533 \qquad [20]$$

$$k_3 \approx 2.2184 \left\langle \left(\frac{V_n}{V_0}\right)^{3/4} \right\rangle_{obj.} \qquad [21]$$

with V_n the volume of the nth object. Using Equations [17-21] it is possible to predict the transverse relaxation of FID and SE experiments of systems that fulfill the SFB criterion. When assuming a linear relation between R_2^* and concentration, the r_2^* relaxivity can be calculated using Eq. [17], by dividing the exponent by the concentration C and the time variable t and by substituting C = ςρ, with ρ the particle density:

$$r_2^*(\Delta\chi, B_0, \rho) = t \cdot k_1 \cdot \varsigma\gamma\Delta\chi B_0 / (C \cdot t) = k_1 \cdot \gamma\Delta\chi B_0 / \rho \qquad [22]$$

Using Eq. [22] to predict R_2^* results in the exactly the same R_2^* value as predicted by SDR using Eq. [10].

Under SFB conditions, the r_2 relaxivity for single SE can be calculated by dividing the exponent in Eq. [18] by the concentration and the time variable TE_{SE}. However, since the exponent in Eq. [18] depends on the TE_{SE} nonlinearly, the r_2 relaxivity is different for each value of TE_{SE}. Therefore, the r_2 relaxivity linearized at a specific echo time can be determined as follows:

$$r_2(\Delta\chi, B_0, \rho, TE_{SE}) = \varsigma \cdot k_3 (TE_{SE}^{\ 3} / 12\tau_0^2\tau_1)^{3/8} / (C \cdot TE_{SE}) = k_3 \cdot TE_{SE}^{\ 1/8} (1/12\tau_0^2\tau_1)^{3/8} / \rho \qquad [23]$$

To summarize, SDR and SFB enable prediction of FID and SE signal decay of diffusive media containing strongly magnetized microspheres. SDR specifically applies when the influence of diffusion may be ignored completely. SFB allows some influence of diffusion on the signal decay time course; however, signal decay should be dominated by static dephasing. Criteria were defined to predict which diffusion regime applies when.

Materials and methods

The applicability and restrictions of the theory of SDR and SFB to predict and quantify the NMR signal decay of diffusive media containing strongly magnetized microspheres were investigated. First, MR experiments were used to validate the in house-built Monte Carlo simulation software. Once validated, Monte Carlo simulations were performed over a wide range of microsphere radii and susceptibility differences. Results of the MC simulations were used to test the predictive value of SDR and SFB and the correctness of their respective criteria of validity.

Study design

Tissue model

A tissue model consisting of two compartments with different magnetic susceptibility (Δχ) was considered; a major compartment, the medium with diffusion coefficient D, occupying a volume fraction of 1-ς; and a minor compartment, representing randomly distributed impenetrable strongly magnetized micron-sized spheres, occupying a volume fraction ς, which is assumed to be small, ς <<1.

MR experiments

MR experiments were conducted to investigate FID and SE signal decay diffusive media containing strongly magnetized microspheres, using agarose gel phantoms. The minor compartment was represented by a homogeneous suspension of HoMS (holmium load = 17% (w/w), $\Delta\chi$ = 800 ppm (15, 31), R = 15 µm, density = 1.4 g/ml) with concentrations ranging from 1-15 mg/ml ($0.0007 < \varsigma < 0.0107$) in a 2% agarose gel matrix (D=2.1 µm²/ms). For multiple gradient echo (MGE) of FID HoMS with a holmium load of 18.6 % (w/w) and $\Delta\chi$~880 ppm were used. FID and SE signals of the HoMS dilution series (1-15 mg/ml) were densely sampled using interleaved MGE sampling of FID and SE, as previously described (8). Monoexponentiality of FID and linearity of the r_2^* relaxivity of HoMS were investigated at varying field strengths (1.5T, 3T and 7T). Ultrashort TE imaging was applied when possible (at 1.5 T and 3 T) to enable sampling of fast decaying signals (31 The signal decay time course of single SE was characterized at varying TE_{SE} by determining of the R_2 and downslope R_2^* of the SE signal as a function of the HoMS concentration. The TE_{SE} was varied (8.2; 14.0; 26.0ms) to indirectly investigate the influence of diffusion on the SE signal decay time course. The r_2 relaxivity of HoMS, linearized at the TE_{SE}, was explored as well.

Monte Carlo simulations

MC simulations were done as described by Weisskoff et al.(32), using 20000 iterations and a random walk step size = 0.02ms. First, similar timing and spin-sphere system parameters were used as applied during MR experiments, to validate the MC simulations with the experiments. Once validated, the MC simulations were utilized to validate the theories of SDR and SFB in predicting the FID and SE signal decay for a wide range of particle radii (1 µm < R < 100 µm) and susceptibility differences (1 ppm < $\Delta\chi$ < 1000 ppm).

Results

Experimental validation of MC simulations and theory

Free induction decay

Multiple gradient echo sampling of FID demonstrated monoexponential signal decay (Figure 1a) over the entire HoMS concentration range (1-15 mg/ml) as determined at 1.5T. A linear relation was observed between the HoMS concentration and the R_2^* relaxation rate for a range of field strengths (1.5T, 3T and 7T), as demonstrated by the regression curves in Figure 1c. MC simulations presented very similar signal behavior, demonstrating monoexponential signal decay and a linear relation between HoMS concentration and R_2^* relaxation

rate (Figure 1b and 1d). The experimentally determined transverse relaxivity r_2^* linearly varied with field strength and was in excellent agreement with MC simulations as well as with the theoretical results obtained with SDR and SFB, as summarized in Table 1.

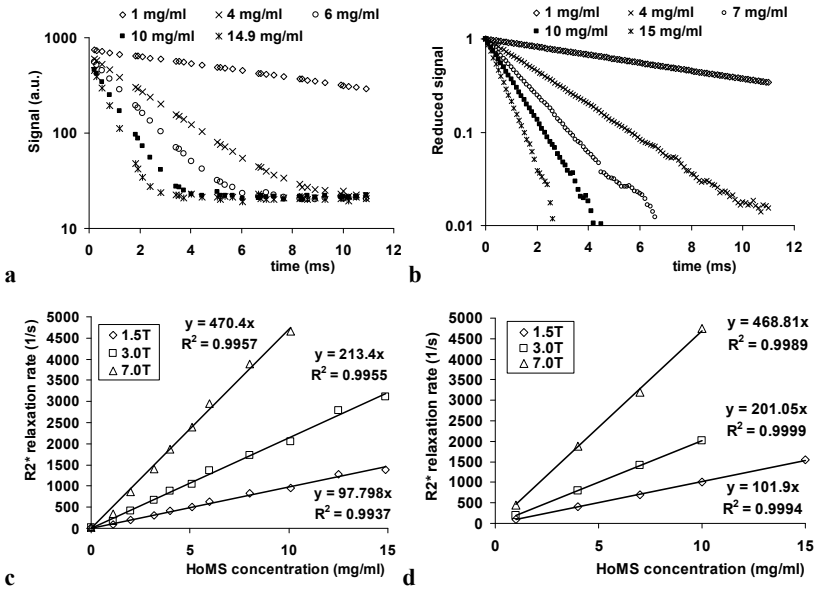

Figure 1 *Densely sampled FID signal of an agarose gel HoMS dilution series determined using MR experiments at 1.5T (a) and using MC simulations (b). Both MR experiments and MC simulations demonstrate linear exponential signal decay. A linear relation was observed between the R_2^* relaxation rate and the HoMS concentration as determined experimentally (c) and using MC simulations (d) for varying field strengths. The slope of these regression curves (c, d) represent the r_2^* relaxivity of HoMS at 1.5T, 3T and 7T.*

Table 1 *Transverse relaxivity (r_2^*) of HoMS with a Δχ=880 ppm at 1.5, 3 and 7 T determined experimentally, by simulation and using SDR and SFB theories.*

B0	1.5T	3.0T	7.0T
Experiment	*98*	*213*	*470*
MC Simulations	*102*	*201*	*469*
SDR+SFB	*102*	*203*	*474*

Spin echo signal decay time course

The SE signal decay time course of the agarose gel HoMS dilution series was densely sampled for three values of TE_{SE} (8.2; 14.0; 26.0ms) using MR experiments at 1.5T and using MC simulations. Results are depicted in Figure 2a and 2b. Experimental

data and MC simulations show similar SE signal behavior on qualitative inspection, as demonstrated by the following observations. First, the height of the SE peak decreased with increasing HoMS concentration, which indicates a T_2 effect. The flattening of the SE peak causes the signal decay close to TE_{SE} to deviate from linear exponential behavior. The time period of non-exponential signal decay with respect to the TE_{SE} increased with increasing TE_{SE}. As a result, the downslope of the SE peak belonging to a certain HoMS concentration, characterized by T_2^*, decreased with increasing TE_{SE}. This deviation from linear exponential signal decay was most likely caused by increasing diffusion sensitivity with increasing TE_{SE}, which clearly demonstrates that the presented signal decay was not in accordance with SDR behavior. When satisfying the SDR conditions, the downslope of the SE peak would exhibit linear exponential behavior. The signal decay presented by the SE with the shortest TE_{SE} mostly resembled linear exponential signal behavior.

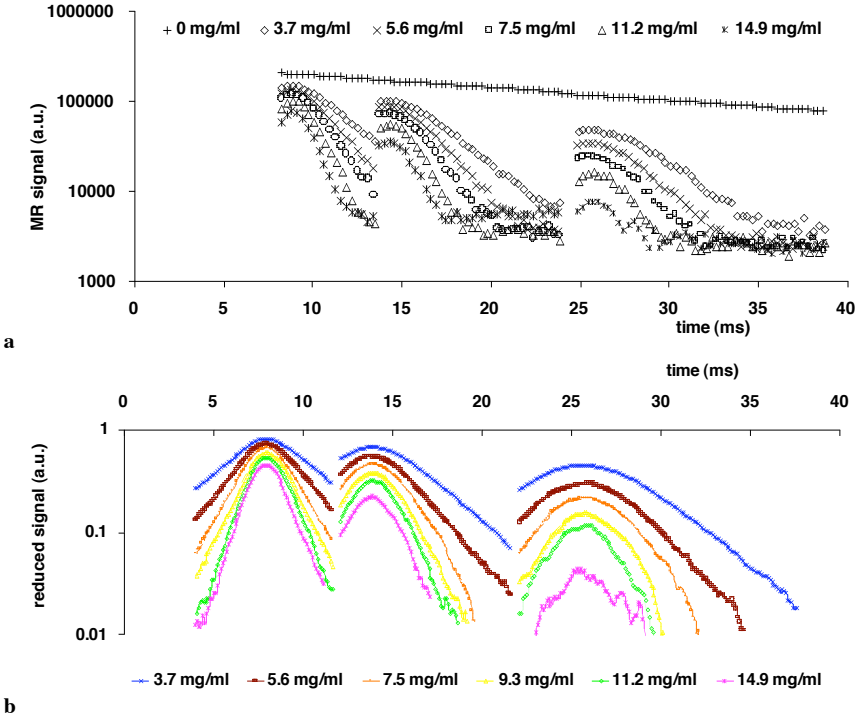

Figure 2 *SE signal decay time course of the agarose gel HoMS dilution series acquired at 1.5T as determined experimentally using an interleaved MGESE sampling scheme (a) and using MC simulations (b) . Results of three separate SE imaging experiments using different values of TE_{SE} (8.2; 14.0; 26.0ms) are presented (a) (For color figure see addendum).*

Single spin echo signal decay

The R_2 relaxation rate associated with the signal decay of a single SE was investigated as a function of TE_{SE}. On qualitative inspection, a small deviation from monoexponential behavior could be observed, as shown in Figure 3a by the nonlinear relation between the logarithm of the SE signal and TE_{SE}. This was in accordance with the predictions of the theory of SFB for single SE signal decay (Eq. [18]) as well as with the results obtained with MC simulations, as depicted in Figs. 3b and 3c, respectively. However, a marked difference can be observed as well. The graphs representing the experimental data (Figure 3a) are steeper as compared to both SFB and MC simulations (Figure 3b and 3c). This was caused by the fact that in the experimental data, the intrinsic T_2 is also incorporated, as compared to the theoretical and simulated data, which both solely present the reduced signal induced by the presence of magnetized microspheres.

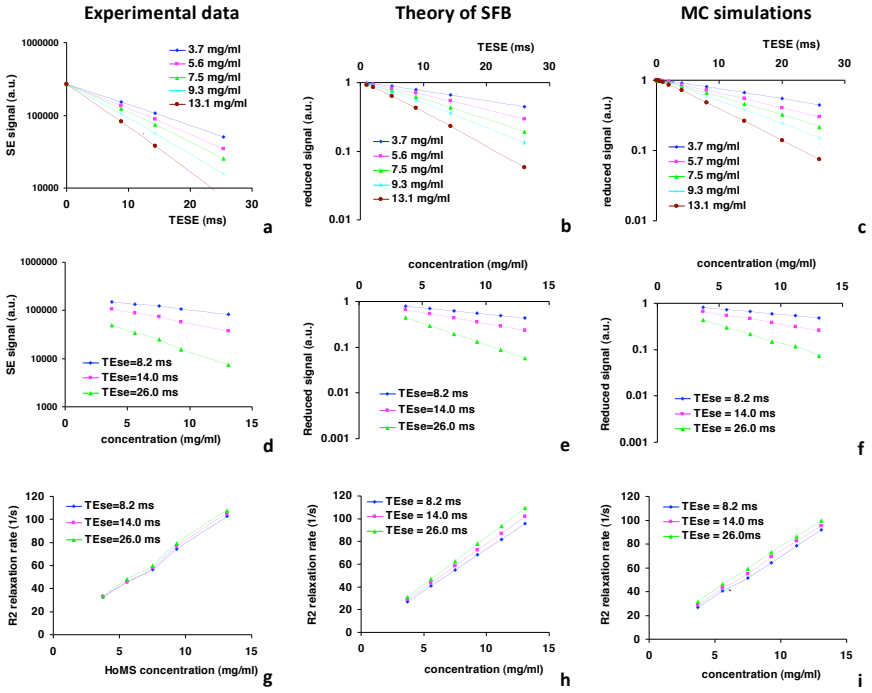

Figure 3 *The logarithm of the single SE signal peak of an agarose gel HoMS dilution series as a function of TESE, demonstrating a slight deviation from linear exponential behavior for a) experimental data, b) SFB theory and c) Monte Carlo simulations. Single SE signal behavior as a function of particle concentration demonstrates linear exponential behavior for d) experimental data, e) SFB theory and f) Monte Carlo simulations. For each value of TESE linear r_2^* relaxivity was found for the HoMS dilution series, as concluded from the linear relation between the R_2^* relaxation rate and the particle concentration observed for Experimental data (g), SFB theory (h) and MC simulations (i) (For color figure see addendum).*

Interestingly, a linear exponential relation was observed between the SE signal at TE_{SE} and the concentration for a specific TE_{SE}, as shown in Figure 3d. Similar behavior was predicted by the SFB (Figure 3e) and by MC simulations (Figure 3f). As a result, the R_2 relaxation rate belonging to a specific TE_{SE} linearly depended on the concentration, as was confirmed by MR experiments, SFB theory and MC simulations (Figure 3g, 3h and 3i). Hence, for each value of TE_{SE}, the r_2 relaxivity can be determined using Eq. [23]. The relation between the r_2 relaxivity of HoMS in an agarose gel matrix with D=2.1 $\mu m^2/ms$ and the TE_{SE} is depicted in Figure 4a. Good agreement was found between MR experiments, SFB theory (Eq. [23]) and MC simulations.

Signal decay of the downslope of the SE peak as a function of TE_{SE} was characterized using experimental data and MC simulations. As was already shown qualitatively in Figure 2, both MR experiments and MC simulations demonstrated a decrease of the SE peak with increasing TE_{SE}, which caused the downslope of the SE peak to flatten and the downslope R_2^* value to decrease. As a result, the SE downslope r_2^* relaxivity decreased with increasing TE_{SE}. This is shown in Figure 4b, demonstrating a good agreement between the downslope r_2^* values obtained experimentally and using MC simulations.

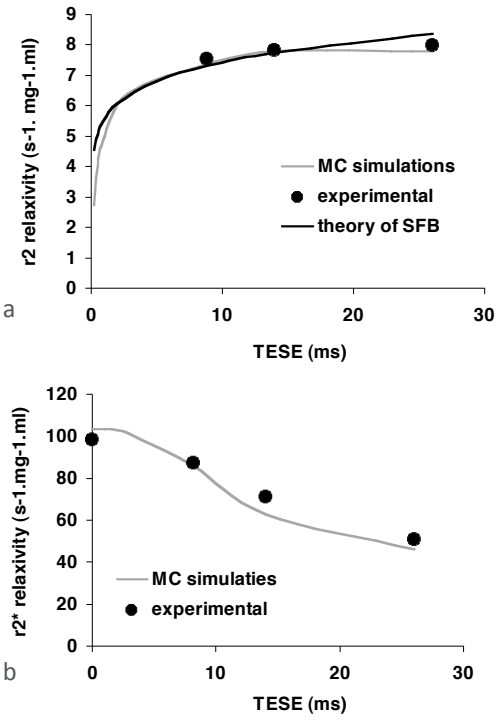

Figure 4 *a) The r_2 relaxivity of HoMS as a function of TESE for single SE as determined experimentally at 1.5T using the agarose gel HoMS dilution series, using MC simulations and predicted by SFB theory. b) The r_2^* relaxivity of HoMS obtained from the FID (first data point) and SE downslope plotted against TESE as determined experimentally and using MC simulations.*

Applicability and restrictions of SDR and SFB for hypothetical spin-sphere systems

In the previous section Monte Carlo simulations and theoretical predictions were demonstrated to be in excellent agreement with experimentally determined FID and SE signal decay for the particular case of HoMS in a diffusive medium, over a wide concentration range and for varying field strengths. Both SFB and SDR correctly predicted the FID signal behavior; SE signal behavior was correctly predicted by SFB theory. Based upon the criteria of validity as defined for SDR (Eq. [4] and Eq. [11]) and SFB (Eq. [16]), this was to be expected for this specific spin-sphere system with R = 15 μm, Δχ = 800 ppm (and Δχ = 880 ppm), D = 2.1 μm^2/ms and B_0 = 1.5T. In the current section, the applicability and restrictions of SDR and SFB were explored for a hypothetical spin-sphere system in which particle radii and susceptibility differences were varied over a relevant range. A diffusive medium containing microspheres of which R and Δχ were varied between 1-100 μm and 1-800 ppm, respectively, was investigated. Other parameters of the spin-sphere system were kept constant: volume fraction ς = 0.00265 (comparable with 3.7 mg/ml HoMS), diffusion coefficient D = 2.1 μm^2/ms and B_0 = 1.5T. FID and SE signal decay predicted by SDR and SFB were validated by MC simulations to investigate the correctness of the criteria of validity for SDR and SFB.

Criteria

To simplify interpretation, the criteria for SDR and SFB were captured into graphs (Figure 5). Figure 5a shows the left-hand side of the SDR criterion for FID signal behavior (Eq. [4]) as a function of the particle radius. For all values of Δχ > 1ppm and particle radii > 1 μm, the criterion was satisfied ($\delta\omega \cdot \tau_D /(6 \cdot \varsigma^{-1/3}) >> 1$), implying that the SDR could be applied to predict the FID signal behavior of these spin-sphere systems, using Eq. [5] and Eq. [9]. Figure 5b depicts the critical echo time TE_c as defined by the additional SDR criterion specifically defined for SE signal decay (Eq. [11]) as a function of the particle radius. To satisfy the criterion, the echo time of a SE experiment should be much smaller than TE_c (TE_{SE} << TE_c). For a system containing microspheres with R = 15 μm and Δχ = 800ppm, which was experimentally studied in the previous section, TE_c ≈ 4 ms. Since TE_{SE} = 8.2 ms, 14.0 ms or 26.0 ms were used, the criterion was not satisfied, implying that a diffusion sensitivity was predicted, which was confirmed by the MR experiments. Figure 5b suggests that to satisfy the SDR criterion for SE, one could increase particle radius, decrease TE_{SE} or decrease Δχ, as long as the SDR criterion for FID is met as well. For the theory of the SFB, a single criterion of validity for both FID (R_2^*) and SE (R_2) experiments was defined. However, a strict criterion ($R_2^{(*)} >> 1/\tau_1$) and a less strict criterion ($R_2^{(*)} >> 1/\tau_2$) was given in

literature (21). Figure 5c. depicts the curves $R_2^{(*)} = 1/\tau_1$ and $R_2^{(*)} = 1/\tau_2$, separating regions that do and do not satisfy SFB conditions. When the $R_2^{(*)}$ of a particular spin-sphere system, as predicted using Eq. [22] or Eq. [23], was located in the region above the depicted graphs in Figure 5c, a system was expected to behave according to the SFB. Figure 5c indicates that systems containing large particles and sytems containing particles which induce high $R_2^{(*)}$ values are most likely to satisfy SFB conditions.

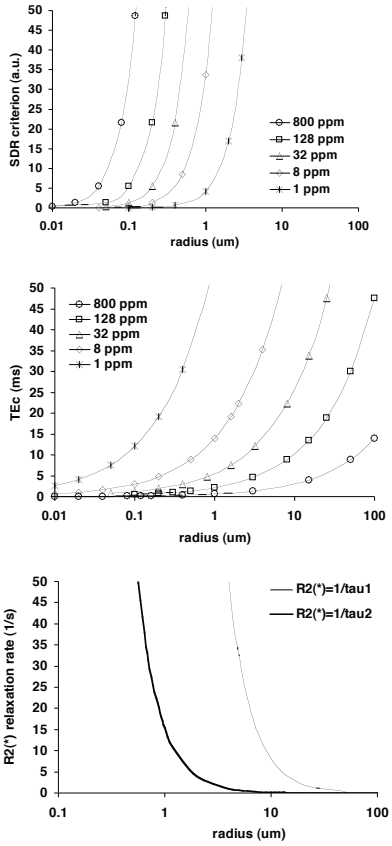

Figure 5

a) Left-hand side of SDR criterion ($\delta\omega \cdot \tau_D / (6 \cdot \varsigma^{-1/3}) >> 1$) sufficient for FID plotted against microsphere radius for varying Δχ. A volume fraction of ς = 0.00265 and D = 2.1 μm²/ms were used.

b) Critical echo time TEc plotted against particle radius for varying Δχ, with constant volume fraction ς = 0.00265 and D = 2.1 μm2/ms. When $TE_{SE} << TE_c = 2.9(\tau_D \cdot t_c^2 / \varsigma)^{1/3}$, and when the SDR criterion for FID is satisfied, a SE experiment of the spin-sphere system is expected to behave according to the SDR.

c) Graphs of the strict criterion ($R_2^{(*)} = 1/\tau_1$) and the less strict criterion ($R_2^{(*)} = 1/\tau_2$) of SFB theory, separating regions that do and do not satisfy the SFB theory.

Free induction decay

SDR and SFB predicted monoexponential signal behavior for FID (Eq. [5] and Eq. [17], respectively), characterized by the transverse relaxation rate R_2^*, which was determined using Eq. [9] and Eq. [22] for SDR and SFB, respectively. The goodness of the prediction of the signal behavior of FID is therefore determined by the accuracy of the predicted R_2^* value. As previously mentioned, SDR and SFB

predict equal values for R_2^*. Figure 6a presents the R_2^* values predicted by these theories for arbitrary spin-sphere systems with varying radius and susceptibility, depicted as straight horizontal lines, indicating insensitivity to particle radius. Excellent agreement with MC simulations was observed, which were represented by the symbols in Figure 6a. Results were in agreement with the SDR criterion, which stated that for $\Delta\chi$ > 1ppm and particle radii > 1 µm, FID signal behavior was predictable using the SDR theory. Furthermore, both criteria defined by the theory of SFB correctly predicted the applicability of the SFB for the entire particle range and susceptibility range, since all R_2^* values located above the curves representing the SFB criteria in Figure 6a. were correctly predicted. However, the strict criterion (thin line) seems to be unnecessarily strict, since many R_2^* values located below the SFB curve were predicted correctly as well. Figure 6b presents R_2^* values as a function of $\Delta\chi$ for varying particle radii predicted using both theories and using MC simulations. Excellent agreement between MC simulations and theory was shown again, confirming insensitivity of R_2^* to particle radius and linear r_2^* relaxivity over the investigated range.

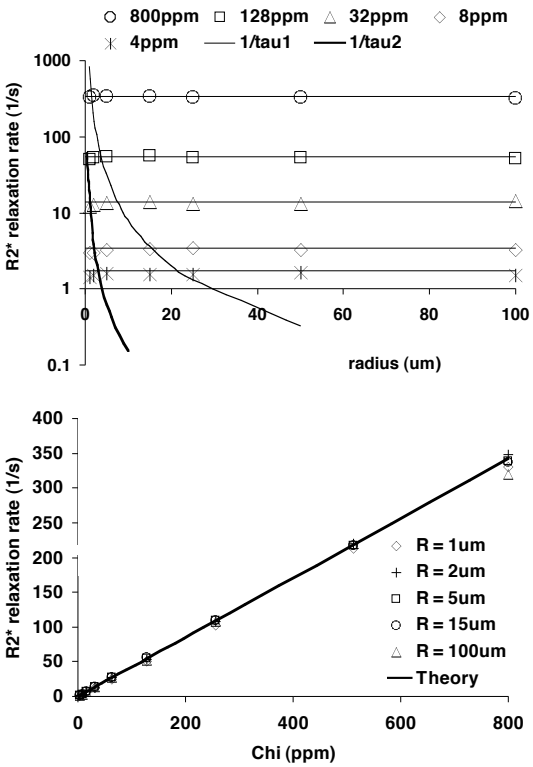

Figure 6

a) R_2^* values obtained with SDR and SFB theory (horizontal lines) and MC simulations (symbols) plotted against particle radius for varying Δχ. R_2^* is shown to be independent of particle radius. Theory correctly predicted R_2^*. Curves represent strict (thin line) and less strict (bold line) SFB criteria.

b) R_2^* plotted as a function of Δχ for varying particle radius. Results obtained with MC simulations (symbols) were in excellent agreement with theory (bold line). A constant volume fraction of ç = 0.00265, D = 2.1 µm²/ms and B_0 = 1.5T were used.

Spin echo

By definition, SDR predicts the signal decay time course of single SE behavior in situations in which the influence of diffusion can be ignored, which in theory results in R_2 values equal to zero. Therefore, no explicit prediction of R_2 other than zero can be made using SDR. However, the SDR criterion for SE experiments does provide information on which value of TE_{SE} to use to discard possible diffusion influence on SE signal decay.

SFB predicts the SE signal amplitude taking into account the possible influence of diffusion. Only the signal amplitude at TESE is predicted by SFB, which does not necessarily have to coincide with the time instance of the occurrence of the SE peak, since the SE peak may shift with respect to TESE (21, 23). SE signal decay predicted by SFB was compared to MC simulations. Figure 7a and 7b present predicted R_2 values (colored curved lines) as a function of particle radius for relatively small (<64 ppm) and large (64-800 ppm) Δχ values, respectively.

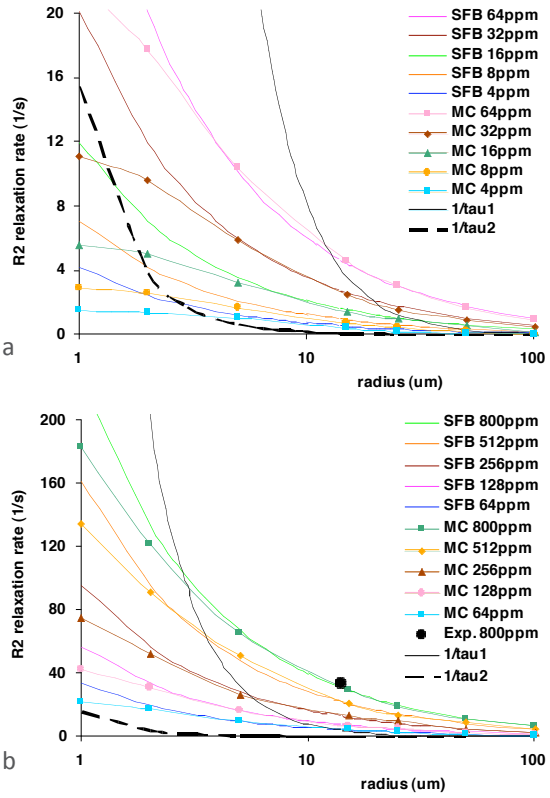

Figure 7 *R_2 obtained with SFB theory (colored lines) and MC simulations (symbols) plotted against particle radius for varying Δχ. Figures a) and b) depict relatively small (<64 ppm) and large (64 800 ppm) Δχ values, respectively. The strict and less strict SFB criteria are depicted by the continuous line and the dashed line, respectively. A constant volume fraction of ς = 0.00265, D = 2.1 μm²/ms and B_0 = 1.5T, TE_{SE} = 14ms were used (For color figure see addendum).*

Both SFB criteria were depicted by the curved black lines. Good agreement was observed between SFB theory and MC simulations (symbols) for R_2 values located above the strict SFB criterion. In Figure 7b the black dot represents the experimentally investigated spin-sphere system (R = 15 µm; 800 ppm), which was in excellent agreement with both theory and MC simulations, as confirmed by the graph. Furthermore, over a wide range of Δχ values, the strict criterion appeared to be unnecessarily strict, since R_2 values below the line of the strict criterion were correctly predicted. However, the less strict criterion was not strict enough, indicated by the fact that theoretical predictions and MC simulations did not agree for all R_2 values above the graph representing the criterion. Figure 8 presents the predicted R_2 value as a function of Δχ for varying particle radii. A nonlinear relation between the R_2 value and Δχ for all particle sizes was presented by MC simulations and by SFB. Although excellent agreement between MC simulations and theory was shown for large particles (> 5 µm), for smaller particles (< 5 µm), SFB theory predicted R_2 values which were too high. This observation was in line with the strict SFB criterion, which predicted that the SFB did not apply to the investigated diffusive medium containing small particles.

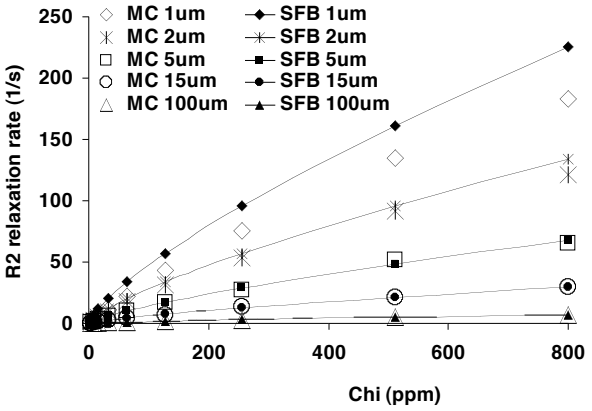

Figure 8 *R_2 obtained with theory (lines) and MC simulations (symbols) plotted against Δχ for varying particle radius, demonstrating a nonlinear relation between R_2 and Δχ. Excellent agreement was observed for large particle radii (≥5 µm).*

Discussion and conclusions

Two well-known diffusion regimes, the static dephasing regime and the theory of strong field behavior, were interpreted and applied to predict and quantify the NMR signal behavior of water protons in diffusive media containing strongly magnetized micron-sized particles. The influence of diffusion coefficient, particle radius, susceptibility and concentration were investigated, as well as the influence of the field strength, the type of imaging sequence and the echo time.

By validation with experimental results, Monte Carlo simulations were shown to accurately predict the signal decay time course of FID and SE of an agarose gel matrix containing varying concentrations of strongly magnetized microspheres at different field strengths and echo times. Then, MC simulations were used to validate NMR signal behavior predictions obtained with SDR and SFB theory and to verify their respective criteria of validity over a wide range of particle radii ($1\ \mu m < R < 100\ \mu m$) and susceptibility differences ($1\ ppm < \Delta\chi < 1000\ ppm$). The investigated range represents a variety of paramagnetic particles or clusters of particles, such as iron or holmium-loaded microspheres (5, 8, 15, 17), endogenous iron accumulations (1, 3) and iron-labeled cells (4, 6, 7, 9, 11-13, 33, 34). When iron-labeled cells are concerned, a huge range of iron content per cell (0.2-30 pg/cell) as well as of cluster size (0.5-20 um) may be expected due to differences in labeling efficiency, lysosomal compartmentalization, cell type and cell viability (4, 6, 9, 12-14, 33). An important issue is whether it is valid to model a cluster of small magnetic dipoles by a single larger magnetized sphere, when considering spin dephasing in the vicinity of a cluster of small paramagnetic particles. For iron-labeled cells this is often assumed (7, 9, 11), although Pintaske et al. reported differences in the signal decay time course related to varying spatial distributions of magnetic dipoles and iron labeled cells (34, 35).

In our study, MR experiments and MC simulations demonstrated monoexponential FID signal behavior for the spin-sphere systems of interest. The R_2^* relaxation rate was shown to be proportional to the concentration and susceptibility of the particles and to field strength. Furthermore, within the investigated range, FID was observed to be insensitive to particle radius and diffusion coefficient. Predictions of both SDR (20) and SFB (21) were in excellent agreement with these findings. It may be concluded that FID signal behavior is well predictable and both diffusion regimes may be applied to quantify strongly magnetized micron-sized particles in a diffusive medium, according to Eq. [10] and [22]. This was recently confirmed for holmium-loaded microspheres (8) and iron-labeled cells (6). Although equal expressions were derived by the theories of SDR and SFB to predict signal behavior of FID, different criteria of validity were proposed. These criteria were shown to correctly predict whether the investigated spin-sphere systems satisfied the diffusion regime.

SE signal behavior of the investigated spin-sphere systems was demonstrated to be influenced by diffusion in many situations in which FID signal behavior was unaffected. Hence, SDR conditions may apply to a spin-sphere system when conducting a FID experiment, while for a SE experiment of the same spin-sphere system, SDR conditions do not necessarily apply. Similar behavior was reported

in literature based on MR experiments (6, 12, 15, 31) as well as on theory (21, 24, 26). The specific SDR criterion for SE experiments was shown to correctly predict the applicability of SDR for SE experiments (Eq. [11]). Therefore, this criterion may be convenient to predict whether the signal decay time course of the SE can be used for quantification according to the static dephasing regime. Determination of R_2^*, R_2 and R_2' of magnetically inhomogeneous systems by either GESFIDE (36) or GESSE (25) may be expected to be inaccurate when the SDR criterion for SE is not satisfied, since the SE downslope exhibits non-monoexponential signal decay. As mentioned in the introduction, Liu et al.(7) and Seppenwoolde et al. (15) used the SE downslope for R_2^* based quantification of iron-labeled cells and holmium-loaded microspheres, respectively, and observed underestimations, which were most likely caused by the influence of diffusion on the SE signal decay time course. Recently, it was shown that by utilizing FID sampling of similar spin-sphere systems, in stead of SE sampling, the accuracy of R_2^*-based quantification of holmium-loaded microspheres strongly improved (8). Similar observations were reported by Liu et al. with regard to R_2^* based quantification of iron-labeled cells (7).

In many cases in which SDR conditions were not satisfied for SE experiments, SFB theory accurately predicted the single SE signal behavior, taking into account the influence of diffusion. Interestingly, for constant TE_{SE}, the MR magnitude signal monoexponentially related to the particle concentration, which may be useful for quantification of contrast agents using pre- and post contrast scans. When using a time series of single SE experiments with varying TE_{SE} for R_2-based quantification of particle concentrations, inaccuracies may be expected, since R_2 was shown to vary with TE_{SE}, which causes the magnitude of multiple single SE peaks in relation to TE_{SE} to deviate from monoexponential behavior. For monodisperse particles with constant $\Delta\chi$, this small deviation may probably be ignored (21). However, for quantification of (clusters of) magnetized particles with variable size or susceptibility, SE based quantification will be complicated, since R_2 depends on both parameters, as was demonstrated by SFB theory. In clinical practice, these observations have important consequences for noninvasive quantitative monitoring of viability and differentiation capacity of iron-labeled cells, currently a topical subject (6, 12, 13). Cell division causes the magnetic label to be divided among a larger number of cells and hence decreases the average $\Delta\chi$ and consequently increases the r_2 relaxivity of the labeled cells, as was shown in the presented data (Figs. 7 and 8). Similar findings were presented for different sized iron labeled cells by Rad et al. (33), who observed that the r_2 of iron incorporated in cells decreased with increasing cell size. This may severely

complicate R_2-based quantitative monitoring of dividing cells. Interestingly, The r_2^* relaxivity of magnetized micron-sized particles is independent of the radius and linearly relates to $\Delta\chi$, as long as SDR conditions apply. Therefore, cell division would not complicate R_2^* based quantification of the amount of iron label present in the ensemble of cells. Complete lyses of cells, however, may cause break down of the SDR condition which would lead to a strong decrease of the r_2^* relaxivity (12).

In conclusion, by exploiting the different influences of particle size, susceptibility, concentration and diffusion on R_2, R_2^* and R_2', MRI is capable of noninvasive quantification of strongly magnetized micron-sized particles. The underlying principles that account for the differences in transverse relaxation rates were explained using MR experiments and MC simulations and it was demonstrated how two well-known diffusion regimes, the static dephasing regime and the theory of strong field behavior, can be applied to predict transverse relaxation of the spin-sphere system under investigation. Detailed knowledge of these processes my aid in understanding and monitoring biophysical processes like lysosomal compartmentalization as well as distinguishing viable cells from lysed cells (6, 12, 13). By careful selection of a specific imaging strategy and dedicated imaging parameters, it was demonstrated that the investigator can choose to either suppress or emphasize specific biophysical phenomena to gain favorable circumstances for MR-based quantification of strongly magnetized micron-sized particles or cells in a diffusive medium.

References

1. Gillis P, Koenig SH. Transverse relaxation of solvent protons induced by magnetized spheres: application to ferritin, erythrocytes, and magnetite. Magn Reson Med **1987**;5(4):323-345.
2. Gillis P, Moiny F, Brooks RA. On T(2)-shortening by strongly magnetized spheres: a partial refocusing model. Magn Reson Med **2002**;47(2):257-263.
3. Gossuin Y, Gillis P, Muller RN, Hocq A. Relaxation by clustered ferritin: a model for ferritin-induced relaxation in vivo. NMR Biomed **2007**;20(8):749-756.
4. Pintaske J, Muller-Bierl B, Schick F. Effect of spatial distribution of magnetic dipoles on Lamor frequency distribution and MR Signal decay--a numerical approach under static dephasing conditions. MAGMA **2006**;19(1):46-53.
5. Gupta T, Virmani S, Neidt TM, Szolc-Kowalska B, Sato KT, Ryu RK, Lewandowski RJ, Gates VL, Woloschak GE, Salem R, Omary RA, Larson AC. MR Tracking of Iron-labeled Glass Radioembolization Microspheres during Transcatheter Delivery to Rabbit VX2 Liver Tumors: Feasibility Study. Radiology **2008**;249(3):845-854.
6. Kuhlpeter R, Dahnke H, Matuszewski L, Persigehl T, von WA, Allkemper T, Heindel WL, Schaeffter T, Bremer C. R2 and R2* mapping for sensing cell-bound superparamagnetic nanoparticles: in vitro and murine in vivo testing. Radiology **2007**;245(2):449-457.
7. Liu W, Dahnke H, Rahmer J, Jordan EK, Frank JA. Ultrashort T2* relaxometry for quantitation of highly concentrated superparamagnetic iron oxide (SPIO) nanoparticle labeled cells. Magn Reson Med **2009**;61(4):761-766.
8. Seevinck PR, Seppenwoolde JH, Zwanenburg JJ, Nijsen JF, Bakker CJ. FID sampling superior to spin-echo sampling for T2*-based quantification of holmium-loaded microspheres: theory and experiment. Magn Reson Med **2008**;60(6):1466-1476.
9. Bowen CV, Zhang X, Saab G, Gareau PJ, Rutt BK. Application of the static dephasing regime theory to superparamagnetic iron-oxide loaded cells. Magn Reson Med **2002**;48(1):52-61.
10. Brown RJS. Distribution of fields from randomly placed dipoles: free-precessing signal decay as a result of magnetic grains. Phys Rev **1961**;121:1379-1382.
11. Ziener CH, Bauer WR, Jakob PM. Transverse relaxation of cells labeled with magnetic nanoparticles. Magn Reson Med **2005**;54(3):702-706.
12. Henning TD, Wendland MF, Golovko D, Sutton EJ, Sennino B, Malek F, Bauer JS, McDonald DM, drup-Link H. Relaxation effects of ferucarbotran-labeled mesenchymal stem cells at 1.5T and 3T: discrimination of viable from lysed cells. Magn Reson Med **2009**;62(2):325-332.
13. Walczak P, Kedziorek DA, Gilad AA, Barnett BP, Bulte JW. Applicability and limitations of MR tracking of neural stem cells with asymmetric cell division and rapid turnover: the case of the shiverer dysmyelinated mouse brain. Magn Reson Med **2007**;58(2):261-269.
14. Bulte JW, Kraitchman DL. Iron oxide MR contrast agents for molecular and cellular imaging. NMR Biomed **2004**;17(7):484-499.
15. Seppenwoolde JH, Nijsen JF, Bartels LW, Zielhuis SW, van Het Schip AD, Bakker CJ. Internal radiation therapy of liver tumors: qualitative and quantitative magnetic resonance imaging of the biodistribution of holmium-loaded microspheres in animal models. Magn Reson Med **2005**;53(1):76-84.

16. Lee KH, Liapi E, Vossen JA, Buijs M, Ventura VP, Georgiades C, Hong K, Kamel I, Torbenson MS, Geschwind JF. Distribution of iron oxide-containing Embosphere particles after transcatheter arterial embolization in an animal model of liver cancer: evaluation with MR imaging and implication for therapy. J Vasc Interv Radiol **2008**;19(10):1490-1496.
17. Nijsen JF, Seppenwoolde JH, Havenith T, Bos C, Bakker CJ, van Het Schip AD. Liver tumors: MR imaging of radioactive holmium microspheres--phantom and rabbit study. Radiology **2004**;231(2):491-499.
18. Hardy P, Henkelman RM. On the transverse relaxation rate enhancement induced by diffusion of spins through inhomogeneous fields. Magn Reson Med **1991**;17(2):348-356.
19. Majumdar S, Zoghbi SS, Gore JC. The influence of pulse sequence on the relaxation effects of superparamagnetic iron oxide contrast agents. Magn Reson Med **1989**;10(3):289-301.
20. Yablonskiy DA, Haacke EM. Theory of NMR signal behavior in magnetically inhomogeneous tissues: the static dephasing regime. Magn Reson Med **1994**;32(6):749-763.
21. Jensen JH, Chandra R. Strong field behavior of the NMR signal from magnetically heterogeneous tissues. Magn Reson Med **2000**;43(2):226-236.
22. Kennan RP, Zhong J, Gore JC. Intravascular susceptibility contrast mechanisms in tissues. Magn Reson Med **1994**;31(1):9-21.
23. Kiselev VG, Posse S. Analytical model of susceptibility-induced MR signal dephasing: effect of diffusion in a microvascular network. Magn Reson Med **1999**;41(3):499-509.
24. Yung KT. Empirical models of transverse relaxation for spherical magnetic perturbers. Magn Reson Imaging **2003**;21(5):451-463.
25. Yablonskiy DA, Haacke EM. An MRI method for measuring T2 in the presence of static and RF magnetic field inhomogeneities. Magn Reson Med **1997**;37(6):872-876.
26. Yablonskiy DA. Quantitation of intrinsic magnetic susceptibility-related effects in a tissue matrix. Phantom study. Magn Reson Med **1998**;39(3):417-428.
27. Cheng YC, Haacke EM, Yu YJ. An exact form for the magnetic field density of states for a dipole. Magn Reson Imaging **2001**;19(7):1017-1023.
28. Haacke EM, Brown RW, Thompson MR, Venkatesan R. Magnetic Resonance Imaging. Physical Principles and Sequence Design. New York: John Wiley & Sons, Inc.; 1999.
29. Seppenwoolde JH, van ZM, Bakker CJ. Spectral characterization of local magnetic field inhomogeneities. Phys Med Biol **2005**;50(2):361-372.
30. Ziener CH, Kampf T, Melkus G, Herold V, Weber T, Reents G, Jakob PM, Bauer WR. Local frequency density of states around field inhomogeneities in magnetic resonance imaging: effects of diffusion. Phys Rev E Stat Nonlin Soft Matter Phys **2007**;76(3 Pt 1):031915.
31. Seevinck PR, Bos C, Bakker CJ. Ultrashort T2* relaxometry using conventional multiple gradient echo sampling with S0 fitting: validation with quantitative UTE (QUTE) imaging. In Proceedings of the 16th Annual Meeting of ISMRM, Toronto, Canada **2008**; p. 1419.
32. Weisskoff RM, Zuo CS, Boxerman JL, Rosen BR. Microscopic susceptibility variation and transverse relaxation: theory and experiment. Magn Reson Med **1994**;31(6):601-610.
33. Rad AM, Arbab AS, Iskander AS, Jiang Q, Soltanian-Zadeh H. Quantification of superparamagnetic iron oxide (SPIO)-labeled cells using MRI. J Magn Reson Imaging **2007**;26(2):366-374.

34. Pintaske J, Muller-Bierl B, Schick F. Geometry and extension of signal voids in MR images induced by aggregations of magnetically labelled cells. Phys Med Biol **2006**;51(18):4707-4718.
35. Pintaske J, Mueller-Bierl B, Schick F. Numerical simulation of magnetic field distortions caused by cells loaded with SPIO nanoparticles. In Proceedings of the 14th Annual Meeting of ISMRM, Seattle, Washington, USA **2006**; p. 1811.
36. Ma J, Wehrli FW. Method for image-based measurement of the reversible and irreversible contribution to the transverse-relaxation rate. J Magn Reson B **1996**;111(1):61-69.

Chapter 10

P.R. Seevinck, T.C. de Wit, J.F.W. Nijsen, M.A.D. Vente and C.J.G. Bakker

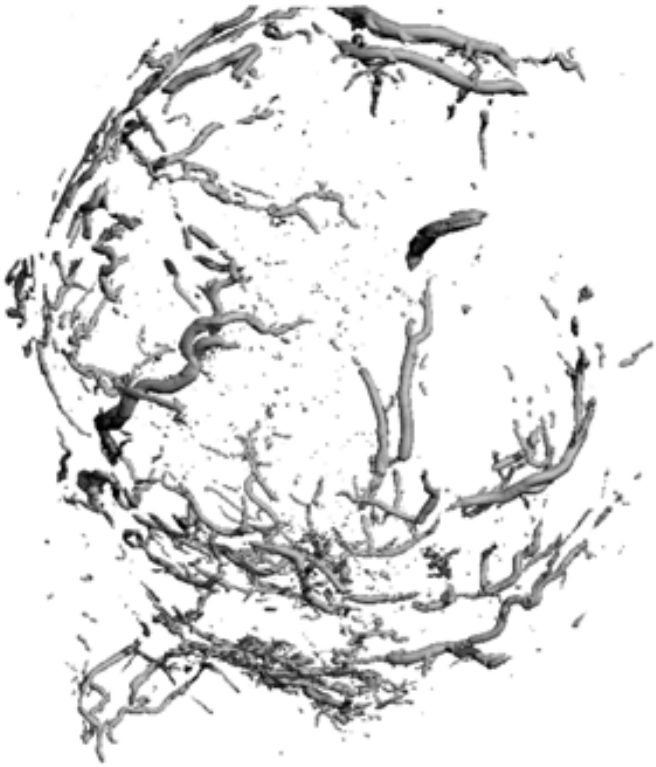

MR-based dosimetry of holmium-166 poly (L-lactic acid) microspheres for internal radiation therapy treatment planning

Abstract

Purpose

To prospectively test the hypothesis that MRI can potentially be used to perform dose calculations of holmium-166 poly (L-lactic acid) microspheres (^{166}Ho-PLLA-MS) for treatment planning of transcatheter radioembolization of hepatic malignancies.

Materials and Methods

MRI and SPECT experiments were conducted using an anthropomorphic agarose gel phantom containing tumor-simulating gel samples with known amounts of ^{166}Ho-PLLA-MS. MRI and SPECT data were used to perform dose calculations which were compared qualitatively and quantitatively to reference data obtained with a dose calibrator.

Results

Excellent agreement was observed both qualitatively and quantitatively when comparing MR-based to SPECT-based dose maps. A regression coefficient of 1.05 with correlation coefficient r^2 of 0.987 was found when relating MR-based ^{166}Ho-PLLA-MS dose calculations to the reference data.

Conclusion

MR-based dosimetry of ^{166}Ho-PLLA-MS in an anthropomorphic gel phantom was demonstrated to be feasible, indicating the potential of MR-based dosimetry for planning, guidance and evaluation of transcatheter radioembolization treatment of hepatic malignancies with ^{166}Ho-PLLA-MS.

Introduction

Internal radiation therapy with radioactive microspheres has proven to be a successful treatment technique for hepatic malignancies, leading to a significant increase in the median survival of patients with liver malignancies (1-4). In transcatheter radioembolization therapies, differences in arterial and portal blood supply to liver tumors and normal liver parenchyma are exploited to gain a high tumor to liver ratio (T/L ratio) (5). However, the large variation in vascularity of tumor and liver observed between patients, including possible arteriovenous shunting, necessitates extensive treatment planning, to assure a favorable dose distribution in each individual patient (6). The currently used radioactive microspheres for internal radiation therapy, yttrium-90 (^{90}Y) microspheres, are pure β-emitters and do not facilitate high quality biodistribution assessment using nuclear imaging. Therefore, Technetium-99m (^{99m}Tc) macroaggregated albumin (MAA) are utilized as a surrogate, aiming to estimate lung-shunt fractions, extrahepatic depositions and intrahepatic dose distributions using planar scintigraphy and single photon emission computed tomography (SPECT). The different size distribution (10-90 μm), shape, density and thus hemodynamic properties of ^{99m}Tc-MAA particles, as well as the sizeable amount (up to 10%) that is well below 30 μm, inevitably lead to discrepancies between the biodistribution of ^{99m}Tc-MAA particles and ^{90}Y microspheres (7-10). Therefore, preprocedural ^{99m}Tc-MAA SPECT scans offer sub-optimal estimations of intraprocedural microsphere distribution in the liver (8, 9).

The aforementioned suggests that it would be ideal to have a single microsphere that is applicable for both pretreatment high resolution biodistribution assessment *and* for the actual radioembolization therapy, which provides dosimetric information for planning, guidance and evaluation of transcatheter radioembolization of hepatic malignancies. Holmium-166 poly (L-lactic acid) microspheres (^{166}Ho-PLLA-MS), which were first proposed early in the 1990's (11), meet these criteria. First, ^{166}Ho-PLLA-MS possess attractive radiation characteristics ($E_{\beta,max}$=1.84MeV, E_{γ}=81 keV, $t_{1/2}$=26.8h) for both therapy and quantitative SPECT imaging, allowing preprocedural dose estimations using a small test dose (6, 12, 13). Second, investigations on stability, biocompatibility, toxicity and efficacy of ^{166}Ho-PLLA-MS, both in vitro and in vivo in animal models, have shown promising results and prove ^{166}Ho-PLLA-MS to be ready for clinical use (14-17). Third, the highly paramagnetic nature of holmium makes it an ideal MR contrast agent (18-21). High resolution visualization of the biodistribution of Ho-PLLA-MS in liver tissue was demonstrated on T_2^*-weighted MR images in animal studies (18, 21). Furthermore, MR-guided catheterization and administration

of Ho-PLLA-MS was shown to allow direct in vivo visualization of microsphere delivery to the tumor site (22). More recently, a fast quantitative MR imaging technique was presented to accurately assess and quantify the biodistribution of Ho-PLLA-MS in liver tissue (20).

The versatile MR imaging possibilities of ^{166}Ho-PLLA-MS in combination with the relatively high spatial and temporal resolution (19), the excellent soft tissue contrast and the quantitative capabilities, make MRI an attractive imaging modality to perform high resolution radiation dosimetry calculations in liver tissue prior to, during and after transcatheter radioembolization with ^{166}Ho-PLLA-MS. Therefore, in the presented study we will prospectively test the hypothesis that MRI can be used to perform dose calculations of ^{166}Holmium-loaded microspheres in an anthropomorphic phantom setup, demonstrating the potential of MR-based treatment planning of transcatheter radioembolization of hepatic malignancies in the near future.

Materials and methods

The feasibility to use MRI for dose calculations of ^{166}Ho-PLLA-MS was investigated using in vitro phantom experiments. A agarose gel phantom mimicking the human torso was used containing regions with known amounts of ^{166}Ho-PLLA-MS in well-defined volumes approximately the size of tumors. SPECT and MRI were used to perform dose calculations. MR-based dosimetric results were compared qualitatively and quantitatively to SPECT based-dosimetry and to reference data obtained with a dose calibrator.

Phantom Preparation

An anthropomorphic ellipse-shaped perspex phantom (short axis = 19 cm; long axis = 30 cm; height = 7 cm; volume ~ 3 L) roughly resembling a cross-section of the human torso was utilized (Figure 1a). Tumors were simulated by agarose gel samples (~ 2x3x3 cm) made in an ice cube container (Figure 1b). Agarose gel was prepared by dissolving 20 g of agarose powder to 1 L of deionized water prior to heating, doped with 28 mg/ml $MnCl_2 \cdot H_2O$ to mimic the T_1 relaxation properties of liver tissue. Small amounts of activated ^{166}Ho-PLLA-MS were administered to the liquid gel in the ice cube containers, varying between 0-6.2 mg per tumor. The Ho-PLLA-MS contained 17% w/w holmium and were prepared as previously described in ref. (13). The specific activity of ^{166}Ho-PLLA-MS after activation by neutron bombardment was determined using a dose calibrator to be 5.005 MBq/mg. The activity of the single tumors was determined as well using the dose calibrator, exactly providing the amount of activity and indirectly the mass of

Ho-PLLA-MS per tumor, calculated by dividing the activity per tumor by the specific activity of ^{166}Ho-PLLA-MS. A total amount of 152Mbq in 26 mg of ^{166}Ho-PLLA-MS was distributed over eight tumors with the following amounts: 1.16, 1.16, 2.28, 2.86, 3.52, 3.95, 5.04, and 6.16mg. As a control, two tumors were made without ^{166}Ho-PLLA-MS. The used amounts were representative for a scout dose, which consists of a total amount of 60 mg used to predict the biodistribution of a treatment dose of roughly 600mg in a liver volume of approximately 1.5L (6, 15).

The anthropomorphic phantom was first filled with a layer of two cm of agarose gel and left three hours to solidify. The tumors were positioned on top of the agarose gel layer (Figure 1c). Then, the phantom was cautiously filled with agarose gel, to prevent trapping of air bubbles.

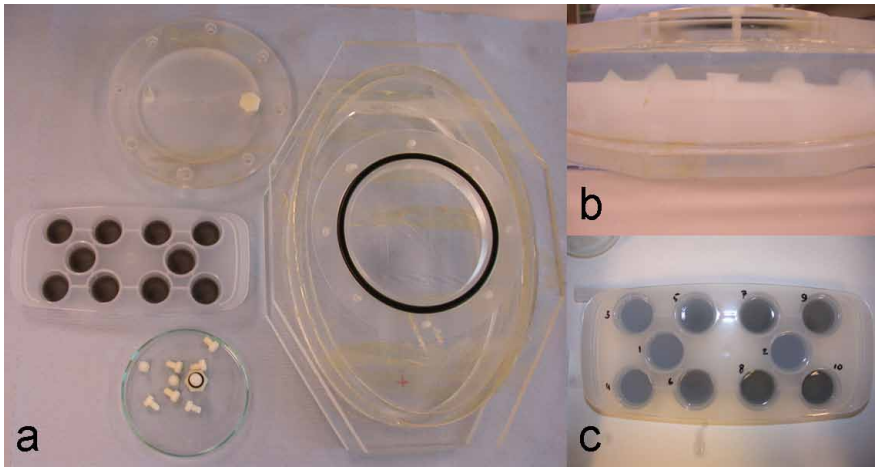

Figure 1 *a) Anthropomorphic ellipse-shaped phantom and ice cube contained. b) Ice cube container filled with agarose gel and small amounts of ^{166}Ho-PLLA-MS. c) Anthropomorphic phantom filled with a 2-cm layer hardened agarose gel (white colored), tumor-simulating agarose gel samples (white colored) and filled-up with liquid agarose gel (transparant).*

SPECT Imaging

SPECT images were acquired using a dual-headed gamma camera equipped with medium energy general purpose collimators (Vertex MCD, Philips Healthcare, Best, The Netherlands). Scanning line sources containing 5.5 GBq Gadolinium-153 were used for attenuation correction (energy window: 100 keV ± 10%). The ^{166}Ho photo peak window was set to 81 keV ± 7.5%. A window centred at 118 keV ± 6%

was used to obtain an estimate for the down-scatter in both the emission and transmission windows. The 360˚ SPECT study consisted of 120 projections for 30 s/angle. The matrix size was 128x128 with an isotropic pixel size of 4.72 mm. The images were reconstructed on a 128x128x128 matrix with isotropic voxel size of 4.72 mm, according to a previously described quantitative iterative reconstruction protocol by De Wit et al. (12). In order to obtain optimal image resolution 50 iterations were used.

MR Imaging

MR imaging experiments were performed on a clinical 3 T MR scanner (Achieva, Philips Healthcare, The Netherlands). A quantitative imaging technique was applied, utilizing multiple gradient echo (MGE) sampling of the free induction decay (MGEFID) to perform T_2^* relaxometry. This method was recently shown to enable accurate high resolution quantitative imaging of Ho-PLLA-MS over a wide concentration range (20). Multislice MR imaging was performed with the following imaging parameters: FOV = 384 x 312 mm; flip angle = 45°; TR/TE1/ΔTE = 400/1.11/0.68 with 16 echoes, isotropic voxel size of 3 mm, 22 slices and total imaging time = 22.8 s.

Data Analysis

MRI

Effective transverse relaxation rate maps (R_2^* maps) were determined pixelwise using a linear-weighted least squares (WLS) fitting algorithm on MGEFID data, assuming monoexponential signal decay, which was demonstrated previously to be valid for Ho-PLLA-MS induced signal decay (20). The R_2^* maps enabled pixelwise estimation of the amount of Ho-PLLA-MS present in the agarose phantom in the follow way. A baseline $R_2^*(0)$ value was determined in a region of the phantom that contained no Ho-PLLA-MS on visual inspection. Using the relation $R_2^*(Ho)=R_2^*(0)+r_{2\ HoMS}^*$[Ho-PLLA-MS], with $r_{2\ HoMS}^*$ the relaxivity of Ho-PLLA-MS, the concentration of Ho-PLLA-MS, [Ho-PLLA-MS], was determined pixelwise in the entire phantom (20, 21). For $r_{2\ HoMS}^*$ a value of 180 $s^{-1}.mg^{-1}.ml$ was used at 3T, which is twice the value as previously determined for 1.5T (19-21) and which was confirmed experimentally. After multiplication by the voxel volume, the Ho-PLLA-MS concentration maps provided the amount of Ho-PLLA-MS present in each voxel, expressed in mg. To allow MR-based dose calculations, 3D Ho-PLLA-MS concentration maps were multiplied by the specific activity (MBq/mg) to provide distribution maps of activity per voxel (Mbq/voxel).

SPECT

The SPECT reconstructions provided an absolute quantitative activity distribution in Mbq/voxel. To simplify dose calculations, the SPECT reconstructions were up-sampled to an isotropic voxelsize of 3 mm.

Dose calculations

Dose calculations were performed using the 3D activity distributions in Mbq per voxel as determined with SPECT and MRI. A 3D ^{166}Holmium dose kernel was calculated (23) using the Monte Carlo code MCNP5 ((vs. 1.20; LANL, Los Alamos, NM), according to the method described in MIRD Pamphlet 17 (24), assuming a tissue density for liver tissue of 1.06 g/cm^3, according to ICRU report 44 (25). A point-symmetric dose kernel was generated on a 29x29x29 matrix (with the source located in the center), utilizing 3 mm isotropic voxels with units [mGy/Mbq]. To calculate the absorbed dose in mGy, the 3D activity maps obtained with MRI and SPECT were convolved with the dose kernel.

Volume of interest (VOI) analysis

For the MRI data, the amount of Ho-PLLA-MS in mg per voxel was calculated as aforementioned. For SPECT data, the 3D activity distribution was divided by the specific activity (MBq/mg) to obtain the amount of Ho-PLLA-MS in mg per voxel. Then, the total amount of Ho-PLLA-MS per tumor was determined using a VOI analysis. On both MRI and SPECT the eight tumors were readily located on the concentration maps of both modalities. The locations of the tumors without Ho-PLLA-MS were not discernable on both MRI and SPECT and were therefore estimated based on prior knowledge, obtained during phantom preparation. Cylinder shaped VOI's were manually drawn around each tumors in such a way that the entire tumor was included, taking into account a 5 mm margin. Summation of the included amount of Ho-PLLA-MS in mg per voxel provided the total amount of Ho-PLLA-MS in mg for each tumor and for both modalities.

Results

First, MR and SPECT images of the agarose gel phantom containing tumor-simulating gel samples with known amounts of ^{166}Ho-PLLA-MS were acquired. Both image modalities depicted eight samples containing ^{166}Ho-PLLA-MS, as shown in Figure 2a and 2b. SPECT images selectively depicted the activated Ho-PLLA-MS and did not depict the agarose gel in the phantom setup. Contrary to SPECT, MR images depicted the agarose gel in the phantom setup, and showed signal voids induced by the presence of Ho-PLLA-MS. In clinical practice, this means that MR provides anatomical reference and SPECT does not.

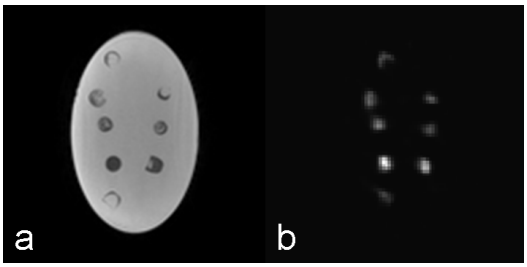

Figure2 *a) T_2*-weighted MR image of the agarose gel phantom with ^{166}Ho-PLLA-MS (isotropic voxel size=3 mm). b) SPECT reconstruction of the agarose gel phantom with ^{166}Ho-PLLA-MS (isotropic voxel size=4.7 mm).*

Next, three dimensional dose distributions were calculated using both the MRI and SPECT data. Excellent agreement was observed both qualitatively and quantitatively when comparing MR-based and SPECT-based dose maps, as shown in Figure 3 and 4. However, several differences were recognized when comparing quantitative dose maps calculated using MRI and SPECT, as shown in Figure 3e-h and 4e-h, respectively. First, the dose distribution in the background gel observed in the MR-based dose maps showed higher variation as well as higher absolute dose values as compared to the SPECT based dose maps. Second, due to its superior spatial resolution MR-based dose maps more accurately delineated the actual shape of the tumor-simulating gel samples. This observation was best appreciated when comparing the sample in the lower right corner in Figure 3f and 3g with Figure 4f and 4g. The SPECT-based dose map depicted a spherical and smooth dose intensity, whereas the MR-based dose pattern resembled the true shape of the gel sample containing ^{166}Ho-PLLA-MS, which was shaped semi-spherical.

Finally, a VOI analysis of the MRI and SPECT data was performed. This analysis revealed an excellent agreement between the amount of Ho-PLLA-MS experimentally determined with SPECT in each tumor and the theoretical amount of Ho-PLLA-MS, as shown in Figure 6a. A slope of 1.0003 with R^2=0.9978 was found for SPECT analysis. For MRI a good correlation was found as well, with a slope of 1.0521 of and a R^2=0.9872, indicating an overestimation of 5%. Table 1 summarizes the amount of Ho-PLLA-MS present in each tumor as determined using the dose calibrator and the amounts experimentally determined using SPECT and MRI.

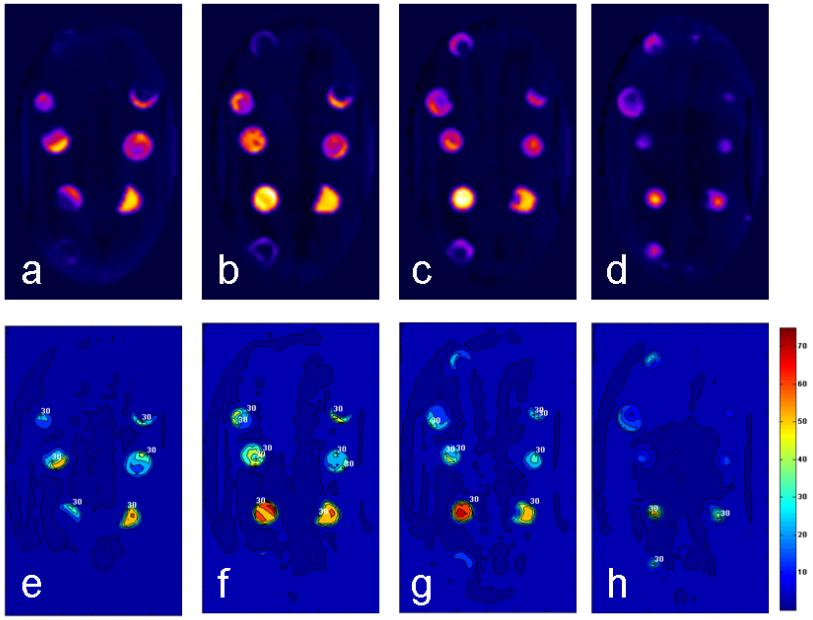

Figure 3 *Qualitative (a-d) and quantitative (e-h) MR-based dose maps of four slices. Even-numbered slices are shown (For color figure see addendum).*

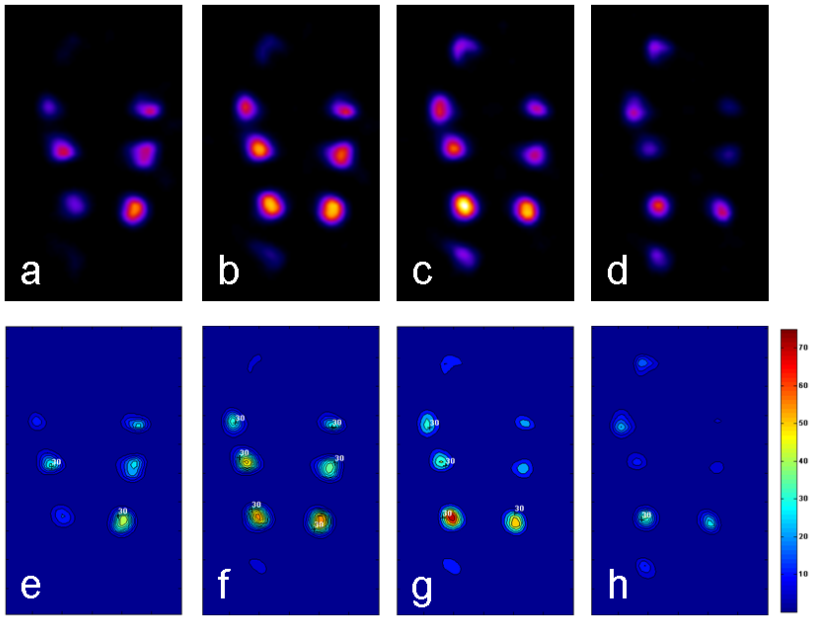

Figure 4 *Qualitative (a-d) and quantitative (e-h) SPECT-based dose maps of four slices. Even-numbered slices are shown (For color figure see addendum).*

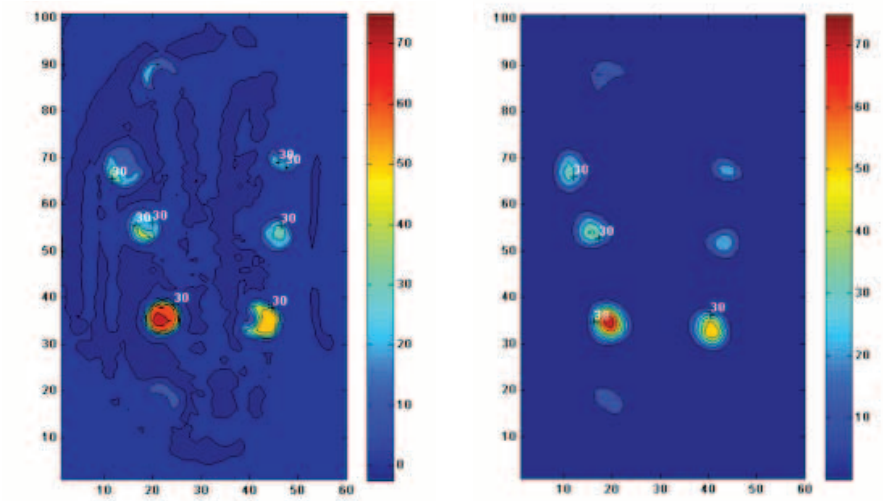

Figure 5 *Quantitative dose distributions (in Gy) determined using MRI and SPECT data.*

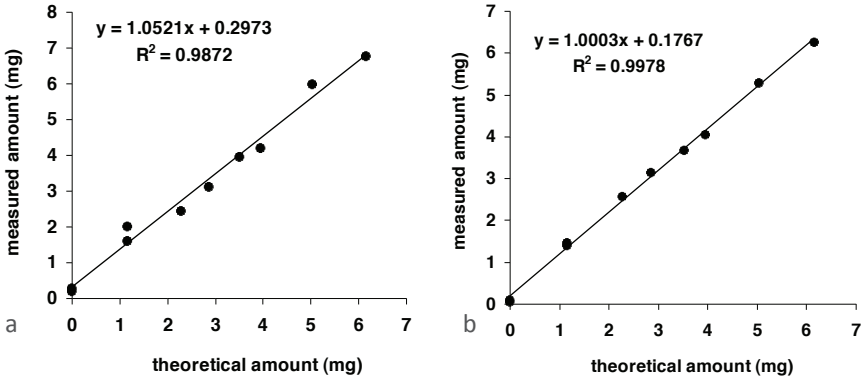

Figure 6 *Experimentally determined amounts of Ho-PLLA-MS in the simulated tumors plotted against the theoretical amount of Ho-PLLA-MS as determined with a dose calibrator. MRI (a) and SPECT (b).*

Table 1 *Total amount of Ho-PLLA-MS estimated per tumor using MRI and SPECT. The first column shows the reference data as determined using the dose calibrator.*

Amount of Ho-PLLA-MS (mg)	MRI, 3x3x3 mm	SPECT 3x3x3 mm
0	0.08	0.04
0	0.18	0.09
1.16	1.48	1.47
1.16	1.89	1.38
2.28	2.33	2.55
2.86	3.01	3.14
3.52	3.84	3.67
3.95	4.09	4.04
6.16	6.65	6.24
5.04	5.87	5.28

Discussion and conclusion

In this study MRI was successfully used to perform accurate dose calculations of ^{166}holmium-loaded microspheres in an anthropomorphic phantom setup. Good agreement was observed between MR-based and conventional SPECT-based dosimetry of ^{166}Ho-PLLA-MS. The results suggest that MRI may be used to perform treatment planning of transcatheter radioembolization of hepatic malignancies with ^{166}Ho-PLLA-MS in a clinical setting. The fact that MRI provides high resolution and excellent soft tissue contrast, has relatively short acquisition times, and allows real-time monitoring during microsphere delivery to the tumor site, makes MRI an attractive modality to guide transarterial radioembolization of hepatic malignancies. Furthermore, the use of a surrogate test dose for treatment planning and dose predictions, which was acknowledged as being sub-optimal in radioembolization using ^{90}Y microspheres (8, 9), would be unnecessary when utilizing ^{166}Ho-PLLA-MS.

The study has some limitations. The straightforward phantom setup simplifies dose calculations for both MRI and SPECT. The homogeneous agarose gel surrounding the tumor-simulating gel samples caused the background signal for both MRI and SPECT to be constant. For MRI, this resulted in a very homogeneous background $R_2^*(0)$ value as compared to the variation of the $R_2^*(0)$ value in human liver tissue (26). Variation in tissue R_2^* would translate into variation in the absorbed dose, when applying MR-based dosimetry. Therefore, in reality, very low concentrations of Ho-PLLA-MS, leading to small local increases

in the R_2^*, would not be detectable when they do not exceed the inherent tissue variation. Therefore, an increased detection limit is expected when applying MR-based dosimetry on liver tissue as compared to the phantom setup (19).

For SPECT-based dose calculations, the presence of a homogeneous background will lead to a more complicated VOI-analysis due to partial volume effects that cause spill-over of tumor-signal to the background, and visa-versa. Although in practice the background is expected to be quite heterogeneous, more research is required to optimize SPECT-based dosimetry for radioembolization applications. Even in the absence of background activity, an apparent background will be present in the reconstructions due to e.g. Bremsstrahlung and scatter. However, the results of the phantom study clearly showed much lower activity levels observed in the background regions as compared to MR-based dosimetry. It is expected that this may be translated to an in vivo setup, indicating that SPECT will be much more sensitive to low levels of radioactivity as compared to MR-based dosimetry. Further investigations are needed to determine absolute lower detection limits of both dosimetry methodologies.

Another important limitation for MR-based dosimetry is the fact that small amounts of Ho-PLLA-MS are difficult to detect in regions containing tissue-air interfaces. Therefore, we hypothesize that for the purpose of identifying and quantifying possible lung shunting nuclear imaging techniques will be essential.

In conclusion, this work demonstrates MR-based dosimetry of ^{166}Ho-PLLA-MS, as performed in an anthropomorphic gel phantom, to be feasible. The results suggest that in the near future MRI potentially enables dosimetric calculations prior to, during and after transcatheter radioembolization of hepatic malignancies, to facilitate dose estimations for treatment planning, real-time quantitative image guidance of microsphere infusion and to evaluate radioembolization treatment.

Acknowledgements

We are grateful to Mark Konijnenberg for providing us with the holmium-166 dose kernel.

References

1. Vente MA, Wondergem M, van dT, I, van den Bosch MA, Zonnenberg BA, Lam MG, van het Schip AD, Nijsen JF. Yttrium-90 microsphere radioembolization for the treatment of liver malignancies: a structured meta-analysis. Eur Radiol **2009**;19(4):951-959.
2. Garrean S, Muhs A, Bui JT, Blend MJ, Owens C, Helton WS, Espat NJ. Complete eradication of hepatic metastasis from colorectal cancer by Yttrium-90 SIRT. World J Gastroenterol **2007**;13(21):3016-3019.
3. Kennedy AS, Coldwell D, Nutting C, Murthy R, Wertman DE, Jr., Loehr SP, Overton C, Meranze S, Niedzwiecki J, Sailer S. Resin 90Y-microsphere brachytherapy for unresectable colorectal liver metastases: modern USA experience. Int J Radiat Oncol Biol Phys **2006**;65(2):412-425.
4. Salem R, Lewandowski RJ, Atassi B, Gordon SC, Gates VL, Barakat O, Sergie Z, Wong CY, Thurston KG. Treatment of unresectable hepatocellular carcinoma with use of 90Y microspheres (TheraSphere): safety, tumor response, and survival. J Vasc Interv Radiol **2005**;16(12):1627-1639.
5. Breedis C, Young G. The blood supply of neoplasms in the liver. Am J Pathol **1954**;30(5):969-977.
6. Vente MAD, de Wit TC, van den Bosch MAAJ, Bult W, Seevinck PR, Zonnenberg BA, de Jong HWAM, Krijger GC, Bakker CJG, van Het Schip AD, Nijsen JFW. Holmium-166 poly(L-lactic acid) microsphere radioembolisation of the liver: technical aspects studied in a large animal model. Eur Radiol **2009**; accepted.
7. Bult W, Vente MA, Zonnenberg BA, van Het Schip AD, Nijsen JF. Microsphere radioembolization of liver malignancies: current developments. Q J Nucl Med Mol Imaging **2009**;53(3):325-335.
8. Gupta T, Virmani S, Neidt TM, Szolc-Kowalska B, Sato KT, Ryu RK, Lewandowski RJ, Gates VL, Woloschak GE, Salem R, Omary RA, Larson AC. MR Tracking of Iron-labeled Glass Radioembolization Microspheres during Transcatheter Delivery to Rabbit VX2 Liver Tumors: Feasibility Study. Radiology **2008**;249(3):845-854.
9. Dhabuwala A, Lamerton P, Stubbs RS. Relationship of 99mtechnetium labelled macroaggregated albumin (99mTc-MAA) uptake by colorectal liver metastases to response following Selective Internal Radiation Therapy (SIRT). BMC Nucl Med **2005**;5:7.
10. Kim HC, Chung JW, Lee W, Jae HJ, Park JH. Recognizing extrahepatic collateral vessels that supply hepatocellular carcinoma to avoid complications of transcatheter arterial chemoembolization. Radiographics **2005**;25 Suppl 1:S25-S39.
11. Mumper RJ, Ryo UY, Jay M. Neutron-activated holmium-166-poly (L-lactic acid) microspheres: a potential agent for the internal radiation therapy of hepatic tumors. J Nucl Med **1991**;32(11):2139-2143.
12. de Wit TC, Xiao J, Nijsen JF, van het Schip FD, Staelens SG, van Rijk PP, Beekman FJ. Hybrid scatter correction applied to quantitative holmium-166 SPECT. Phys Med Biol **2006**;51(19):4773-4787.
13. Nijsen JF, Zonnenberg BA, Woittiez JR, Rook DW, Swildens-van W, I, van Rijk PP, van Het Schip AD. Holmium-166 poly lactic acid microspheres applicable for intra-arterial radionuclide therapy of hepatic malignancies: effects of preparation and neutron activation techniques. Eur J Nucl Med **1999**;26(7):699-704.

14. Nijsen JF, van Het Schip AD, van Steenbergen MJ, Zielhuis SW, Kroon-Batenburg LM, van de WM, van Rijk PP, Hennink WE. Influence of neutron irradiation on holmium acetylacetonate loaded poly(L-lactic acid) microspheres. Biomaterials **2002**;23(8):1831-1839.
15. Vente MA, Nijsen JF, de Wit TC, Seppenwoolde JH, Krijger GC, Seevinck PR, Huisman A, Zonnenberg BA, van d, I, van Het Schip AD. Clinical effects of transcatheter hepatic arterial embolization with holmium-166 poly(L: -lactic acid) microspheres in healthy pigs. Eur J Nucl Med Mol Imaging **2008**.
16. Zielhuis SW, Nijsen JF, Krijger GC, van Het Schip AD, Hennink WE. Holmium-loaded poly(L-lactic acid) microspheres: in vitro degradation study. Biomacromolecules **2006**;7(7):2217-2223.
17. Zielhuis SW, Nijsen JF, Seppenwoolde JH, Bakker CJ, Krijger GC, Dullens HF, Zonnenberg BA, van Rijk PP, Hennink WE, van Het Schip AD. Long-term toxicity of holmium-loaded poly(L-lactic acid) microspheres in rats. Biomaterials **2007**;28(31):4591-4599.
18. Nijsen JF, Seppenwoolde JH, Havenith T, Bos C, Bakker CJ, van Het Schip AD. Liver tumors: MR imaging of radioactive holmium microspheres--phantom and rabbit study. Radiology **2004**;231(2):491-499.
19. Seevinck PR, Seppenwoolde JH, de Wit TC, Nijsen JF, Beekman FJ, van Het Schip AD, Bakker CJ. Factors affecting the sensitivity and detection limits of MRI, CT, and SPECT for multimodal diagnostic and therapeutic agents. Anticancer Agents Med Chem **2007**;7(3):317-334.
20. Seevinck PR, Seppenwoolde JH, Zwanenburg JJ, Nijsen JF, Bakker CJ. FID sampling superior to spin-echo sampling for T2*-based quantification of holmium-loaded microspheres: theory and experiment. Magn Reson Med **2008**;60(6):1466-1476.
21. Seppenwoolde JH, Nijsen JF, Bartels LW, Zielhuis SW, van Het Schip AD, Bakker CJ. Internal radiation therapy of liver tumors: qualitative and quantitative magnetic resonance imaging of the biodistribution of holmium-loaded microspheres in animal models. Magn Reson Med **2005**;53(1):76-84.
22. Seppenwoolde JH, Bartels LW, van der WR, Nijsen JF, van Het Schip AD, Bakker CJ. Fully MR-guided hepatic artery catheterization for selective drug delivery: a feasibility study in pigs. J Magn Reson Imaging **2006**;23(2):123-129.
23. konijnenberg MW, Vente MAD, de Wit TC, de Jong HWAM, van Het Schip AD, Nijsen JFW. Hepatic dosimetry for holmium-166 and yttrium-90 radioembolization: comparison of MIRD, dose-point kernel, and MCNP. submitted
24. Bolch WE, Bouchet LG, Robertson JS, Wessels BW, Siegel JA, Howell RW, Erdi AK, Aydogan B, Costes S, Watson EE, Brill AB, Charkes ND, Fisher DR, Hays MT, Thomas SR. MIRD pamphlet No. 17: the dosimetry of nonuniform activity distributions--radionuclide S values at the voxel level. Medical Internal Radiation Dose Committee. J Nucl Med **1999**;40(1):11S-36S.
25. International Commission on Radiation Units and Measurements. Tissue substitutes in radiation dosimetry and measurement. Bethesda, MD: 1989. Report nr 44. Available from: ICRU.
26. Schwenzer NF, Machann J, Haap MM, Martirosian P, Schraml C, Liebig G, Stefan N, Haring HU, Claussen CD, Fritsche A, Schick F. T2* relaxometry in liver, pancreas, and spleen in a healthy cohort of one hundred twenty-nine subjects-correlation with age, gender, and serum ferritin. Invest Radiol **2008**;43(12):854-860.

Addenda

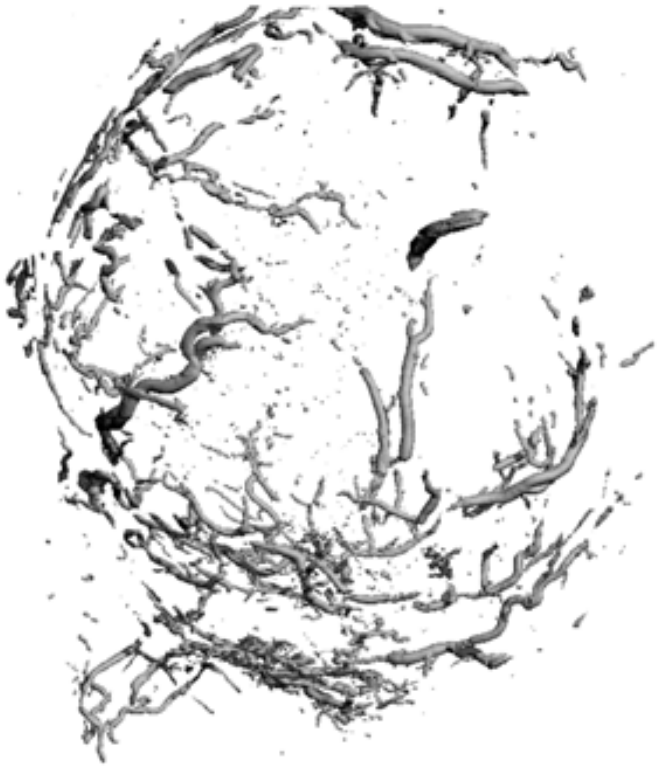

Summary and future directions

Nederlandse samenvatting
Dankwoord
List of publications
Curriculum vitae
Color figures

Summary

Liver cancer is a major cause of morbidity and mortality worldwide. A limited number of patients is eligible for surgical resection, which is the treatment option of choice. Despite recent improvements in response rates and in median survival, systemic chemotherapy has not achieved a significant improvement of patient survival. Furthermore, due to the low tolerance of healthy liver parenchyma to radiation the role of external radiotherapy remains limited. A relatively novel radiotherapy treatment option is selective internal radiation therapy using microspheres loaded with a high-energy beta-emitting radioisotope. In this treatment modality, often referred to as radioembolization, radioactive microspheres are administered directly into the hepatic artery using a catheter. Targeting of tumors is accomplished by exploiting the predominance of the arterial blood supply to liver tumors, while normal parenchyma largely depends on portal blood supply. Ideally, this results in a high tumor-to-liver ratio, leading to an increased radiation dose to the tumor tissue while minimizing exposure to healthy liver parenchyma. To assure a favorable dose distribution in each individual patient, extensive treatment planning is necessary, which requires noninvasive biodistribution assessment. Specifically for this purpose, holmium-166 loaded poly (L-lactic acid) microspheres (^{166}Ho-PLLA-MS) have been developed at the Department of Nuclear Medicine of the University Medical Center Utrecht during the last decade. Due to their multimodal imaging properties, which enable noninvasive biodistribution assessment, ^{166}Ho-PLLA-MS are believed to be an improvement as compared to the already clinically applied yttrium-90 microspheres, which lack high quality medical imaging possibilities.

In this dissertation, the qualitative and quantitative multimodal imaging possibilities of ^{166}Ho-PLLA-MS were explored and exploited to enable accurate biodistribution assessment and dose calculations for planning, image-guidance and evaluation of arterial radioembolization of unresectable liver malignancies.

In **Chapter 2** an overview was given of the strengths and limitations of magnetic resonance imaging (MRI), X-ray computed tomography (CT) and Single Photon Emission Computed Tomography (SPECT), with respect to their capabilities to detect and quantify the spatial distribution of multimodal diagnostic agents in general, and ^{166}Ho-PLLA-MS in particular. Phantom experiments were performed to enable a comparative evaluation of the three imaging modalities using standard equipment and scan protocols under signal-known-exactly conditions. SPECT was demonstrated to have the highest sensitivity and lowest detection limit for ^{166}Ho-PLLA-MS, followed by MRI and CT, respectively. The factors affecting the sensitivity and detection limits were discussed and the findings were extrapolated to other diagnostic tasks, types of contrast agents, other experimental conditions and scan protocols. It was concluded that when comparing imaging modalities with respect to their capabilities to detect and quantify the spatial distribution of multimodal diagnostic agents, other factors should be considered as well, such as the fact that SPECT does not provide anatomical reference and requires much longer acquisition times. Furthermore, the diagnostic sensitivity of SPECT depends on the activated fraction of Ho-PLLA-MS, whereas the sensitivity of MRI and CT are independent of the activated fraction.

In **Chapter 3** we described the preparation and characterization of microspheres with ultra high holmium content, developed to increase specific activity and enhance multimodal diagnostic properties. The prepared microspheres had a smooth surface and were resistant to 6 hours of neutron irradiation. It was shown that the mean particle size can be tailored for different tumor treatment approaches by adapting the processing parameters. An increase in holmium content from 17% to 45% (*w/w*) was obtained, which led to a 2.6 fold increase in radioactivity per microsphere. The enhanced specific activity was determined to allow for the incorporation of tumoricidal radioactive doses in small volumes necessary for direct intratumoral microbrachytherapy. Additionally, it was found that the diagnostic sensitivity on MRI and CT more than doubled which enabled the detection of microgram amounts of microspheres in liver tissue and which is expected to facilitate image-guided drug delivery.

In **Chapter 4** micro-computed tomography (microCT) was shown to enable high resolution qualitative and quantitative assessment of the 3D distribution of Ho-PLLA-MS in vitro and in tumorous tissue after hepatic arterial

radioembolization of a Vx2 tumor in a rabbit. In vitro experiments demonstrated reliable and accurate detection of single Ho-PLLA-MS in agarose gel phantoms, as validated by light microscopy. MicroCT of Vx2 tumor-bearing liver tissue revealed that the microspheres mainly lodged in the highly vascularized periphery of the tumor. An extremely heterogeneous distribution was observed, with arterioles containing aggregates of thousands of microspheres, as well as arterioles with only few microspheres, which was confirmed by histological examinations. Cluster analysis revealed a highly skewed cluster volume distribution towards small volumes. The total amount of microspheres in the tumor determined by microCT was in good agreement with results obtained with a low background gamma counter (gold standard), presenting a 4.4 % underestimation. From these results it was concluded that microCT provides valuable insight on the process of microsphere aggregation in the neovasculature of tumor tissue after hepatic arterial radioembolization and potentially allows 3D dose calculations for treatment optimization.

In **Chapters 5 and 6** we presented qualitative results obtained with two MR-based positive contrast techniques. Selective depiction of Ho-PLLA-MS in liver tissue in the presence of macroscopic magnetic field distortions was investigated in **Chapter 5**, using a method called susceptibility gradient mapping (SGM). In SGM, the echo shift, which is related to the susceptibility gradient, is calculated by determination of the local echo shift using a short-term Fourier transform. By applying SGM, it was possible to distinguish macroscopic field gradients from local magnetic field distortions induced by Ho-PLLA-MS, as opposed to conventional T_2^* contrast, which was unable to discriminate signal voids induced by both types of magnetic field distortion.

In **Chapter 6** a novel 3D imaging technique was presented, applying RAdial Sampling with Off-resonance Reception (RASOR), which was designed to enable accurate depiction and localization of small paramagnetic objects with high positive contrast, while suppressing long T_2^* components. The RASOR imaging technique is a fully frequency encoded 3D ultrashort TE (UTE) center-out acquisition method, which utilizes a large excitation bandwidth and off-resonance reception. By manually introducing an offset to the central reception frequency, the magnetic field disturbance causing the typical radial signal pile-up in 3D center-out sampling can be compensated for, resulting in a hyperintense signal at the exact location of the small paramagnetic object. The underlying principle of RASOR was demonstrated both theoretically and using 1D time domain simulations. Experimental verification was done with a gel phantom containing three paramagnetic objects with very different geometry and susceptibility,

viz., subvoxel stainless steel spheres, paramagnetic brachytherapy seeds and a puncture needle. In all cases, RASOR was shown to generate high positive contrast exactly at the location of the magnetized object, as confirmed by CT imaging.

In **Chapters 7, 8 and 9** MR methodologies were presented, which aim at improving quantitative assessment of the distribution of Ho-PLLA-MS in liver tissue. **Chapter 7** demonstrated both theoretically and experimentally that multiple gradient echo sampling of the FID (MGEFID) is superior to MGE sampling of the spin echo (MGESE) for T_2^*-based quantification of Ho-PLLA-MS. An interleaved sampling strategy was applied to characterize the MR signal behavior of FID and SE signals of gels and perfused rabbit livers containing Ho-PLLA-MS in great detail. Diffusion sensitivity was demonstrated for MGESE sampling, resulting in nonexponential signal decay on both sides of the SE peak and in an underestimation of the Ho-PLLA-MS concentration. Other than MGESE sampling, MGEFID sampling was demonstrated to be insensitive to diffusion, to exhibit exponential signal decay and to allow accurate T_2^*-based quantification of Ho-PLLA-MS. MGEFID was shown to correctly estimate the integral amount of inhomogeneously distributed Ho-PLLA-MS in liver tissue, up to a clinically relevant limit. The experimental findings could be explained with the theory of NMR signal behavior in magnetically inhomogeneous tissues. HoMS were shown to satisfy the static dephasing regime when investigated with MGEFID and to violate the static dephasing conditions for MGESE at longer echo times typically used in SE.

In **Chapter 8** a post-processing method, S_0-fitting, was presented to increase the upper limit of the detectable R_2^* range and hence the upper limit of the concentration of paramagnetic agents such as Ho-PLLA-MS using straightforward MGEFID sampling. S_0-fitting involves the incorporation of the estimated initial amplitude of the FID curve, S_0, in a monoexponential fitting algorithm. The accuracy and robustness of the S_0-fitting method were evaluated and results were compared qualitatively and quantitatively to R_2^* maps and regression curves obtained with quantitative ultrashort TE imaging (qUTE). Applying S_0-fitting dramatically increased the detectable R_2^* range as compared to conventional T_2^* relaxometry, up to 3000 s^{-1}. A good agreement was observed both quantitatively, for in vitro experiments, as well as qualitatively, for ex vivo rabbit liver experiments containing Ho-PLLA-MS, when validated with qUTE imaging. The influence of erroneously estimating S_0 was evaluated and demonstrated to be of minor concern. S_0-fitting was concluded to be a robust and accurate post-processing method capable of estimating ultrahigh R_2^* values and, therefore, to be suitable for MR-based quantitative imaging of high concentrations of endogeneous and exogeneous (super-) paramagnetic substances. The method

does not put any constraints on the MR pulse sequence as long as it is a MGE sampling scheme.

Chapter 9 demonstrated the feasibility to predict and quantify the signal decay time course of FID and SE of diffusive media containing strongly magnetized impenetrable micron-sized particles by exploring and exploiting two well-known diffusion regimes, the static dephasing regime (SDR) and the strong field behavior (SFB). MR experiments and Monte Carlo simulations demonstrated that SDR and SFB enable accurate prediction of the signal decay time course of FID and SE when applied to a specific spin-sphere system, viz., Ho-PLLA-MS in an agarose gel matrix, while varying concentration, field strength and echo time. The applicability and restrictions of both theories were explored over a wide range of particle radii ($1\ \mu m < R < 100\ \mu m$) and susceptibility differences ($1\ ppm < \Delta\chi < 1000\ ppm$). MC simulations were used to validate SDR and SFB in predicting transverse relaxation and to verify their respective criteria of validity. Results suggest that by carefully choosing imaging and timing parameters, accurate prediction of signal decay as well as quantification of paramagnetic particles such as iron-labeled microspheres or cells and large endogenous iron accumulations is feasible using either SDR or SFB.

In **Chapter 10** the feasibility to utilize quantitative MR data for dosimetric calculations of ^{166}Ho-PLLA-MS for treatment planning of transcatheter radioembolization of hepatic malignancies was investigated and compared to the currently used modality, SPECT. MRI and SPECT experiments were conducted using an anthropomorphic agarose gel phantom containing tumor-simulating gel samples with known amounts of ^{166}Ho-PLLA-MS. Dose calculations using MRI and SPECT data were compared qualitatively and quantitatively to reference data obtained with a dose calibrator. Excellent agreement was observed both qualitatively and quantitatively when comparing MR-based to SPECT-based dose maps. A regression coefficient of 1.05 with correlation coefficient r^2 of 0.987 was found when relating MR-based ^{166}Ho-PLLA-MS dose calculations to the reference data. From the results it was concluded that MR-based dosimetry is a promising tool for planning, guidance and evaluation of transcatheter radioembolization treatment of hepatic malignancies with ^{166}Ho-PLLA-MS.

Future directions

Although we have extensively investigated the multimodal imaging possibilities of ^{166}Ho-PLLA-MS and successfully challenged several research questions, it must be acknowledged that our findings expose certain gaps and that there is ample room for future investigations. Taking into account the upcoming phase I clinical

trial on hepatic arterial radioembolization of unresectable liver malignancies using ^{166}Ho-PLLA-MS at the end of 2009, at least five important MRI-related research areas can be discerned which will be shortly presented. These topics are (1) implementation of the proposed quantitative MRI methodologies into clinical practice; (2) investigation of the influence of longitudinal aggregation of Ho-PLLA-MS on MR-based quantification; (3) investigation of the predictive value of a ^{166}Ho-PLLA-MS scout dose; (4) real-time monitoring of ^{166}Ho-PLLA-MS administration under fluoroscopy and MRI guidance; (5) MR-based dosimetry.

1) Currently, a phase I clinical trial on hepatic arterial radioembolization of unresectable liver malignancies using ^{166}Ho-PLLA-MS is being prepared. Although treatment planning and biodistribution prediction will initially be done using quantitative SPECT, MR imaging is included in the protocol during screening prior to the treatment, one week after administration of the therapeutic dose as well as during follow up 4 months later. To fully benefit from the possibilities MRI offers, the proposed quantitative and qualitative MRI methodologies will have to be adjusted and prepared for clinical practice. The main aspects that will have to be taken into account involve breathing movement, macroscopic magnetic field inhomogeneities due to air in the lungs, chemical shift between water and fat tissue and the limited scan time permitted during patient scanning. Several ways to cope with these issues have been addressed in the literature. For example, to overcome breathing artifacts, respiratory triggering or scanning during breathhold can be applied. Macroscopic magnetic field inhomogeneities can be compensated for using phase information. Furthermore, by either applying fat-suppression or by using in-phase scan times, water-fat chemical shift influences can be suppressed. And finally, to speed up scan times, advanced scan techniques may be applied, including high SENSE factors and partial echo acquisition. Implemention of these issues is not as straightforfard as it may seem and therefore requires serious attention in the near future.

2) MicroCT revealed a high degree of clustering of Ho-PLLA-MS in the microvasculature and arterioles in the periphery of the tumor, which resulted in elongated paramagnetic structures, some of which measured several millimeters long and several hundreds of micrometers in diameter (Chapter 4). Since size and shape of paramagnetic objects may have a pronounced influence on the spatial and temporal characteristics of the NMR signal, it may be expected that clustering will influence MR-based quantification. Furthermore, knowing that the elongated, cigar-like shape is a less efficient signal killer on T_2^*-weighted images as compared to the spherical shape, a high degree of clustering in arterioles may

cause underestimation. Therefore, we hypothesize that the underestimation of the integral amount of Ho-PLLA-MS present in liver tissue, as was observed at higher administered Ho-PLLA-MS doses (Chapter 7), may be a direct consequence of the elongated aggregations of Ho-PLLA-MS. Further research should be conducted to better understand the influence of longitudinal clustering of Ho-PLLA-MS on NMR signal decay, aiming to eventually enable accurate MR-based quantification, independent of the concentration and degree of clustering of Ho-PLLA-MS.

3) An essential element of successful radioembolization of hepatic malignancies is preprocedural biodistribution assessment, aiming at prediction of the therapeutic dose distribution in the liver. To this end, a scout dose of ^{166}Ho-PLLA-MS is administered prior to the actual therapeutic dose. In the phase I clinical trial, it will be investigated whether the distribution of the scout dose is representative for the therapeutic dose and eventually correlates with the radiation dose distribution in patients. Due to its superior sensitivity and good quantitative properties, SPECT will be used to investigate this issue. However, the long acquisition times and lack of anatomical references are suboptimal and prevent real-time monitoring with SPECT. Since both MRI and X-ray fluoroscopy are fast, do provide anatomical reference and have been shown to enable depiction of HoMS, we suggest that these modalities should be considered for treatment planning. The main drawback compared to SPECT is the lower sensitivity of MRI and specifically of X-ray radiographic techniques for Ho-PLLA-MS. Future investigation should clarify whether this compromises the use of fluoroscopy and MRI for biodistribution prediction.

4) Administration of ^{166}Ho-PLLA-MS during radioembolization therapy is currently being done under fluoroscopy guidance, enabling accurate catheter positioning and monitoring of retrograde flow. Due to the relatively low sensitivity of radiographic imaging techniques for ^{166}Ho-PLLA-MS, detection of small amounts (scout doses) will be very difficult. Therapeutic amounts of ^{166}Ho-PLLA-MS, however, are expected to be detectable using fluoroscopy, and may facilitate a rough estimate of the microsphere biodistribution and radiation dose distribution. A promising alternative, due to the higher sensitivity, is MR guidance of ^{166}Ho-PLLA-MS administration. This approach would enable real-time monitoring of infusion of small amounts of ^{166}Ho-PLLA-MS and would facilitate highly selective targeting of tumors while sparing healthy liver parenchyma. In combination with recent developments in MR-based dosimetry this would provide real-time determination of the radiation dose distribution (Chapter 10). These developments encourage further research into the use of MRI for real-time monitoring of ^{166}Ho-PLLA-MS administration.

5) MR guidance of the administration procedure of ^{166}Ho-PLLA-MS in combination with MR-based dosimetry is expected to provide feedback of the radiation dose distribution during the administration procedure, eventually enabling more precise deposition of the radiation dose. Furthermore, since the sensitivity of MRI for holmium-loaded microspheres is independent of the activated fraction of holmium-166, MR-based dosimetry is also expected to enable assessment of the biodistribution and radiation dose distribution in the liver after the decay of holmium-166, which is particularly convenient for treatment evaluation. The feasibility of MR-based dosimetry of ^{166}Ho-PLLA-MS in an agarose gel phantom was demonstrated in Chapter 10. Translation into clinical practice, however, still needs to be done, taking into account all the difficulties that are typically encountered during in vivo scanning.

Once these challenges have been met, which we expect to be possible within a few years, MRI will meet all the criteria to be incorporated into the clinical protocol, in addition to nuclear and X-ray radiographic imaging techniques. For clinical practice this implies that a comprehensive combination of imaging modalities will be available, covering all requirements for a fully image-guided radioembolization treatment procedure. Clinical research will have to reveal how to exploit these opportunities in a way which will eventually lead to an optimal radioembolization treatment procedure for patients suffering from unresectable liver malignancies.

Addenda

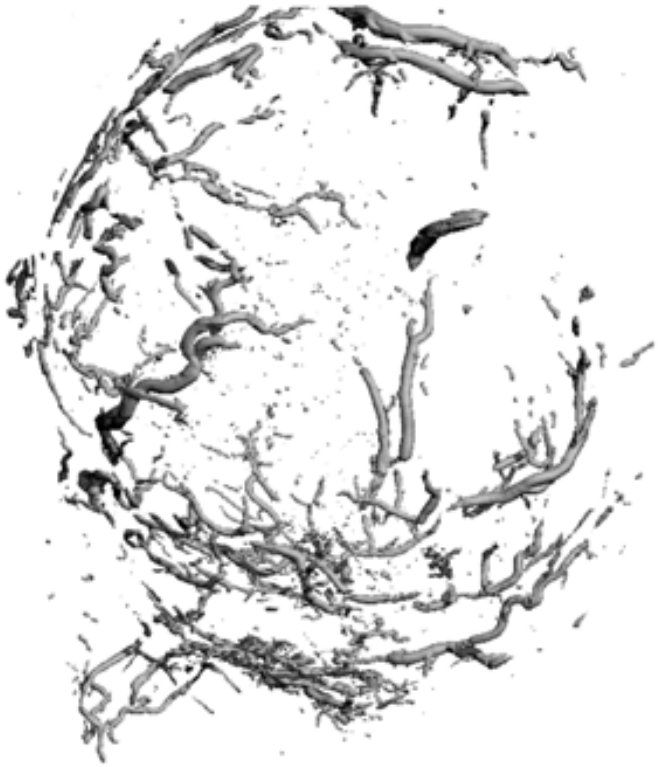

Summary and future directions

Nederlandse samenvatting

Dankwoord
List of publications
Curriculum vitae
Color figures

Levermaligniteiten, zowel primaire als gemetastaseerde, zijn een veelvoorkomende doodsoorzaak in de westerse wereld. De voorkeursbehandeling bestaat uit het chirurgisch verwijderen van de tumoren, echter slechts een beperkt aantal patiënten komt in aanmerking voor deze ingreep. Conventionele radiotherapie en chemotherapie hebben vanwege uiteenlopende oorzaken geen significante verbetering van de overlevingskansen opgeleverd. Recentelijk zijn wel verbeteringen gerapporteerd in mediane overleving als gevolg van nieuwe chemotherapie combinaties.

Een veelbelovende alternatieve therapie is selectieve interne radiotherapie met behulp van kleine bolletjes, ook wel microsferen genoemd, beladen met radio-isotopen die hoogenergetische bèta deeltjes uitzenden. Bij deze therapie, ook wel radioembolisatie genoemd, worden de radioactieve microsferen direct in de leverarterie ingebracht met behulp van een katheter. Tumorselectiviteit van de radioactieve microsferen wordt verkregen door gebruik te maken van de exclusief arteriële afhankelijkheid van levermaligniteiten. Hierdoor ondervinden de tumoren een verhoogde stralingsbelasting, terwijl de dosis op het gezonde leverweefsel minimaal blijft. Om een voordelige dosisverdeling te waarborgen is uitgebreide planning van de therapie noodzakelijk, zodat voorspeld kan worden wat de ruimtelijke verdeling van de radioactieve microsferen en dus de dosisverdeling zal zijn. Met dit als doelstelling zijn gedurende de laatste tien jaar holmium-166 beladen poly (L-lactic acid) microsferen (^{166}Ho-PLLA-MS) ontwikkeld op de afdeling Nucleaire Geneeskunde van het Universitair Medisch Centrum Utrecht. De uitstekende multimodale beeldvormingseigenschappen van ^{166}Ho-PLLA-MS, die onderzoek van de ruimtelijke verdeling van ^{166}Ho-PLLA-MS mogelijk maken, worden gezien als een belangrijke verbetering ten opzicht van de reeds klinisch gebruikte yttrium-90 beladen microsferen, die deze eigenschappen niet bezitten.

Het doel van dit proefschrift is de kwalitatieve en kwantitatieve multimodale beeldvormingsmogelijkheden van ^{166}Ho-PLLA-MS te onderzoeken op hun bruikbaarheid voor nauwkeurige bepaling van de ruimtelijke verdeling van de microsferen en de daaraan gekoppelde dosisverdeling ten behoeve van planning, beeldgestuurde behandeling en evaluatie van intra-arteriële radioembolisatie van niet-reseceerbare levertumoren.

In **Hoofdstuk 2** wordt een overzicht gegeven van de beperkingen en sterke punten van magnetic resonance imaging (MRI), x-ray computed tomography (CT) en Single Photon Emission Computed Tomography (SPECT) met betrekking tot het detecteren en kwantificeren van de ruimtelijke verdeling van multimodale contrastmiddelen in het algemeen, en ^{166}Ho-PLLA-MS in het bijzonder. Met behulp van fantoomexperimenten is een vergelijkend onderzoek uitgevoerd, gebruik makende van stadaard apparatuur en scan protocollen en onder bekende omstandigheden. Daaruit is gebleken dat SPECT de hoogste gevoeligheid en laagste detectielimiet heeft, gevolgd door MRI en CT. Factoren die de gevoeligheid en detectielimieten beïnvloeden zijn bediscussieerd in het licht van andere diagnostische taken, experimentele omstandigheden en klinische doelstellingen en scan protocollen. Geconcludeerd is dat om tot een relevante vergelijking te komen van beeldvormingmodaliteiten, ook andere eigenschappen in overweging genomen dienen te worden, zoals het feit dat SPECT geen anatomische referentie verschaft en een veel langere totale scan tijd vergt. Daarnaast is de gevoeligheid van SPECT afhankelijk van de geactiveerde fractie van Ho-PLLA-MS, terwijl de gevoeligheid van zowel MRI als CT onafhankelijk is van de geactiveerde fractie.

Hoofdstuk 3 beschrijft de vervaardiging en karakterisering van microsferen met een ultrahoge holmium belading, ontwikkeld om specifieke activiteit en multimodale gevoeligheid te verhogen. De vervaardigde microsferen vertoonden een glad oppervlak en waren bestand tegen zes uur bestraling met neutronen ten behoeve van activering. Gedemonstreerd werd dat de gemiddelde deeltjesgrootte gestuurd kan worden voor verschillende kankerbehandelingsmethodieken door bepaalde preparatiestappen aan te passen. Een verhoging van de holmium belading van 17% naar 45% werd gerealiseerd, wat leidde tot een verhoging van de specifieke activiteit met een factor 2.6. Deze verhoging in specifieke activiteit maakt het mogelijk tumoricidale radioactieve dosis in kleine volumes te incorporeren, wat een vereiste is voor intra-tumorale microbrachytherapie. Daarnaast is de gevoeligheid van zowel MRI als CT voor deze nieuwe microsferen meer dan verdubbeld, wat de detectie van microgrammen in leverweefsel mogelijk maakt. Het mag verwacht worden dat dit op zijn beurt beeldgestuurde toediening van holmium-beladen microsferen mogelijk maakt.

In **Hoofdstuk 4** wordt gedemonstreerd dat micro-computed tomography (microCT) hoge resolutie kwalitatieve en kwantitatieve analyse van de driedimensionale ruimtelijke verdeling van Ho-PLLA-MS *in vitro* en in tumoreus weefsel na radioembolisatie van een Vx2 tumor in een konijn mogelijk maakt. Betrouwbare en nauwkeurige detectie van individuele microsferen is aangetoond in agarose gel met fantoomexperimenten en gevalideerd met licht microscopie. MicroCT beelden van tumor-dragend leverweefsel na radioembolisatie hebben laten zien dat microsferen voornamelijk vast lopen in de goed gevasculariseerde rand van de tumoren. Een extreem heterogene verdeling van microsferen werd aangetroffen, met arteriolen die clusters van duizenden microsferen bevatten, maar ook vaten die slechts enkele microsferen bevatten, wat bevestigd werd door histologisch onderzoek. Cluster analyse ontwaarde een uiterst scheve verdeling ten faveure van kleine opeenhopingen. Kwantitatieve analyse van de totale hoeveelheid Ho-PLLA-MS bepaald met microCT vertoonde een sterke overeenkomst met de hoeveelheid bepaald met een techniek op basis van gamma straling (de gouden standaard). Geconcludeerd mag worden dat microCT meer inzicht verschaft in de processen die een rol spelen bij de mate van clustering en de ruimtelijke verdeling van microsferen in de neovasculatuur van tumoreus weefsel na radioembolisatie, en welke invloed clustering uiteindelijk heeft op de dosisverdeling.

In **Hoofdstuk 5 en 6** worden kwalitatieve observaties gepresenteerd verkregen met twee op MRI gebaseerde positief contrast technieken. In **Hoofdstuk 5** wordt het selectief afbeelden van Ho-PLLA-MS in lever weefsel in de aanwezigheid van macroscopische magnetische veld inhomogeniteiten onderzocht, gebruik makende van een methode, genaamd “susceptibility gradient mapping” (SGM). In SGM wordt de echo shift, die veroorzaakt wordt door magnetische veld verstoringen, bepaald met behulp van een lokale Fourier transformatie. Door gebruik te maken van SGM is het mogelijk gebleken onderscheid te maken tussen macroscopische en lokale magnetische veldverstoringen, veroorzaakt door de aanwezigheid van Ho-PLLA-MS, wat niet mogelijk is met de conventionele T_2^*gewogen contrast mechanismes. Dit is gedemonstreerd *in vivo* in varkens na intra-arteriële radioembolisatie van de lever.

In **Hoofdstuk 6** wordt een nieuwe driedimensionale MR beeldvormings-techniek gepresenteerd, die gebruik maakt van RAdial Sampling met Off-resonance Reception (RASOR), specifiek ontworpen voor het realistisch afbeelden en nauwkeurig lokaliseren van kleine paramagnetische objecten met hoog positief contrast. Daarbij kan indien gewenst het achtergrond signaal onderdrukt worden. De RASOR techniek is een volledig frequentie-gecodeerde driedimensionale acquisitiemethodiek, die gebruik maakt van hele korte

echotijden, een grote excitatie bandbreedte en off-resonance signaalontvangst. Door bewust de ontvangstfrequentie anders in te stellen dan de eigenlijke centrale ontvangstfrequentie, kunnen de lokale magnetische veldinhomogeniteiten die geometrische verstoringen in het MR beeld veroorzaken, gecompenseerd worden, wat uitendelijk resulteert in het ontstaan van lokale hyperintensiteiten precies op de posities van de kleine paramagnetische objecten. Het principe van RASOR is theoretisch en met 1D simulaties onderbouwd. Experimentele verificatie is gedemonstreerd met behulp van drie objecten van verschillende vorm en susceptibiliteit in agarose gelfantomen, namelijk kleine roestvast stalen kogeltjes, brachytherapie zaadjes en een bioptnaald. In alle gevallen was de RASOR techniek in staat hoog positief contrast te genereren precies op de positie van de objecten, zoals bevestigd is met CT beelden.

In **Hoofdstuk 7, 8 en 8** worden MR technieken en algoritmen gepresenteerd, die het verbeteren van het bepalen van de ruimtelijke verdeling van Ho-PLLA-MS in lever weefsel tot doel hebben. **Hoofdstuk 7** toont zowel theoretisch als experimenteel aan dat meervoudige gradient echo bemonstering van de free induction decay (MGEFID) superieur is aan MGE bemonstering van de spin echo (MGESE) voor T_2^* gebaseerde kwantificering van Ho-PLLA-MS. Gebruik makend van een specifieke bemonsteringsstrategie is het MR signaal heel dicht bemonsterd om het signaal zo goed mogelijk te kunnen karakteriseren. Diffusiegevoeligheid is aangetoond voor MGESE, wat tot niet-exponentieel signaalgedrag en een onderschatting van de aanwezige hoeveelheid Ho-PLLA-MS in lever weefsel leidde. MGEFID signaal gedrag was ongevoelig voor diffusie, vertoonde exponentieel verval en maakte nauwkeurige bepaling van de hoeveelheid Ho-PLLA-MS mogelijk, tot een klinisch relevante grens. De experimentele bevindingen waren in lijn met de theorie die NMR signaal gedrag in magnetisch inhomogene weefsels beschrijft. Aangetoond is dat, signaalgedrag van lever weefsel met Ho-PLLA-MS voldoet aan de “static dephasing theory” wanneer bemonsterd met MGEFID, echter wanneer bemonsterd met MGESE voldoet het signaal gedrag niet aan deze theorie.

In **Hoofdstuk 8** wordt een postprocessing methode gepresenteerd, S_0-fitting, die specifiek ontwikkeld is voor het verhogen van de bovenlimiet van de te bepalen transversale relaxatiesnelheid R_2^* en dus de concentratie van paramagnetische materialen zoals Ho-PLLA-MS. Deze methode, die gebruik maakt van conventionele MGEFID bemonstering, incorporeert de geschatte initiële waarde van de free induction decay curve, S_0, in een exponentieel fit algoritme. De nauwkeurigheid en robuustheid van de S_0-fitting methodiek zijn onderzocht en vergeleken met een andere, kwantitatieve methode die gebruik maakt van hele korte echo tijden (qUTE). Een sterk verhoogde bovengrens van

de R_2^* waarde werd gevonden wanneer het S_0-fitting algoritme gebruikt werd. Een goede overeenkomst werd gevonden, zowel kwalitatief als kwantitatief, met de qUTE methode. Geconcludeerd mag worden dat het S_0-fitting algoritme geschikt is voor het met behulp van MRI bepalen van hoge concentraties van zowel endogene and exogene paramagnetische stoffen.

In **Hoofdstuk 9** wordt gedemonstreerd dat het mogelijk is zowel free induction decay als spin echo signaal gedrag van waterige systemen met paramagnetische deeltjes van microgrootte te voorspellen en te kwantificeren, gebruik makende van twee relaxatie theorieën, het static dephasing regime (SDR) en het strong field behavior (SFB). Resultaten verkregen met Monte Carlo simulaties waren in overeenstemming met MRI experimenten. Ook waren Monte Carlo simulaties in staat om signaal gedrag te voorspellen voor uiteenlopende magnetische veldsterktes, echo tijden en concentraties Ho-PLLA-MS in agarose gel. De toepasbaarheid en limitaties van beide relaxatie theorieën is onderzocht voor een brede range aan deeltjes grootte en susceptibiliteitverschillen. Door vergelijking met de gevalideerde Monte Carlo simulaties en experimenten is er aangetoond dat bij zorgvuldig gebruik van de gestelde criteria, beide theorieën in staat zijn het signaal gedrag te voorspellen.

In **Hoofdstuk 10** wordt onderzocht of kwantitatieve MR data gebruikt kan worden voor dosimetrie van ^{166}Ho-PLLA-MS voor planning van intra-arteriele radioembolisatie van levertumoren. Fantoomexperimenten werden uitgevoerd, gebruik makend van een antropomorfisch agarose fantoom dat gel samples met een bekende hoeveelheid ^{166}Ho-PLLA-MS bevatte, ter simulaties van tumoren. Dosisberekeningen op basis van MR data werden vergeleken met de huidige standaard, SPECT, en met referentie data verkregen met een dosis calibrator. Een uitstekende overeenkomst werd gevonden, zowel kwalitatief als kwantitatief, tussen dosisberekeningen op basis van MRI data, SPECT data en de referentie data. Op basis van deze resultaten mag geconcludeerd worden dat op MR data gebaseerde dosimetrie een veelbelovende optie is voor planning, beeldgestuurde toediening en evaluatie van intra-arteriële radioembolisatie van levertumoren met ^{166}Ho-PLLA-MS.

Addenda

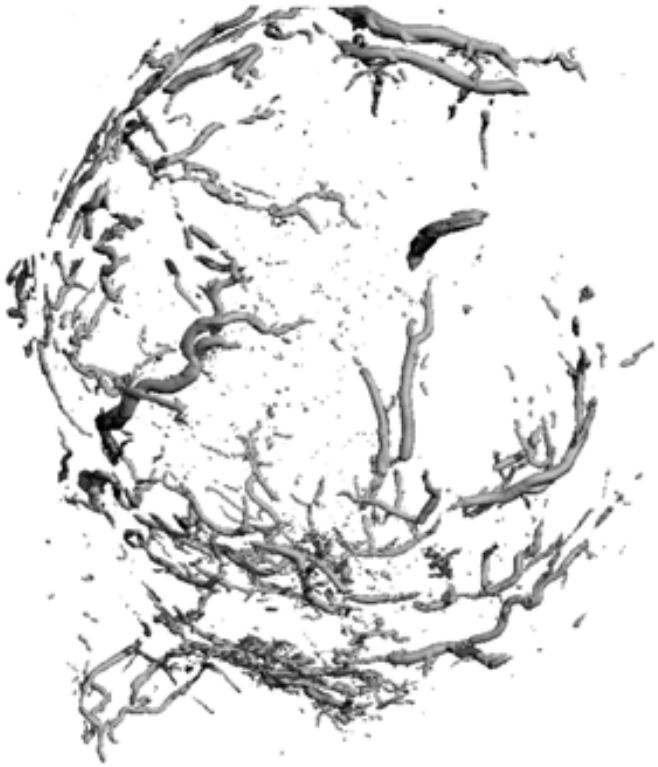

Dankwoord

Eindelijk is het dan zover, mijn proefschrift is een feit. Terugdenkend aan de afgelopen vier en een half jaar overheerst een gevoel van blijdschap, trots en dankbaarheid. Ik grijp deze gelegenheid graag aan om iedereen te bedanken die op wetenschappelijk, dan wel persoonlijk vlak, heeft bijgedragen aan de totstandkoming van dit proefschrift.

De begeleiding

- Dr. C.J.G. Bakker, co-promotor, beste Chris, ik ben je heel dankbaar, jij was voor mij een wetenschappelijk klankbord van ongekende waarde. Je hebt me enorm gestimuleerd zelf na te denken en de vrijheid gegeven mijn eigen ideeën te ontwikkelen. Het laatste jaar van mijn promotie heb ik je bestookt met manuscripten met de vraag daar weer 'even' kritisch naar te kijken, en nooit bespeurde ik enige 'manuscriptmoeheid'. Ik heb veel geleerd van jouw schrijfstijl en genoten van jouw gedrevenheid en creativiteit. Bedankt!
- Prof. dr. ir. M.A. Viergever, promotor, beste Max, ik dank je voor het vertrouwen dat je in me hebt gesteld en de mogelijkheden die me geboden werden binnen het Image Sciences Institute me te ontplooien en te ontwikkelen als wetenschapper.
- Dr. ir. Jan-Henry Seppenwoolde, beste Jan-Henry, ik had me geen betere dagelijkse begeleiding kunnen voorstellen. Ik ben je heel dankbaar voor de wijze waarop je mij wegwijs hebt gemaakt binnen het ISI, binnen het holmium onderzoek en binnen de wereld van de susceptibiliteit, op de MRI scanners en in de soms harde wetenschappelijke wereld. Ik vond het heel jammer dat je besloot de wetenschap en Nederland te verlaten. Gelukkig vergaat het jou, je vrouw en jullie kinderen goed in Ecuador. Nogmaals bedankt.

- Dr. Frank Nijsen, beste Frank, ruim 10 jaar onderzoekservaring met holmium heeft jou een enorme dosis kennis en kunde opgeleverd, waar ik de afgelopen jaren dankbaar gebruik van heb mogen maken. Ik bewonder je doorzettingsvermogen en vind het fantastisch dat eind 2009 uiteindelijk een fase I studie van start gaat, waarin gelukkig ook nog een plekje voor MRI is wegelegd…

De leescommissie

- De leden van de leescommissie: prof. dr. C.T.W. Moonen, prof. dr. ir. W.E. Hennink, prof. dr. P.R. Luijten, prof. dr. W.P.Th.M. Mali, en prof. dr. K. Nicolay. Ik ben u allen dankbaar voor uw bereidheid mijn proefschrift te beoordelen.

Mede-onderzoekers en co-auteurs

- Prof. dr. Tobias Schaeffter, Dear Tobias, thank you for having me for a visit to King's College in London and for your interest in the research we conduct in Utrecht. Furthermore, I am grateful that you were willing to join the defense of my dissertation.
- Prof. dr. Freek Beekman, beste Freek, ik ben je dankbaar voor je kritische houding tijdens de totstandkoming van mijn eerste artikel.
- Dr. ir. Lars Mulder, beste Lars, ik dank je voor al je tijd en energie met betrekking tot het microCT onderzoek, ik denk dat het uiteindelijk zijn vruchten heeft afgeworpen.
- Dr. M.A.A.J. van den Bosch, beste Maurice. Het is fijn te ervaren dat er concrete interesse is vanuit de kliniek om onze MR fysisch-georiënteerde bevindingen ook daadwerkelijk in de praktijk toe te passen.
- Dr. Clemens Bos, beste Clemens, bedankt voor de levendige discussies, de hulp met Ultrashort TE imaging, en je kritische blik op mijn manuscripten.

De nucleaire

- Dr. Fred van het Schip, beste Fred, mede dankzij jou ben ik als AiO aangenomen bij het "holmium project". En ook tijdens het afsluiten van mijn AiO-zijn, tijdens de verdediging, zal jij, van achter de tafel betrokken zijn bij de ondervraging. Bedankt. Daarnaast bedank ik je voor je bijdrage aan de wetenschappelijke discussies die we hadden tijdens de holmium meetings.
- Dr. B.A. Zonnenberg, beste Bernard, ik heb altijd versteld gestaan van de dingen die jij weet van allerlei uiteenlopende vakgebieden. Ook jou wil ik bedanken voor je bijdrage aan de wetenschappelijke discussies die we hadden tijdens de holmium meetings.

- Wouter Bult, alias de bultmeister! Naast briljant wetenschappelijk onderzoek op het gebied van microsferen of bollen, hebben wij in de privésfeer voornamelijk met ballen van doen gehad, en wel golfballen. Uiteraard dank ik je “enorm” dat je me overtuigd hebt lid te worden bij golfclub Amelisweerd. Evenzogoed betreur ik het “enorm” dat je zelf nu de handdoek in de ring gooit! Hoe dan ook, onze gezamenlijke activiteiten in het lab, achter de scanner, op de golfbaan of in de kroeg heb ik erg gewaardeerd, of zoals jij het zelf zou zeggen: mijn dankbaarheid grenst aan hondsdolheid!
- Dr. Vente, beste Maarten, je bent me net voorgegaan bij het behalen van de graad van doctor, met een proefschrift waaruit mijns inziens blijkt dat jij beschikt over een ongekende hoeveelheid kennis op het gebied van radio-embolisatie van levertumoren. Ik heb daar dan ook dankbaar gebruik van gemaakt tijdens het schrijven van manuscripten. Veel respect heb ik voor de manier waarop jij met proefdieren omgaat. Bedankt voor de verhelderende discussies, al dan niet onder het genot van een biertje.
- Beste Remmert, dank voor al die momenten waarop jij me geholpen hebt bij het fabriceren van agarose gel fantomen, wat we samen min of meer tot een kunst verheven hebben. Jij had altijd wel weer een praktische oplossing voor de problemen waar ik in het lab tegenaan liep.
- Beste Tim, bedankt voor het wegwijs maken op de SPECT scanners, je assistentie bij allerlei softwarematige uitdagingen (imageJ) en je hulp bij de op MR data gebaseerde dosis berekeningen met behulp van het holmium-166 dosis kernel.
- Alle andere personen van de afdeling nucleaire geneeskunde wil ik graag bedanken voor de gezellige momenten en nuttige discussies, en in het bijzonder: Chris, Agnes, Rosanne, Tjitske en Marnix, bedankt.

Het ISI

- Martijn, alias Bom, mn roomie voor meer dan vier jaar. Zelfs toen jij in Boston zat verzorgde je de muziek via een VPN, super mooi! Bedankt voor de fijne tijd, eerst op de AiO gang, toen op de staf gang, maar ook buiten het werk om in Utrecht, Amsterdam, Berlijn en Honolulu. Je weet pas wat je mist als je t niet meer hebt! Maar wat mij betreft zijn wij er nog niet klaar mee…
- Sara, ik heb onze discussies op wetenschappelijk, maar ook op sociaal maatschappelijk vlak altijd heel erg kunnen waarderen, of het nu was tijdens de MRfys etentjes, de cursus in Essen, een van de ISMRM meetings of gewoon op het terras in Utrecht, bedankt. Laten we daar vooral niet mee ophouden!
- Beste Gerrit, beste Hendrik, de harde kern van het holmium-gerelateerde MR onderzoek, ik wil jullie bedanken voor alle wetenschappelijke discussies en

jullie kritische blikken op mijn manuscripten. Ik hoop niet dat ik al het gras voor jullie voeten heb weggemaaid. Wie weet hebben jullie nog iets aan mijn bevindingen, ik blijf in ieder geval graag betrokken bij jullie onderzoek. Hendrik, jouw enthousiasme werkt aanstekelijk. Gerrit, ik hoop dat je volharding om spin echo's te gebruiken voor kwantificatie tot succes zal leiden.

- Beste Koen en Wilbert, het lijkt me gepast jullie gezamenlijk te bedanken voor de fantastische organisatie van allerlei 'uitjes', zoals de fietsenrally's, de jaarlijkse radiologiefeesten, maar ook de gezelligheid in de stafgang. Zonder smaakmakers zoals jullie is de groep een stuk minder groep. Dank.
- Wilbert, bedankt voor de (on)zinnige discussies en gezelligheid!
- Koen, wie had dat gedacht, een innige wetenschappelijke samenwerking. Bedankt voor het programmeren van de Monte Carlo simulaties, en de gezellige momenten tijdens soeppietijd!
- Beste Rick, uiteindelijk heb ik het aan jou te danken dat ik bij het ISI ben binnengekomen. Daarnaast dank ik je voor je flexibele houding tijdens de afrondende fase van mijn proefschrift.
- Beste Gerard, bedankt voor de hulp bij het oplossen van alle issues tussen mij en mijn computer en het rustig beantwoorden van al mijn vragen.
- Dames van het secretariaat, beste Renée, Jacqueline en Marjan, jullie stonden (en staan) altijd klaar om een helpende hand te bieden, bedankt.
- Beste Nicky, Sandra en Bas, onze reis in de camper rondom Seattle was fantastisch, bedankt.
- Alle andere AiO's en post-docs van het ISI wil ik graag bedanken voor de gezellige momenten en (on)zinnige discussies, en in het bijzonder: Patrik, Joffrey, Maartje, Jeroen, Adrienne, Casper, Stefan en Marius.

De onmisbare ondersteuning

- Beste Greet en Niels, bedankt voor jullie enthousiasme en vaardigheid achter de MRI scanners.
- Beste medewerkers van de fotografie van de afdeling Radiologie, Jan, Eugene, Karin en Roy, bedankt voor de hulp bij het opmaken en printen van posters (veelal last-minute), en voor de lay-out van dit proefschrift.
- Beste dierverzorgers en biotechnici van het GDL, en in het bijzonder Hans Vosmeer en Nico Attevelt, bedankt voor jullie goede zorgen en assistentie bij de experimenten.
- Beste Henk te Biesebeek, jouw directe, snelle en accurate werkwijze kan ik waarderen en heeft mij meerdere malen erg geholpen. Bedankt.

Vrienden en familie

- Ten slotte wil ik ook mijn vrienden en familie bedanken. Een gelegenheid als deze, waarbij je de kans hebt om de waardering voor jarenlange vriendschap op papier te zetten, doet zich maar weinig voor.

- De BMT studievrienden, plus aanhang: Jeroen en Angelique, Saskia en Jean, Bram en Roos, Debbie en Bart, Erik en Inge, Eva en Alexander, Lars en Marielle, Wilfred en Eveline. Bedankt voor de heerlijke 'Ardennenweekendjes', mannanstapavonden en andersoortig gezelligheid!
- Mijn 'Eerselse' homies: Michiel, Freek, Jasper, Brutus, Willem, Sam, Guus, Christel, Thijs en Pieter. Al 15 jaar lang geniet ik van onze avonturen en de onvoorwaardelijke vriendschap. Da ge bedankt zèt dè witte...
- Pieter, dat jij, als representative van de Eersel posse, me wilt bijstaan als paranimf, vind ik fantastisch. En Michiel, heel fijn dat ook jij deze ceremoniële, doch voor mij waardevolle rol, wilt vervullen.
- Broer en zus, lieve Michiel en Sas, niet omdat jullie broer en zus zijn, maar omdat ik bij jullie altijd terecht kan. Bedankt!
- Lieve pap en mam, zo lang ik me kan herinneren, is het heerlijk thuiskomen. Dank voor jullie grenzeloos vertrouwen en onvoorwaardelijke steun. Dank voor alles!

- Lieve Doreen, met jou heb ik alles gedeeld, wanneer het goed ging, maar ook wanneer het tegen zat. Jij hebt me al die jaren bijgestaan met je levensvreugde en intensiteit! Het is heerlijk om nu samen met jou dit hoogtepunt te kunnen vieren, en weer nieuwe avonturen en uitdagen aan te gaan! Kus.

Addenda

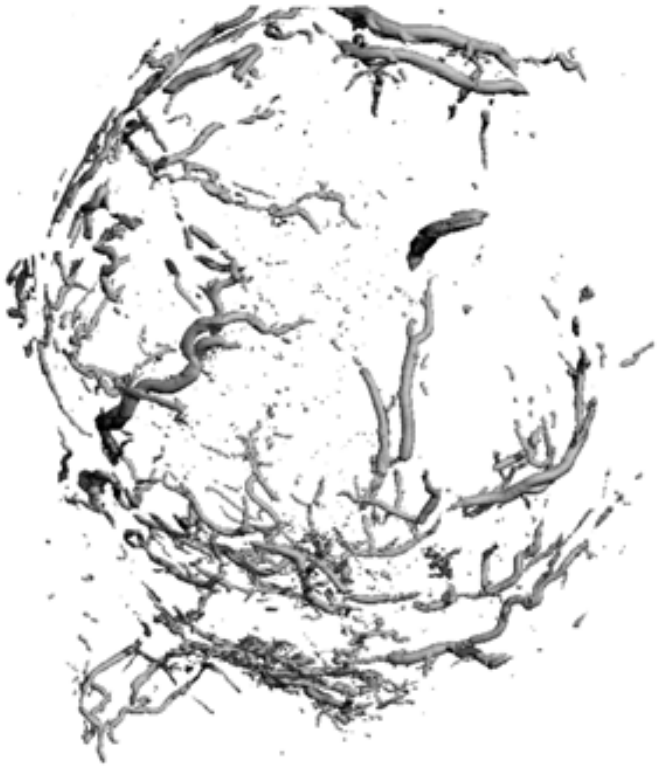

Journal articles

P.R. Seevinck, J-H. Seppenwoolde, T.C. de Wit, J.F.W. Nijsen, F.J. Beekman, A.D. van het Schip, C.J. Bakker. Factors affecting the sensitivity and detection limits of MRI, CT and SPECT for multimodal diagnostic and therapeutic agents. *Anticancer Agents Med Chem. 2007 May;7(3):317-34*

M.A.D. Vente. J.F.W. Nijsen, T.C. de Wit, J.H. Seppenwoolde, G.C. Krijger, **P.R. Seevinck,** A. Huisman, B.A. Zonnenberg, T.S.G.A.M. van den Ingh and A.D. van het Schip. Clinical effects of transcatheter hepatic arterial embolization with holmium-166 poly(L -lactic acid) microspheres in healthy pigs. *Eur J Nucl Med Mol Imaging. 2008 Jul;35(7):1259-71*

P.R. Seevinck, J-H. Seppenwoolde, J. Zwanenburg, J.F.W. Nijsen and C.J.G. Bakker. FID sampling superior to spin echo sampling for T_2^*-based quantification of holmium-loaded microspheres: Theory and experiment. *MRM 2008 Dec;60(6):1466-76*

M. Talelli, C.J.F. Rijcken, T. Lammers, **P.R. Seevinck,** G. Storm, C.F. van Nostrum, W.E. Hennink. Superparamagnetic iron oxide nanoparticles encapsulated in biodegradable thermosensitive polymeric micelles: Towards a combined drug delivery and imaging system. *Langmuir. 2009 Feb 17;25(4):2060-7*

W. Bult, **P.R. Seevinck,** G.C. Krijger, T. Visser, W.E. Hennink, C.J.G. Bakker, A.D. van het Schip, J.F.W. Nijsen. Microspheres with ultra high holmium content for radioablation of malignancies. *Pharm. Res. 2009 Feb 25;26(6):1371-1378*

P.R. Seevinck, C. Bos, M.A. Viergever and C.J.G. Bakker. Ultrashort T2* relaxometry using conventional multiple gradient echo sampling with S_0 estimation: Validation with quantitative UTE (qUTE) imaging. *Submitted*

P.R. Seevinck, H de Leeuw C. Bos, and C.J.G. Bakker. Highly localized positive contrast of small paramagnetic objects using 3D center-out RAdial Sampling with Off-resonance Reception (RASOR). *Submitted*

P.R. Seevinck, L. Mulder, J.F.W. Nijsen, M.A.D. Vente, M.A.A.J. van den Bosch, C.J.G. Bakker. Quantitative 3D microCT imaging of holmium-166 microspheres in a rabbit liver tumor model after transarterial radioembolization. *Submitted*

P. R. Seevinck, K. L. Vincken, G. H. van de Maat, M.A. Viergever, and C. J.G. Bakker. Predicting transverse relaxivity for MR-based quantification of strongly magnetized micron-sized particles or cells subjected to diffusion: theory, experiments and Monte Carlo simulations. *Submitted*

P.R. Seevinck, T.C. de Wit, J.F.W. Nijsen, M.A.D. Vente and C.J.G. Bakker. MR-based dosimetry of holmium-166 loaded poly (L-lactic acid) microspheres for internal radiation therapy treatment planning. *In preparation*

M.A.D. Vente, T.D. de Wit, M.A.A.J. van den Bosch, W.Bult, **P.R. Seevinck**, B.A. Zonnenberg, H.W.A.M. de Jong, G.C. Krijger, C.J.G. Bakker, A.D. van het Schip, J.F.W. Nijsen. Holmium-166 poly(L-lactic acid) microsphere radioembolization of the liver: technical aspects studied in a large animal model. *European Radiology. In press*

M.A.D. Vente, W. Bult, K. Peremans, H. Haers, E. Vandermeulen, **P.R. Seevinck**, A.D. van het Schip, R. de Roos, C.J.G. Bakker, G.C. Krijger, J.F.W. Nijsen. Interstitial microbrachytherapy using small holmium-166 acetylacetonate microspheres for radioablation of intrahepatic malignancies. *Submitted*

Conference proceedings (abstracts)

(1st and 2nd authorship only)

P.R.Seevinck, K.L. Vincken, G.H. van de Maat, C.J.G. Bakker. Quantitative analysis of transverse relaxation due to strongly magnetized micron-sized spheres subjected to unrestricted diffusion in gradient echo and spin echo imaging: Validation of theory with experiments and Monte Carlo simulation. *International Society of Magnetic Resonance in Medicine, Honolulu, Hawaii, USA, 2009*

P.R. Seevinck, H. de Leeuw, C. Bos, C.J.G. Bakker. High positive contrast generation of a subvoxel susceptibility deviation in ultrashort TE (UTE) radial center-out imaging at 3T. *International Society of Magnetic Resonance in Medicine, Honolulu, Hawaii, USA, 2009*

P.R. Seevinck, G. Varma, H. de Leeuw, J. Senegas, T. Schaeffter, C.J.G. Bakker. Selective depiction of holmium-loaded microspheres (HoMS) using susceptibility gradient mapping (SGM): initial experience in animal models. *International Society of Magnetic Resonance in Medicine, Honolulu, Hawaii, USA, 2009*

W. Bult, **P.R. Seevinck**, G.C. Krijger, C.J.G. Bakker, W.E. Hennink, A.D. van het Schip, J.F.W. Nijsen. Multifunctional microspheres with ultrahigh holmium load for imaging and therapy *International Society of Magnetic Resonance in Medicine, Honolulu, Hawaii, USA, 2009*

H. de Leeuw, **P.R. Seevinck**, G.H. van de Maat, and C.J.G. Bakker. High resolution phase gradient mapping as a tool for the detection and analysis of local field disturbances. *International Society of Magnetic Resonance in Medicine, Honolulu, Hawaii, USA, 2009*

G.H. van de Maat, **P.R. Seevinck**, K.L. Vincken, H. de Leeuw, and C.J.G. Bakker. Multi-echo spin-echo (MESE) signal behavior of paramagnetic holmium-166 loaded microspheres for radiotherapy: experiment and simulation. *International Society of Magnetic Resonance in Medicine, Honolulu, Hawaii, USA, 2009*

P.R. Seevinck, G. Varma, H. de Leeuw, J. Senegas, T. Schaeffter, C.J.G. Bakker. Selective depiction of holmium-loaded microspheres (HoMS) using susceptibility gradient mapping (SGM): initial experience in animal models. *International Society of Magnetic Resonance in Medicine Benelux, Antwerp, Belgium, 2008*

P.R. Seevinck, J-H. Seppenwoolde, J.J.M. Zwanenburg, C.J.G. Bakker. Improved T2* based quantification of holmium-loaded microspheres in gels and liver tissue using multiple gradient echo sampling of FID rather than SE signals. *International Society of Magnetic Resonance in Medicine, Toronto, Canada, 2008*

P.R. Seevinck, C. Bos, C.J.G. Bakker. Ultrashort T2* relaxometry using conventional multiple gradient echo sampling with S_0 fitting: Validation with quantitative UTE (QUTE) imaging. *International Society of Magnetic Resonance in Medicine, Toronto, Canada, 2008*

P.R. Seevinck, W. Bult, JFW Nijsen, M.A.D. Vente, R. de Roos, A.D. van het Schip, C.J.G. Bakker. Highly-loaded holmium microspheres for test dose detection and biodistribution prediction in internal radiation therapy of liver malignancies. *International Society of Magnetic Resonance in Medicine, Toronto, Canada, 2008*

P.R.Seevinck, J.H. Seppenwoolde, J.J.M. Zwanenburg, C.J.G. Bakker. Ultradense sampling of FID and SE signals using an interleaved multiple gradient echo sequence for improved T2* mapping. *International Society of Magnetic Resonance in Medicine, Berlin, Germany, 2007*

P.R.Seevinck, J.H. Seppenwoolde, T.C. de Wit, J.F.W. Nijsen, F.J. Beekman, A.D. van het Schip, C.J.G. Bakker. Sensitivity and detection limits of MRI, CT and SPECT for Holmium-loaded microspheres. *International Society of Magnetic Resonance in Medicine, Seattle, Washington, USA, 2006*

P.R.Seevinck, J.H. Seppenwoolde, T.C. de Wit, J.F.W. Nijsen, F.J. Beekman, A.D. van het Schip, C.J.G. Bakker. Multimodality imaging of therapeutic holmium-loaded poly(L-lactic acid) microspheres: Sensitivity and detection limits of MRI, CT, and SPECT. *European Association of Nuclear Medicine, Athens, Greece, 2006*

Invited presentations

P.R. Seevinck. MR guided drug delivery: holmium-loaded microspheres for trans-catheter radioembolization of liver malignancies: experiences in animal models. *Joint meeting of the 'MR of cancer' and ' Molecular and cellular imaging' study groups, International Society of Magnetic Resonance in Medicine, Honolulu, Hawaii, USA, 2009*

P.R. Seevinck, C. Bos, W. Bult, JFW Nijsen, C.J.G. Bakker. Quantitative and qualitative MR imaging using Ultrashort TE at 3T for image guided radioembolization of liver metastases. *7th International symposium on High Field MR in clinical applications, Bonn, Germany, 2008*

Addenda

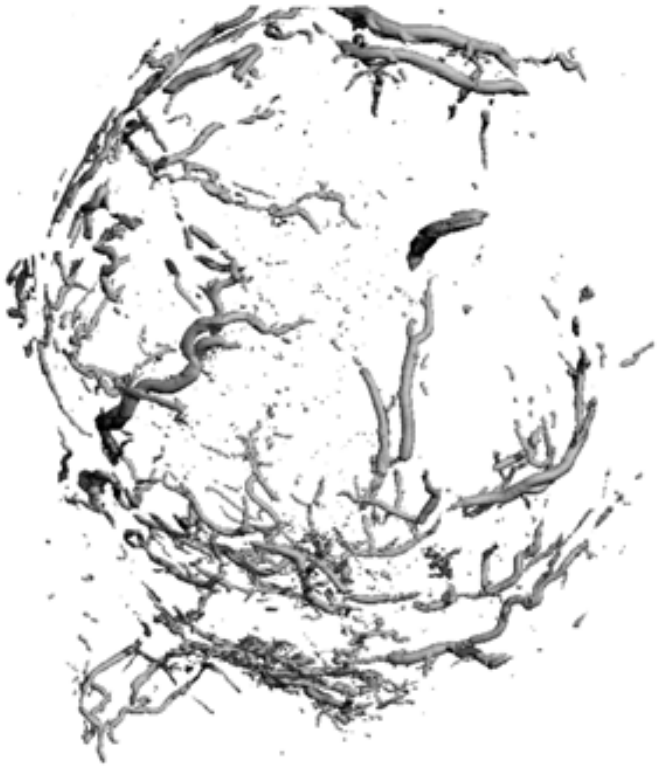

Work hard, play hard.

The author was born January 20, 1979, in Pretoria, South Africa. He graduated from grammar school (Rythovius College, Eersel, the Netherlands) in 1997 and started studying biomedical engineering at the Eindhoven University of Technology in the same year. Before completing his B.Sc degree in 2000, he decided to take some time off to explore his own mind as well as the west-coast of the United Stated, traveling from Canada to Mexico in a home-built camper van (1979 Ford E150 V8 econoline).

Upon his return, he decided to continue his studies. As a graduate student in 2002, he discovered the beauty of Magnetic Resonance Imaging during an internship at the Centre for Magnetic Resonance, University of Queensland, Brisbane, Australia. In 2004 he obtained his M.Sc degree in the Biomedical NMR group of prof. dr. Klaas Nicolay, Department of Biomedical Engineering, Eindhoven University of Technology. His master's thesis was entitled: "High resolution diffusion tensor imaging, as applied to *ex vivo* mouse heart".

In 2005 he accepted a PhD position at the Image Sciences Institute (prof. dr. ir. Max Viergever and dr. Chris Bakker) and the Department of Nuclear Medicine of the University Medical Center Utrecht. During this period he conducted research into novel MR image acquisition techniques and quantitative image processing. The research was aimed in particular at improving biodistribution assessment and dose calculations of ^{166}holmium-loaded microspheres for the planning, image-guidance and evaluation of internal radiation therapy of unresectable liver malignancies.

Addenda

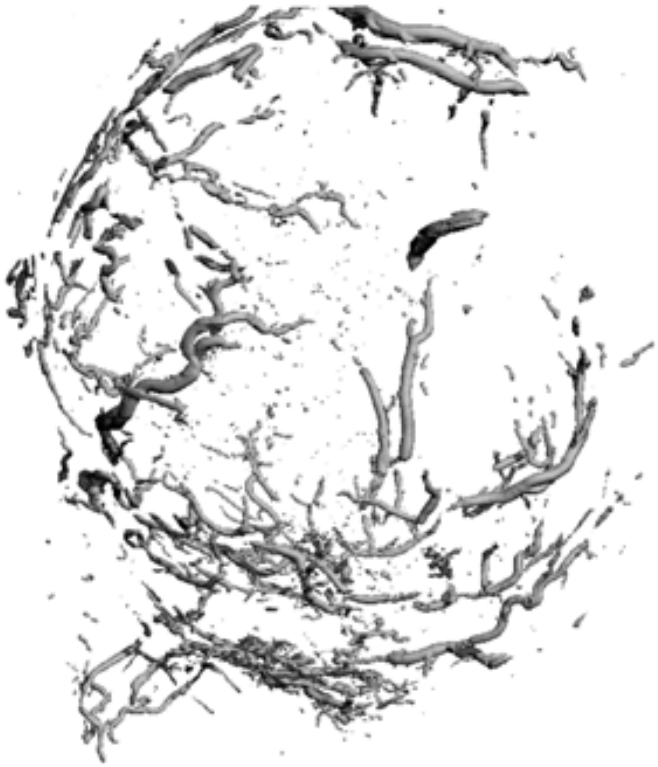

Color figures

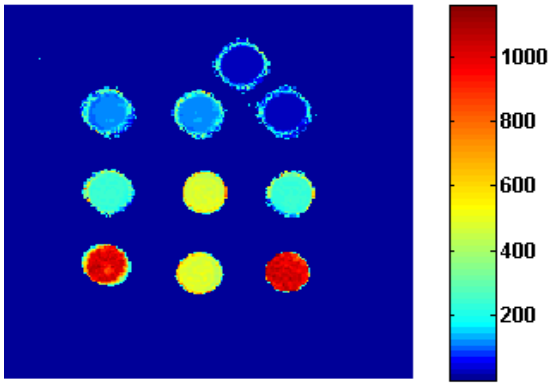

Chapter 3, Figure 2 *A) Calculated R_2* relaxation rate map of the HoAcAc-MS dilution series in duplicate, containing [0.0; 0.5; 0.9; 1.9; 3.8] mg/ml agarose.*

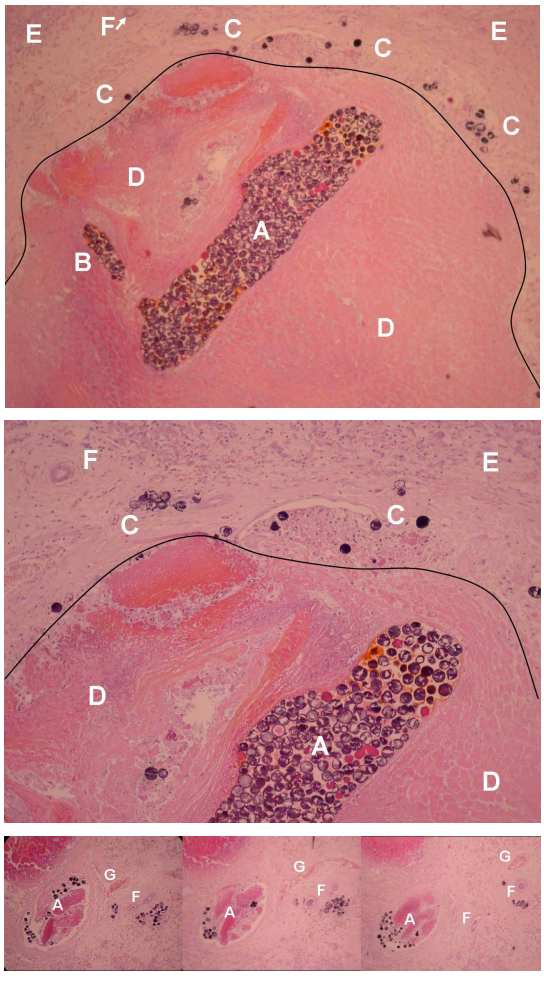

Chapter 4, Figure 9 *Light micrographs of HE-stained 4-µm thick liver tissue sections after radioembolization with ^{166}Ho-PLLA-MS (original magnification, x40). a) Liver tissue section depicting: (A) a large Ho-PLLA-MS cluster longitudinally stacked in an arteriole, (B) a small side branch arteriole containing Ho-PLLA-MS, (C) connective tissue with small Ho-PLLA-MS clusters and single Ho-PLLA-MS, (D) necrotic liver tissue, (E) tumor tissue, (F) bile duct. b) Enlarged view of image a). c) Three slices sectioned at 80 µm apart, showing an arteriole (A) with several Ho-PLLA-MS, indicating intermitted longitudinal microsphere clustering. Also shown are blood vessels (H) belonging to the portal system and bile ducts (G).*

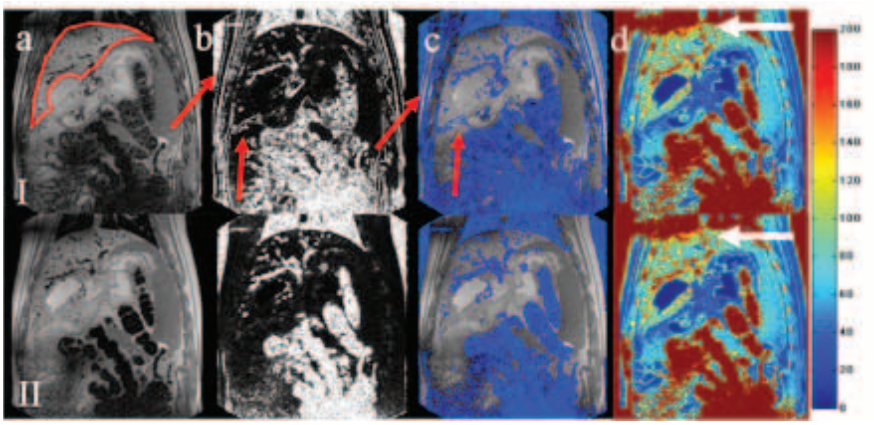

Chapter 5, Figure 3 *In vivo coronal images of a pig liver, after administration of 600 mg of HoMS, obtained using a 3D multiple gradient echo scan in breath-hold. Row I represents the 1st echo, row II the 3rd echo. a) T_2*-w images, with the liver delineated in red. b) 2D SG maps of the left-right and through-plane echo shift, discarding the feet-head direction. c) SG maps in blue overlaid on the T_2*-w images. d) R_2* maps. Red arrows indicate positive contrast generation at water-fat interfaces. White arrows indicate the influence of macrospcopic magnetic field inhomogeneities on the R_2* value, in the vicinity of the tissue-air interface between liver and lung.*

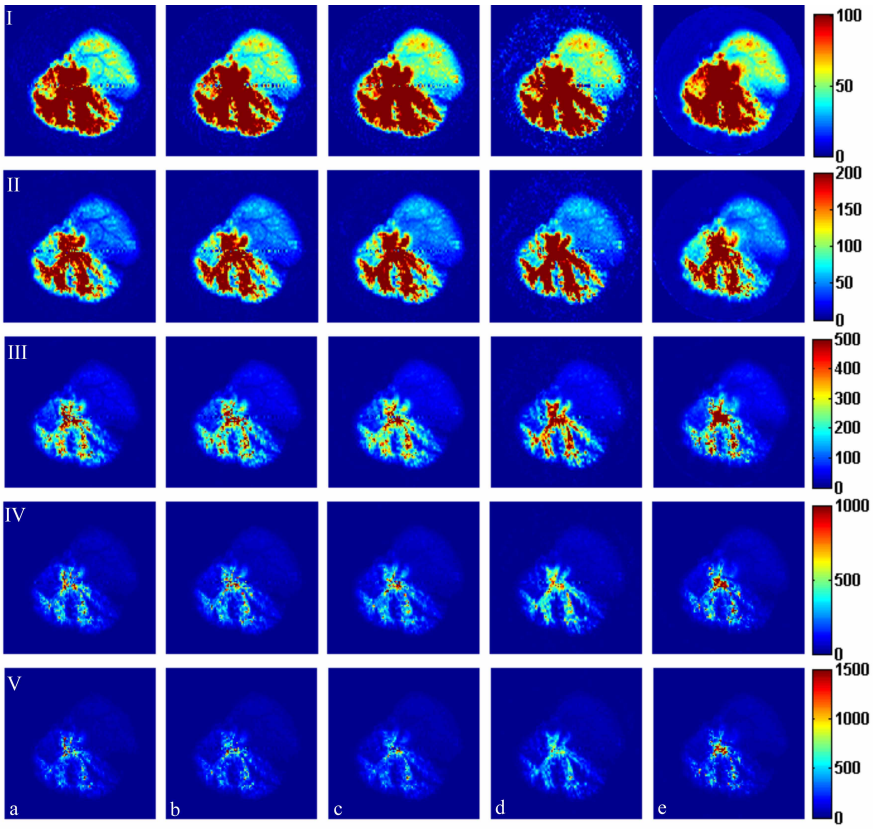

Chapter 7, Figure 6 *R_2* maps of an excised rabbit liver with HoMS determined with iMGESE with different values for TE_{SE}; a) 35.0ms; b) 25.0ms; c) 13.9ms; d) 8.2ms and e) iMGEFID. Different color scaling is used in series I, II, III, IV and V, with maximum R_2* values in s^{-1} of 100, 200, 500, 1000 and 1500, respectively. Similar R_2* values were estimated in regions of liver tissue containing no or low concentrations of HoMS for both MGEFID and MGESE data, as shown in image series I and II. In regions containing high HoMS concentrations distinct differences are observed between iMGEFID and iMGESE data. The iMGEFID image (e) shows more pixels with a high R_2* values as shown in image series IV and V. Furthermore, the maximum R_2* value estimated with MGEFID is higher than the maximum R_2* value for MGESE and exceeds 1500 s^{-1}.*

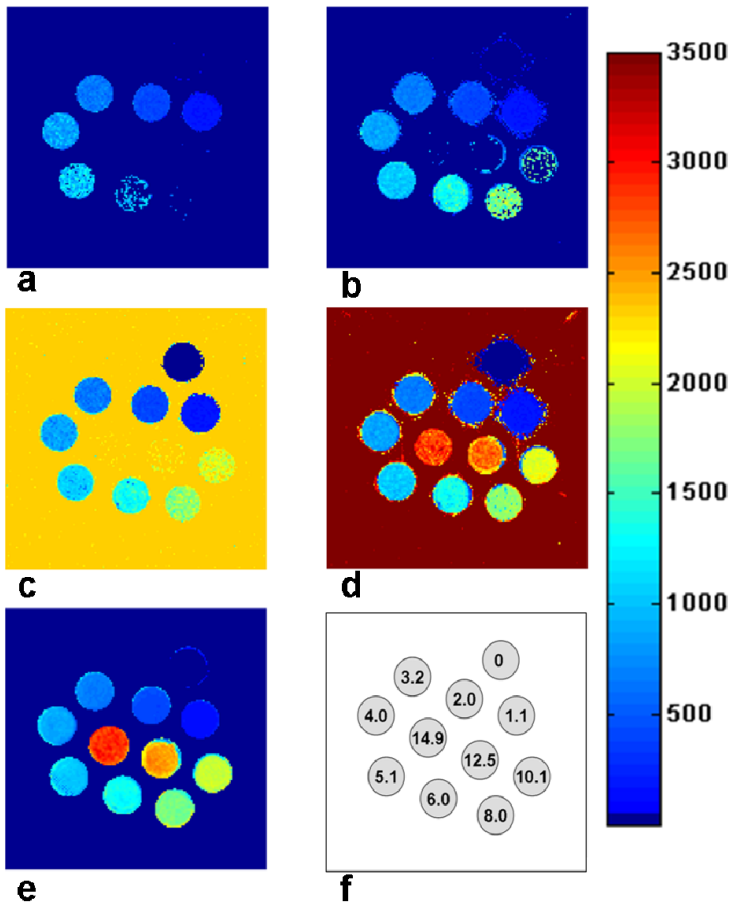

Chapter 8, Figure 3 *R_2^* maps of the Ho-PLLA-MS dilution gel phantom determined with conventional R_2* estimation (a, b), with S_0-fitting (c, d) and using qUTE data (e). MGE data was acquired with low (a, c) and high SNR (b, d) by increasing the number of signal averages from 1 (a, c) to 32 (b, d). Increasing the SNR increased the detectable R_2^* range, both with conventional fitting (a, b) and with S_0-fitting (c, d). S_0-fitting dramatically increased the detectable R_2^* range compared to conventional WLS fitting (b, d). When using the S_0-fitting algorithm, the background was assigned the value of $R_{2\,max}^*$, as shown in c) and d). A good agreement is shown between the R_2^* map obtained from qUTE data and with high SNR data in combination with S_0-fitting (d, e). A schematic overview of the Ho-PLLA-MS concentrations in mg/ml is depicted in f).*

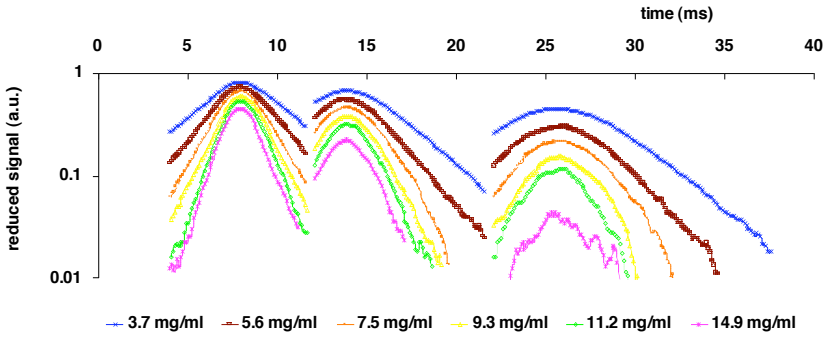

Chapter 9, Figure 2 *b SE signal decay time course of the agarose gel HoMS dilution series obtained determined using MC simulations using different values of TESE (8.2; 14.0; 26.0ms).*

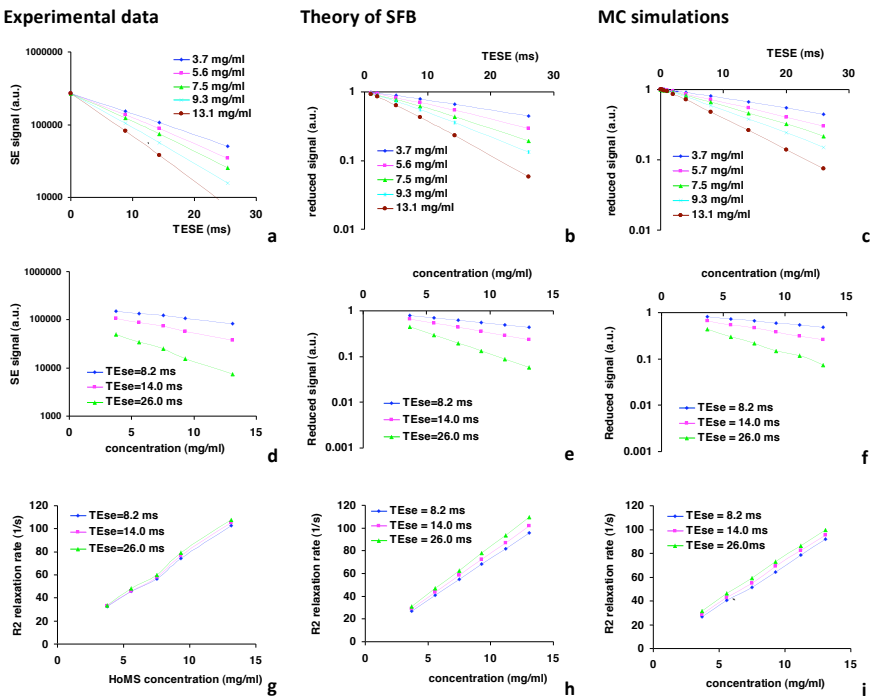

Chapter 9, Figure 3 *The logarithm of the single SE signal peak of an agarose gel HoMS dilution series as a function of TESE, demonstrating a slight deviation from linear exponential behavior for a) experimental data, b) SFB theory and c) Monte Carlo simulations. Single SE signal behavior as a function of particle concentration demonstrates linear exponential behavior for d) experimental data, e) SFB theory and f) Monte Carlo simulations. For each value of TESE linear r_2^* relaxivity was found for the HoMS dilution series, as concluded from the linear relation between the R_2^* relaxation rate and the particle concentration observed for Experimental data (g), SFB theory (h) and MC simulations (i).*

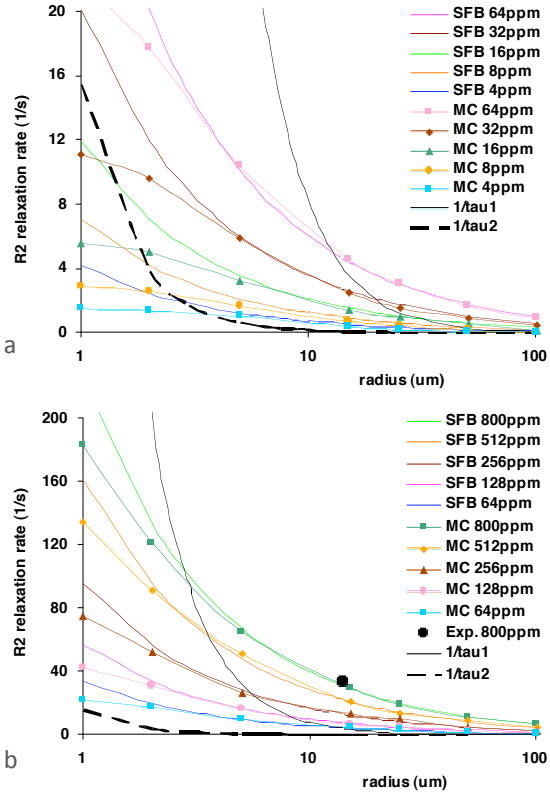

Chapter 9, Figure 7 *R_2 obtained with SFB theory (colored lines) and MC simulations (symbols) plotted against particle radius for varying Δχ. Figures a) and b) depict relatively small (<64 ppm) and large (64 800 ppm) Δχ values, respectively. The strict and less strict SFB criteria are depicted by the continuous line and the dashed line, respectively. A constant volume fraction of ς = 0.00265, D = 2.1 μm²/ms and B_0 = 1.5T, TE_{SE} = 14ms were used.*

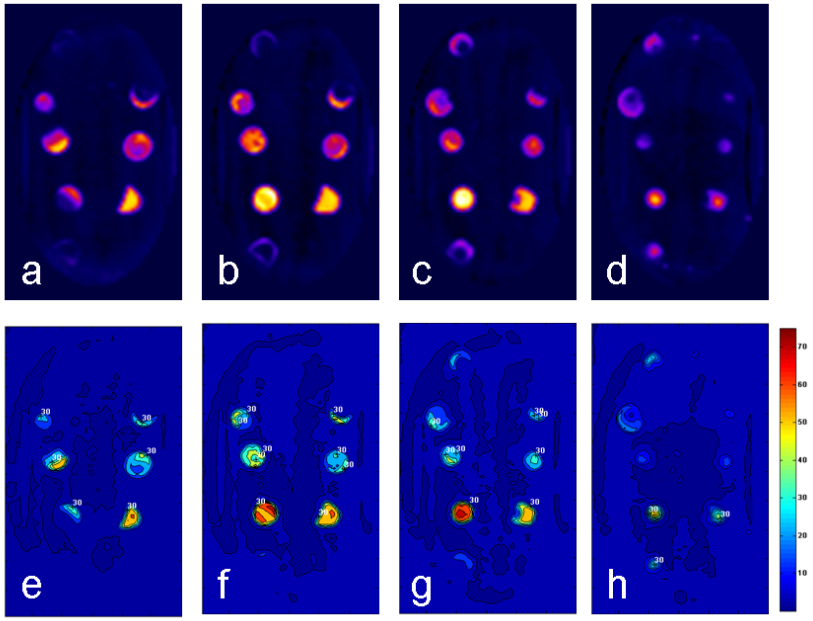

Chapter 10, Figure 3 *Qualitative (a-d) and quantitative (e-h) MR-based dose maps of four slices. Even-numbered slices are shown.*

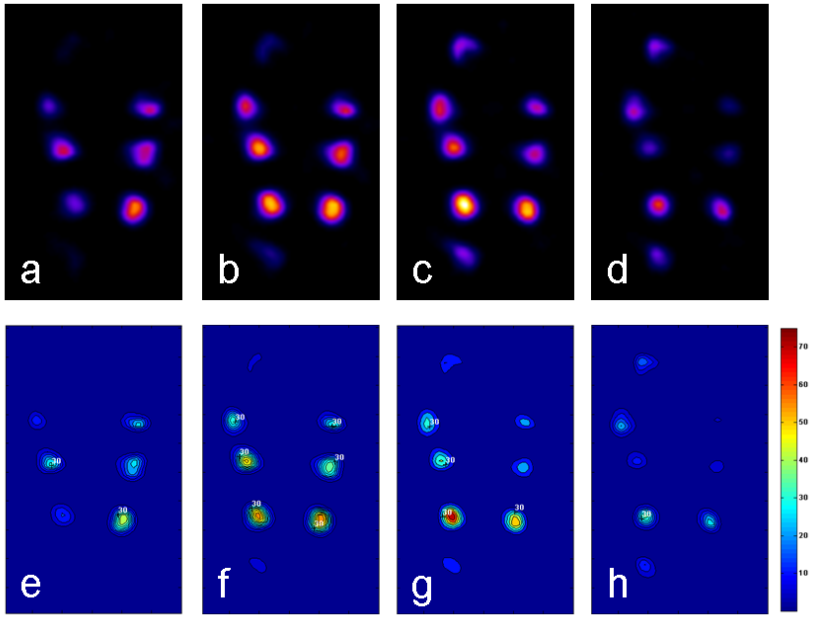

Chapter 10, Figure 4 *Qualitative (a-d) and quantitative (e-h) SPECT-based dose maps of four slices. Even-numbered slices are shown.*